Theory and Applications of the Aerodynamic Aerosol Classifier

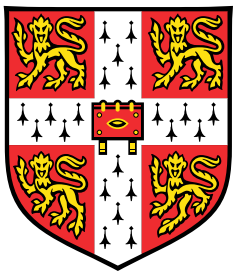

Tyler James Johnson

Department of Engineering
University of Cambridge

This dissertation is submitted for the degree of
Doctor of Philosophy

Churchill College

October 2020

This thesis is dedicated to my parents,
Kris and Jim Johnson,
for their unwavering support and inspiration.

Declaration

This dissertation is the result of my own work and includes nothing which is the outcome of work done in collaboration except as declared in the Preface and specified in the text. It is not substantially the same as any that I have submitted, or, is being concurrently submitted for a degree or diploma or other qualification at the University of Cambridge or any other University or similar institution except as declared in the Preface and specified in the text. I further state that no substantial part of my dissertation has already been submitted, or, is being concurrently submitted for any such degree, diploma or other qualification at the University of Cambridge or any other University or similar institution except as declared in the Preface and specified in the text. It does not exceed the prescribed word limit for the relevant Degree Committee.

Tyler James Johnson
October 2020

Abstract

Aerosols are found in almost all indoor or outdoor environments, and have significant impacts on climate, environment and human health. These implications and prevalence have driven rapid growth in aerosol research and led to a variety of particle instruments being developed over the past seven decades. The Aerodynamic Aerosol Classifier (AAC) is a relatively new instrument, which selects aerosol particles based on their relaxation times or aerodynamic diameters. This dissertation demonstrates that the novel operating principle of the AAC has the potential to address a variety of challenges facing the field of aerosol science.

To explore the potential, this work advances the development and knowledge of the AAC, resulting in novel methodologies for measuring the aerodynamic size and bipolar charge distributions of an aerosol. First, the performance of the AAC is determined by characterising its transfer function experimentally using tandem AACs. These results demonstrate that the transmission efficiency of the AAC is 2.6 to 5.1 times higher (which corresponds to higher measurement signals) than that of a neutraliser-Differential Mobility Analyser (DMA), a system that is widely-used in aerosol research. However, the AAC transfer function is 1.3 to 1.9 times broader than predicted by theory.

Using this characterised transfer function, the deconvolution theory to accurately measure the aerodynamic size distribution of an aerosol by stepping the AAC setpoint whilst in series with a particle detector is developed and validated experimentally against commercial instruments. While this approach overcomes the low classification resolutions and set measurement ranges (which focus on larger particles) of previous methodologies for aerodynamic sizing, it requires the AAC setpoint to be stepped and stabilised before each measurement, which forces trade-offs between measurement time and step resolution. To overcome this limitation, this thesis is the first to develop and validate the transfer function and its corresponding deconvolution theory to allow the AAC setpoint to be scanned continuously, rather than stepped, during size distribution measurements. This approach is validated experimentally against the stepping AAC (agreement within 2% if aerosol source stability is considered) and calibration particles (agreement within 8.7%). Scanning the AAC is also shown to reduce its measurement time (1.1 to 2.6 times faster), while increasing the resolution of the measured size distribution (6.1 to 9.0 times higher classes per decade).

This work is also the first to leverage the advantages of the AAC to develop improved methodologies for measuring the bipolar charge distribution of spherical particles. It is demonstrated that using an AAC in tandem with a DMA overcomes significant limitations of the commonly used tandem DMA system (such as multiply-charged particle artefacts and low measurement signals). This approach is used to quantify the significant charging effects (up to a 0.084 difference in a charge fraction) of different sample flow rates through a radioactive neutraliser, free-ions downstream of the neutraliser, or different neutralisers. To study non-spherical particles, this approach is then expanded by demonstrating an AAC and DMA in tandem can select homogeneous, non-spherical particles. The bipolar charge distribution of the homogeneous particles is then measured using another DMA downstream. The bipolar charging of non-spherical, soot aggregates is shown to deviate significantly (up to a 0.069 difference in a charge fraction) from widely-used charging theory, but can be accounted for using a charging equivalent diameter.

The novel AAC methodologies developed and validated in this thesis are intended to allow others to further characterise the sizing and bipolar charging of aerosols. There are also opportunities to expand the AAC to other applications based on the foundational theory developed in this work. Ultimately, these outcomes will lead to a greater understanding of aerosol science.

Acknowledgements

I would like to express my gratitude to my supervisor, Adam Boies, for his significant support and insights. His enthusiasm for science and wide range of knowledge is inspiring. I would also like to acknowledge the considerable guidance and contributions of Jason Olfert and Jonathan Symonds. I truly enjoyed working with all three of them, and appreciate the substantial time and effort they invested in me and this project.

My pursuit of a PhD would also not have been possible without the assistance of the Sir Winston Churchill Society of Edmonton, Cambustion and C-FER Technologies. Their generous support led to this amazing opportunity and allowed me to focus on my studies.

I was also fortunate to work with a variety of collaborators. In addition to those previously mentioned, I would like to acknowledge the expertise, support and insights of Robert Nishida, Martin Irwin and Xiao Zhang. The contributions of each collaborator are highlighted by a footnote at the start of each chapter. I look forward to future collaborations.

The experiments completed in this project utilized equipment from Cambustion, and a large portion of the resulting data was collected at their facility. This work would not have been possible without the help of Chris Nickolaus, Kingsley Reavell, David Walker, Simon Payne, Andrew Ellison, Joe Evans, Kristian Hoffman and Zoran Hadzhiivanov. In addition to being a helpful resource at Cambustion, I also appreciate the insights and support provided by Nick Collings as the project advisor. I enjoyed the camaraderie and innovative atmosphere of Cambustion.

I would also like to thank Rebecca Sawalmeh for her general support at Churchill College and help settling into Cambridge. The support of Fiona Smail within the research group and laboratory are also greatly appreciated. As well, I would like to acknowledge my colleagues and friends, including Brian, Robert and Christian, for the helpful discussions and memorable experiences in Cambridge.

I want to thank my family for their unwavering support. They instilled in me the importance of doing your best and working towards your goals. Above all, I thank my wife, Kim, for her endless encouragement and understanding. She wholeheartedly supported this crazy idea of moving to another continent and returning to university.

Table of contents

List of figures

List of tables

Nomenclature

Acronyms and Abbreviations

^{137}Cs	Caesium-137 Isotope
^{14}C	Carbon-14 Isotope
^{204}Tl	Thallium-204 Isotope
^{210}Po	Polonium-210 Isotope
^{241}Am	Americium-241 Isotope
^{63}Ni	Nickel-63 Isotope
^{85}Kr	Krypton-85 Isotope
^{90}Sr	Strontium-90 Isotope
AAC	Aerodynamic Aerosol Classifier
Abs	Absolute
AEMSA	Aerosol Electrical Mobility Spectrum Analyser
AMS	Aerosol Mass Spectrometer
APM	Aerosol Particle Mass Analyser
APS	Aerodynamic Particle Sizer
Ave	Average
BCMS	Bipolar Charge Measurement System
BOLAR	Bipolar Charge Analyser

CGO Crumpled Graphene Oxide

CMD Count Median Diameter

CNF Carbon Nanofibre

CNT Carbon Nanotube

CPC Condensation Particle Counter

CPD Classes per Decade

CPMA Centrifugal Particle Mass Analyser

D Diffusing

DAPS Differential Aerodynamic Particle Sizer

DEHS Di-Ethyl-Hexyl-Sebacat

DMA Differential Mobility Analyser

DMPS Differential Mobility Particle Sizer

DOP Di-Octyl Phthalate

DOS Di-Octyl Sebacate

E-SPART Electrical Single Particle Aerodynamic Relaxation Time

EAA Electrical Aerosol Analyser

ELPI Electrical Low Pressure Impactor

ESP Electrostatic Precipitator

FWHM Full Width at Half Maximum

GMD Geometric Mean Diameter

GSD Geometric Standard Deviation

HEPA High Efficiency Particulate Arrestance

HF High-flow

ISO International Organization for Standardization

Kn Knudsen number

LDV Laser Doppler Velocimetry

LF Low-flow

LT Limited Trajectory

MC Multiple Charging

MOUDI Micro-Orifice Uniform Deposit Impactor

MPSS Mobility Particle Size Spectrometer

MWCNT Multi-wall Carbon Nanotube

NaCl Sodium Chloride (i.e. salt)

ND Non-Diffusing

NGI Next Generation Impactor

OMAC Opposed Migration Aerosol Classifier

OPC Optical Particle Counter

$PM_{2.5}$ Particulate matter consisting of particles smaller than 2.5 µm

POA Poly (α-olefin) oligomer

PS Particle Streamline

PSL Polystyrene Latex

SEM Scanning Electron Microscope

SMAC Surface-discharge Microplasma Aerosol Charger

SMPS Scanning Mobility Particle Sizer

SPART Single Particle Aerodynamic Relaxation Time

TAAC Tandem Aerodynamic Aerosol Classifiers

TDMA Tandem Differential Mobility Analysers

TEOS Tetraethoxysilane

TF Transfer Function

TOF Time-of-Flight

UDA Up-Down Agreement

Classifier Properties

$\dot{\omega}$ Instantaneous angular acceleration/deceleration of AAC classifier (rad s^{-2})

ω Instantaneous angular speed of AAC classifier (rad s^{-1})

t_f Resident time of particles in classifier assuming plug flow (s)

E Force field within classifier (N kg^{-1} for centrifugal)

F Force within classifier (N)

K Time integral of the angular speed function of the AAC classifier (s^{-1})

L Classification length of classifier (m)

Q Flow rate (m^3 s^{-1})

r Radial position within classifier (m)

r_1 Inner radius of classifier (m)

r_2 Outer radius of classifier (m)

U Mean speed of gas flow in classifier (m/s)

V Electric potential difference of DMA classifier or ESP (V)

z Axial position within classifier (m)

Detector Properties

η Non-dimensional counting efficiency of particle detector

t_c Counting time of particle detector (s)

t_{det} Response time of particle detector, including the transport time of the particles within detector (s)

Transfer Function Properties

$\bar{\Omega}$ Non-dimensional, average transfer function of classifier over counting time of particle detector

$\bar{\tau}^*$ Average particle relaxation time setpoint of AAC over counting time of particle detector (s)

β Non-dimensional flow parameter of classifier

β^* Non-dimensional deconvolution parameter of transfer function

d_a^* Particle aerodynamic diameter setpoint of AAC (m)

δ Non-dimensional classifier flow parameter

δ_{dep} Non-dimensional deposition parameter

λ_d Non-dimensional diffusional transmission efficiency

λ_Ω Non-dimensional transmission efficiency of classifier

λ_e Non-dimensional classifier entrance/exit transmission efficiency

μ_Ω Non-dimensional width factor of transfer function

N_{det} Particle number concentration that passes through the classifier (cm^{-3})

Ω Non-dimensional transfer function of classifier

τ^* Particle relaxation time setpoint of AAC (s)

τ_x Particle relaxation time of $\Omega_{AAC,sc}$ boundary x (s)

τ_{max} Maximum particle relaxation time corresponding to non-zero value of transfer function (s)

τ_{min} Minimum particle relaxation time corresponding to non-zero value of transfer function (s)

$\tau_{x,tc}$ Particle relaxation time of $\Omega_{AAC,sc}$ boundary x shifted by t_c (s)

A Non-dimensional area under transfer function

c_{sc} Constant portion of K_{sc} when in terms of t_m (s^{-1})

$c_{\mu x}$ Coefficients x of fit for transfer function broadening (Non-dimensional or non-physical units depending on the constant)

$c_{\tau x,\mathrm{B}}$ Grouped constant of boundary x for $\Omega_{\mathrm{AAC,sc,PS,B}}$ (s)

$c_{\tau x}$ Grouped constant of boundary x for $\Omega_{\mathrm{AAC,sc,LT}}$ (s)

c_{Bx} Constant x of $\Omega_{\mathrm{AAC,sc,PS,B}}$ (Non-dimensional or s^{-1} depending on the constant)

c_{fx} Constant x of $\Omega_{\mathrm{AAC,sc,LT}}$ (Non-dimensional or s^{-1} depending on the constant)

f_x Non-dimensional component x of transfer function based on limited trajectory theory

$h_{\max}$ Non-dimensional maximum height of transfer function

L_{eff} Length of circular tube with the same diffusion deposition as the classifier (m)

$w_{\max}$ Non-dimensional maximum width of transfer function

Math Properties

Δ Mathematical difference

$\delta(x-a)$ Dirac delta function

$\mathcal{EI}(x)$ Exponential integral function

γ Euler's Constant (0.5772156649)

$\mathcal{H}(x-a)$ Heaviside function

$\ln(x)$ Natural logarithmic function (i.e. with base e)

$\log(x)$ Logarithmic function with base 10

$\mathcal{F}(x)$ Generalized hypergeometric function

$\mathcal{J}(x)$ Integral of $j(x)$ with respect to x

$j(x)$ Generic mathematical function that is only a function of x

a Generic constant for integral forms/definition of functions

b Generic constant for integral forms

C Constant that is any real number and greater than one

p Constant that is any real number

u Generic variable for substitutions or integration by parts or Uncertainty

v Generic variable for integration by parts

w Generic variable for common equation forms or integration by parts

x Generic variable for generic functions or for subscripts of boundary constants of transfer function

y Generic variable for common equation forms/integration by parts, or subscripts of boundary constants of transfer function

Scanning Properties

τ_{sc} Time constant of scan (s)

t_d Delay time for particles to travel from classifier outlet to particle detector and be detected (s)

t_{in} Inlet time of particles during scan (s)

t_m Measurement time of particles (i.e. time exit classifier) during scan (s)

t_r Time the particle detector reports its concentration measurement relative to the start of the scan (s)

t_{sc} Scan time (s)

ω_E Angular speed of AAC classifier at end of scan (rad s^{-1})

ω_S Angular speed of AAC classifier at start of scan (rad s^{-1})

n_{sc} Non-dimensional number of measurements collected during scan

t Time (s)

t_t Residence time of classified particles in the tubing between the classifier outlet and detector inlet (s)

Other Instrument Properties

$\bar{V}_t$ Average flow velocity within the tube between classifier outlet and inlet of particle detector (m/s)

d_t Inner diameter of tube between classifier outlet and inlet of particle detector (m)

$d_{\mathrm{a,50}}$ Particle 50% aerodynamic cut-off diameter corresponding to a particular ELPI impactor stage (m)

I Current measured from particle grounding on particular ELPI impactor stage (A)

L_{t} Length of tube between classifier outlet and inlet of particle detector (m)

Aerosol Properties

α_{c_c} Non-dimensional coefficient to calculate the Cunningham slip correction factor (2.33)

β_{c_c} Non-dimensional coefficient to calculate the Cunningham slip correction factor (0.966)

χ Non-dimensional shape factor of particle

d_{a} Aerodynamic diameter of particle (m)

d_{m} Mobility diameter of particle (m)

$\frac{\mathrm{d}N}{\mathrm{d}\log x}$ Spectral density of aerosol in terms of a particle property x (cm^{-3})

γ_{c_c} Non-dimensional coefficient to calculate the Cunningham slip correction factor (0.4985)

λ Mean free path of the surrounding gas (m)

μ Viscosity of surrounding gas (Pa s or kg s^{-1} m^{-1})

N_{tot} Total number concentration of particles (cm^{-3})

ρ_{eff} Effective density of particle (kg m^{-3})

ρ_{o} Unit density (1000 kg m^{-3})

ρ_{p} Particle density (kg m^{-3})

τ Relaxation time of particle (s)

B Mechanical mobility of particle (s kg^{-1})

C_c Non-dimensional Cunningham slip correction factor

D Diffusion coefficient of the particles (m^2 s^{-1})

d_p Particle diameter of interest (m)

d_{ve} Particle volume equivalent diameter (m)

d_{eq} Equivalent charging diameter of particle (m)

D_m Non-dimensional mass-mobility exponent

d_{ve} Volume equivalent diameter of particle (m)

e Elemental charge (1.60×10^{-19} C)

f_n Non-dimensional charge fraction of particles with charge state n

k Mass-mobility prefactor constant (non-physical units)

m Mass of particle (kg)

N Particle number concentration of the aerosol as a function of a particle property, such as τ or d_a (cm^{-3})

n Non-dimensional charge state of particle

N_i Ion concentration (cm^{-3})

P Pressure of surrounding gas (Pa)

S Sutherland Constant for Air (110.4 K)

T Temperature of surrounding gas (K)

Z_p Electrical mobility of particle ($m^2\ V^{-1}\ s^{-1}$)

Frequent Subscripts, Superscripts and Accents

$'$ Notation to distinguish variable of integration from similar variable in integral limits

$*$ Denotes particle property corresponding to setpoint of classifier (i.e. the peak of its transfer function)

$\bar{}$ Denotes average of parameter over counting time (t_c) of particle detector

$\dot{}$ Denotes derivative of parameter with respect to time

tc Shifted by counting time of particle detector

τx Boundary x of transfer function in terms of particle relaxation time

$\tilde{}$ Non-dimensional particle property normalized by the classifier setpoint

c_c Cunningham Slip

i Particular instant of an parameter

n Particle charge state

+ Assumes $\tau_{sc} > 0$

- Assumes $\tau_{sc} < 0$

0 At reference conditions ($P_0 = 101325$ Pa and $T_0 = 296.15$ K) or Uncharged portion of aerosol particles

1 Particle property after upstream classification or Inner or LT component number or Intercept of f_1 and c_{f31} or Equation Form 1

12 Classification agreement between classifiers of similar measurands in tandem

13 LT inner boundary Condition with f_1

2 Particle property after downstream classification or Outer or LT component number or Intercept of f_2 and c_{f31} or Equation Form 2

23 LT inner boundary Condition with f_2

3 LT component number

a Aerodynamic or Aerosol

B Balanced classifier flows

c Centrifugal or Counting or Critical

d Drag or Delay

det Particle detector

down Down scan

E End of scan

e Electrostatic

exh	Exhaust
f	Fitting parameter for tandem classifier configurations
Fx	Form x of equation/integral
I	Idealized
in	Classifier inlet
Int	X-intercept
L	Lower
LT	Limited Trajectory
m	Mobility or Measurement
max	Maximum
min	Minimum
ND	Non-diffusing
NI	Non-idealized
out	Classifier outlet
PS	Particle Streamline
r	Radial direction
S	Start of scan
s	Sample
sc	Scanning operation
sh	Sheath
ss	Steady-state/stepping operation
t	Tube between classifier outlet and inlet of particle detector
U	Upper
UB	Unbalanced classifier flows
up	Up scan

Chapter 1

Introduction

1.1 Motivation

Aerosols consist of solid or liquid particles suspended colloidally in a gas [84]. These multiphase mixtures are commonly found in both indoor or outdoor environments and are produced by a variety of natural phenomena (such as fog/clouds, dust suspended by wind or salt atomized from ocean spray) and artificial processes (such as combustion, manufacturing or spraying mechanisms). Aerosol particles influence the global climate by scattering or absorbing solar radiation, and act as heterogeneous nucleation sites during fog or cloud formation [64]. Airborne particles also adversely affect human health [265], and the concentration of particulate matter smaller than 2.5 µm ($PM_{2.5}$) has been linked to millions of premature deaths per year [150, 34]. Particles smaller than 100 nm, often referred to as ultrafines, travel deep into human airways and even pass into the circulatory system [205]. Aerosols also impact the environment, causing meteorological variations [123, 164] and amplifying ambient pollution [281].

Given these consequences, governments and regulatory organizations have started to regulate emission sources of nanoparticles, such as automotive [94, 69] and turbine [222, 93] engine exhaust. However, to establish and enforce meaningful regulations, aerosol particles and processes must be thoroughly characterised and understood. This level of understanding requires multiple properties of the particles to be known simultaneously [140], such as their size, concentration, morphology and mass.

The size distribution is a fundamental property of an aerosol that commonly governs the behaviour of its particles. Since aerosol particles are often non-spherical, equivalent diameters are used to describe them, such as aerodynamic diameter. In the absence of diffusion or other thermo/photophoretic effects, aerodynamic diameter can be used to describe particle motion [239]. This diameter captures the behaviour of the particle when its inertia dominates,

such as deposition during inhalation [55], settling in the atmosphere [84] and separation by cyclones, impactors or filters [141].

The electrostatic charge on an aerosol particle also affects many of its other properties. The deposition of particles in human airways has been shown to significantly increase with their charge [186, 255, 35, 55]. Furthermore, the charge of particles can impact their collection in a filter [84, 251] and introduce electrostatic effects during gravimetric measurements [84, 232]. The dynamics of the particles are influenced by their charge as well, and can be used to control particle deposition [125, 236], agglomeration [178, 202] and synthesis [253, 163] to build nanostructures [134, 160]. The charge of particles is also used to directly [113, 53, 176, 193, 192] or indirectly [261, 21, 122] characterise the size distribution of an aerosol or a moment of its size distribution based on an equivalent particle diameter, such as mobility or aerodynamic diameter. These characteristics are captured by the charge distribution of the aerosol, which describes the fraction of particles at each charge state. The charge state of a particle is an integer quantity that reflects the net presence, absence or balance of elemental charges (i.e. electrons), and results in the particle becoming negatively, positively or neutrally charged, respectively.

Particles acquire charge through many different mechanisms, including static electrification, flame charging, or electrolytic charging [84], as well as exposure to bipolar ions [66, 233], unipolar ions [208], or ultraviolet light [115]. Bipolar diffusion charging is the most common charging mechanism to occur naturally due to the presence of both positive and negative ions in ambient air [84].

If an aerosol is exposed to a sufficient number of bipolar ions over a long enough period, the charge distribution obtained by a particular size and concentration of particles will not change if the particle concentration decreases, or the ion concentration or their exposure time to the particles increases [4, 88, 181, 182, 41, 92]. When the the bipolar charge distribution achieves this convergence and independence, it is commonly referred to as the steady-state charge distribution [254, 87]. Due to these advantages, this charging process is often produced artificially by introducing a sufficient concentration of positive and negative ions produced from a radioactive source, electromagnetic radiation (such as x-ray) or other gas ionizing mechanisms. For these applications, as well the charge reduction of highly-charged aerosols, bipolar diffusion charging is frequently referred to as neutralisation as it reduces the overall charge of the aerosol to an approximately neutral state.

Due to this advantage, neutralisation is regularly used with electrostatic classifiers, which is one of the most common methodologies to characterise submicron particles [60]. Recently, neutralisation has also been utilized in a new low-cost sensor to determine the first-moment of a particle size distribution (i.e. particle concentration times mean diameter) [192]. However,

the uncertainty in the charge distribution of the neutralised particles propagates into the total measurement error of both the electrostatic classifiers [242, 151] and low-cost sensor [192].

1.2 Background information

These consequences and applications have driven rapid growth in aerosol research and led to a variety of particle classifiers being developed over the past seven decades. Since aerosol particles often have non-spherical morphologies, equivalent diameters are used to quantify particular properties of the particles. These equivalent diameters are based on a particle's behaviour to known forces (F_1 and F_2) as shown in Figure 1.1 or an intrinsic property of the particle, such as equivalent volume or surface area.

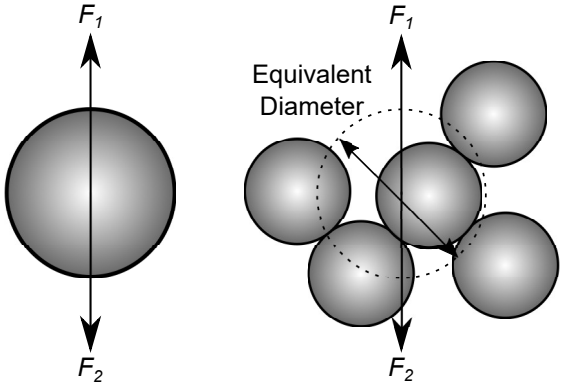

Fig. 1.1 Example to illustrate the concept of equivalent particle diameter.

1.2.1 Particle properties and aerosol classifiers

A particle's mobility (B) describes its ease of motion and is quantified by the constant velocity it obtains from a known external force [84]. For example, the mobility of a particle with a known mass can be determined by its settling velocity. This parameter is the primary consideration for smaller particles where the Brownian motion of the particles dominates their inertia [141].

The Differential Mobility Analyser (DMA) is the most common instrument used to measure particle mobility [60] and will be used extensively to support this work. It classifies particles based on their electrical mobility (Z_p) by applying an electric potential difference between concentric cylinders to induce an electrostatic force on each charged particle [133]. This electrostatic force (F_e) causes each charged particle to move radially and is counteracted by its drag force (F_d), as shown in Figure 1.2. Each particle's residence time in the classifier

is controlled by the total axial flow in the classifier (i.e. combined sheath and sample flows). Thus, only particles with a narrow range of electrostatic force to drag ratios (i.e. electrical mobilities) follow the correct trajectory and pass through the DMA [228]. By knowing or assuming the charge states (n) of the classified particles, their equivalent mobility diameter (d_{m}) is determined from their electrical mobility (Z_{p}).

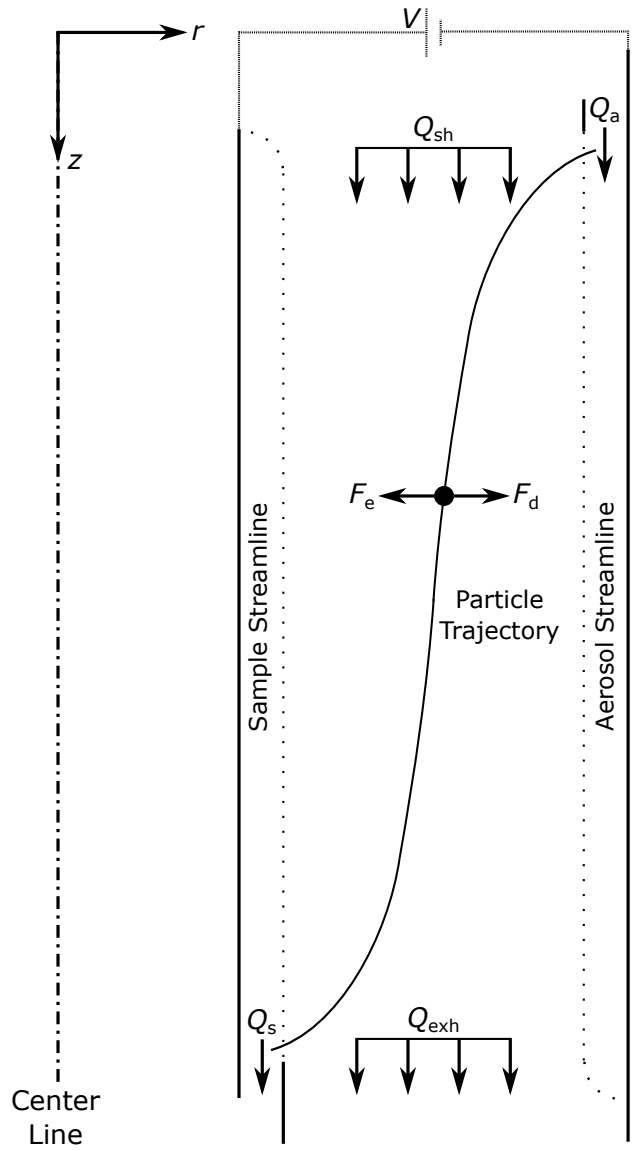

Fig. 1.2 Operating principle of the DMA, where V is the electric potential difference across the classifier, Q_{a} and Q_{s} are the aerosol flow rate entering and leaving the classifier, respectively, and Q_{sh} and Q_{exh} are the sheath flow rate entering and leaving the classifier, respectively.

Mass is another important particle characteristic as many emission regulations are based on particle mass and number volume concentrations [108]. It can also provide insights into the particle morphology when considered with other particle properties, such as mobility diameter [42, 49]. The Aerosol Particle Mass (APM) analyser [50] and Centrifugal Particle Mass Analyser (CPMA) [198] classify particles by their mass-to-charge ratio. Both instruments pass the aerosol between spinning concentric cylinders with an electric potential difference between them, inducing opposing centrifugal (F_c) and electrostatic (F_e) forces on each particle proportional to its mass (m) and charge ($n\,e$), respectively. Only particles with the correct mass-to-charge ratio have balanced external forces and pass through the classifier. The CPMA classifies with a higher transmission efficiency than the APM by spinning the inner cylinder faster than the outer, producing a Couette flow between the cylinders and a force gradient that causes particles of the correct mass-to-charge ratio to move to the centre of the classifier gap [199].

The aerodynamic diameter (d_a) is the equivalent diameter of a particle with the same settling velocity as a spherical particle with unit density ($\rho_o = 1000$ kg/m^3). These equivalent diameters (i.e. d_m and d_a) and mass (m) of a particle are related to its relaxation time (τ, i.e. time constant for the particle to reach its terminal velocity) by [84]:

$$\tau = m\,B = m\,\frac{Z_p}{n\,e} = \frac{C_c(d_a)\,\rho_o\,d_a^2}{18\mu} = \frac{C_c(d_m)\,\rho_{eff}\,d_m^2}{18\mu} = \frac{C_c(d_{ve})\,\rho_p\,d_{ve}^2}{18\mu\,\chi}, \tag{1.1}$$

where C_c is the Cunningham slip factor, μ is the surrounding gas viscosity, ρ_{eff} is the effective density of the particle and and e is the elemental charge (1.60×10^{-19} C), ρ_p is the particle material density, d_{ve} is the volume equivalent diameter and χ is the particle shape factor [84, 42]. This equation highlights that electrostatic instruments (such as the DMA, CPMA or APM) classify particles based on their charge states (n), which is a distribution that can vary with particle morphology, size and composition [74, 72]. As a result of these uncertain charge states, electrostatic aerosol instruments are susceptible to errors from multiply-charged particles.

1.2.2 Aerodynamic Aerosol Classifier

The Aerodynamic Aerosol Classifier (AAC) was recently developed by Tavakoli and Olfert [238] and overcomes this charging limitation by classifying particles based on their relaxation time (τ). Particle relaxation time, or a measure of a particle's mass-to-drag, is completely independent of particle charge. This particle property is the primary consideration where its inertia dominates and is directly related to aerodynamic diameter (d_a), as shown in Equation 1.1.

The AAC selects particles of a single aerodynamic diameter (in reality, a narrow range of aerodynamic diameters distributed about its setpoint) by passing the aerosol sample between two spinning concentric cylinders. The centrifugal force (F_c) applied to each particle is controlled by the classifier speed, while their residence time in the classifier is controlled by the total axial flow in the classifier (i.e. combined sheath and sample flows). This centrifugal force (F_c) causes each particle to move radially and is counteracted by its drag force (F_d), as shown in Figure 1.3. Particles with aerodynamic diameters smaller than the AAC setpoint have insufficient radial movement within the classifier and thus remain entrained in the sheath flow, while larger aerodynamic diameters have excessive radial movement and impact the outer surface of the classifier. Thus, only particles within a narrow range of aerodynamic diameters follow the correct trajectory and pass through the AAC classifier [238].

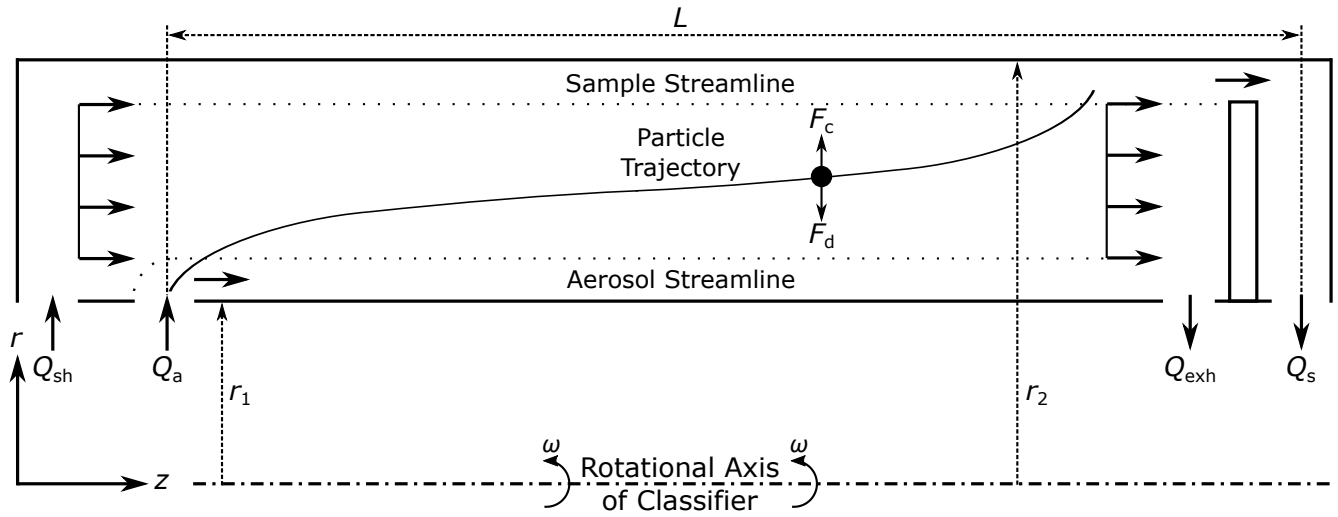

Fig. 1.3 Operating principle of AAC, where ω is the classifier angular speed, Q_a and Q_s are the aerosol flow rate entering and leaving the classifier, respectively, and Q_{sh} and Q_{exh} are the sheath flow rate entering and leaving the classifier, respectively.

The average relaxation time (τ^*) of the particles selected by the AAC was determined by Tavakoli and Olfert [238] to be:

$$\tau^* = \frac{Q_{sh} + Q_{exh}}{\pi\omega^2(r_1 + r_2)^2 L}, \tag{1.2}$$

where ω is the classifier rotational speed, r_1 is the classifier inner radius, r_2 is the classifier outer radius, L is the classifier length, Q_{sh} is the sheath flow rate entering the classifier and Q_{exh} is the sheath flow rate leaving the classifier, as shown in Figure 1.3.

Transfer function

The transfer function of an aerosol classifier quantifies the probability of each particle passing through the instrument as a function of the classifier measurand. This property is required to accurately operate the classifier and derive meaningful, accurate data from its raw measurements. This approach is often used to describe the performance of aerosol classifiers, such as the DMA [133, 86], APM [50] or CPMA [199].

Previous studies have developed different models that can be used to represent the AAC transfer function (TF) as shown in Figure 1.4 over the non-dimensional particle relaxation time domain ($\tilde{\tau}$), which is defined as the particle relaxation time (τ) normalized by the AAC setpoint (τ^*). For example at the peak ($\tilde{\tau} = 1$), the non-diffusing transfer functions estimates 100% transmission efficiency for particles with that relaxation time ($\tau = \tau^*$). Tavakoli and Olfert [238] developed the non-diffusing (ND) transfer function for the AAC following particle streamline theory and considered diffusion (D) by assuming that it spreads the particles in a Gaussian distribution about the ND model. The non-diffusing and diffusing log-normal (Log) approximations of the AAC transfer function were calculated by applying the theory developed by Stolzenburg and McMurry [229] to represent the DMA transfer function log-normally. This theory can be directly applied to the AAC given that the AAC transfer function based on particle streamline theory with diffusion determined by Tavakoli and Olfert [238] has the same form as that of the DMA [228].

Due to non-ideal particle or flow behaviours within an aerosol classifier, such as particle diffusion/impaction or developing/mixing flows, respectively, a portion of particles with the desired property are unintentionally lost during classification. This loss is quantified by the transmission efficiency of a classifier, which reflects the fraction of particles with the desired property that actually pass through the classifier and is captured by the amplitude of its transfer function. While these losses in electrostatic instruments are usually quite low [120], the transmission efficiencies of these classifiers are limited by the fraction of particles that obtain the correct charge state. The AAC avoids this limitation by classifying particles independent of their charge state.

1.2.3 Aerodynamic sizing of particles

Since the aerodynamic diameter of a particle is proportional to its inertial range (also referred to as stopping distance), abrupt changes of flow directions or centrifugal forces are commonly used to characterise this particle property. While centrifuges [85, 227], impactors [210] and cascade impactors [175] can be used for this purpose, these measurements are limited to one particle size at a time, or testing must be stopped to quantify the particles collected at each

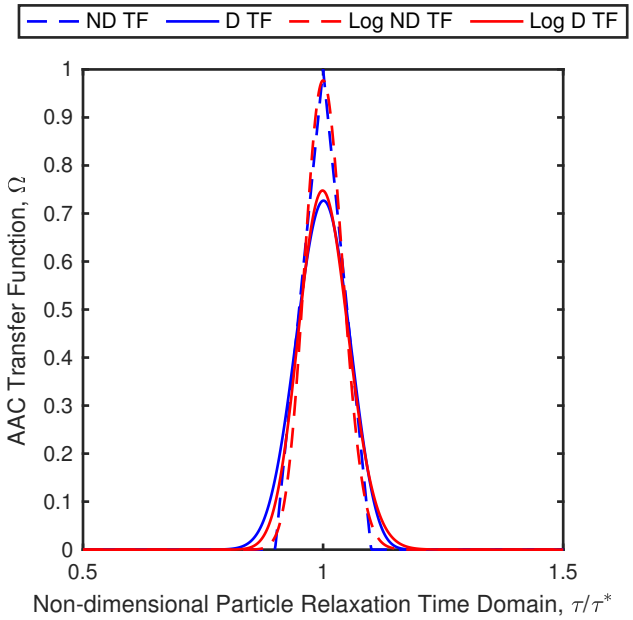

Fig. 1.4 Different theoretical representations of the AAC transfer function (TF) with balanced classifier flows. The non-diffusing (ND) and diffusing (D) transfer functions were developed by Tavakoli and Olfert [238] and the lognormal (Log) transfer functions were developed following Stolzenburg and McMurry [229]. The diffusing transfer functions shown represent an AAC setpoint equivalent to a 75 nm particle mobility diameter.

centrifuge location or impactor stage. To overcome these limitations, Keskinen et al. [122] developed the Electrical Low Pressure Impactor (ELPI), which is a cascade impactor that quantifies the particles collected at each stage based on their electrostatic discharge upon collection. While this approach quantifies the aerodynamic size distribution in real-time, similar to other impactors, it requires high sample flow rates and low pressures to measure submicron particles. Its measurements also depend on the unipolar charge distribution of the aerosol, which varies with particle size, morphology and composition [20, 201, 74].

The Aerodynamic Particle Sizer (APS) spectrometer is also commonly used to measure the aerodynamic size distribution of an aerosol. This instrument uses the fact that the acceleration of aerosol particles through a nozzle is proportional to their aerodynamic diameters [40]. This velocity is quantified by the APS measuring the time-of-flight (TOF) of the particles using two intersecting laser beams [272]. However, the nozzle can break up or deform liquid particles due to the large velocity gradients it generates [16, 30]. While this methodology allows for near real-time characterisation of an aerosol across a broad size range (up 20 µm), its measurements are limited to larger particles ($>$ 500 nm) and must be corrected for particle density at larger sizes ($>$5 µm) and densities ($>$ 2 g/cm^3) [30].

1.2.4 Bipolar diffusion charging of particles

Bipolar diffusion charging involves ionizing gas molecules, using radioactive sources [156, 95], x-ray radiation [225, 79], or other methods [7, 231, 78, 145], to produce positive and negative ions. These ions collide with the aerosol particles due to diffusive and electrostatic forces, producing a mixture of positively, negatively and neutrally charged particles [266, 66]. With sufficient ion concentrations and minimum exposure time to the ions, for a particular particle size and maximum concentration, this charging process also causes the particles to attain a charge distribution which does not change with higher ion or lower particle concentrations, or longer interaction times between them [4, 88, 181, 182, 41, 92]. The resulting charge distribution is often referred to as the steady-state charge distribution [254, 87] to reflect that the charging process reaches a steady-state. For example at this steady-state, the rate of particles with n charges that reach $n+1$ charges from positive charge transfer is equal to the reverse rate of particles with $n+1$ charges that reach n charges from negative charge transfer [66].

The $N_{\mathrm{i}}t$ product (product of charger ion concentration, N_{i} and particle residence time, t) has been traditionally used to quantify the efficiency of aerosol chargers and if the aerosol reaches a steady-state charge distribution [22, 41]. However, de La Verpilliere et al. [41] showed that $N_{\mathrm{i}}t$ is not an accurate parameter to characterise bipolar charging of high concentration particle concentrations, especially at small particle sizes. Covert et al. [39] also demonstrated that Krypton-85 radioactive aerosol neutralisers do not achieve steady-state charging for aerosol flow rates greater than 2 L/min with particle number concentrations greater than 10^3 cm^{-3}. While ISO Standard 15900 2009 (Determination of particle size distribution) [95] mentions this upper concentration limit, it does not provide a method to determine or account for it. Furthermore, current models of aerosol charging predict particle morphology affects the aerosol charge distribution produced by a bipolar [72] or unipolar [74] charger.

Due to these challenges, as well as the effects of a particle's electrostatic charge on its intrinsic and extrinsic properties, bipolar diffusion charging has been an active area of research since the early 1900s. However, these charging studies have primarily used electrostatic classifiers (such as the DMA), thus introducing challenges and errors associated with low transmission efficiencies and multiply-charged particles, respectively.

1.3 Problem statement

Due to the climate, health and environmental consequences of aerosols, as well as opportunities for engineered nanoparticles and nanostructures, there is a need to comprehensively mea-

sure the aerodynamic size and bipolar charging of aerosol particles. While these properties have been previously characterised, these studies were based on electrostatic or aerodynamic methodologies with some limitations. Electrostatic approaches depend on particle charging, which often introduce significant errors from multiple charging and have low transmission efficiencies due to limitations of particle charging. Previous aerodynamic methodologies often have low classification resolutions and set measurement ranges, which focus on larger particles. Some aerodynamic methodologies also depend on particle charging and have challenges detecting low particle concentrations.

To address these gaps, there is an opportunity to measure the aerodynamic size and bipolar charge distributions of aerosol particles using the AAC. This approach would leverage the high transmission efficiency and independence from particle charging during classification using the AAC. Given this independence from particle charging, it is slightly counter-intuitive that the AAC could be used to study the charging of particles. However, the challenge of previous charging studies is producing a monodispersed aerosol prior to charging and the AAC provides an opportunity to overcome this limitation. Furthermore, the classification setpoint and resolution of the AAC can be quickly and easily changed by varying the classifier speed and sheath flow [238]. The AAC can also be used in combination with other aerosol instruments since it does not collect the classified aerosol sample. Therefore, developing and validating these AAC methodologies will likely benefit the scientific community and be utilized by others in the future.

1.4 Organisation of thesis

After this introduction, Chapter 2 provides a review of previous methodologies used to measure the aerodynamic size or bipolar charging of particles, including their advantages/disadvantages and sequential development. The research opportunities identified by this review are then summarized and directly motivate the objectives discussed at the end of that chapter. Chapter 3 characterises the transfer function of the AAC experimentally, then develops and validates theory which allows the AAC to measure the aerodynamic size distribution of an aerosol by stepping its setpoint upstream of a particle detector. This approach is improved upon in Chapter 4 by scanning rather than stepping the AAC setpoint, enhancing the spectral resolution of the size distribution, while reducing measurement time. Chapter 5 develops and demonstrates a new methodology, an AAC and DMA in tandem, to measure the bipolar charge distribution of spherical particles. This approach is expanded upon in Chapter 6 by demonstrating an AAC and DMA in tandem can select homogeneous, non-spherical particles, then using another DMA downstream to measure the bipolar charging

of the tandem-classified particles. Finally, the outcomes and contributions of this work are summarized in Chapter 7.

Chapter 2

Literature Review

2.1 Introduction

To understand the challenges of measuring the aerodynamic size or bipolar charge distributions of nanoparticles, this chapter[1] summarizes previous methodologies used for similar purposes. This review highlights the advantages/disadvantages and sequential development of each approach. Furthermore, this summary is organized into two categories based on particle property. The first section discusses methodologies to measure the aerodynamic size distribution of an aerosol, while the second and third sections discuss methodologies to measure the bipolar charge distribution of an aerosol. These latter sections further distinguish between previous charging studies of spherical or non-spherical particles. The research opportunities identified by this review are summarized in the fourth section and directly motivate the objectives of this work outlined in the fifth section.

2.2 Measuring aerodynamic size distributions of particles

Inertial impactors introduce a sharp change in flow direction to separate particles based on their aerodynamic diameters. Particles below the cut-off size of the impactor follow the

[1] This chapter is partially based on:

- an article by Johnson et al. [104] published by Taylor & Francis Group in Aerosol Science and Technology on 13/03/2018, available online: https://doi.org/10.1080/02786826.2018.1440063;
- an article by Johnson et al. [109] published by Taylor & Francis Group in Aerosol Science and Technology on 23/11/2020, available online: https://doi.org/10.1080/02786826.2020.1830941;
- an article by Johnson et al. [106] published by Elsevier in the Journal of Aerosol Science on 07/02/2020, available online: https://doi.org/10.1016/j.jaerosci.2020.105526; and
- an article by Johnson et al. [107] published by Elsevier in the Journal of Aerosol Science on 23/11/2020, available online: https://doi.org/10.1016/j.jaerosci.2020.105705.

gas streamlines, while particles with larger inertia maintain their original trajectory and impact onto the flow obstruction [174]. Virtual impactors also separate particles based on their inertia, but rather than introduce a flow obstruction it splits the flow into two streams, usually a major flow through a perpendicular annular slit and a minor flow aligned with the flow inlet [38]. Particles below the cut-off size of the virtual impactor follow the major flow streamlines, while particles with larger inertia maintain their original trajectory and are carried out by the minor flow. This approach avoids fragmentation and re-entrainment of the large particles during impaction [29]. Chein and Lundgren [29] classified Arizona road dust particles between 980 nm and 10 µm based on aerodynamic diameter, albeit with a broader distribution (GSD of 1.16 to 1.48), using an impactor and virtual impactor with a clean air core in series. Rao et al. [210] used a pre-impactor stage followed by a main stage with a clean outer sheath airflow in series with a vibrating reed electrometer to measure the aerodynamic size distribution of an aerosol down to 130 nm by varying the upstream pressure. While impactors are simple and robust, their resolution is limited (by particle diffusion and flow effects) and it is difficult to change their cut-off diameter quickly (i.e. need to alter its geometry or flow conditions) [29].

Cascade impactors take this concept one step further by arranging multiple impactors in series to measure the aerodynamic size distribution of an aerosol [141]. The cut-off aerodynamic diameter for each impactor decreases with each sequential stage. For example, Marple et al. [175] developed an eight-stage Micro-Orifice Uniform Deposit Impactor (MOUDI) that collected particles down to 56 nm. The particles collected on each impactor plate can be quantified by counting under a microscope, weighing or other analysis, such as x-ray fluorescence. However, these measurement principles require testing to be stopped to quantify the particles collected on each stage and only provide averages over the sampling period. To overcome these limitations, Keskinen et al. [122] developed the Electrical Low Pressure Impactor (ELPI), a cascade impactor that quantifies the particles collected at each stage based on their electrostatic discharge upon collection. While this approach quantifies the aerodynamic size distribution in real-time, similar to other impactors, it requires high sample flow rates and low pressures to measure submicron particles. Furthermore, the size range and resolution of its measurements is limited by the number of impactor stages and their corresponding cut-off diameters. Recently, the resolution of the ELPI has been significantly improved through advanced inversion techniques [221]. However, its measurements also depend on the unipolar charge distribution of the aerosol, which varies with particle size, morphology and composition [20, 201, 74].

Centrifuges are used to induce a centrifugal force significantly larger than the Earth's gravitation force by rotating the aerosol in a rigid body at high angular speeds. This large

centrifugal force amplifies the trajectory produced from a submicron particle's mass-to-drag ratio relative to the effects of Brownian motion [141]. The location particles deposit along the surface of the centrifuge is based on their aerodynamic size [227, 85]. Similar to impactors, this approach requires testing to be stopped to quantify the particles collected at each location and only provides averages over the sampling period.

Cyclones constrict the sample flow into a jet that flows tangentially on the inner surface of the cylinder/cone in a downwards spiral [141]. This flow rotation induces a centrifugal force on the particles causing ones larger than the cut-off size to be deposited on the cyclones' inner surface [141]. This separation method can collect large quantities of particles, but usually requires high sample flows and has a low cut-off resolution [239].

Dahneke and Flachsbart [40] showed that expanding an aerosol sample through a nozzle into a vacuum chamber separates the particles by their aerodynamic diameter, with smaller particles gaining a larger side-ward velocity during nozzle expansion. This concept was expanded with the development of the aerodynamic lens [159], a series of contractions and enlargements that focus particles to the flow centre. Kielser and Kruis [124] used an aerodynamic lens with a clean, centre sheath flow to classify particles based on their aerodynamic diameter. This system, referred to as the Differential Aerodynamic Particle Sizer (DAPS), is capable of measuring aerodynamic size distributions (between 80 nm and 3 μm in 4 minutes) by changing the system pressure to shift the particle aerodynamic diameter selected by the lens and counting the corresponding particle number concentration with an electrometer [14]. Similar to the ELPI, the DAPS requires the particle charge distribution produced by its unipolar charger to be known and sufficient particle concentrations to generate detectable aerosol currents.

Furthermore, the gas expansion from an aerosol passing through an aerodynamic lens into a vacuum chamber causes smaller particles to reach higher velocities than larger particles due to varying particle inertia [99]. Using this principle with a time-of-flight (TOF) chopper wheel to modulate the particle beam travelling over a known distance, Jayne et al. [99] measured the vacuum aerodynamic diameter of particles in an Aerosol Mass Spectrometer (AMS). While the AMS collects a large amount of particle characterisation data (i.e. size, mass and chemical composition), these instruments are complex to operate. The Aerodynamic Particle Sizer (APS) Spectrometer also utilizes TOF measurements. The APS measures the aerodynamic size distribution of an aerosol by accelerating it through a nozzle and measuring each particle's TOF between two laser beams relative to the gas velocity [272]. While the APS allows for rapid characterisation, the nozzle can produce a large velocity gradient (up to 1/3 the speed of sound) between the particles and surrounding gas, resulting in liquid particle deformation/breakup [16, 30]. Its measurements must also be corrected for particle density,

which becomes a significant correction for particles with aerodynamic diameters greater than 5 µm and densities greater than 2 g/cm^3 due to falling outside of the Stokes regime[2] [30].

Flagan [61] suggested that an opposed migration aerosol classifier (OMAC) applying a centrifugal force (rather than an electrostatic force) could also be used to classify particles by their aerodynamic diameter. However, to the knowledge of the author, this concept was never validated experimentally. Alternatively, Mazumder and Kirsch [183] measured the aerodynamic size distribution of an aerosol by exposing them to an acoustic excitation of a known frequency and calculating the phase shift between the medium and the suspended particles. This approach is referred to as the Single Particle Aerodynamic Relaxation Time (SPART) analyser, and later evolved into the Electrical SPART (E-SPART) by replacing its oscillating acoustic field with an oscillating electrostatic field and charging the particles with a unipolar charger upstream of the analyser [213]. However, both the SPART and E-SPART are limited to particles larger than 300 nm due to light scattering limitations at smaller particle sizes [213].

2.3 Measuring bipolar charging of spherical particles

Particle charging has been studied since the early 1900s, before many of the modern challenges and applications previously described were realized. These measurement methodologies can be organized into three broad categories: trajectory observations, electrostatic classification and aerodynamic classification. Electrostatic classification is the most common method used to characterise particle charging and is further broken down into five subcategories: electrostatic precipitation and electrical polarity classification, as well as low-pass, band-pass, and accelerated, band-pass electrical mobility classification.

2.3.1 Trajectory observations

Based on observing the velocities induced by gravity and an external electrical field on charged oil particles, Millikan [188] discovered the elemental charge and its discrete value of 1.6×10^{-19} C within 2% error. Using a similar method, Lissowski [155] measured the charge distribution of oil droplets neutralised by exposure to radium for particles between 280 nm and 560 nm using ultramicroscopy, and between 2 µm and 4 µm by photographing the particle oscillations as the electrostatic field direction was cycled. By tracking the settling and horizontal displacement of droplets in a horizontal electric field using dark field illumination with a camera, Dodd [44] measured the size and charge of conductive droplets (mercury,

[2] A flow regime where viscous forces dominate inertial forces [141].

1 to 6 µm) and five different types of non-conducting oil droplets (2 to 50 µm). By also observing gravitational and electrostatic displacements of particles neutralised by x-ray radiation, Gunn and Woessner [75] and Woessner and Gunn [274] collectively measured the bipolar charge distributions of pure water droplets (6.64 and 8 µm), silica dust (1.4 µm), sulphur particles (2.7 µm) and salt water droplets (3.26 µm from condensation or 2.7 µm by spraying). Other methodologies explored between 1941 and 1997 similar to Millikan's (1910) original approach are summarized by Brown [24], which include various improvements such as keeping the particles static in the observation cell and limiting thermal convection during the measurements.

In the early 1980s, Adachi and various collaborators studied the charging of particles by observing them in an electrostatic field using a video camera to record the light from a laser scattered by the particles. This approach was used to determine the charged fraction, mean charge or electrical mobility size distribution of ten different particle sources (520 nm to 2.06 µm) before and after neutralisation using ^{241}Am [139], and of DOP particles (720 nm to 1.92 µm) after neutralisation using 10 or 100 µCi ^{241}Am in air [6, 5]. This method was later improved by using a differential mobility analyser (DMA; Knutson and Whitby [133]) to generate a monodispersed aerosol based on electrical mobility, then passing the classified particles through the charger of interest, growing them through vapour condensation if initially too small for observation (i.e. $<$300 nm) and finally using laser spectrometry with a camera to record their trajectory in an electrostatic field. The improved method was used extensively by Adachi and various collaborators to measure the total charge, and the fraction of particles with either negative or positive charges for 4 to 100 nm particles exposed to bipolar or unipolar ions from ^{241}Am [1] and for 4.5 to 40 nm particles neutralised by ^{241}Am in nitrogen [137], to study the response of an ionizing smoke detector from 75 nm to 2.09 µm particles [3], to show the divergence from the steady-state charge distribution at high ratios of particle (30 nm, 100 nm or 1.08 µm) to ion concentrations [4], and to demonstrate bipolar charging using a dual-needle corona ionizer with 340 nm to 1.15 µm particles [7] or an AC corona ionizer with 5 to 80 nm particles [128]. For larger particles (greater than 300 or 600 nm depending on the study), these studies generated the monodispersed particles by using a Le Mar-Sinclair type generator (i.e. condensing oil vapour on ultrafine particles) or using polystyrene latex (PSL) particles rather than using a DMA.

Fjeld et al. [58, 59] used a similar approach to study the charging of particles exposed to bipolar ions from ^{241}Am in an external electrostatic field and also generated larger monodispersed aerosols using polystyrene latex (PSL) particles (1 to 4.2 µm) or a vibrating orifice particle generator (4.95 to 12 µm) rather than using a DMA. Jantunen and Reist [96] also studied bipolar charging in an external electrostatic field by exposing 30 µm lycopodium

spores neutralised by ^{210}Po and photographing the particle trajectory through the charging zone and exit. Expanding on these trajectory observation methodologies, Ahn and Chung [10] developed the Aerosol Electrical Mobility Spectrum Analyser (AEMSA), which uses a mobility analyser to separate the particles by electrical mobility, while incorporating a saturator/condenser system with a laser and CCD camera to detect the particle positions. This study measured the charge fractions of monodispersed salt particles (20 to 200 nm) generated by a TDMA system (i.e. two DMAs operated in series) and neutralised by x-ray radiation or ^{241}Am. The AEMSA was later used by Lee and Ahn [147] to monitor the charge states of ambient particles (80 to 200 nm) during lightning events. Alternatively, Withers et al. [273] used Laser Doppler Velocimetry (LDV) to measure the velocity of particles of a known size (720 nm or 1.9 µm PSL) in an electrostatic field to determine their charge after atomization. Foot et al. [63] then expanded this technique to characterise the charge of polydispersed aerosols by concurrently using light scattering to size the particles.

2.3.2 Electrostatic precipitation

To avoid the manual counting methods of observing particle trajectory (with the exception of the AEMSA and LDV approach), which are labour-intensive and challenging to collect representative sample sizes, other charging studies used an electrostatic precipitator (ESP) upstream of a particle detector. When no voltage or a high voltage is applied to the ESP, the particle detector measures the total or uncharged particle concentration, respectively. This method accelerates the measurements, but only provides the fraction of the particles with no charge, rather than their charge distribution. Using this method, Nolan and Kennan [195] measured the uncharged fraction of platinum particles (approximately 15 to 285 nm, sized based on diffusion), and Rich et al. [214] measured the uncharged fraction of nichrome particles neutralised using ^{210}Po and compared the results to charging theory to predict the average size of the particles (20 to 100 nm). Flanagan and O'Connor [62] also used an ESP and nucleus counters in tandem to measure the charged fraction of a polydispersed aerosol and the time for it to reach a steady-state charge distribution based on the exposure time to ions produced by ^{210}Po. Servaas and Krider [224] used this method as well to determine the uncharged fraction of platinum particles with a mean diameter of 10 nm neutralised by ^{210}Po, although the aerosol monodispersity was questionable. Similarly, Pollak and Metnieks [204] measured the charged fraction of nichrome particles aged in a large volume chamber (4200 L) to those neutralised by ^{210}Po, and Pollak and Metnieks [203] measured the charged fraction of 10 to 80 nm particles (sized using a diffusion battery).

To limit the effects of polydispersed aerosols on the uncharged fraction measurements, more recent charging studies used additional equipment with an ESP. Using a DMA in

tandem with an ESP and Condensation Particle Counter (CPC, Agarwal and Sem [8]), Liu et al. [158] measured the charged fraction of salt particles (50, 100 or 500 nm) after different residence times within the ^{210}Po neutraliser, Rogak and Flagan [215] measured the uncharged fraction of 72 to 725 nm PSL, and 40 to 794 nm particles composed of ammonium sulphate or titanium dioxide to investigate the effects of particle morphology on bipolar charge distributions, and Romay and Pui [217] measured the uncharged fraction of silver particles (5 to 50 nm) in high-purity helium after unipolar charging from ^{210}Po ions in an external electrostatic field. Similarly, Shimada et al. [225] and Hernandez-Sierra et al. [83] measured the uncharged fraction of silver particles (10 to 30 nm) in nitrogen, and salt particles (3.5 to 10 nm) in air, respectively, to demonstrate using x-ray radiation to neutralise particles and a custom corona ionizer to charge particles, respectively. Many other recent studies use a similar methodology to measure the uncharged fraction of size-resolved particles, but these studies also apply other methods to determine more detailed charging characteristics and are described below.

2.3.3 Low-pass electrical mobility classification

While the ESP methods captured all of the charged particles with a sufficiently high ESP voltage, other studies varied the ESP voltage to only capture particles with electrostatic mobilities greater than a threshold (i.e. low-pass filter). Thomas and Rimberg [241] and Tardos et al. [237] determined the average charge per particle after neutralisation using ^{90}Sr (264 nm to 1.305 µm) or corona charging (1.04 µm), respectively, based on the penetration of PSL particles (i.e. monodispersed) through an ESP with different capture voltages. Using the same approach, but with an improved data inversion process, John and Davis [103] measured the charge distribution of 357 nm PSL particles before and after ^{85}Kr neutralisation. Kojima and Sekikawa [136] measured the uncharged fraction of urban air particles (15 to 70 nm) neutralised by ^{210}Po using another neutraliser (also ^{210}Po) and a vibrating reed electrometer to detect the particles that passed through the ESP at different capture voltages.

Johnston [110] used an optical particle counter (OPC), configured to only detect a set range of particle sizes (i.e. 0.5-0.7, 0.7-1.4, 1.4-3, 3-5 or 5-10 µm), to measure the concentration of charged particles downstream of an 'elutriator[3]' with different capture voltages to determine the charged fraction of 600 nm and 4 µm coal dust particles before and after exposure to ions of one polarity from ^{204}Tl. This method was then used to measure the charge distribution of ambient particles at 13 factories, two quarries and one mine [111], and to measure the charge distribution of 600 nm to 7.5 µm particles from four powder dispensers

[3]ESP with symmetric outlets to sample particles by polarity.

with different dusts, salt particles after atomization and ambient dust [112]. Similarly, Adachi et al. [2] developed a system to automatically measure the size (120 nm to 7.5 µm) and charge distributions for particles in a cleanroom using a LAS-X OPC to size the particles passing through an ESP with different capture voltages. Applying the same methodology (ESP and LAS-X in series), Forsyth et al. [65] measured the mean charge per particle after generation of alumina dust (150 to 300 nm), Arizona road dust (260 nm to 2.6 µm), potassium chloride (150 to 300 nm), sodium chloride (150 to 750 nm) and di-octyl sebacate (DOS; 150 nm to 2 µm) particles.

Applying a similar method, but using a Scanning Mobility Particle Sizer (SMPS, Wang and Flagan [261]) or OPC downstream of the ESP depending on the aerosol source, Tsai et al. [244] measured the average charge of sodium chloride particles (10 to 800 nm) after generation or neutralisation (^{210}Po or ^{85}Kr). Also using particle penetration, but through a filter rather than an ESP, Liebhaber et al. [154] found using an OPC downstream of the filter can provide a threshold indication of the charge state of ambient particles from 100 to 700 nm.

The mobility resolution of an ESP (i.e. the classification gradient of the low-pass filter) was improved with the development of the mobility analyser, which used a clean sheath flow at the ESP inlet to greatly reduce the variability in the particle capture distances within its electrostatic field. While this instrument had different forms, it was realized that the deposition location of a particle in a mobility analyser is a function of its electrical mobility (i.e. size and charge). By visually examining the particle deposition locations, Gillespie and Langstroth [70] determined the charge distribution of silica powder (300 nm to 1.85 µm) at different times after aerosolization, Megaw and Wells [185] demonstrated the distinct deposition locations of 730 nm PSL particles with up to 7 elemental charges, and Bricard et al. [23] determined the charge distribution of 714 nm PSL particles before and after ^{210}Po neutralisation. Whitby and Peterson [264] and Maltoni et al. [165] both automated this manual counting approach using a photometric scanner to quantify the concentrations of the deposited particles and used this process to determine the average charge of polydispersed dye particles (CMD of 90 nm to 2.6 µm), and the charge distribution of 780 nm carnauba wax particles, respectively. However, these deposition studies focused on the charging of larger particles likely due to the challenges of observing smaller particles.

The electrical aerosol analyser (EAA) took the mobility analyser one step further by incorporating a corona charger on its inlet and a Faraday cup aerosol electrometer on its outlet to quantify the electrical mobility distribution of an aerosol. Using a partially disassembled EAA upstream of a CPC and an aerosol electrometer in parallel, Vomela and Whitby [259] measured the average charge per particle from unipolar charging of methylene blue dye (50 to

300 nm), copper oxide (90 to 270 nm) or kerosene soot (50 to 160 nm) particles. Kasper and Shaw [121] determined the average charge of iron-oxide aggregates (with mean, flow-aligned mobility diameters of 210 to 550 nm) using an EAA and centrifuge in parallel to measure the electrical mobility and aerodynamic size distributions of the particles, respectively. Burtscher et al. [27] used an EAA to quantify the size distribution of particles downstream of an ESP (i.e. total or uncharged portion) to measure the uncharged fraction of polydispersed particles (with mean diameters of 24 to 424 nm) produced by burning different materials.

Using a similar methodology (mobility analyser and CPC in series), Takahashi and Kudo [233] measured the uncharged fraction of polydispersed aerosols (zinc or lead with geometric mean diameters of 100 or 140 nm, respectively), and the exposure time to ions produced by ^{241}Am required for the particles to reach a steady-state charge distribution. Kojima [135] took this approach one step further to study ^{241}Am neutralisation by using a monodispersed aerosol source (PSL) with a mobility analyser and CPC in series to measure the charge distribution of size-resolved particles (480 nm to 1.1 µm) and the same approach as Kojima and Sekikawa [136] to measure the single charge fractions of urban air or ammonium sulfate particles (10 to 64 nm). Also using a monodispersed aerosol with a mobility analyser and particle counter in tandem, Fjeld et al. [57] and Gauntt et al. [68] measured the mean charge of monodispersed PSL particles (310 nm to 1.09 µm) exposed to ions from ^{241}Am in an external electric field.

2.3.4 Band-pass electrical mobility classification

The methodology of using an ESP or EAA as a low-pass filter for particle electrical mobility was improved by instead using a DMA to select a narrow range of particle electrical mobilities (i.e. band-pass filter). Hoppel and Frick [88] measured and compared the ratios of negatively to positively charged particles of ammonium sulfate (18 to 180 nm) neutralised by four different ion sources using a DMA in tandem with a particle detector, while alternating the polarity of the DMA classification voltage. Using a DMA in tandem with a optical aerosol spectrometer, Porstendörfer et al. [207] measured the charge distribution of DOS particles (500 nm to 2 µm) neutralised by ^{241}Am or ^{14}C, while Emets et al. [51] measured the charge distribution of potassium iodine particles (500 nm to 2 µm) after ageing and calcium nitrate particles (450 nm to 1.8 µm) neutralised by ^{210}Po, and Vishnyakov et al. [258] resolved the high charge states (15 to 306 elemental charges) of particles (average size of 225, 335 or 1000 nm) produced during welding.

However, the size-spectral resolutions of optical aerosol spectrometers are limited. To obtain higher resolution results, some studies generated a monodispersed aerosol and resolved the different electrical mobilities corresponding to each particle charge state by stepping the

setpoint of a DMA and measuring the corresponding concentrations of the classified particle with a CPC. Using a vibrating orifice generator to produce monodispersed particles, Liu and Pui [156] measured the median charge of 2.53 µm DOP (di-octyl phthalate) particles as a function of residence time in a ^{85}Kr neutraliser with four different activity levels, while Liu and Pui [157] measured the bipolar charge distribution of DOP particles (530 nm, 550 nm and 1170 nm), and the ratio of charged to uncharged NaCl and methylene blue particles (20 nm and 200 nm). To demonstrate the reduction in multiply-charged particles by neutralisation using a low-activity ^{63}Ni or x-ray source, respectively, Gupta and McMurry [76] measured the charge distribution of 605 nm PSL particles, and the single and multiple charge fractions of PSL particles (90 nm to 1.09 µm) at different flow rates, while Han et al. [79] measured the charge distribution of 207 nm and 791 nm PSL particles at varying x-ray intensities. Han et al. [79] also measured the charged distribution of polydispersed silicon dioxide particles neutralised at different x-ray intensities using a DMA to select a narrow range of particle electrical mobilities (300 and 600 nm) and collecting Scanning Electron Microscope (SEM) images to determine the actual size of the classified particles.

To characterise the particle charging of polydispersed aerosol sources, other studies began using tandem DMAs (TDMA), with the first DMA (DMA 1) generating a monodispersed aerosol and the second DMA (DMA 2) stepping its voltage to resolve the different electrical mobilities corresponding to each particle charge state. Metayer et al. [187] used a TDMA to measure the positive and negative charge fractions of salt particles (10 to 75 nm). This methodology was also used to investigate the neutralisation (^{85}Kr or ^{241}Am) of small particles (under 40 nm and as small as 4 nm) which have high Knudsen numbers (i.e. in the free-molecular regime) and deviate from charging theory [206, 91, 212, 254]. Six studies [211, 13, 39, 117, 41, 92] also characterised the charging of small particles (collectively between 2.3 and 50 nm) using a TDMA, but focused on identifying conditions where the steady-state charge distribution from bipolar charging isn't reached based on particle residence time (i.e. charger flow rate and size) in the neutraliser (collectively evaluating ^{241}Am, ^{210}Po, ^{85}Kr, x-ray and AC corona neutralisation), as well as particle and ion concentrations. The TDMA methodology was also used by Jiang et al. [101] to investigate the performance of six bipolar neutralisers (^{210}Po with two activities, ^{85}Kr with two activities, ^{241}Am and x-ray) for neutralising 70 nm DOS particles over a range of sample flows (0.3 to 5 L/min) and neutraliser ages.

The effects of gas properties on particle charging were also investigated using the TDMA methodology, including gas temperature (298 to 373 K) on the charge fractions of salt particles (approximately 20 to 100 nm) neutralised using ^{210}Po [269], gas humidity on the charge fractions of silver particles (approximately 7 to 50 nm) neutralised by ^{241}Am or x-ray

radiation [149], gas ion mobility on the charge fractions of gold nanospheres (50 and 70 nm) and nanorods (30 to 70 nm mobility diameter) neutralised by ^{210}Po [72], and gas composition (argon or nitrogen) on the charge fractions of silver, salt or carbon particles neutralised using ^{85}Kr (5 to 100 nm) [267, 268], or neutralised using ^{63}Ni (28 to 55 nm) [226]. The TDMA methodology was also used to verify and contrast the performance of new chargers, including neutralisation using a Surface-discharge Microplasma Aerosol Charger (SMAC) versus ^{241}Am by measuring the charge distribution of DOS particles (10 to 200 nm) [145], neutralisation using a carbon fibre ionizer versus ^{85}Kr by measuring the charge distribution of sodium chloride, ammonium nitrate, ammonium sulfate or glutaric acid particles (20 to 120 nm) [78], and neutralisation using x-ray radiation versus ^{241}Am by measuring the charge and positive to negative charge ratios of salt particles (10 to 30 nm) [148] or by measuring the charge fractions of salt particles (30 to 130 nm) [279].

2.3.5 Accelerated, band-pass electrical mobility classification

To decrease the measurement time of the TDMA system, some studies scanned rather than stepped the voltage of the downstream DMA. The scanning DMA inversion was originally developed by Wang and Flagan [261] to accelerate mobility-size distribution measurements and is commonly referred to as a Scanning Mobility Particle Sizer (SMPS). By using a DMA-SMPS to quantify the concentration peaks that correspond to different charge states and neglecting multiply-charged particles from the upstream DMA, Romay et al. [216] measured the positively charged and uncharged fractions of salt particles (50 to 500 nm and 203 nm, respectively) neutralised by a dual-polarity sonic jet corona charger. Using a similar approach, He and Dhaniyala [82] measured the charge distribution of sucrose particles (12 to 48 nm) neutralised using ^{85}Kr, ^{210}Po or x-ray radiation with different particle concentrations (100 to 700 cm^{-3} or 5000 to 900 cm^{-3}) and flow rates (0.15 to 6 L/min). At these smaller particle sizes (less than 60 nm) the portion of multiply-charged particles [266] and resulting effects on the TDMA measurements significantly decrease.

To expand this approach to larger particles, Kim et al. [127] developed a correction to estimate and remove the effect of multiply-charged particles by assuming the particles followed a Boltzmann charge distribution. This methodology was verified by measuring the charge distribution of salt particles (50 to 200 nm) neutralised by ^{210}Po, and then used to measure the in-situ charge distribution of soot particles (50 to 200 nm) produced in an ethylene burner [127]. Xiao et al. [276] improved this correction by solving the multiple charge correction iteratively rather than assuming a Boltzmann charge distribution, and used this approach to measure the charge distribution of neutralised particles (70 to 300 nm) with either spherical (DOS or ammonium sulfate) or aggregate (diesel soot or silver) morphologies.

Also using a DMA-SMPS system, Qi and Kulkarni [209] verified the performance of a dual-corona ionizer for bipolar charging of aerosols with 10 to 500 nm particles (silver $<$50 nm and PSL $>$50 nm). No multiple charge correction was required for this setup as monodispersed PSL particles were used when multiple charging would become significant in the upstream DMA (i.e. greater than 60 nm). However all of these scanning TDMA studies neglect the transfer function width of the upstream DMA, and that the SMPS inversion assumes the aerosol concentration is constant over the width of its transfer function, thus introducing error into the results [230].

To simplify the data inversions and limit the errors from scanning the DMA, other studies utilized ratios from within the same or different DMA scans. Based on the ratio of the areas under the DMA scan, Ahn et al. [11] measured the in-situ double-to-single charge ratio of silicon oxide particles (approximately 15 to 115 nm) from a flame reactor normalized by the same ratio after neutralisation, and Mamakos [166] measured the positive double-to-single and triple-to-single charge ratios of spherical (DOS and emery oil), soot and spark-generated graphite particles (approximately 20 to 400 nm) neutralised using ^{85}Kr or x-ray radiation. By comparing DMA scans with and without the neutraliser in place, Yang et al. [277] measured the single and double charge fractions of DOS or ammonium sulfate particles (100 to 900 nm) neutralised by ^{85}Kr, ^{210}Po or x-ray with flow rates from 0.3 to 5 L/min. Wild et al. [271] showed the transfer function of a scanning DMA can be used to measure the charge fraction of distinguishable states (i.e. distance between charge peaks must be larger than the width of the DMA transfer function). This approach was verified using salt particles (60 or 135 nm) neutralised by ^{85}Kr and comparing the results against those determined from lognormal fits of the TDMA scans [271]. However, it was unclear if the developed SMPS inversion theory accounted for the effects of the upstream DMA.

Since an aerosol's charge distribution affects its electrical mobility, comparing electrical mobility distributions of an aerosol source offers a simpler and quicker option than TDMA measurements, but its results are usually more qualitative. Four studies [231, 280, 189, 116] verified the neutralisation performance of x-ray radiation and AC corona discharge by comparing SMPS scans of various aerosol sources (collectively DOS, gold, pentaerythritol, 60 nm PSL, Bacteriophage MS2 and Ovalbumin solution) to those measured using a reference neutraliser with an SMPS (collectively ^{241}Am, ^{210}Po or ^{85}Kr). Using a similar approach, Wiedensohler et al. [270] compared SMPS scans of ambient air using five different neutralisers (^{241}Am, ^{85}Kr, ^{63}Ni, bipolar corona discharge and x-ray radiation) to assess the uncertainty of bipolar diffusion chargers in Mobility Particle Size Spectrometer (MPSS) measurements. This approach was also used to study the effects on particle charging due to free-ions downstream of a ^{85}Kr neutraliser [12], and the effects due to particles (3.5 to

50 nm) being highly charged before ^{85}Kr or ^{210}Po neutralisation [100]. To study the effects of ambient ions on particle formation, Laakso et al. [146] and Gagné et al. [67] compared electrical mobility scans of ambient air from a Differential Mobility Particle Sizer[4] (DMPS) before and after neutralisation (referred to as the Ion-DMPS) to determine the size-resolved, median charge state of the particles. Similarly, Enghoff and Svensmark [52] compared SMPS scans with and without a ^{85}Kr neutraliser to determine the median charge state (approximately 3 to 70 nm) of sulphuric acid particles exposed to varying levels of gamma rays from ^{137}Cs.

This methodology can produce more quantitative results by using SMPS scans collected with a neutraliser that generates a known particle charge distribution as a reference and applying more advanced inversion algorithms. By minimizing the difference between the two SMPS scans, Buckley et al. [26] fitted the parameters of the Modified Boltzmann Distribution [33] to determine the charge distribution of ambient air particles, while Tigges et al. [243] fitted polynomial parameters (analogous to Wiedensohler [266]) to determine the charge distribution of ambient air neutralised using x-ray radiation.

2.3.6 Electrical polarity classification

Another common electrostatic approach to characterise particle charging utilizes a Gerdien condenser, which is similar to an ESP but usually with a lower voltage generating the external electric field, to separate the particles by their charge polarity. Using this approach, Kulon et al. [144] and Kulon and Balachandran [143] developed the Bipolar Charge Measurement System (BCMS) to characterise, in near real-time, the total positive and negative charges of large particles (1 to 10 µm) in an aerosol. The BCMS consists of five Gerdien condensers in series, each with a different precipitation voltage to capture a different range of particle sizes. The particles captured at each condenser stage are quantified by measuring the corresponding aerosol current of one particle polarity. Balachandran et al. [15] used the BCMS to measure the total positive and negative charges of two pharmaceutical powders. Using a similar approach, Baxter et al. [18] used one Gerdien condenser with different capture voltages to characterise the total positive and negative charges of sucrose particles during four transient releases. This technique was expanded by Joe et al. [102] to include an SMPS downstream of the Gerdien condenser to determine the neutral, positive and negative charge fractions of salt particles before and after ^{241}Am neutralisation.

[4] Similar to an SMPS with a DMA and CPC in tandem, but the DMA voltage is stepped rather than scanned.

2.3.7 Aerodynamic classification

Other methods that characterised particle charging focused on aerodynamic classification techniques. Glover and Chan [71] turned off the corona charger in the ELPI (Electrical Low Pressure Impactor, Keskinen et al. [122]) and used its 13 stage cascade impactor (cut-off diameters from 28 nm to 10 µm) and corresponding aerosol electrometers to measure the aerodynamic diameter resolved net charge of pharmaceutical particles from two different metered dose inhalers. Okuda et al. [196] also measured the net charge on particles by using a $PM_{2.5}$ impactor upstream of a high efficiency particulate arrestance (HEPA) filter. The net charge of the ambient, $PM_{2.5}$ particles collected on the filter were quantified two different ways, using a Faraday cage and surface potential measurements.

To measure more than net charge, Yli-Ojanperä et al. [278] developed the BOLAR (Dekati Ltd.) to characterise the bipolar charge of powders and inhaled aerosols using five sets of impactors and Gerdien condensers in parallel, which measure the positive and negative aerosol current at each impactor cut-off size. While this instrument allows near real-time measurements, it focuses on inhaled aerosols. Thus, its smallest cut-off size is only 950 nm, and its size resolution is low (approximately 4 classes per decade up to 11.57 µm). Wong et al. [275] used the BOLAR to measure the bipolar electrostatic charge from dry powder inhalers and compared it to the net charged measured by an ELPI (with its charger disabled). Following a similar approach as the BOLAR, Rowland et al. [219] used two Gerdien condensers in parallel downstream of the second stage (6.4 µm cut-off) of a Next Generation Impactor (NGI) to measure the charge-to-mass ratio of aerosol from three metered dose inhalers using high-performance liquid chromatography to determine the collected aerosol mass.

Järvinen et al. [98] took these aerodynamic approaches one step further by using a DMA to select particles with a narrow range of electrical mobilities then an ELPI with its corona charger turned off to resolve the size that corresponds to each charge state of each DMA classified particle. While this method requires the particle effective density to be known, Järvinen et al. [98] demonstrated its capabilities to measure the two-dimensional charge distribution[5] of 30 nm to 1 µm DOS particles that were unipolarly charged.

2.4 Measuring bipolar charging of non-spherical particles

In contrast to the spherical particle focus of Section 2.3, a large portion of naturally occurring and human-made particles have non-spherical morphologies, such as soot produced by a

[5] Particle concentration is shown as a function of particle size and charge state on a two-dimensional contour plot.

variety of combustion sources [197]. To address this gap, this section focuses on approaches for characterising the bipolar charging of non-spherical particles.

Similar to other trajectory observation approaches discussed for spherical particles in Section 2.3.1, Onischuk et al. [200] and Karasev et al. [119] measured the charge distribution of soot aggregates produced by a propane diffusion flame by observing the trajectory of the particles in an external electrostatic field. Both studies used a video camera to track the aggregates by capturing the laser light they scattered. Dua et al. [46] measured the charge distribution (up to 5 charge states) after neutralisation (using ^{204}Tl) of singlet, doublet and triplet aggregates formed of 500 nm polystyrene latex (PSL) particles based on their deposition location within a parallel plate mobility spectrometer. Similarly, based on the deposition location in an electrostatic precipitator (ESP), Vincent et al. [257] measured the positive and negative charge fractions of asbestos fibres (lengths of ≈ 2 to 8 µm and aspect ratios > 3) after aerosolization, and again, after neutralisation using an AC corona charger. This study also measured the charge distribution of the polydispersed fibres, as a function of their length, based on their penetration through a different ESP. The manual counting aspects of this approach were reduced by Vincent et al. [256] using an optical particle counter (OPC) to count and size the particles that passed through a symmetric, split-flow variation[6] of an ESP. This study measured the median charge and cumulative charge distribution of jute, cotton, flax, glass fibre and asbestos fibre between 700 nm and 10 µm. Similar ESP-OPC approaches were also utilized by six different studies to characterise the charging of particles with approximately spherical morphologies, as summarized in Section 2.3.3.

As demonstrated by Section 2.3.2, electrostatic precipitation (ESP) is the most common methodology for quantifying the uncharged fraction of an aerosol. An ESP with sufficiently high capture voltage collects all of the charged particles, thus allowing the uncharged particles to be quantified using a particle detector, such as a condensation particle counter (CPC; Agarwal and Sem [8]). Conversely, at sufficiently low capture voltages, all of the particles pass through the ESP, and the total particle concentration is measured. By comparing the mobility-equivalent size distribution measured by an Electrical Aerosol Analyser (EAA) downstream of an ESP with and without a high capture voltage, Burtscher et al. [27] measured the charged fraction of particles ($d_\mathrm{m} = 24$ to 424 nm) produced during combustion of wood (flaming or smouldering), cotton wicks, polyurethane, heptane (with 3% toluene) and alcohol. Using the same ESP-EAA approach, Kittelson et al. [131] measured the total charged fraction of polydispersed soot ($d_\mathrm{m} = 10$ to 1000 nm) from a diesel engine in terms of both particle number and volume, and compared it to the total charged fractions (in terms of number)

[6]This variation is referred to as an electrostatic elutriator which has symmetric outlets to partially separate the particles passing through by their polarity.

measured in parallel by an ESP-CPC. Jung and Kittelson [114] improved on this approach by replacing the EAA with a Scanning Mobility Particle Sizer (SMPS; Wang and Flagan [261]), increasing the resolution of the size distribution measurements and allowing the charged fraction resolved by particle electrical mobility to be measured. This approach was used to measure the charged fraction of diesel soot ($d_m \approx 8$ to 180 nm) produced from different engine speeds/loads and diesel compositions.

The size resolution of this approach was further improved by placing a DMA upstream of the ESP to first select particles with a narrow range of electrical mobilities. Using this DMA-ESP-CPC approach and ^{85}Kr to neutralise the particles before classification, Matsoukas and Friedlander [179] measured and compared the charged fraction of flame-generated aggregates ($d_m = 10$ to 200 nm) to spheres of zinc nitrate (30 to 200 nm), while Rogak and Flagan [215] quantified the uncharged fraction of PSL particles (72 to 725 nm), ammonium sulfate spheres (40 to 794 nm) and titanium oxide agglomerates ($d_m = 40$ to 794 nm). Kulkarni et al. [142] first validated this approach (including ^{85}Kr neutralisation) by measuring the uncharged fraction of spherical particles (100 to 660 nm composed of sulfate or DEHS), and then, measured the uncharged fraction of single-wall carbon nanotubes (CNT; $d_m = 100$ to 1000 nm, and aspect ratios of ≈ 3). Ku et al. [140] expanded this work to particles with higher aspect ratios (> 10) by measuring the uncharged fraction of carbon nanofibres (CNF; $d_m =$ 400 to 700 nm) and multi-walled carbon nanotubes (MWCNT; $d_m = 188$ to 594 nm), both neutralised using ^{210}Po. Similar to other DMA-ESP-CPC studies, Ku et al. [140] validated their approach by also measuring the uncharged fraction of spherical particles, specifically PSL (400 and 600 nm) and DEHS (700 nm). Table 2 of Ku et al. [140] summarizes previous investigations of the bipolar charging of non-spherical particles and is a useful overview. Most recent studies, including many of those discussed below, also used this DMA-ESP-CPC approach to determine the uncharged fraction of an aerosol.

To gain insights into the magnitude of charge acquired by individual particles, other studies measured the average charge per particle. A DMA was used to select particles with a narrow range of electrical mobilities, followed by a CPC and electrometer in parallel to measure the number and total charge of the classified particles, respectively. Using this approach, Wen et al. [263] measured the average charge per aggregate of iron oxide (primary particle sizes of 41 to 81 nm, thicknesses less than 0.1 µm and aspect ratios of 10 to several 100s), while Kittelson et al. [130] measured the average charge per soot aggregate ($d_m \approx 40$ to 270 nm) produced by three different diesel engines.

The charge of a particle affects its electrical mobility, and thus the charge distribution of an aerosol affects its equivalent size distribution based on electrical mobility [84]. Based on this principle, Maricq [168] measured the charged fraction (as well as negatively and

positively charged fractions) of soot from a McKenna, ethylene burner ($d_m \approx 3$ to 65 nm) or a light-duty diesel engine ($d_m \approx 10$ to 260 nm) by comparing SMPS scans with and without a neutraliser. In later studies, Maricq also used this methodology to complete similar measurements on soot produced by a premixed burner with different fuels [170] or by three light-duty engines [171]. These studies also determined the charge distribution (up to four charge states) of the soot particles using a tandem DMA (TDMA). The first DMA selects particles with a narrow range of electrical mobilities. The classified particles are then re-neutralised, and their resulting charge states are identified by the corresponding change in their electrical mobilities, measured using the second DMA. At low charge states (< 6), the dominant charge states usually appear as separate peaks in the measured distribution.

This TDMA approach (i.e. band-pass electrical mobility classification) is the most common methodology used to measure the individual charge fractions of submicron particles, as demonstrated in Section 2.3.4. Following this approach, Ahlberg and Hansson [9] measured the charge distribution (up to six charge states) of ^{85}Kr neutralised singlets, doublets, triplets and quadruplets formed of 364 nm PSL particles, while Drayton [45] measured the charge fractions (up to four charge states) of titanium oxide agglomerates ($d_m = 20$ to 215 nm). Following the same concept as the TDMA, Moon [190] used a DMA in tandem with an EAA to measure the charge fractions of soot ($d_m = 42$ to 266 nm) from three diesel engines; however, the study points to the low resolution of the EAA limiting the results.

Also using a TDMA, Tanaka et al. [235] measured the -2 to -1 charge ratio of carbon nanofibers ($d_m = 20$ to 90 nm, and aspect ratios of 4.6 to 39.4) neutralised using ^{241}Am, while Gopalakrishnan et al. [72] measured the single-to-double charge ratios of gold spheres (52 and 73 nm) or rods ($d_m \approx 30$ to 70 nm) neutralised by ^{210}Po. While the ratio approach of these studies does not provide absolute charge fractions, it does simplify the data inversion for the TDMA measurements and eliminates some sources of error, such as the uncertainty in the transmission efficiency of the DMA [166].

To accelerate TDMA measurements, many studies scan the downstream DMA (i.e. operate it in SMPS mode) to reduce the measurement time of the size distribution at the cost of accuracy. This approach (i.e. accelerated, band-pass electrical mobility classification, as discussed in Section 2.3.5 for charging studies of spherical particles) was used by Maricq [169] to measure charge distribution (up to 4 charge states) of soot particles ($d_m \approx 15$ to 85 nm) from a premixed ethylene–air flame at heights of 12 to 30 mm above the burner. Maricq [172] also used this approach to measure the ^{210}Po neutralised charge distribution (at least two charge states of each polarity) of POA oil droplets ($d_m \approx 11$ to 320 nm), flame-generated soot aggregates ($d_m \approx 15$ to 390 nm) and diesel soot ($d_m \approx 25$ to 290 nm). Similarly, Maricq [173] used this approach to investigate the coagulation and thermal equilibrium charging

(up to 4 charge states) of flame-generated soot ($d_m \approx 5$ to 100 nm) and diesel soot ($d_m = 25$ to 150 nm). Also using a DMA and SMPS in tandem, Ahn et al. [11] measured the double-to-single charge ratio of silicon oxide particles ($d_m \approx 15$ to 115 nm) sampled from three different heights (10, 40 and 80 mm) above a H_2/O_2/TEOS diffusion flame. Kim et al. [127] verified the DMA-SMPS approach by measuring the charge distribution (up to two charge states) of NaCl particles ($d_m = 50$ to 200 nm) neutralised using ^{210}Po and then measured the charge distribution of soot ($d_m = 50$ to 200 nm) produced by a laminar diffusion flame burning ethylene.

Following the DMA-SMPS approach, Sahu et al. [223] measured the in-situ charge distribution (up to two charge states) of titanium oxide ($d_m = 25$, 40 or 60 nm) from a flame reactor with and without copper doping, while Xiao et al. [276] measured the charge distribution (up to two charge states) of spherical particles (dioctyl sebacate [DOS] or ammonium sulfate) or aggregates[7] with mobility diameters between 70 and 300 nm, and neutralised using ^{210}Po. Mamakos [166] also used a DMA-SMPS to measure the +2 to +1 and +3 to +1 charge ratios for spherical (emery oil or DOS), flame-generated soot and spark-generated graphite particles ($d_m \approx 20$ to 400 nm) neutralised using x-ray radiation or ^{85}Kr. Also using a DMA-SMPS system, Nie et al. [191] measured the positive single and double charge fractions of crumpled graphene oxide (CGO) particles ($d_m = 60$ to 180 nm) synthesized at four different temperatures (between 200 and 800°C).

2.5 Research opportunities

2.5.1 Measuring aerodynamic size distributions of particles

As highlighted by Section 2.2 of this review chapter, methodologies for measuring the aerodynamic size distribution of an aerosol have steadily improved over the last 50 years. The near real-time sampling times and improved spectral resolution of measurements using the ELPI, APS or DAPS have overcome the temporal and resolution limitations of more simple approaches, such as impactors, centrifuges or cyclones. However, these improved approaches also have limitations.

The ELPI requires high sample flow rates (> 10 L/min) and low pressures (which may alter the properties of volatile particles) to measure submicron particles. Furthermore, its measurement range is limited by the number of impactor stages and their corresponding cut-off diameters. Similarly, the measurement range and resolution of the APS depends on

[7] Silver aggregates with a fractal dimension of 1.78 when unsintered and ≈ 3 when sintered at 600°C, or diesel soot particles with a fractal dimension of ≈ 1.75.

many factors, including the particle acceleration produced by its nozzle and the minimum particle size detected by its opticals. This operating principle can also deform or break-up liquid particles [16, 30], and its measurements must also be corrected for particle density at larger aerodynamic diameters (greater than 5 µm) with densities greater than 2 g/cm^3 [30].

In contrast, the operating principle of the AAC allows its classification range and resolution to be easily adjusted by changing the speed and sheath flow of the classifier [238]. Furthermore, unlike the ELPI and DAPS, classifying particles using the AAC does not depend on their charge distribution [240]. The AAC can also classify particles as small as 25 nm [28], overcoming the minimum size the APS (i.e. 500 nm) and SPART/E-SPART (i.e. 300 nm) can characterise. The high transmission efficiency of the AAC allows aerosols with low particle concentrations (as low as tens of particles per cm^3 with an appropriate particle detector) to be characterised. This detection contrasts with that of the ELPI and DAPS, which require sufficient particle concentrations to generate detectable aerosol currents. Therefore, there is an opportunity to leverage these advantages of the AAC to measure the aerodynamic size distribution of an aerosol.

2.5.2 Measuring bipolar charge distributions of particles

As highlighted by Sections 2.3 and 2.4 of this review chapter, approaches for measuring the bipolar charge distribution of spherical or non-spherical particles have focused on electrostatic methodologies, which are frequently affected by multiply-charged particles at sizes other than those of interest. For example, larger particles with higher charge can behave the same way in an external electric field (i.e. have the same electrical mobility) as smaller particles with lower charge. This effect is demonstrated by the example TDMA measurements in Figure 2.1, where the particles were re-neutralised between the upstream and downstream DMAs (DMA 1 and 2 with setpoints of $d^*_{\mathrm{m},1}$ and $d^*_{\mathrm{m},2}$, respectively). The labels at the top of the plot denote the charge state n_1 or n_2 of each particle after classification by the upstream or downstream DMA (i.e. $n_1 \rightarrow n_2$), respectively. Therefore, the singly-charged particles classified by the upstream DMA (i.e. particles with the mobility size intended for classification) are denoted by the $1 \rightarrow n_2$ labels, while the remaining labels highlight the artefacts from multiply-charged particles also classified by the upstream DMA. A portion of these artefacts is visible as stand-alone peaks. For example, peaks at larger equivalent diameters than the setpoint of the upstream DMA (e.g. $3 \rightarrow 2$ or $2 \rightarrow 1$) or peaks between the single and double charge peak classified by the downstream DMA (e.g. $3 \rightarrow 4$, $2 \rightarrow 3$ or $3 \rightarrow 5$). However, a portion of these artefacts also overlap with the peaks classified by the downstream DMA (e.g. $2 \rightarrow 2$ or $3 \rightarrow 3$ overlap with $1 \rightarrow 1$), thus making them challenging

to distinguish. This effect is well known and has also been demonstrated in previous charging studies [46, 45, 127, 142, 223, 276, 191].

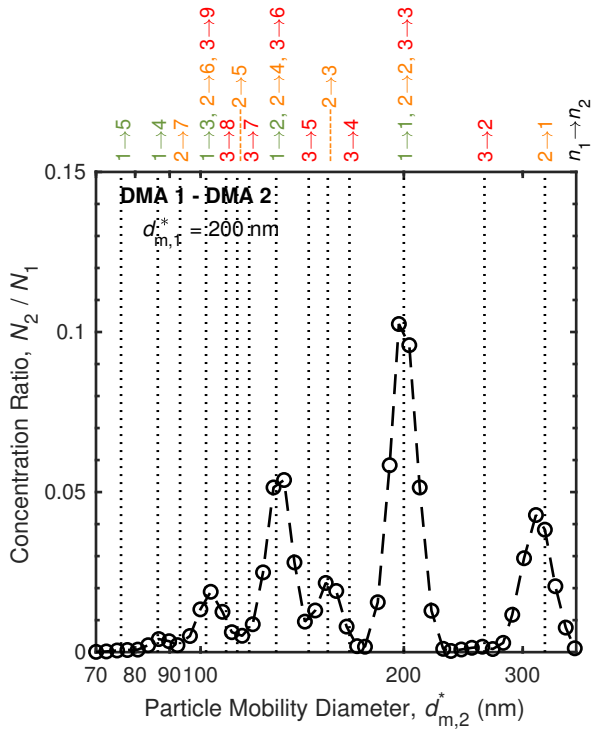

Fig. 2.1 Example results from a TDMA scan, where DMA 1 and DMA 2 have setpoints of $d^*_{m,1}$ and $d^*_{m,2}$, respectively, while N_1 and N_2 are the particle number concentrations after classification by DMA 1 and DMA 2, respectively.

The magnitude of this effect depends on the size and charge distributions of the aerosol, as well as the methodology being utilized and its setpoints/operating conditions. For example, Rogak and Flagan [215], using the DMA-ESP-CPC approach to measure the charged fraction of different aerosols, estimated the multiply-charged fraction was about 10% for most samples analysed. However, as a double-check for the same methodology (i.e. DMA-ESP-CPC), Kulkarni et al. [142] estimated the ratio of multiply-charged particles in the sample varied from 5% to 25% for sulfate particles and from 3% to 58% for CNTs, based on SMPS measurements downstream of the ESP. Furthermore, these proportions were determined after implementing two controls (i.e. low-activity neutraliser and impactor) to reduce multiply-charged particles.

For the TDMA approach, Mamakos [166] estimated the effect of multiply-charged particles was 6.5% or less based on the ratio of multiple to single charge fractions predicted by Wiedensohler [266]. However, this simulation assumed the size of the aerosol follows a

lognormal distribution consisting of smaller particles with geometric mean diameters (GMD) between 40 to 80 nm. For example, a DMA set at 55 nm will also classify doubly-charged particles with mobility diameters of 80 nm (or the upper GMD considered by Mamakos [166]). The predicted ratio of charge fractions of +1 particles at 55 nm to +2 particles at 80 nm is 0.12 [266]. However, since the proportion of multiply-charged particles increases with their size [266], this charge ratio significantly increases as larger particles are considered. For example, a DMA set at 250 nm will also classify doubly-charged particles with mobility diameters of 415 nm. The predicted ratio of charge fractions of +1 particles at 250 nm to +2 particles at 415 nm is 0.48 [266] or four times higher than the previous ratio with smaller particles. These charge fraction ratios, combined with the aerosol size distribution (i.e. its amplitude and width), determine the concentration of particles at each charge state classified by the DMA.

To limit multiple charging effects biasing the charging results [216, 127, 271, 276, 215], previous TDMA studies of particle charging focused on small particle sizes [212, 254, 52], used an upstream DMA setpoint larger than the CMD of the source aerosol [268, 215, 82], used a low activity neutraliser [76, 79], used a correction algorithm [127, 276] or used an impactor to remove particles larger than the single charge setpoint [247, 249].

The AAC would avoid these multiple charging effects as it produces a monodisperse aerosol, which is independent of the charge states of the particles [240]. Also, since the AAC does not require the particles to be charged during classification, the charge fractions from aerosol sources can be directly measured. This advantage avoids the complicated approach of the TDMA, which requires a back-propagated inversion by comparing the upstream DMA electrical mobility setpoint and downstream electrical mobility size distribution with a known charge distribution, such as done by Kim et al. [127]. This aspect of the AAC also allows uncharged particles to be easily generated by using an ESP in tandem. In contrast, methodologies with upstream electrostatic classification require the aerosol to be charged, classified, re-neutralised and then passed through an ESP [1, 158, 226, 217, 225, 83, 78, 280, 271, 209, 82, 279], thus significantly reducing the concentration of the classified, uncharged particles. Therefore, there is an opportunity to leverage these advantages of the AAC to measure the bipolar charge distribution of an aerosol.

2.6 Objectives

The overall objective of this work is to develop AAC methodologies, including the supporting theory and experimental validation, that allow the AAC to measure the aerodynamic size and bipolar charge distributions of an aerosol. These approaches will leverage the advantages of

the AAC to overcome the limitations of previous methodologies for similar purposes. The following objectives must be addressed to realize these applications:

1. **Measuring the aerodynamic size distribution of aerosol particles**

   a) **Steady-state or stepping measurements**
   This objective will develop the AAC methodology to measure the aerodynamic size distribution of an aerosol by stepping the AAC setpoint upstream of a particle detector, such as CPC or electrometer. This objective is divided into the following sub-objectives:

      i. Characterising the losses and broadening of the AAC transfer function due to non-ideal particle behaviour, such as diffusion and impaction;
      ii. Developing the inversion theory for the transfer function of the steady-state or stepping AAC to calculate the aerodynamic size distribution of an aerosol ($\mathrm{d}N/\mathrm{d}\log(d_\mathrm{a})$) from the raw measurements of a stepping AAC-particle detector system (i.e. number concentration of classified particles measured as a function of AAC setpoint, $N_\mathrm{det}(d_\mathrm{a}^*)$);
      iii. Validating the characterisation (Sub-objective 1ai) and inversion (Sub-objective 1aii) of the steady-state transfer function by using the stepping AAC to measure the size distribution of an aerosol source in parallel to SMPS, CPC and ELPI measurements; and
      iv. Estimating the effects of changing gas temperatures and pressures within the AAC on the particle aerodynamic diameter it classifies.

   b) **Scanning measurements**
   This objective will expand upon Objective 1a and develop the AAC methodology to accelerate measurements of aerodynamic size distribution by continuously scanning the AAC setpoint upstream of a particle detector, such as CPC or electrometer. This objective is divided into the following sub-objectives:

      i. Determining the required profile for angular classifier speed of the scanning AAC to simplify the derivation of its transfer function and sequential inversion;
      ii. Deriving the transfer function of the scanning AAC;
      iii. Developing the inversion theory for the transfer function of the scanning AAC to calculate the aerodynamic size distribution of an aerosol ($\mathrm{d}N/\mathrm{d}\log(d_\mathrm{a})$) from the raw measurements of a scanning AAC-particle detector system (i.e. number concentration of classified particles measured as a function of AAC setpoint and scan time, $N_\mathrm{det}(d_\mathrm{a}^*, t)$); and

iv. Validating the derivation (Sub-objective 1bii) and inversion (Sub-objective 1biii) of the scanning transfer function by comparing the size distribution the scanning AAC measures to the one measured by a stepping AAC-particle detector system of the same aerosol source.

2. **Measuring the bipolar charge distribution of aerosol particles**

   a) **Spherical particles**
   This objective will develop the AAC methodology to measure the bipolar charge distribution of spherical particles by using an AAC and DMA in tandem. This objective can be divided into the following sub-objectives:

      i. Developing the inversion theory for the tandem AAC-DMA to calculate the bipolar charging fractions of the particles based on the ratio of the particle concentrations measured upstream (N_1) and downstream (N_2) of the stepping DMA;
      ii. Validating the inversion theory of the tandem AAC-DMA (Sub-objective 2ai) using an aerosol source with a known charge distribution; and
      iii. Characterising different bipolar aerosol chargers using the experimental system and theory developed in Sub-Objective 2ai.

   b) **Non-spherical particles**
   This objective will expand upon Objective 2a and develop the AAC methodology to measure the bipolar charge distribution of non-spherical particles by using an AAC-DMA-DMA system. This objective can be divided into the following sub-objectives:

      i. Demonstrating an AAC and DMA in tandem can generate an aerosol of homogeneous, non-spherical particles using scanning electron microscope (SEM) images and electrical mobility measurements of the tandem-classified particles;
      ii. Developing the inversion theory for the AAC-DMA-DMA system to calculate the bipolar charging fractions of the non-spherical particles based on the ratio of the particle concentrations measured upstream (N_1) and downstream (N_2) of the stepping DMA;
      iii. Characterising the bipolar charge distribution for a subset of flame soot aggregates to provide insights into the bipolar charging of non-spherical particles using the experiment setup and theory developed in Sub-Objectives 2bi and 2bii.

This evolution for the AAC is similar to that of the DMA and CPMA. For example, the DMA became a key instrument in a Scanning Mobility Particle Sizer (SMPS, [261]) and a

Tandem Differential Mobility Analyser (TDMA, [228]). For both methodologies, advanced correction [81] and inversion methods [229, 77] were developed to derive meaningful results from the raw data. Similarly, the CPMA was further developed to measure the transient density of particles [108] and the aerosol mass concentration [43].

Chapter 3

Measuring Aerodynamic Size Distributions using the Steady-State AAC

3.1 Introduction

This chapter[1] addresses Objective 1a and develops the AAC methodology to measure the aerodynamic size distribution of an aerosol by stepping the AAC setpoint upstream of a particle detector. This new approach leverages the high transmission efficiency, independence from particle charging, and adjustable classification range and resolution of the AAC. Therefore, the methodology of stepping the AAC improves upon the low classification resolutions and set measurement ranges (which focus on larger particles) of previous methodologies (such as the ELPI and APS) used for a similar purpose.

To collect accurate measurements of a size distribution, non-ideal particle behaviour within the AAC, such as particle diffusion and impaction, must be accounted for by characterising the transfer function of the AAC. While the transfer functions of various DMA designs have been characterised using tandem classifier configurations [90, 56, 19, 177, 120, 153], to date there has been limited characterisation of the AAC. Tavakoli et al. [240] characterised the AAC transfer function using two alternative methods due to the existence of only one AAC at that time (i.e. the first prototype, which is physically quite different to the commercially available version). Using polystyrene latex (PSL) particles and assuming their atomized size distribution was normally distributed with a known effective density, the theoretical transfer function convolution was compared to the PSL concentrations measured upstream

[1] This chapter is based on an article by Johnson et al. [104] published by Taylor & Francis Group in Aerosol Science and Technology on 13/03/2018, available online: https://doi.org/10.1080/02786826.2018.1440063.

and downstream of the AAC using a CPC. The prototype was also characterised using an AAC-DMA system, however the tandem deconvolution required both the theoretical DMA and AAC transfer functions. Thus differences between the theoretical and experimental DMA transfer functions, as well as uncertainty in particle effective density, likely introduced errors into the characterisation of the AAC transfer function.

3.1.1 Outline of chapter

In light of these uncertainties and a recommendation by Tavakoli et al. [240], this chapter first characterises the AAC transfer function using a tandem AAC (TAAC) system to quantify the transmission efficiency and transfer function broadening from non-ideal particle behaviour. Based on this characterised transfer function, its inversion is then developed allowing the AAC and a particle detector (such as a CPC or electrometer) system to accurately measure the aerodynamic size distribution of an aerosol source from 32 nm to 3 µm. This upper size limit is dictated by the 3775 CPC used for this work and could be expanded up to 6.8 µm with the appropriate particle detector. The characterisation and inversion of the AAC transfer function are validated by comparing the size distributions of different aerosols measured with an AAC-CPC system against parallel measurements taken with a SMPS, a CPC and an ELPI. Finally, the effects of changing gas temperatures and pressures between AAC measurements are estimated based on theory to determine their significance on particular applications, such as the TAAC system utilized in this chapter.

3.2 Experimental setup

3.2.1 Characterisation of AAC transfer function

The tandem AAC (TAAC) setup used to characterise the AAC transfer function is shown in Figure 3.1. The upstream AAC (AAC 1) was set at a constant setpoint $(d^*_{\mathrm{a},1})$ while the downstream AAC (AAC 2) stepped through the domain of the classified particles $(d^*_{\mathrm{a},2})$ and recorded the number concentration of the twice-classified particles (N_2) measured by a TSI 3775 CPC. This measurement with AAC 2 is henceforth referred to as a step-scan. The 3775 CPC utilizes a 300 cm^3/min aerosol sample flow and has a 4 nm minimum detectable particle size [246]. Before and after stepping, AAC 2 was bypassed to directly measure the particle number concentration classified by AAC 1 (N_1).

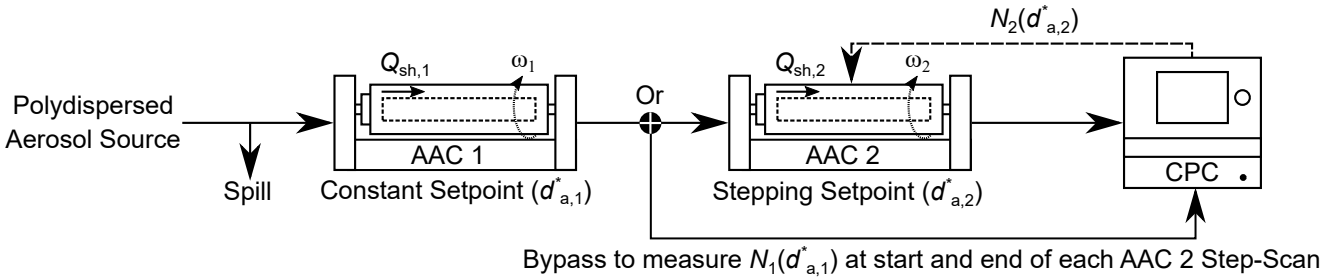

Fig. 3.1 Tandem AAC experimental setup used to characterise the AAC transfer function.

At reference classifier conditions (296.15 K and 101,325 Pa), the AAC can classify aerodynamic particle diameters from 32 nm to 3 µm at low flow[2] (LF) and from 202 nm to 6.8 µm at high flow[3] (HF) by changing the classifier speed (20 to 700 rad/s at LF and 20 to 500 rad/s at HF). Thus five different aerodynamic sizes, spaced equally across each of these ranges logarithmically, were selected to characterise the AAC transfer function. At low flow AAC 1 was set at 50, 125, 325, 825, or 2100 nm, while at high flow AAC 1 was set 300, 600, 1200, or 2400 nm. The endpoints of these size ranges (e.g. 50 nm at low flow) were selected to be offset from the AAC's classification bounds (e.g. 32 nm at low flow), thus allowing AAC 2 to characterise both sides of the distribution classified by AAC 1. At each of these AAC 1 setpoints, five independent AAC 2 step-scans were completed, including measuring N_1 prior to (pre) and after (post) each AAC 2 step-scan. To limit uncertainties from an unstable aerosol source, a step-scan was repeated if the stability of its pre/post N_1 measurements or the agreement between these values was not within 6%. This threshold was selected based on the other uncertainties within the experimental setup and only increases the propagated particle concentration uncertainty from 11.2% to 12.7% with the 10% CPC measurement uncertainty [246] and assuming an indirect AAC uncertainty contribution of 5%. These experiments were repeated with the AAC positions reversed to determine the transfer function variations between the two AACs.

The AAC transfer function was not characterised at aerodynamic diameter setpoints larger than 3000 nm, as this was above the 3 µm particle size limit of the 3775 CPC. Attempts were made to measure the concentration of particles classified by the AAC at 4800 nm using a Palas GmbH Welas® digital 1000H optical aerosol spectrometer. While the optical data showed the AAC is capable of classifying particles in this size range, the twice-classified number concentrations (N_2) were too low for the Welas® to accurately quantify. Given that the particle concentration was detectable after classification by one AAC, but not two, indicates that the losses in the AAC at this size range should also be considered. Thus, characterising

[2]Sample and sheath flow rates of $Q_a = 0.3$ & $Q_{sh} = 3$ L/min, respectively.
[3]Sample and sheath flow rates of $Q_a = 1.5$ & $Q_{sh} = 15$ L/min, respectively.

the AAC transfer function above 3 µm with a larger underlying size distribution or using a different particle counter[4] should be considered in future work.

3.2.2 Validation of size distribution deconvolution

The AAC-CPC system used to characterise different aerosol sources in parallel to SMPS, CPC and ELPI measurements is shown in Figure 3.2. The AAC stepped through the aerodynamic diameter domain of the source (d_{a}^{*}) and recorded the corresponding number concentration (N_{det}) of the classified particle measured by a 3775 CPC. For both the TAAC and size distribution validation measurements, the conductive tubing lengths of each aerosol sample flow path were the same, and therefore no particle loss correction was required. HEPA filtered make-up air was added as close as possible to the ELPI inlet to maintain a similar sample flow rate and thus particle line losses as the sample lines of the other instruments.

A TSI SMPS, consisting of ^{85}Kr neutraliser, 3080 DMA (with 3081 long column) and 3775 CPC in series, measured the mobility size distribution of each aerosol source. The SMPS was operated with an aerosol and sheath flow of 0.3 and 3 L/min, respectively, corresponding to a 14.6 to 661 nm mobility scan range or 13.4 to 629 nm aerodynamic scan range for a particle density of 914 kg/m^3. Similar to the AAC-CPC system, the DMA setpoint (d_{m}^{*}) was changed, and the corresponding classified particle number concentration (N_{det}) was measured and recorded as a function of its mobility diameter setpoint. However, the DMA voltage was scanned exponentially to reduce the overall measurement time to 3 minutes, compared to an AAC-CPC measurement time of 10 to 15 minutes. To avoid introducing disagreement between different CPCs, the same 3775 CPC was used downstream of the AAC or DMA. The AAC or DMA was also bypassed to allow the CPC to directly measure the total particle number concentration (N_{tot}) of the polydispersed aerosol.

A Dekati Classic ELPI® quantified the aerosol's aerodynamic size distribution from 43.3 nm to 8.59 µm using a corona charger to produce a known particle charge distribution before passing the sample through 12 impactor stages. The cut-off aerodynamic diameter for each impactor decreases with each sequential stage. The current produced from the particles colliding with each impactor plate was then independently measured. By using the measured currents (I_i) and knowing the cut-off size for each stage $(d_{\mathrm{a50},i})$ the aerodynamic size distribution of the aerosol was determined.

The characterisation and deconvolution of the AAC transfer function were validated by comparing the lognormal distribution parameters fitted to the size distributions determined

[4] Such as an optical particle counter optimized for the size range of interest or an electrometer if the particle charge distribution is known.

from the AAC-CPC system to those fitted to the SMPS, CPC and ELPI measurements of the same aerosol source.

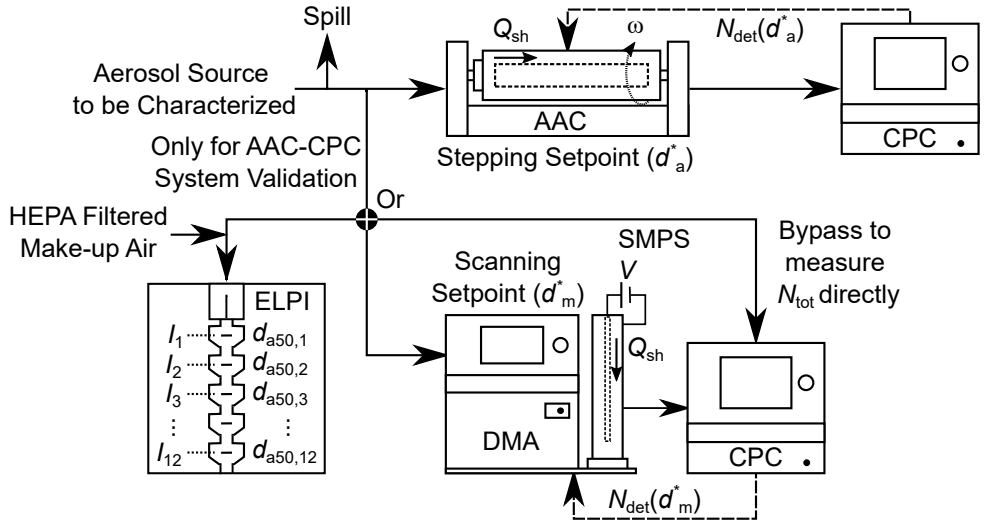

Fig. 3.2 AAC-CPC system used to measure the aerodynamic size distribution of an aerosol. This system was validated by comparing against ELPI, SMPS and CPC measurements collected in parallel.

3.2.3 Aerosol sources

The polydispersed aerosols used for these experiments were generated by atomizing different oils with a BGI Collison or TSI 9302 constant output nebulizer. Through multiple design iterations and testing of the particle generation inputs (compressed air control, liquid volume or feed-rate, and dilution system), either system was able to produce a total particle number concentration stable within 6% over the 10 to 15 minutes measurement time. DOS (Bis(2-Ethylhexyl) sebacate) and 702 diffusion pump oils were selected due to their low vapour pressures (i.e. resistance to evaporation) and forming particles with a known spherical morphology and density (DOS: 914 kg/m^3 and 702 oil: 1070 kg/m^3). These characteristics allowed an accurate conversion between aerodynamic and mobility size distributions. The AAC transfer function was characterised using DOS particles, then validated (including its inversion) with both aerosol sources.

The BGI Collison nebulizer produced a slightly narrower mobility size distribution of DOS particles with a larger count median diameter (CMD) and higher total particle number concentration (N_{tot}) than the TSI nebulizer (312 nm, 1.90 GSD and 5.05×10^7 cm^{-3} versus 250 nm, 1.97 GSD and 1.97×10^7 cm^{-3}, respectively). Therefore, the Collison was used

to collect any of the TAAC data for AAC 1 setpoints ($d^*_{a,1}$) greater than 300 nm. The TSI 9302 constant output nebulizer was used to collect the remaining TAAC DOS data (i.e. $d^*_{a,1} < 300$ nm). During validation, the TSI nebulizer produced a mobility size distribution of 702 oil particles with a 287 nm CMD, 1.73 GSD and 2.46×10^7 cm^{-3} total particle number concentration. To limit the particle sizes produced by the TSI nebulizer for either oil, the liquid feed rate was controlled to 6 ml/hour using a Harvard Apparatus Model 22 syringe pump.

For either nebulizer, a liquid trap was used to remove excess fluid mobilized during atomization, while a Cambustion rotating disk diluter was used to control the particle number concentration upstream of the different experimental setups. The dilution ratio was set to ensure the CPC operated below its photometric mode ($< 5 \times 10^5$ particles per cm^3) in any of the previously described experimental setups (i.e. measuring N_1 or N_2 in the TAAC setup and $N_{det}(d^*_a)$, $N_{det}(d^*_m)$ or N_{tot} in the validation setup).

3.3 Theory

3.3.1 Characterisation of AAC transfer function

Non-ideal particle behaviour within the AAC, such as particle diffusion and impaction, must be considered for accurate measurements of size distribution. This chapter follows the methodology developed by Martinsson et al. [177] to characterise the DMA transfer function and quantifies the non-ideal particle behaviour within the AAC using a tandem AAC (TAAC) system and comparing its results against its theoretical tandem deconvolution. The non-diffusing or triangular AAC transfer function (Ω_{ND}) developed by Tavakoli and Olfert [238] based on particle streamline theory was selected for the TAAC deconvolution due to ease of parameterization and is represented as:

$$\begin{aligned}\Omega_{ND}(\tilde{\tau}, \beta, \delta) = \frac{1}{2\beta(1-\delta)} \big[&|\tilde{\tau} - (1+\beta)| + |\tilde{\tau} - (1-\beta)| \\ &- |\tilde{\tau} - (1+\beta\,\delta)| - |\tilde{\tau} - (1-\beta\,\delta)| \big],\end{aligned} \tag{3.1}$$

where β and δ are non-dimensional parameters for the classifier flows defined as:

$$\beta = \frac{Q_s + Q_a}{Q_{sh} + Q_{exh}}, \tag{3.2}$$

$$\delta = \frac{Q_s - Q_a}{Q_s + Q_a}. \tag{3.3}$$

The aerosol flow rate entering or leaving the classifier is denoted by Q_a or Q_s, respectively, while the sheath flow rate entering or leaving the classifier is denoted by Q_{sh} and Q_{exh}, respectively.

Due to current configuration of the commercial AAC, this work only considered balanced (B) classifier flows ($Q_{sh} = Q_{exh}$ and $Q_a = Q_s$). Therefore $\delta = 0$ (as per Equation 3.3), and as derived in Section A.1, the non-diffusing AAC transfer function (Equation 3.1) simplifies to:

$$\Omega_{ND,B}(\tilde{\tau}, \beta) = \frac{1}{2\beta}\left[|\tilde{\tau} - (1+\beta)| + |\tilde{\tau} - (1-\beta)| - 2\,|\tilde{\tau} - 1|\right]. \tag{3.4}$$

To capture the non-ideal particle behaviour, a transmission efficiency (λ_Ω) and transfer function width factor (μ_Ω) were introduced into this triangular transfer function (similar to Martinsson et al. [177]) as follows:

$$\begin{aligned}\Omega_{ND,B,NI}(\tilde{\tau}, \beta, \lambda_\Omega, \mu_\Omega) = \frac{\lambda_\Omega\,\mu_\Omega^2}{2\beta}\Bigg[&\left|\tilde{\tau} - \left(1 + \frac{\beta}{\mu_\Omega}\right)\right| \\ &+ \left|\tilde{\tau} - \left(1 - \frac{\beta}{\mu_\Omega}\right)\right| - 2\,|\tilde{\tau} - 1|\Bigg].\end{aligned} \tag{3.5}$$

As demonstrated in Section A.1.2, the transmission efficiency scales the integrated area under the transfer function to quantify particle losses. The width factor scales the full width at half maximum (FWHM) of the transfer function to quantify its broadening due to particle diffusion and other sources, such as classifier flow effects and setpoint variations. This parameterized transfer function ($\Omega_{ND,B,NI}$) is represented in Figure 3.3.

Based on this transfer function, the theoretical particle number concentration ratio measured between upstream (N_1) and downstream (N_2) of AAC 2 was determined using the TAAC deconvolution as follows:

$$\frac{N_2(\tau_2^*)}{N_1} = \frac{\int \eta(d_{a,2})\,\Omega_{ND,B,NI,1}\,\Omega_{ND,B,NI,2}\,d\tau}{\int \eta(d_{a,1})\,\Omega_{ND,B,NI,1}\,d\tau}, \tag{3.6}$$

where $\Omega_{ND,B,NI,1}$ is a function of τ_1, τ_1^*, β_1, $\lambda_{\Omega,1}$, $\mu_{\Omega,1}$, while $\Omega_{ND,B,NI,2}$ is a function of τ_2, $\tau_{12}^* \cdot \tau_2^*$, β_2, $\lambda_{\Omega,2}$, $\mu_{\Omega,2}$. The classification agreement between AAC 1 and 2 (i.e. τ_2^*/τ_1^*) is quantified by τ_{12}^*, and $\eta(d_a)$ is the counting efficiency at aerodynamic diameter (d_a) of the particle counter downstream of the tandem AACs.

To simplify this deconvolution, it was assumed that the particle counting efficiency was constant over the narrow aerodynamic diameter range stepped through by AAC 2 (i.e. $\eta(d_{a,1}) = \eta(d_{a,2,i})$, and that AAC 1 and 2 had the same transfer function width factor (i.e. $\mu_{\Omega,1} = \mu_{\Omega,2}$). To maximize validity of the latter, AAC 1 and 2 were operated with the same sample and sheath flow rates for each TAAC data-point collected. Since N_1 was measured

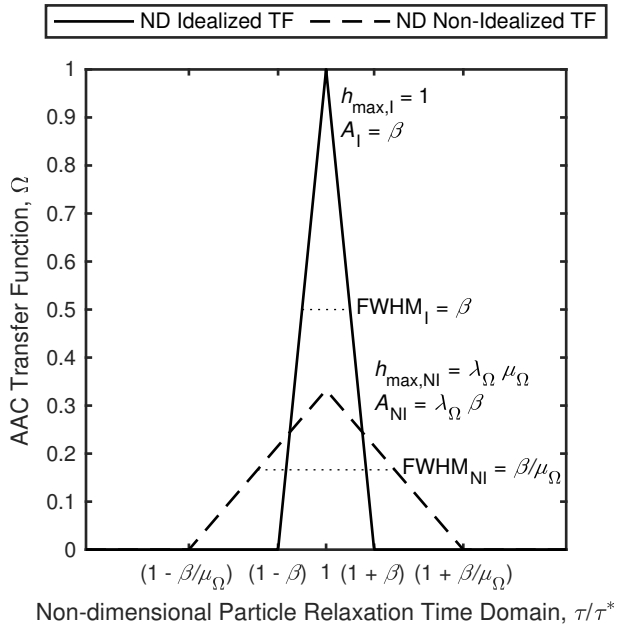

Fig. 3.3 Idealized (Equation 3.1) and non-idealized (Equation 3.5) transfer function of the AAC operating with balanced classifier flows.

directly, the losses within AAC 1 were already accounted for and $\lambda_{\Omega,1} = 1$ was used for the theoretical TAAC deconvolution. By comparing this theoretical N_2/N_1 concentration ratio (Equation 3.6) to the concentrations measured experimentally and minimizing the difference between them using least-squares minimization, the transmission efficiency $(\lambda_{\Omega,2})$ and transfer function width factor $(\mu_{\Omega,2})$ for AAC 2, as well as the classification agreement τ^*_{12} between AAC 1 and 2, were determined.

3.3.2 Deconvolution of size distribution

As developed in the Appendix A (full derivation Section A.2), the theory to convert the raw measurements $(N_{\mathrm{det}}(d^*_{\mathrm{a},i}))$ collected using an AAC (operating with balanced classifier flows) and particle detector (such as a CPC or electrometer) to represent the aerodynamic size distribution of an aerosol source $(\mathrm{d}N/\mathrm{d}\log d_{\mathrm{a}})$ can be summarized as:

$$\left.\frac{\mathrm{d}N(d_{\mathrm{a}})}{\mathrm{d}\log d_{\mathrm{a}}}\right|_{d^*_{\mathrm{a},i}} = \frac{N_{\mathrm{det}}(d^*_{\mathrm{a},i})\ln(10)}{\eta(d^*_{\mathrm{a},i})\left.\frac{\mathrm{d}\log d_{\mathrm{a}}}{\mathrm{d}\log\tau}\right|_{d^*_{\mathrm{a},i}}\beta^*_{\mathrm{ss},i}}, \tag{3.7}$$

where N_{det} is the number concentration of the particles classified by the AAC and η is the counting efficiency of the particle counter downstream of the AAC, both at AAC setpoint $d^*_{\mathrm{a},i}$.

The deconvolution parameter ($\beta^*_{\mathrm{ss},i}$) based on the idealized or non-idealized transfer functions (Equations 3.4 or 3.5, respectively) of the steady-state AAC operating with balanced flows is derived in Section A.3.1 or A.3.2, respectively. The solution for the non-idealized variation ($\beta^*_{\mathrm{ss,B,NI}}$) is as follows:

$$\beta^*_{\mathrm{ss,B,NI}} = \lambda_\Omega \, \mu_\Omega \left[\ln\left(\frac{1+\frac{\beta}{\mu_\Omega}}{1-\frac{\beta}{\mu_\Omega}} \right) + \frac{\mu_\Omega}{\beta} \ln\left(1 - \left(\frac{\beta}{\mu_\Omega} \right)^2 \right) \right], \tag{3.8}$$

while the solution for the idealized variation ($\beta^*_{\mathrm{ss,B,I}}$) is summarized by Equation A.38. As per Section A.4, the logarithmic ratio to shift from the particle relaxation time to aerodynamic diameter domain ($\frac{\mathrm{d}\log d_\mathrm{a}}{\mathrm{d}\log \tau}$) was found to be:

$$\frac{\mathrm{d}\log d_\mathrm{a}}{\mathrm{d}\log \tau} = C_c(d_\mathrm{a}) \, d_\mathrm{a} \left[2d_\mathrm{a} + \alpha_{c_c} \, \lambda + \beta_{c_c} \, \lambda \, \exp\left(-\gamma_{c_c} \, \frac{d_\mathrm{a}}{\lambda} \right) \left(1 - \frac{\gamma_{c_c} \, d_\mathrm{a}}{\lambda} \right) \right]^{-1}, \tag{3.9}$$

where Kim et al. [126] determined $\alpha_{c_c} = 2 \times 1.165 = 2.33$, $\beta_{c_c} = 2 \times 0.483 = 0.966$ and $\gamma_{c_c} = 0.997/2 = 0.4985$. The Cunningham slip correction factor (C_c) and mean free path (λ) can be determined from Equations A.41 and A.42, respectively. When the CPC is connected to the AAC serially, the internal AAC software automatically records the CPC measurements, calculates the size distribution inversion (i.e. Equations 3.7 to 3.9) and outputs the results in a tab delimited text file.

In the interest of completeness, the inversion for the steady-state AAC operating with unbalanced (UB) classifier flows is derived in Section A.7. However, future work is required to validate this theory experimentally. The unbalanced classifier flow configuration is harder to implement as it requires three independent flow control points, rather than two. Similar to a DMA, Tavakoli and Olfert [238] predicted unbalanced flows will produce an AAC transfer function shaped as a trapezoid with higher classification resolution as the aerosol sample to sheath ratio (β) decreases.

3.4 Characterisation of AAC transfer function

The AAC transmission efficiency, transfer function width and classification agreement factors (each an average of five AAC 2 step-scans at each AAC 1 setpoint) for two different AACs (denoted as AAC A and AAC B) are shown in Figure 3.4. The error bars represent the 95% confidence interval (CI) of each average assuming a t-distribution.

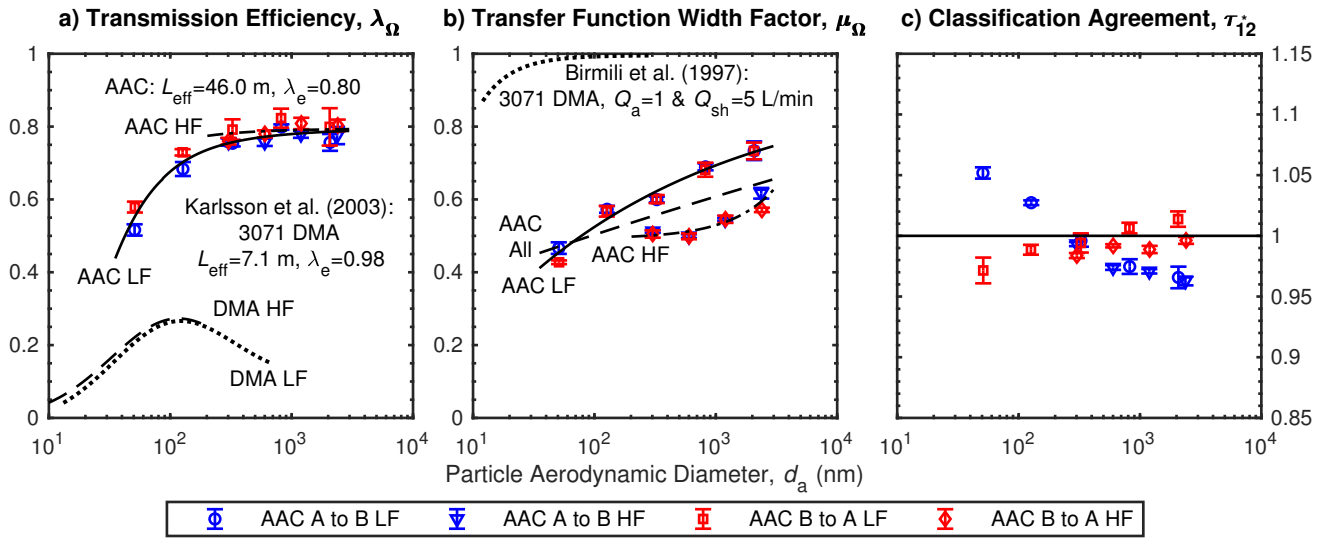

Fig. 3.4 Characterisation of the AAC transfer function, where low-flow (LF) corresponds to $Q_a = 0.3$ L/min and $Q_{sh} = 3$ L/min, while high-flow (HF) corresponds to $Q_a = 1.5$ L/min and $Q_{sh} = 15$ L/min. The lines shown near the λ_Ω and μ_Ω values of the AAC transfer function (i.e. in subfigures a and b, respectively) are corresponding fits (as described in Sections 3.4.1 and 3.4.2, respectively) to estimate these parameters across the classification range of the AAC at different classifier flow conditions (AAC LF, AAC HF or AAC All).

3.4.1 Transmission efficiency, λ_Ω

To estimate the transmission efficiency of the AAC across its entire classification range, the transmission efficiencies ($\lambda_{\Omega,\mathrm{AAC}}$) measured experimentally were fitted with the following relationship using least-squares minimization:

$$\lambda_{\Omega,\mathrm{AAC}} = \lambda_\mathrm{d}\,\lambda_\mathrm{e}, \tag{3.10}$$

where λ_e is the classifier entrance/exit transmission efficiency and λ_d is the diffusional transmission efficiency defined by Karlsson and Martinsson [120] as:

$$\lambda_\mathrm{d} = \begin{cases} 0.819e^{-11.5\delta_\mathrm{dep}} + 0.0975e^{-70.1\delta_\mathrm{dep}} + 0.0325e^{-179\delta_\mathrm{dep}} & \text{if } \delta_\mathrm{dep} \geq 0.007 \\ 1 - 5.50\delta_\mathrm{dep}^{\frac{2}{3}} + 3.77\delta_\mathrm{dep} + 0.814\delta_\mathrm{dep}^{\frac{4}{3}} & \text{if } \delta_\mathrm{dep} < 0.007 \end{cases}. \tag{3.11}$$

The non-dimensional deposition parameter (δ_dep) is determined by:

$$\delta_\mathrm{dep}(d_\mathrm{m}) = \frac{L_\mathrm{eff}\,D(d_\mathrm{m})}{Q_\mathrm{a}}, \tag{3.12}$$

where L_{eff} is the length of a circular tube with the same particle deposition from diffusion as the classifier, D is the diffusion coefficient of the particles and Q_{a} is the aerosol flow rate entering the classifier.

The DMA transmission efficiency ($\lambda_{\Omega,\text{DMA}}$) was also estimated using Equation 3.10 with input parameters experimentally determined by Karlsson and Martinsson [120], and multiplying by the fraction of particles with a single negative charge state. This charge fraction was estimated following Wiedensohler [266]. Even though the AAC effective deposition length is significantly longer than the DMA (L_{eff} of 46.0 m versus 7.1 m, respectively) and its entrance/exit losses are higher (λ_{e} of 0.8 versus 0.98, respectively), the charging fraction is the dominate factor for the DMA transmission efficiency and limits it to less than 30%. Thus the AAC classifying particles independent of their charge not only avoids multiple charging artefacts, but allows for transmission efficiencies approximately 2.6 to 5.1 times higher than a DMA for the same particle size.

3.4.2 Width factor of transfer function, μ_{Ω}

Contrary to the transfer function theory developed by Tavakoli and Olfert [238] for the AAC, its transfer function is 1.5 to 2.4 times (i.e. μ_{Ω} ratio of DMA and AAC at each particle size) experimentally broader than the DMA transfer function characterised by Birmili et al. [19]. The width of the DMA transfer function starts to deviate from theory below 100 nm due to particle diffusion with a maximum difference of less than 14%. The width of the AAC transfer function deviates across its entire measurement range from that predicted by particle streamline theory. This discrepancy may be due to a classifier flow effect as the width of the AAC transfer function increases with increasing classifier flows (i.e. $\mu_{\text{AAC,HF}} < \mu_{\text{AAC,LF}}$). The trend of the AAC transfer function broadening at high flow (i.e. positive power coefficient, $c_{\mu 2}$) is also in contrast to the broadening trends observed in the AAC at low flow or DMA (i.e. negative power coefficients, $c_{\mu 2}$). Further investigation is required to prove this hypothesis and develop possible improvements. This additional broadening can be negated by operating the AAC at a higher classifier resolution (i.e. higher sheath to sample flow ratio).

Based on fitting the experimental data of this work and Birmili et al. [19], the transfer function width factor of the AAC ($\mu_{\Omega,\text{AAC}}(d_{\text{a}})$) or a 3071 DMA ($\mu_{\Omega,\text{DMA}}(d_{\text{m}})$) across their entire classification range can be estimated from:

$$\mu_{\Omega}(d_{\text{p}}) = c_{\mu 1}\, d_{\text{p}}^{\,c_{\mu 2}} + c_{\mu 3} \tag{3.13}$$

where d_{p} is the particle diameter in nm and the fitted coefficients for transfer function broadening are summarized in Table 3.1.

Table 3.1 Fitted coefficients to estimate transfer function broadening as function of particle size.

Instrument	$c_{\mu 1}$	$c_{\mu 2}$	$c_{\mu 3}$
AAC LF	-1.201	-0.2387	0.9244
AAC HF	1.056e-05	1.181	0.4923
AAC All	-1.73	-0.0316	1.999
DMA [19]	-11.05	-1.739	0.9956

The additional error from using these curves to estimate the broadening of the AAC transfer function ranges from -4.2% to 3.7% for the flow-dependent fits (i.e. AAC LF and HF) and from -12.8% to 17.4% for the flow independent fit (i.e. AAC All). The flow-independent fit considered all of the broadening factors experimentally measured at both low and high flow, and is intended as an approximation of the transfer function broadening at other flow conditions where the AAC transfer function has not yet been characterised.

This characterisation focused on spherical particles to establish the fundamental theory for AAC classification; however, future work should expand the transfer function characterisation to non-spherical particles or aggregates. Based on theory [238], varying particle morphology does not affect the AAC classification setpoint (i.e. the AAC classifies particles based solely on their relaxation time). However, varying effective particle density (often resulting from varying particle morphology) will affect a particle's equivalent mobility diameter relative to its aerodynamic diameter, and thus, change the losses and broadening of the AAC transfer function due to particle diffusion. It is predicted varying effective density will only significantly affect the AAC transfer function where diffusion dominates (i.e. small mobility particle sizes, $<$100 nm) or large particles with high effective densities where impaction on the classifier inlet and outlet begin to dominate.

3.4.3 Setpoint agreement, τ_{12}^*

The classification agreement between AAC A and AAC B was 3% or better for 16 of the 18 data-points, as shown in Figure 3.4c. It is hypothesized that the linear trends for classification agreement, also shown in Figure 3.4c, are due to applying a linear sheath flow rate calibration that neglects the temperature changes of the sheath air caused by frictional heating from varying classifier speeds.

3.5 Validation of size distribution deconvolution

The characterisation and deconvolution of the AAC transfer function was validated by comparing the size distributions and particle concentrations measured with an AAC-CPC system against parallel measurements taken with a SMPS and CPC as shown in Figure 3.5. The aerodynamic size distributions measured by the AAC were converted to mobility size distributions using the equations derived in Section A.5. Including the transmission efficiency and width factors within the deconvolution of transfer function (i.e. non-idealized inversion) greatly improved agreement with the SMPS and CPC measurements as shown in Table 3.2. Without this correction, the AAC measurements at low or high flow underestimated the total particle number concentration by 20.2% to 28.6% as shown by the "Raw" measurements in Table 3.2.

The mobility size distributions measured by the SMPS were corrected for multiple charging (MC) effects following He and Dhaniyala [81] based on the particle charge fractions estimated by the bipolar charging models of Wiedensohler [266] and Gunn and Woessner [75]. This correction greatly improved agreement with the AAC and CPC measurements. Relative to the raw SMPS measurements, the MC correction increased the reported CMD_m by 13.5%, 20.0% and 16.6%, and decreased the reported N_{tot} by 50.8%, 56.8% and 55.7% for the three aerosol sources (DOS Constant Output, DOS Collison and 702 oil Constant Output, respectively).

The agreement between the corrected SMPS and AAC size distribution measurements ranged from 1.3% to 5.9% for mobility count median diameter (CMD_m) and 0.1% to 4.5% for geometric standard deviation (GSD). The total particle number concentration (N_{tot}) from the corrected AAC measurements agreed within 0.1% to 6.6% of those measured by the CPC, as summarized in Table 3.2. The disagreement between the SMPS and CPC measurements of total particle number concentration was more than twice that of the AAC, with the multiple charge corrected SMPS measurements overestimating the total particle number concentration by 11.8%, 19.7% and 10.4% for the three aerosol sources (DOS Constant Output, DOS Collison and 702 oil Constant Output, respectively).

The methodology of stepping the AAC was further validated by comparing its measurements of aerodynamic size distribution to those collected in parallel using an ELPI. The size distribution measured by the ELPI was slightly narrower and larger (in terms of aerodynamic count median diameter, CMD_a) compared to the distributions measured by the AAC as shown in Figure 3.6. Considering the lower resolution of the Classic ELPI (approximately 5 size classes per decade), there was reasonable agreement between the measured aerodynamic size distributions of the same aerosol source, as shown in Table 3.3 (within 18.2% of CMD_a, 7.7% of GSD and 22.4% of total particle number concentration). It should be noted that

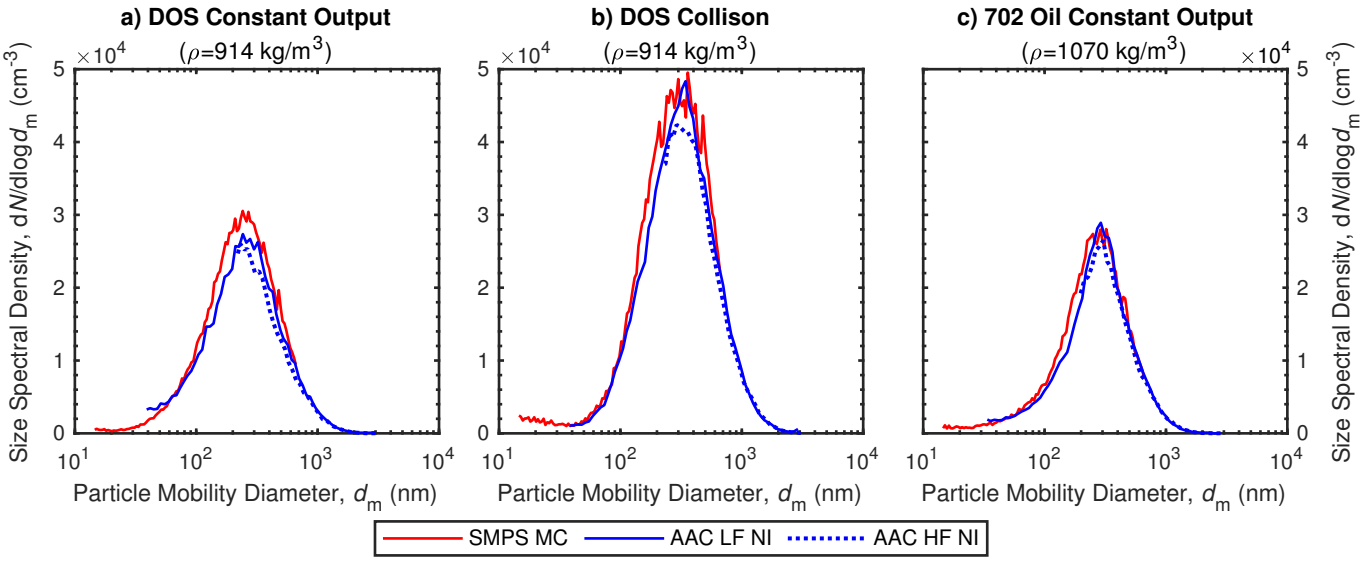

Fig. 3.5 Corrected SMPS and AAC measurements of the same aerosols.

Table 3.2 Comparison of mobility size distributions measured by the SMPS (corrected for multiple-charging) and AAC (converted using known effective density) in parallel. The direct measurements of the AAC-CPC system (denoted as Raw) were corrected for transfer function losses and broadening (denoted as NI).

Aerosol Source	AAC Flow	CMD_m (nm)	GSD	N_{tot} (x10^4 cm^{-3})	% Difference from SMPS/CPC: CMD_m	GSD	N_{tot}
DOS Constant	LF-Raw	259.5	1.93	1.37	5.4%	-2.2%	-28.6%
	LF-NI	250.2	1.97	1.88	1.6%	0.1%	-2.3%
DOS Collison	LF-Raw	318.8	1.87	2.33	4.1%	-4.6%	-20.2%
	HF-Raw	312.2	1.87	2.28	1.9%	-4.6%	-22.0%
	LF-NI	311.5	1.90	3.12	1.7%	-3.5%	6.6%
	HF-NI	310.2	1.88	2.90	1.3%	-4.5%	-0.9%
702 oil Constant	LF-Raw	292.4	1.70	1.13	7.9%	-5.2%	-25.6%
	HF-Raw	283.7	1.72	1.13	4.7%	-4.4%	-25.7%
	LF-NI	287.0	1.73	1.52	5.9%	-4.0%	-0.1%
	HF-NI	282.2	1.72	1.44	4.1%	-4.4%	-5.5%

the spatial resolution of newer commercial cascade impactors has increased by an order of magnitude due to improved inversion techniques [17, 97] and future work should investigate the AAC agreement with these instruments.

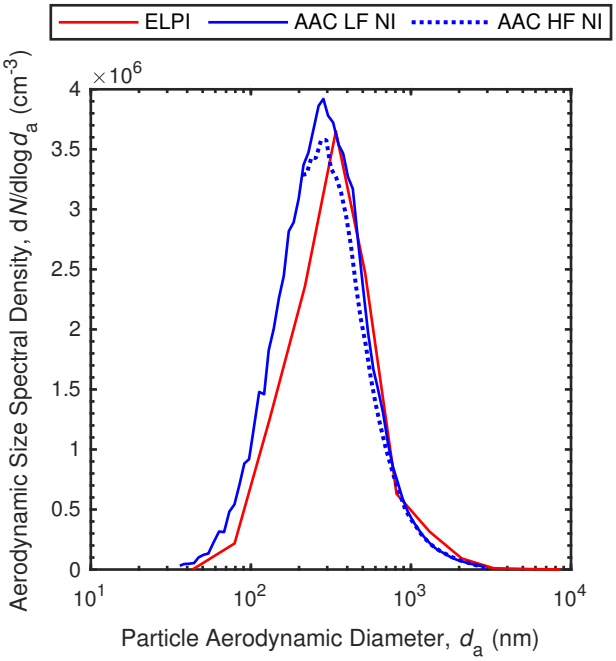

Fig. 3.6 Corrected AAC (NI) and ELPI measurements of the same aerosol.

Table 3.3 Comparison of aerodynamic size distributions measured by the ELPI and AAC (corrected for transfer function losses and broadening, denoted as NI) in parallel.

Aerosol Source	AAC Flow	CMD_a (nm)	GSD	N_{tot} (x10^6 cm^{-3})	% Difference from ELPI: CMD_a	GSD	N_{tot}
DOS	LF-NI	277.5	1.85	2.55	-14.1%	7.2%	22.4%
Constant	HF-NI	264.3	1.86	2.38	-18.2%	7.7%	14.3%

3.6 Theoretical effects of varying gas conditions on AAC classification

It was hypothesized that the aerodynamic diameter of a particle will vary with the surrounding gas conditions. To estimate this effect, DeCarlo et al.'s (2004) theory regarding the relationship between a particle's aerodynamic diameter and its volume equivalent diameter (an intrinsic particle property) was expanded as outlined in Section A.6. Based on this

derivation, the effects of varying gas conditions on the aerodynamic diameter selected by the AAC are only a function of the change in Knudsen number[5] (at the conditions it was classified at versus the conditions of interest), the particle shape factor (χ), and the ratio of particle density (ρ_p) to unit density (ρ_o). This outcome is reflected in Equation A.68 of Section A.6 and demonstrated in Figure 3.7.

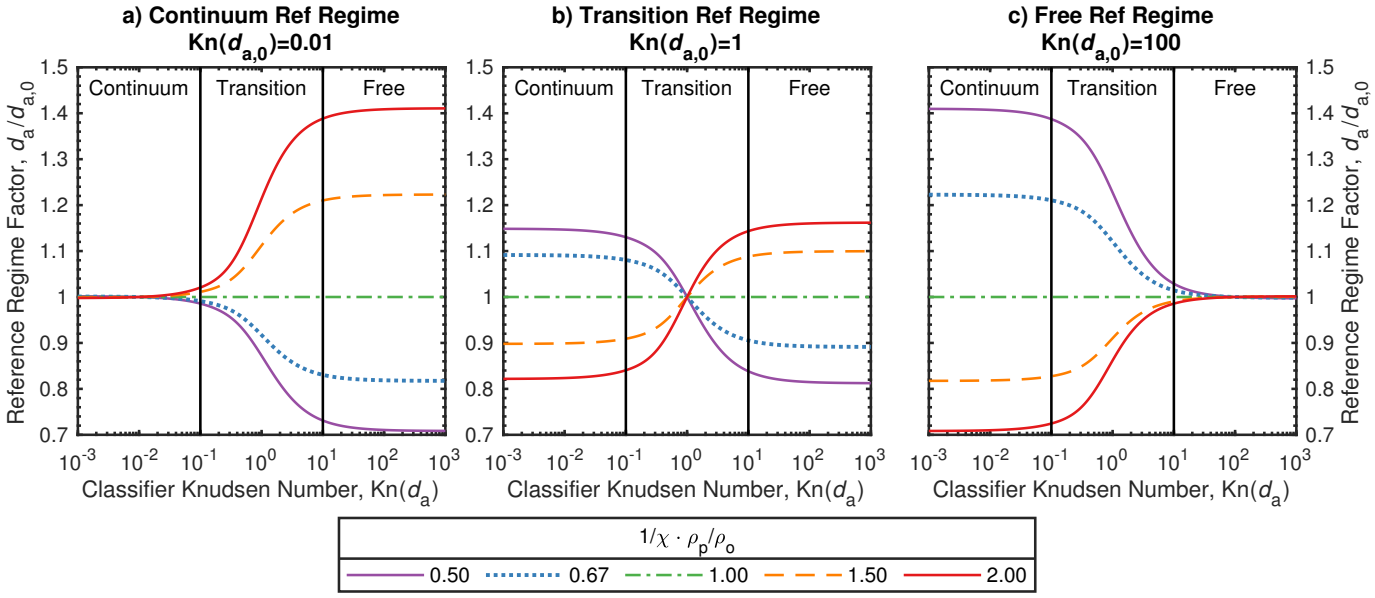

Fig. 3.7 Theoretical effects of varying gas conditions on the particle aerodynamic diameter selected by the AAC. These estimates are based on iteratively solving Equations A.65 to A.68 at each classifier Knudsen number and particle property factor ($1/\chi \cdot \rho_p/\rho_o$).

While the change in aerodynamic diameter is significant when measuring in different regimes, continuum versus free molecular for example, the shift becomes less than 1.5% when only considering the AAC classifier operating range (0 to 40 °C and 0.9 to 1.1 atm), as shown in Figures 3.8 and 3.9. The shift in aerodynamic diameter for a 100 nm particle from changing gas pressure (Figure 3.8b) or temperature (Figure 3.9b) is larger than that of 10 or 1000 nm particles from changing gas pressure (Figures 3.8a or 3.8c, respectively) or temperature (Figures 3.9a or 3.9c, respectively) due to their corresponding regimes. A 100 nm particle at reference conditions corresponds to the transition regime. As shown in Figure 3.7b, the transition regime has large shifts within it to capture the significant gradients between the continuum and free molecular regimes.

[5]The Knudsen number (Kn) is the ratio of the gas mean free path to the particle diameter as per Equation A.67 of Appendix A.

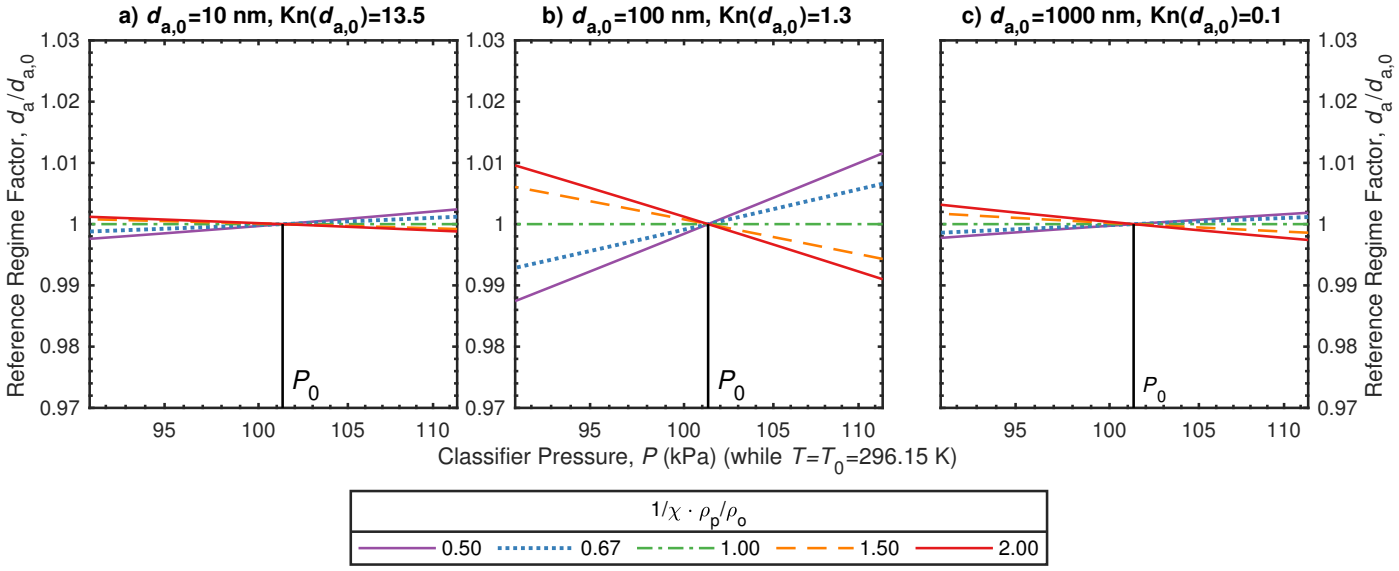

Fig. 3.8 Theoretical change in particle aerodynamic diameter measured by the AAC as the gas pressure varies from 1 atm (assumed P_0) across the AAC's operating range (0.9 to 1.1 atm).

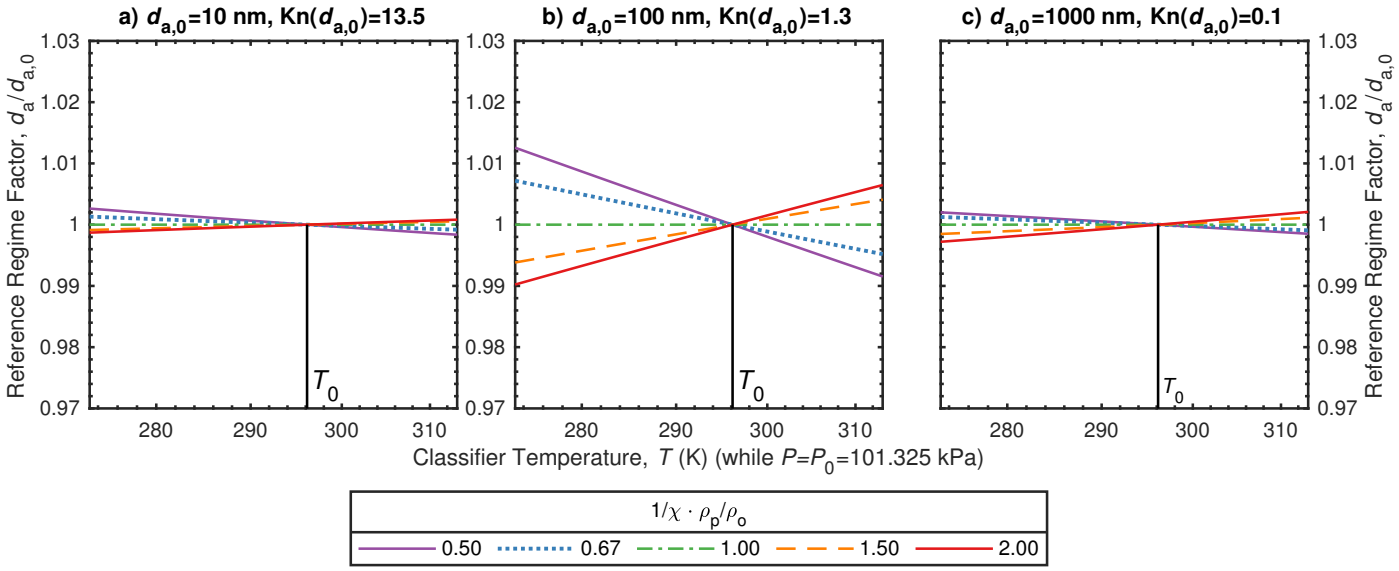

Fig. 3.9 Theoretical change in particle aerodynamic diameter measured by the AAC as the gas temperature varies from 23 °C (assumed T_0) across the AAC's operating range (0 to 40 °C).

3.7 Conclusions

The AAC transfer function was characterised using a tandem AAC system with setpoints between 32 nm to 3 µm. The transmission efficiency of the AAC increases as particle size increases and ranges from 44% and 80% across its classification limits. Since the AAC classifies particles independent of their charge state, its transmission efficiency is 2.6 to 5.1 times higher than a neutraliser-DMA system for the same particle size. However, the width of the AAC transfer function deviates more from theory than that of the DMA. While preliminary results indicate this additional broadening may be due to a classifier flow effect, additional research is required to validate this hypothesis.

The AAC transfer function characterisation and deconvolution were validated by comparing the size distribution measured with an AAC-CPC system against parallel measurements taken with a SMPS, CPC and ELPI. It was determined the multiple charge correction for SMPS measurements or transfer function characterisation for AAC measurements must be considered to measure an aerosol size distribution accurately. The corrected size distributions measured by the AAC agreed within 6.6% for all lognormal distribution parameters measured (CMD, GSD and N_{tot}). The aerodynamic size distribution measured by the ELPI also agreed within 22.4% of the AAC measurements at low or high flow. The effects of changing gas conditions on the particles classified by the AAC were also predicted and found to be small ($<$1.5%) within its operating range.

Chapter 4

Measuring Aerodynamic Size Distributions using the Scanning AAC

4.1 Introduction

This chapter[1] addresses Objective 1b and develops the AAC methodology to accelerate measurements of aerodynamic size distribution by continuously scanning the AAC setpoint upstream of a particle detector. While stepping the AAC (as developed and demonstrated in Chapter 3) improves upon the low classification resolutions and set measurement ranges of previous methodologies, this approach forces trade-offs between measurement time and step resolution. No AAC measurements are collected while changing setpoints or during the time required for particles at the new setpoint to travel through the classifier and reach the detection region of the downstream particle detector. Therefore, collecting measurements with the stepping AAC takes significantly longer (minutes to tens of minutes) than the near real-time methodologies, such as the ELPI, APS, and E-SPART. This challenge of measurement time versus step resolution is similar to the one which prompted the evolution of the Differential Mobility Analyser (DMA).

As previously discussed in Section 1.2.1, the DMA classifies particles by their electrical mobilities. Similar to the AAC, the DMA uses concentric cylinders and a sheath flow of particle-free air, but induces an electrostatic force on the particles (rather than a centrifugal force) by applying a potential difference between the cylinders [133]. The DMA was first used to measure the electrical mobility size distribution of an aerosol by stepping its setpoint upstream of a particle detector [132]. This methodology is commonly referred to as the Differential Mobility Particle Sizer (DMPS). However, similar to the stepping AAC,

[1]This chapter is based on an article by Johnson et al. [109] published by Taylor & Francis Group in Aerosol Science and Technology on 23/11/2020, available online: https://doi.org/10.1080/02786826.2020.1830941.

this approach resulted in long measurement times and trade-offs with step resolution. To overcome this limitation, Wang and Flagan [261] showed that continuously varying the electrostatic field of the DMA following an exponential function produces a mean field strength (i.e. average DMA voltage during the time a particle is in the classifier) that is equivalent to the field strength at steady-state. This approach forms the basis of the Scanning Mobility Particle Sizer (SMPS), an instrument that is widely used in aerosol research.

Others have built upon this original theory to further improve the accuracy, scan time or usability of the SMPS. For example, as the scans of the SMPS are accelerated the effect of viscous flow in the DMA classifier or the downstream plumbing/detector become significant. Therefore, additional theory is required to account for the smearing of particle residence times [36, 167, 47] and detection times [220, 37, 118]. The effects of particle diffusion [48, 89] and entrance/exit geometry of the classifier [161] on the transfer function of the SMPS have also been investigated. These studies have led to the recent work of Mai et al. [162] and Kanaparthi et al. [118], which independently developed more advanced inversion theories to account for many of these effects on SMPS measurements.

4.1.1 Outline of chapter

Based on this evolution, this chapter develops the theory to continuously scan, rather than step, the AAC setpoint upstream of a particle detector. First, the SMPS theory developed by Wang and Flagan [261] is expanded to the AAC to determine the required speed profile of its classifier. Assuming uniform axial flow of the gas in the classifier, the resulting transfer function of the scanning AAC based on limited trajectory theory ($\Omega_{sc,LT}$) is derived and compared to the corresponding solution of the steady-state AAC developed by Tavakoli and Olfert [238]. These results are then used to expand the experimental characterisation of the steady-state AAC, which account for non-idealized particle and flow behaviours within the classifier and is summarized in Section 3.3.1, to the scanning AAC. This non-idealized transfer function of the scanning AAC ($\Omega_{sc,PS,B}$) is derived based on the particle streamline theory of the steady-state AAC operating with balanced classifier flows developed by Tavakoli and Olfert [238]. The averages of these scanning transfer functions (i.e. $\bar{\Omega}_{sc,LT}$ and $\bar{\Omega}_{sc,PS,B}$) over the counting time of the downstream particle detector are then determined. Finally, the deconvolution factors are derived to calculate the aerodynamic size distribution of the aerosol from the concentrations of the classified particles measured during scanning.

This scanning theory is validated by comparing the aerodynamic size distribution from three different aerosol sources (DOS [Bis(2-Ethylhexyl) sebacate], salt and soot) measured by a scanning AAC to ones measured by a stepping AAC, as previously developed in Chapter 3. The scanning AAC is further validated by measuring polystyrene latex (PSL) particles of

known sizes between 100 nm and 2.02 µm. Finally, the validity and effect of assuming uniform flow within the classifier and downstream plumbing/particle detector (i.e. neglecting the smearing of particle residence and detection times due to the flows being viscous) are discussed.

4.2 Theory

For readability of this chapter and its corresponding appendix (Appendix B), only the notations required to differentiate multiple instances of the same parameter within the same section, table or figure are used. The title of a section and captions/labels of a table or figure are used to clarify the common instances of the parameter.

For example, consider the transfer function of the AAC denoted as Ω_{AAC}. If only one combination of instances is included within a section, such as the AAC operating at steady-state (ss) considering idealized (I), limited trajectory (LT) theory, the AAC transfer function within this section will be denoted as Ω_{AAC} rather than $\Omega_{\mathrm{AAC,ss,LT,I}}$. To avoid the ambiguity of this reduced notation, the title of this section (and also the header if it is an appendix section) would include steady-state (ss), idealized (I) and limited trajectory (LT). Please see Section B.1 of Appendix B for further details.

4.2.1 Radial trajectories of particles

Starting from first principles, the centrifugal force field (E_{c}) at radial position r within the AAC classifier that has angular speed ω at time t can be calculated by:

$$E_{\mathrm{c}}(t, r) = \omega^2(t)\, r. \tag{4.1}$$

This centrifugal force field induces a centrifugal force (F_{c}) on a particle proportional to its mass m at radial position r within the AAC classifier:

$$F_{\mathrm{c}} = m\, \omega^2(t)\, r. \tag{4.2}$$

However, the radial movement of the particle is counteracted by a drag force (F_{d}) from the surrounding gas molecules [84]:

$$F_{\mathrm{d}} = \frac{1}{B}\frac{\mathrm{d}r}{\mathrm{d}t}, \tag{4.3}$$

where B is the mobility of the particle and $\mathrm{d}r/\mathrm{d}t$ is the velocity of the particle in the radial direction. Applying Newton's first law of motion in the radial direction and neglecting the

radial acceleration of the particle[2] (i.e. $\mathrm{d}^2r/\mathrm{d}t^2 = 0$), the first-order differential equation describing the radial velocity of a particle with relaxation time τ and radial position r within the spinning classifier is:

$$\begin{aligned} \sum F_\mathrm{r} &= m\frac{\mathrm{d}^2 r}{\mathrm{d}t^2} = F_\mathrm{c} - F_\mathrm{d} \\ \frac{\mathrm{d}r}{\mathrm{d}t} &= \tau\,\omega^2(t)\,r. \end{aligned} \tag{4.4}$$

This differential equation (Equation 4.4) can be solved as a separable equation for a particle at radial position r_in at time t_in which moves to radial position r after time t:

$$\begin{aligned} \frac{1}{\tau}\int_{r_\mathrm{in}}^{r}\frac{1}{r'}\mathrm{d}r' &= \int_{t_\mathrm{in}}^{t_\mathrm{in}+t}\omega^2(t')\,\mathrm{d}t' \\ \tau &= \frac{\ln\left(\frac{r(t_\mathrm{in}+t)}{r_\mathrm{in}(t_\mathrm{in})}\right)}{\int_{t_\mathrm{in}}^{t_\mathrm{in}+t}\omega^2(t')\,\mathrm{d}t'}. \end{aligned} \tag{4.5}$$

During steady-state operation, the angular speed of the AAC classifier is constant (i.e. $\omega(t) = \omega$) and the denominator of Equation 4.5 becomes the simple integration of a constant. However during scanning operation, additional considerations are required for the angular speed profile of the AAC classifier ($\omega(t)$).

4.2.2 Angular speed profile of AAC classifier during scanning

To simplify the deconvolution of the transfer function of the scanning AAC, the angular speed profile of the AAC classifier ($\omega(t)$) must produce a proportional change in the centrifugal force field over time t, and the resulting critical particle trajectories it induces, that are independent of the times that the particles arrive at the classifier inlet (t_in) as follows:

$$\frac{E_\mathrm{c}(t_\mathrm{in}+t,\,r)}{E_\mathrm{c}(t_\mathrm{in},\,r)} = j(t), \tag{4.6}$$

where j is a generic function that is only a function of t. This criteria is similar to that set by Wang and Flagan [261] for the electrostatic force field generated by changing the voltage of a DMA classifier during SMPS operation. As derived in Section B.2 for the scanning AAC, this independence from t_in is achieved by the angular speed profile of:

[2]The radial acceleration of the particle is neglected as the relaxation time of the particle is orders of magnitude smaller than the time over which the centrifugal force field changes. For example, the maximum particle relaxation time classified by the AAC is 140×10^{-6} s [28] and the time constant (τ_sc) of a typical AAC scan is tens of seconds.

$$\omega^2(t) = \omega_S^2 \exp\left(\frac{t}{\tau_{sc}}\right), \tag{4.7}$$

as shown by the ratio of centrifugal fields (Equation 4.6), based on the definition of E_c (Equation 4.1), simplifying to:

$$\frac{E_c(t_{in}+t,\, r)}{E_c(t_{in},\, r)} = \exp\left(\frac{t}{\tau_{sc}}\right). \tag{4.8}$$

The time constant of the scan (τ_{sc}), also derived in Section B.2, is:

$$\tau_{sc} = \frac{t_{sc}}{2\ln\left(\frac{\omega_E}{\omega_S}\right)}, \tag{4.9}$$

where ω_S and ω_E are the initial and final angular speeds of the AAC classifier during the scan, respectively. Therefore, the AAC completing an up scan (i.e. $\omega_E > \omega_S$) is reflected in a positive scan time constant (i.e. $\tau_{sc} > 0$), while a down scan (i.e. $\omega_E < \omega_S$) is reflected in a negative scan time constant (i.e. $\tau_{sc} < 0$). An example of the required speed ($\omega(t)$) and acceleration ($\dot{\omega}(t)$) profiles for the AAC classifier for a 600 s scan from 20 to 700 rad/s is shown in Figure B.1 of Appendix B.

Interestingly, it is also shown in Section B.2 that $\omega^p(t) = \omega_S^p C^{\frac{t}{\tau_{sc}}}$ (where p and C are constants that are any real numbers, and C must be greater than one) also satisfies t_{in} independence (i.e. Equation 4.6). Furthermore, due to the relationship between $\omega(t)$ and τ_{sc}, the same angular speed profile of the AAC classifier is required regardless of the values of p and C. However, for consistency with previous studies of the scanning DMA and the centrifugal force field generated in the AAC, this work uses $C = e$ and $p = 2$ as shown in Equation 4.7.

4.2.3 Minimum scan time

The scan time (t_{sc}) of the AAC is limited by the angular acceleration/deceleration the classifier can achieve as a function of its angular speed (i.e. the acceleration/deceleration capacity of the classifier). As derived in Section B.2.1, the required angular acceleration of the classifier ($\dot{\omega}(t)$) over a scan is linearly proportional to its required angular speed ($\omega(t)$) by a factor of $1/(2\tau_{sc})$. Therefore, as derived in Equations B.15 and B.16, the minimum scan time ($t_{sc,min}$) the AAC can achieve is:

$$t_{sc,min} = \frac{\omega(t)}{\dot{\omega}_{max}(\omega(t))} \ln\left(\frac{\omega_E}{\omega_S}\right), \tag{4.10}$$

where for an up scan $\dot{\omega}_{\max}$ is the acceleration capacity of the AAC classifier at the end speed of the scan (i.e. $\omega(t) = \omega_{\mathrm{E}}$), while for a down scan $\dot{\omega}_{\max}$ is the deceleration capacity of the AAC classifier at the start speed of the scan (i.e $\omega(t) = \omega_{\mathrm{S}}$).

The minimum scan time varies slightly between different AACs due to variations in the acceleration/deceleration capacities of the classifiers caused by small differences in drive belt tension, as well as changes in bearing friction and motor efficiency over the lifetime of the instrument. To account for this variation, the scan time limitations of each AAC should be periodically updated by measuring the maximum acceleration and deceleration the classifier can achieve as a function of its angular speed. An example of these acceleration and deceleration capacities for multiple AACs and the variation between them is shown in Figure B.2.

4.2.4 Uniform axial flow

The radial position (r) of a particle at time t can be related to its axial position (z) in the classifier by assuming the axial flow within the classifier is uniform (i.e. independent of its radial position). This assumption is commonly referred to as plug flow and the validity of this assumption is discussed in Section 4.5. Therefore, the axial velocity of the flow ($\mathrm{d}z/\mathrm{d}t$) is treated as a constant (U) as follows:

$$\frac{\mathrm{d}z}{\mathrm{d}t} = U = \frac{Q_{\mathrm{a}} + Q_{\mathrm{sh}}}{\pi(r_2^2 - r_1^2)} = \frac{Q_{\mathrm{sh}}}{\pi(r_2^2 - r_{\mathrm{a}}^2)} = \frac{Q_{\mathrm{s}}}{\pi(r_2^2 - r_{\mathrm{s}}^2)}, \tag{4.11}$$

where Q_{a} is the aerosol flow rate entering the classifier, Q_{sh} is the sheath flow rate entering the classifier, Q_{s} is the sample flow rate leaving the classifier, r_1 is the classifier inner radius, r_2 is the classifier outer radius, r_{a} is the classifier radius at the outer edge of the aerosol streamlines, and r_{s} is the classifier radius at the inner edge of the sample streamlines. These radii are illustrated in the simplified schematic of the AAC classifier geometry shown in Figure B.3.

For plug flow, the particle residence time along the critical trajectory in the classifier (t_{f}) is independent of particle relaxation time (τ). Therefore, based on the axial velocity of the aerosol in classifier (Equation 4.11):

$$t_{\mathrm{f}} = \frac{L}{U} = \frac{\pi L\left(r_2^2 - r_1^2\right)}{Q_{\mathrm{a}} + Q_{\mathrm{sh}}}, \tag{4.12}$$

where L is the length of the region that classifies the particles within the AAC classifier. The dimensions of the AAC classifier used in this work were 56 mm, 60 mm and 206 mm for r_1, r_2 and L, respectively.

4.2.5 Overall trajectories of particles assuming uniform axial flow

Assuming uniform axial flow and based on Equation 4.5, the relaxation time (τ) of a particle that migrates from r_{in} to r_{out} (i.e. the radial position of the particle at the classifier inlet and outlet, respectively) over its residence time in the classifier (i.e. $t = t_{\text{f}}$, as defined by Equation 4.12) is:

$$\tau = \frac{1}{K} \ln\left(\frac{r_{\text{out}}}{r_{\text{in}}}\right). \tag{4.13}$$

where:

$$K = \int_{t_{\text{in}}}^{t_{\text{in}}+t_{\text{f}}} \omega^2(t')\,\mathrm{d}t'. \tag{4.14}$$

During steady-state (ss) operation the classifier speed of the AAC is constant (i.e. $\omega(t) = \omega$) and K (Equation 4.14) becomes:

$$K_{\text{ss}} = \int_{t_{\text{in}}}^{t_{\text{in}}+t_{\text{f}}} \omega^2\,\mathrm{d}t' = \omega^2\, t_{\text{f}}, \tag{4.15}$$

while during scanning (sc) operation, the classifier speed of the AAC ($\omega(t)$) continuously varies following Equation 4.7 and K (Equation 4.14) becomes:

$$\begin{aligned} K_{\text{sc}}(t_{\text{in}}) &= \int_{t_{\text{in}}}^{t_{\text{in}}+t_{\text{f}}} \omega_{\text{S}}^2 \exp\left(\frac{t'}{\tau_{\text{sc}}}\right)\mathrm{d}t' \\ K_{\text{sc}}(t_{\text{in}}) &= \omega_{\text{S}}^2\, \tau_{\text{sc}} \exp\left(\frac{t_{\text{in}}}{\tau_{\text{sc}}}\right)\left[\exp\left(\frac{t_{\text{f}}}{\tau_{\text{sc}}}\right) - 1\right]. \end{aligned} \tag{4.16}$$

The time during the AAC scan can also be expressed as measurement time (t_{m}), which is the time the particles leave the classifier as follows:

$$t_{\text{m}} = t_{\text{in}} + t_{\text{f}}. \tag{4.17}$$

Therefore, K_{sc} (Equation 4.16) can also be expressed in terms of t_{m} (defined in Equation 4.17) as follows:

$$\begin{aligned} K_{\text{sc}}(t_{\text{m}}) &= \int_{t_{\text{m}}-t_{\text{f}}}^{t_{\text{m}}} \omega_{\text{S}}^2 \exp\left(\frac{t}{\tau_{\text{sc}}}\right)\mathrm{d}t' \\ K_{\text{sc}}(t_{\text{m}}) &= \omega_{\text{S}}^2\, \tau_{\text{sc}} \exp\left(\frac{t_{\text{m}}}{\tau_{\text{sc}}}\right)\left[1 - \exp\left(\frac{-t_{\text{f}}}{\tau_{\text{sc}}}\right)\right]. \end{aligned} \tag{4.18}$$

Table 4.1 Transfer function of the steady-state (ss) or scanning (sc) AAC based on limited trajectory (LT) theory.

Parameter	Equation		Appx. Eqn
τ_{max}	$\frac{1}{K}\ln\left(\frac{r_2}{r_1}\right)$	(4.19)	B.21
τ_{min}	$\frac{1}{2K}\ln\left(\frac{Q_a+Q_{sh}-Q_s\left(1-r_1^2/r_2^2\right)}{Q_a+Q_{sh}-Q_{sh}\left(1-r_1^2/r_2^2\right)}\right)$	(4.20)	B.24
τ^*	$\frac{\tau_{min}+\tau_{max}}{2}$	(4.21)	B.25
f_1	$\frac{Q_a+Q_{sh}\,r_1^2/r_2^2-\exp\left(-2\tau K\right)\left[Q_a+Q_{sh}-Q_s\left(1-r_1^2/r_2^2\right)\right]}{Q_a\left(1-r_1^2/r_2^2\right)}$	(4.22)	B.28
f_2	$\frac{Q_a+Q_{sh}}{Q_a}\left(\frac{\exp\left(-2\tau K\right)-r_1^2/r_2^2}{1-r_1^2/r_2^2}\right)$	(4.23)	B.31
f_3	$\frac{Q_s}{Q_a}$	(4.24)	B.32
Ω_{AAC}	$\max[0,\,\min(f_1,\,f_2,\,f_3,\,1)]$	(4.25)	B.33

Where K equals K_{ss} (Equation 4.15) or K_{sc} (Equation 4.18) for the steady-state or scanning AAC, respectively.

4.2.6 Idealized transfer function of AAC: limited trajectory & uniform axial flow

Limited trajectory theory is commonly used to estimate the transfer function of aerosol instruments, including the steady-state DMA [86], scanning DMA [261], and steady-state AAC [238]. Therefore, this approach was used to derive the transfer function of the scanning AAC assuming uniform axial flow, as shown in Section B.3. Based on this derivation, the steady-state [238] and scanning AAC transfer functions have the same form (i.e. same shape) as summarized by the similar equations in Table 4.1. The shape of the transfer function of the scanning AAC is also independent of the measurement time (t_m), but this result is only valid when uniform axial flow is a reasonable assumption (i.e. sufficiently long scan times) as discussed in Section 4.5. The shape of these transfer functions with balanced or unbalanced

classifier flows is triangular or trapezoidal, respectively, as shown in Figure B.4. These shapes agree with those previously found by Tavakoli and Olfert [238] for the steady-state AAC.

Therefore, the transfer function of the steady-state AAC has a constant shape and position in the particle relaxation time domain (i.e. AAC setpoint, τ^*) as K_{ss} (Equation 4.15) is a constant. The transfer function of the scanning AAC with a sufficiently long scan time also has a constant shape, but its setpoint (τ^*_{sc}) varies as K_{sc} changes based on the time (i.e. Equations 4.16 or 4.18 for t_{in} or t_m, respectively) the particles are classified during the scan.

An example illustrating these transfer function characteristics is shown in Figure 4.1 for the scanning AAC completing a 600 s up scan with balanced classifier flows ($Q_a = 0.3$ L/min and $Q_{sh} = 3$ L/min), and the steady-state AAC operating with the same parameters as those at the start and end of the scan. This figure also demonstrates the range of particle relaxation times measured by the scanning AAC is smaller than measured by the steady-state AAC due to the residence time of the particles in the classifier (t_f). This effect is discussed in Section 4.2.9 and is expanded to also consider the effects of the counting time of the particle detector downstream of the scanning AAC.

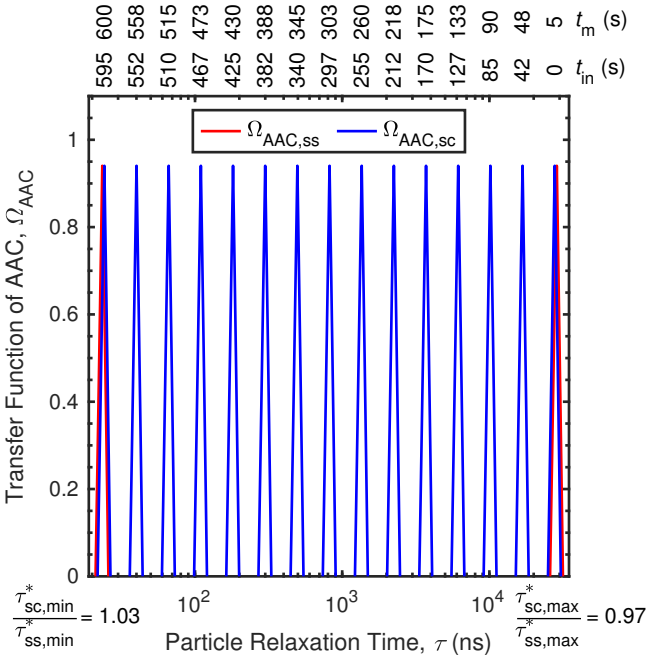

Fig. 4.1 Example of the transfer function (Ω_{AAC}) of the steady-state (ss) or scanning (sc) AAC based on limited trajectory theory (as summarized in Table 4.1), where $\Omega_{AAC,sc}$ is shown at 15 different times (in terms of t_{in} or t_m) over a 600 s scan from $\omega_S = 20$ rad/s to $\omega_E = 700$ rad/s, while $\Omega_{AAC,ss}$ is only shown at the start and end speeds of the scan (i.e. ω_S and ω_E, respectively).

However, the transfer function based on limited trajectory theory is an idealized representation of AAC classification. It neglects non-ideal particle behaviour within the classifier, such as diffusion and impaction, which affect the height (i.e. transmission efficiency) and width (i.e classification resolution) of the transfer function.

4.2.7 Non-idealized transfer function of AAC: balanced flows, particle streamline & uniform axial flow

To capture the non-ideal particle behaviour within the AAC, consider the outcome from the previous section that the steady-state and scanning AAC transfer functions have the same form (as summarized in Table 4.1) for sufficiently long scan times. Therefore, the transfer function of the steady-state AAC based on particle streamline theory with balanced (B) flow, developed by Tavakoli and Olfert [238] and previously parameterized in Section 3.3.1 to capture non-idealized particle and flow behaviours, can also describe the scanning AAC. The adaption of this theory to the scanning AAC operating with balanced flows is shown in Section B.4 and summarized in Table 4.2. For context, this table also shows the parallel parameters based on limited trajectory theory. Russell et al. [220] used a similar approach to adapt the transfer function of the steady-state DMA developed by Knutson and Whitby [133] based on particle streamline theory to the SMPS.

Similar to Chapter 3, the transmission efficiency (λ_Ω) scales the area under the transfer function to account for particle losses, while the width factor (μ_Ω) scales the full width at half maximum (FWHM) of the transfer function to account for broadening due to particle diffusion and other effects, such as the entrance and exit effects of the AAC classifier and non-idealized classifier flow. An example of the idealized and non-idealized transfer function based on particle streamline theory is shown in Figure B.5. The non-dimensional flow parameter (β) controls the classification resolution of the AAC (i.e. FWHM of its transfer function) and is equivalent to [238]:

$$\beta = \frac{Q_\mathrm{s} + Q_\mathrm{a}}{Q_\mathrm{sh} + Q_\mathrm{exh}}, \tag{4.32}$$

where Q_exh is the sheath flow rate leaving the classifier.

An example comparing the idealized and non-idealized representation of the transfer function of the scanning AAC operating with balanced classifier flows ($Q_\mathrm{a} = 0.3$ L/min and $Q_\mathrm{sh} = 3$ L/min) based on limited trajectory and particle streamline theory, respectively, is shown in Figure 4.2. The idealized transfer function based on particle streamline theory can also be represented by setting λ_Ω and μ_Ω equal to 1. This idealized representation predicts a transmission efficiency of one at the setpoint (τ^*_sc) of the scanning AAC, while

Table 4.2 Transfer function of the scanning AAC based on limited trajectory (LT) theory or with balanced classifier flows based on particle streamline (PS) theory.

Parameter	Limited Trajectory (LT) Theory	Particle Streamline (PS) Theory with Balanced (B) Classifier Flows	Appx. Eqn	
			LT	PS
$\Omega_{\mathrm{AAC,sc}}$	$\max[0, \min(f_1, f_2, f_3, 1)]$ (4.26)	$\frac{\lambda_\Omega \mu_\Omega^2}{2\beta}\left[\left\lvert \frac{\tau}{\tau^*_{\mathrm{sc,B}}} - \left(1+\frac{\beta}{\mu_\Omega}\right)\right\rvert + \left\lvert \frac{\tau}{\tau^*_{\mathrm{sc,B}}} - \left(1-\frac{\beta}{\mu_\Omega}\right)\right\rvert - 2\left\lvert \frac{\tau}{\tau^*_{\mathrm{sc,B}}} - 1\right\rvert\right]$ (4.27)	B.33	B.69
τ^*_{sc}	$c_{\tau*}\exp\left(\frac{-t_{\mathrm{m}}}{\tau_{\mathrm{sc}}}\right)$ (4.28)		B.50	B.78
$c_{\tau*}$	$\frac{1}{2c_{\mathrm{sc}}}\left[\ln\left(\frac{r_2}{r_1}\right) + \frac{1}{2}\ln\left(\frac{Q_{\mathrm{a}}+Q_{\mathrm{sh}}-Q_{\mathrm{s}}\left(1-r_1^2/r_2^2\right)}{Q_{\mathrm{a}}+Q_{\mathrm{sh}}-Q_{\mathrm{sh}}\left(1-r_1^2/r_2^2\right)}\right)\right]$ (4.29)	$\frac{1}{c_{\mathrm{sc}}}\frac{2\left(r_2^2-r_1^2\right)}{(\beta+1)\left(r_1+r_2\right)^2}$ (4.30)	B.52	B.79
c_{sc}	$\omega_{\mathrm{S}}^2\,\tau_{\mathrm{sc}}\left[1-\exp\left(\frac{-t_{\mathrm{f}}}{\tau_{\mathrm{sc}}}\right)\right]$ (4.31)		B.45	B.80

the comparable representation based on limited trajectory theory predicts less than one. This discrepancy in transmission efficiencies between the two theories is also observed in the corresponding transfer functions of the steady-state AAC, and is due to the particle streamline model neglecting the divergence of the centrifugal force field [238]. However, this divergence is captured by the non-ideal parameters, λ_Ω and μ_Ω, which characterise the non-idealized transfer function of the AAC based on a parameterized model derived using particle streamline theory. Based on the values previously determined for these parameters in Section 3.4, the non-idealized transfer function of the scanning AAC also becomes shorter

and broader as the aerodynamic diameter[3] setpoint ($d^*_{a,sc}$) of the scanning AAC decreases from 3000 nm to 30 nm, as shown in Figure 4.2.

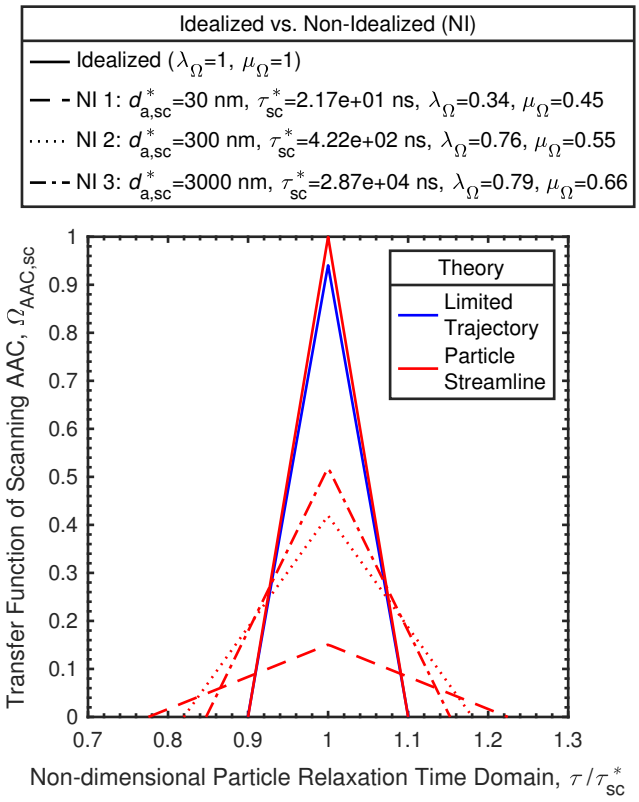

Fig. 4.2 Example comparing the transfer function of the scanning AAC with balanced classifier flows based on limited trajectory or particle streamline theory.

4.2.8 Average transfer function of scanning AAC over detector time

To determine the concentration of particles with relaxation time τ that pass through the AAC classifier at different measurement times (t_m), the change in the transfer function of the scanning AAC ($\Omega_{AAC,sc}$) over the counting time[4] of the downstream particle detector must be considered. Neglecting smearing effects of flow downstream of the AAC (as discussed later in Section 4.6), the average transfer function of the scanning AAC ($\bar{\Omega}_{AAC,sc}$) over the counting interval (t_c) of the detector can be estimated by:

[3]This example assumes the aerosol is at standard conditions ($P = 101.325$ kPa and $T = 296.15$ K) and that the particles have an effective density of 1000 kg/m^3. This density results in the mobility and aerodynamic diameters of the particles being equivalent.

[4]The time period for the particle detector to collect and report one measurement of particle number concentration.

$$\bar{\Omega}_{\mathrm{AAC,sc}} = \frac{1}{t_\mathrm{c}} \int_{t_\mathrm{m}}^{t_\mathrm{m}+t_\mathrm{c}} \Omega_{\mathrm{AAC,sc}}(\tau, t'_\mathrm{m})\, \mathrm{d}t'_\mathrm{m}. \tag{4.33}$$

This integral is solved for the idealized transfer function of the scanning AAC based on limited trajectory theory (i.e. Equation 4.26) in Section B.5 and for the non-idealized transfer function of the scanning AAC with balanced classifier flows based on particle streamline theory (i.e. Equation 4.27) in Section B.6. These appendix sections solve the integral by utilizing the Heaviside function ($\mathcal{H}$), defined as follows:

$$\mathcal{H}(x-a) = \begin{cases} 0 & \text{if } x-a<0 \\ 0.5 & \text{if } x-a=0, \\ 1 & \text{if } x-a>0 \end{cases} \tag{4.34}$$

to represent the mathematical discontinuities in the transfer function of the scanning AAC ($\Omega_{\mathrm{AAC,sc}}$ defined in Equations 4.26 or 4.27) in a single equation. The derivations also use the fact that the boundary conditions of $\Omega_{\mathrm{AAC,sc}}$ are of the form:

$$\tau_x = c_{\tau x} \exp\left(\frac{-t_\mathrm{m}}{\tau_\mathrm{sc}}\right), \tag{4.35}$$

where $c_{\tau x}$ represents the grouped constants of boundary x shown in Figures B.4 and B.5, and summarized in Tables B.2 and B.3 for the transfer function based on limited trajectory and particle streamline theory, respectively.

Based on this consistent form (i.e. Equation 4.35), the inequality relations based on particle relaxation time (i.e. $\tau > \tau_x$) used within the piecewise or Heaviside representation of the transfer function of the scanning AAC are equivalent to:

$$\tau > \tau_x \rightarrow \tau > c_{\tau x} \exp\left(\frac{-t_\mathrm{m}}{\tau_\mathrm{sc}}\right). \tag{4.36}$$

However, the isolation of t_m in this inequality (i.e. Equation 4.36) depends on the sign of τ_sc (i.e. up or down scan). If $\tau_\mathrm{sc} > 0$,

$$t_\mathrm{m} > \tau_\mathrm{sc} \ln\left(\frac{c_{\tau x}}{\tau}\right), \tag{4.37}$$

while if $\tau_\mathrm{sc} < 0$ (i.e. the inequality sign flips as dividing both sides by a negative number):

$$t_\mathrm{m} < \tau_\mathrm{sc} \ln\left(\frac{c_{\tau x}}{\tau}\right). \tag{4.38}$$

Based on these inequalities (i.e. Equations 4.37 and 4.38), the Heaviside function limits can be converted from the particle relaxation time (τ) to measurement time (t_m) domain as follows:

$$\mathcal{H}(\tau - \tau_x) = \mathcal{H}\left(\frac{\tau_{sc}}{|\tau_{sc}|}\left(t_m - \tau_{sc}\ln\left(\frac{c_{\tau x}}{\tau}\right)\right)\right). \tag{4.39}$$

Using this approach, the solutions for $\bar{\Omega}_{AAC,sc}$ (Equation 4.33) based on limited trajectory or particle streamline theory are summarized in Table 4.3, where the boundary conditions τ_x are determined using Equation 4.35 and the t_c shifted boundary conditions $\tau_{x,tc}$ are determined as follows:

$$\tau_{x,tc} = c_{\tau x}\exp\left(\frac{-(t_m + t_c)}{\tau_{sc}}\right). \tag{4.40}$$

An example comparing the average transfer function of the scanning AAC ($\bar{\Omega}_{AAC,sc}$) operating with balanced classifier flows ($Q_a = 0.3$ L/min and $Q_{sh} = 3$ L/min) over three different counting times (i.e. $t_c = 0.1$, 1 or 10 s) of the downstream particle detector is shown in Figure 4.3. This figure shows the idealized and non-idealized representations of the average transfer function for 600 s scans based on limited trajectory and particle streamline theory, respectively.

Figure 4.3a and 4.3b show the average transfer functions at the start and end of the up scan, respectively, from 20 to 700 rad/s over 600 s, and demonstrates that the shape of the idealized average transfer function based on limited trajectory theory does not change over the scan duration. However, the shape of the non-idealized average transfer function based on particle streamline theory does change over the scan duration to account for the changes in particle losses and transfer function broadening as the setpoint of the AAC (i.e. particle size of interest) changes.

Figure 4.3c shows the transfer functions at the start of the down scan from 700 to 20 rad/s over 600 s. Therefore, during an up scan, the average setpoint of the scanning AAC (i.e. peak of the average transfer function denoted by $\bar{\tau}^*_{sc}$) over t_c is smaller than the instantaneous setpoint of the scanning AAC (τ^*_{sc}) at the start of the counting interval of the particle detector. Conversely, $\bar{\tau}^*_{sc}$ is larger than τ^*_{sc} during a down scan. This difference is due to the scanning AAC classifying increasingly smaller or larger particle relaxation times during an up or down scan, respectively. As expected, Figure 4.3 demonstrates that the average transfer function becomes broader and its amplitude lower as the counting time (t_c) increases. These changes are due to the longer counting time causing the AAC to scan across a larger range of particle relaxation times at each detector measurement.

Table 4.3 Average transfer function of the scanning AAC over the counting time of the downstream particle detector.

Parameter	Limited Trajectory (LT) Theory	Particle Streamline (PS) Theory with Balanced (B) Classifier Flows	Appx. Eqn	
			LS	PS
$\bar{\Omega}_{\mathrm{AAC,sc}}$	$\left[\frac{c_{f11}\,\tau_{\mathrm{sc}}}{t_{\mathrm{c}}}\mathcal{EI}\left(c_{\tau\min}\,c_{f12}\right)-\frac{c_{f13}}{t_{\mathrm{c}}}\left(t_{\mathrm{m}}-\tau_{\mathrm{sc}}\ln\left(\frac{c_{\tau\min}}{\tau}\right)\right)\right]$ $\left[\mathcal{H}\left(\tau-\tau_{\min}\right)-\mathcal{H}\left(\tau-\tau_{\min,\mathrm{tc}}\right)\right]$ $+\left[-\frac{c_{f11}\,\tau_{\mathrm{sc}}}{t_{\mathrm{c}}}\mathcal{EI}\left(c_{f12}\,\tau\exp\left(\frac{t_{\mathrm{m}}}{\tau_{\mathrm{sc}}}\right)\right)\right]\left[\mathcal{H}\left(\tau-\tau_{\min}\right)-\mathcal{H}\left(\tau-\tau_{13}\right)\right]$ $+\left[\frac{c_{f11}\,\tau_{\mathrm{sc}}}{t_{\mathrm{c}}}\mathcal{EI}\left(c_{f12}\,\tau\exp\left(\frac{t_{\mathrm{m}}+t_{\mathrm{c}}}{\tau_{\mathrm{sc}}}\right)\right)+c_{f13}\right]$ $\left[\mathcal{H}\left(\tau-\tau_{\min,\mathrm{tc}}\right)-\mathcal{H}\left(\tau-\tau_{13,\mathrm{tc}}\right)\right]$ $+\left[-\frac{c_{f11}\,\tau_{\mathrm{sc}}}{t_{\mathrm{c}}}\mathcal{EI}\left(c_{\tau13}\,c_{f12}\right)+\left(\frac{c_{f13}}{t_{\mathrm{c}}}-\frac{c_{f31}}{t_{\mathrm{c}}}\right)\left(t_{\mathrm{m}}-\tau_{\mathrm{sc}}\ln\left(\frac{c_{\tau13}}{\tau}\right)\right)\right]$ $\left[\mathcal{H}\left(\tau-\tau_{13}\right)-\mathcal{H}\left(\tau-\tau_{13,\mathrm{tc}}\right)\right]$ $+c_{f31}\left[\mathcal{H}\left(\tau-\tau_{13,\mathrm{tc}}\right)-\mathcal{H}\left(\tau-\tau_{23,\mathrm{tc}}\right)\right]$ $+\left[\frac{c_{f21}\,\tau_{\mathrm{sc}}}{t_{\mathrm{c}}}\mathcal{EI}\left(c_{\tau23}\,c_{f22}\right)+\left(\frac{c_{f31}}{t_{\mathrm{c}}}-\frac{c_{f23}}{t_{\mathrm{c}}}\right)\left(t_{\mathrm{m}}-\tau_{\mathrm{sc}}\ln\left(\frac{c_{\tau23}}{\tau}\right)\right)\right]$ $\left[\mathcal{H}\left(\tau-\tau_{23}\right)-\mathcal{H}\left(\tau-\tau_{23,\mathrm{tc}}\right)\right]$ $+\left[\frac{c_{f21}\,\tau_{\mathrm{sc}}}{t_{\mathrm{c}}}\mathcal{EI}\left(c_{f22}\,\tau\exp\left(\frac{t_{\mathrm{m}}+t_{\mathrm{c}}}{\tau_{\mathrm{sc}}}\right)\right)+c_{f23}\right]$ $\left[\mathcal{H}\left(\tau-\tau_{23,\mathrm{tc}}\right)-\mathcal{H}\left(\tau-\tau_{\max,\mathrm{tc}}\right)\right]$ $+\left[-\frac{c_{f21}\,\tau_{\mathrm{sc}}}{t_{\mathrm{c}}}\mathcal{EI}\left(c_{f22}\,\tau\exp\left(\frac{t_{\mathrm{m}}}{\tau_{\mathrm{sc}}}\right)\right)\right]\left[\mathcal{H}\left(\tau-\tau_{23}\right)-\mathcal{H}\left(\tau-\tau_{\max}\right)\right]$ $+\left[-\frac{c_{f21}\,\tau_{\mathrm{sc}}}{t_{\mathrm{c}}}\mathcal{EI}\left(c_{\tau\max}\,c_{f22}\right)+\frac{c_{f23}}{t_{\mathrm{c}}}\left(t_{\mathrm{m}}-\tau_{\mathrm{sc}}\ln\left(\frac{c_{\tau\max}}{\tau}\right)\right)\right]$ $\left[\mathcal{H}\left(\tau-\tau_{\max}\right)-\mathcal{H}\left(\tau-\tau_{\max,\mathrm{tc}}\right)\right]$ (4.41)	$\left[-\frac{\lambda_\Omega\,\mu_\Omega\,c_{\mathrm{BL}}}{t_{\mathrm{c}}}\left(t_{\mathrm{m}}-\tau_{\mathrm{sc}}\ln\left(\frac{c_{\tau\min,\mathrm{B}}}{\tau}\right)\right)+\frac{c_{\mathrm{B2}}\,c_{\tau\min,\mathrm{B}}}{c_{\tau*,\mathrm{B}}}\right]$ $\left[\mathcal{H}\left(\tau-\tau_{\min,\mathrm{B}}\right)-\mathcal{H}\left(\tau-\tau_{\min,\mathrm{B,tc}}\right)\right]$ $+\left[-\frac{c_{\mathrm{B2}}}{c_{\tau*,\mathrm{B}}}\tau\exp\left(\frac{t_{\mathrm{m}}}{\tau_{\mathrm{sc}}}\right)\right]$ $\left[\mathcal{H}\left(\tau-\tau_{\min,\mathrm{B}}\right)-\mathcal{H}\left(\tau-\tau^*_{\mathrm{sc,B}}\right)\right]$ $+\left[\lambda_\Omega\,\mu_\Omega\,c_{\mathrm{BL}}+\frac{c_{\mathrm{B2}}}{c_{\tau*,\mathrm{B}}}\tau\exp\left(\frac{t_{\mathrm{m}}+t_{\mathrm{c}}}{\tau_{\mathrm{sc}}}\right)\right]$ $\left[\mathcal{H}\left(\tau-\tau_{\min,\mathrm{B,tc}}\right)-\mathcal{H}\left(\tau-\tau^*_{\mathrm{sc,B,tc}}\right)\right]$ $+\left[\frac{\lambda_\Omega\,\mu_\Omega}{t_{\mathrm{c}}}\left(c_{\mathrm{BL}}-c_{\mathrm{BU}}\right)\left(t_{\mathrm{m}}-\tau_{\mathrm{sc}}\ln\left(\frac{c_{\tau*,\mathrm{B}}}{\tau}\right)\right)-2c_{\mathrm{B2}}\right]$ $\left[\mathcal{H}\left(\tau-\tau^*_{\mathrm{sc,B}}\right)-\mathcal{H}\left(\tau-\tau^*_{\mathrm{sc,B,tc}}\right)\right]$ $+\left[\lambda_\Omega\,\mu_\Omega\,c_{\mathrm{BU}}-\frac{c_{\mathrm{B2}}}{c_{\tau*,\mathrm{B}}}\tau\exp\left(\frac{t_{\mathrm{m}}+t_{\mathrm{c}}}{\tau_{\mathrm{sc}}}\right)\right]$ $\left[\mathcal{H}\left(\tau-\tau^*_{\mathrm{sc,B,tc}}\right)-\mathcal{H}\left(\tau-\tau_{\max,\mathrm{B,tc}}\right)\right]$ $+\left[\frac{c_{\mathrm{B2}}}{c_{\tau*,\mathrm{B}}}\tau\exp\left(\frac{t_{\mathrm{m}}}{\tau_{\mathrm{sc}}}\right)\right]$ $\left[\mathcal{H}\left(\tau-\tau^*_{\mathrm{sc,B}}\right)-\mathcal{H}\left(\tau-\tau_{\max,\mathrm{B}}\right)\right]$ $+\left[\frac{\lambda_\Omega\,\mu_\Omega\,c_{\mathrm{BU}}}{t_{\mathrm{c}}}\left(t_{\mathrm{m}}-\tau_{\mathrm{sc}}\ln\left(\frac{c_{\tau\max,\mathrm{B}}}{\tau}\right)\right)+\frac{c_{\mathrm{B2}}\,c_{\tau\max,\mathrm{B}}}{c_{\tau*,\mathrm{B}}}\right]$ $\left[\mathcal{H}\left(\tau-\tau_{\max,\mathrm{B}}\right)-\mathcal{H}\left(\tau-\tau_{\max,\mathrm{B,tc}}\right)\right]$ (4.42)	B.92	B.133
Boundary Constants	$c_{\tau\min}$, $c_{\tau13}$, $c_{\tau23}$ and $c_{\tau\max}$: Summarized in Table B.2	$c_{\tau\min,\mathrm{B}}$, $c_{\tau*,\mathrm{B}}$ and $c_{\tau\max,\mathrm{B}}$: Summarized in Table B.3	N/A	
Other Constants	c_{f11}, c_{f12}, c_{f13}, c_{f21}, c_{f22} and c_{f23}: Summarized in Table B.2 c_{f31}: Defined by Equation B.38	c_{BL}, c_{BU} and c_{B1}: Summarized in Table B.5 c_{B2}: Defined by Equation B.132		

Where $\mathcal{H}(x-a)$ and $\mathcal{EI}(x)$ are the Heaviside and Exponential Integral Functions defined by Equations 4.34 and B.101, respectively.

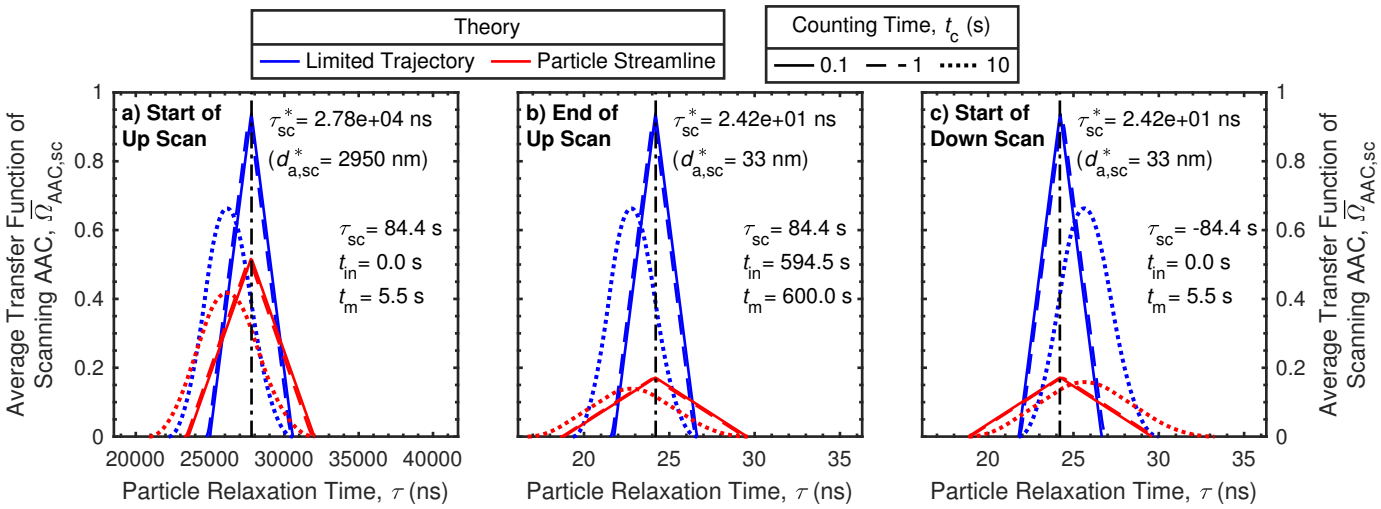

Fig. 4.3 The average transfer function of the scanning AAC ($\bar{\Omega}_{AAC,sc}$) based on idealized limited trajectory or non-idealized particle streamline theory over three different particle detector counting times (t_c), where subplots a), b) and c) show the transfer functions at the start of the up scan, end of the up scan and start of the down scan, respectively. The vertical line in each subplot, denoted with a black, dash-dot line style, shows the instantaneous setpoint of the scanning AAC (in terms of relaxation time, τ^*_{sc} or aerodynamic diameter[3], $d^*_{a,sc}$) at the start of the counting interval of the particle detector.

4.2.9 Parameters of scanning AAC

Similar to the average transfer function (i.e. Equation 4.33), the counting time of the particle detector also affects the average setpoint ($\bar{\tau}^*_{sc}$) and classes per decade (CPD) of the measurements collected by the scanning AAC. The CPD is the number of measurements collected across one decade of the parameter of interest. For the stepping or scanning AAC, the CPD corresponds to the number of amplitude measurements of the size distribution collected across one decade of particle relaxation time (e.g. 100 to 1,000 ns, or 2,300 ns to 23,000 ns). Therefore, as the CPD increases, the change in particle size between consecutive measurements becomes smaller, and characteristics of the size distribution are more clearly identified, such as multi-modal distributions. This parameter can be directly adjusted on the DMPS or stepping AAC by changing the number of setpoint steps across the size range of interest. However, for the scanning AAC or SMPS and maintaining the one-to-one correspondence[5] between the raw data and reported measurements, the maximum CPD is limited by the counting time of the downstream particle detector.

[5]The data inversion does not use assumptions, such as interpolation or averaging, to increase or decrease the CPD of the reported measurements.

The effects of counting time (t_c) on these parameters of the scanning AAC can be quantified by solving the following equations:

$$\bar{\tau}^*_{sc} = \frac{1}{t_c}\int_{t_m}^{t_m+t_c} \tau^*_{sc}(t'_m)\,dt'_m, \tag{4.43}$$

and

$$\mathrm{CPD}_{sc} = \frac{n_{sc}-1}{|\log(\bar{\tau}^*_{sc,S}) - \log(\bar{\tau}^*_{sc,E})|}, \tag{4.44}$$

where n_{sc} is the number of measurements collected that are logarithmically spaced between the average setpoints of the AAC at the start and end of the scan (i.e. $\bar{\tau}^*_{sc,S}$ and $\bar{\tau}^*_{sc,E}$, respectively). These two equations are solved in Sections B.7.1 and B.7.2, respectively.

Furthermore, the range of particle relaxation times measured by the scanning AAC is smaller than the steady-state AAC due to the residence time of particles in the classifier (t_f as defined in Equation 4.12). Measurements cannot be collected until the particles at the classifier inlet at the start of the scan pass through it (i.e. $t_m = t_f$). Measurements can also only be collected for particles that experience the changing centrifugal force field during their entire residence time within the classifier. Therefore, measurements cannot be collected for particles at the classifier outlet after the scan duration (i.e $t_m = t_{sc}$). These limitations offset the start and end of AAC scan relative to its steady-state setpoint by $\bar{\tau}^*_{sc}/\tau^*_{ss}|_S$ and $\bar{\tau}^*_{sc}/\tau^*_{ss}|_E$, respectively, as derived in Section B.7.3.

The solutions for these parameters of the scanning AAC (i.e. $\bar{\tau}^*_{sc}$, CPD_{sc}, $\bar{\tau}^*_{sc}/\tau^*_{ss}|_S$ and $\bar{\tau}^*_{sc}/\tau^*_{ss}|_E$) are summarized in Table 4.4. These equations are the same for either limited trajectory or particle streamline theory due to τ^*_{sc} having the same form based on either theory (i.e. $c_{\tau*}\exp(-t_m/\tau_{sc})$ as summarized in Table 4.2). Based on these solutions (i.e. Table 4.4), the parameters for some example[6] AAC scans are shown in Table 4.5. This table demonstrates that a down scan can be completed quicker than an up scan due to the higher deceleration capacity of the AAC relative to its acceleration as shown in Figure B.2. However, as the scan time decreases the scan range becomes slightly narrower and the classes per decade (CPD) of the measurements collected decrease.

For context, a standard SMPS measurement using a 3080 Electrostatic Classifier with a 3081 DMA (TSI Inc., Shoreview, MN, USA) at low-flow (LF: $Q_a = 0.3$ L/min and $Q_{sh} = 3$ L/min) completes an up scan in 120 s at 64 CPD, while measuring particles with electrical mobility diameters from 14 to 698 nm. To scan across a similar size range in aerodynamic diameter (approximately 30 to 700 nm), the minimum time of the up scan or down scan of

[6]These scan values correspond to the particle detector operating with a 1 s counting time (t_c), and the acceleration and deceleration capacity measured for AAC 2, as shown in Figure B.2.

Table 4.4 Parameters of the scanning AAC.

Parameter	Equation		Appx. Eqn
$\bar{\tau}^*_{sc}$	$\frac{-c_{\tau*}\,\tau_{sc}}{t_c}\left[\exp\left(\frac{-(t_m+t_c)}{\tau_{sc}}\right)-\exp\left(\frac{-t_m}{\tau_{sc}}\right)\right]$	(4.45)	B.146
CPD_{sc}	$\frac{1}{\left\lvert\log\left(\exp\left(\frac{-t_c}{\tau_{sc}}\right)\right)\right\rvert}$	(4.46)	B.149
$\left.\frac{\bar{\tau}^*_{sc}}{\tau^*_{ss}}\right\rvert_S$	$\frac{-t_f}{t_c\left[\exp\left(\frac{t_f}{\tau_{sc}}\right)-1\right]}\left[\exp\left(\frac{-t_c}{\tau_{sc}}\right)-1\right]$	(4.47)	B.151
$\left.\frac{\bar{\tau}^*_{sc}}{\tau^*_{ss}}\right\rvert_E$	$\frac{-\omega_E^2\,t_f}{\omega_S^2\,t_c\exp\left(\frac{t_{sc}-t_f}{\tau_{sc}}\right)\left[\exp\left(\frac{t_f}{\tau_{sc}}\right)-1\right]}\left[\exp\left(\frac{-t_c}{\tau_{sc}}\right)-1\right]$	(4.48)	B.152

Where $c_{\tau*}$ equals Equation 4.29 or Equation 4.30 for the scanning AAC based on limited trajectory theory or particle streamline theory operating with balanced classifier flows, respectively.

Table 4.5 Parameters of the AAC during example scans.

Flow	Scan	Speed (rad/s)		Min Scan Time[6], t_{sc} (s)	Scan Constant, τ_{sc} (s)	Range[3] of Steady-State				Range[3,6] of Scanning				Classes per Decade[6]
						τ^*_{ss} (ns)		$d^*_{a,ss}$ (nm)		$\bar{\tau}^*_{sc}$ (ns)		$\bar{d}^*_{a,sc}$ (nm)		
		ω_S	ω_E			Min	Max	Min	Max	Start	End	Start	End	
LF	Up	20	700	607	85.3	23	28708	32	3000	27637	24	2942	33	196
	Down	700	20	153	-21.5					27	25808	37	2840	49
HF	Up	20	500	333	51.7	230	143541	203	6803	140667	230	6734	203	119
	Down	500	20	107	-16.7					245	143143	211	6793	38
LF	Up	76	700	379	85.3	23	1988	32	735	1914	24	720	33	196
	Down	700	76	95	-21.5					27	1787	37	693	49

Where low-flow (LF) corresponds to 0.3 and 3 L/min sample and sheath flow (i.e. Q_a and Q_{sh}), respectively; high-flow (HF) corresponds to 1.5 and 15 L/min sample and sheath flow (i.e. Q_a and Q_{sh}), respectively; and the corresponding residence time (t_f) of the particles in the classifier is 5.5 and 1.1 s for LF and HF, respectively.

the AAC[6] at low-flow is 379 or 95 s, respectively. These parameters correspond to scans with 196 and 49 CPD, respectively. Therefore, completing a consecutive up and down scan with these parameters takes 474 s, while completing only a down scan takes[7] 235 s. These up, down and combined scan times (379, 235 and 474 s, respectively) correspond to 3.2, 2.0

[7]This estimate assumes the AAC is not spinning at the start of the down scan, and it takes approximately 140 s to reach the starting speed of 700 rad/s.

and 1.8[8] times longer than a standard SMPS measurement, while at a similar or higher CPD (64 vs 49 or 196).

One key advantage of the scanning AAC is the broad range and upper limit of its particle sizing, scanning in ten minutes or less from approximately 30 to 2900 nm at low-flow and from approximately 200 to 6800 nm at high-flow (HF: $Q_a = 1.5$ L/min and $Q_{sh} = 15$ L/min). Shorter scan times are also possible if the scan range is focused on a smaller range of interest. For example, a portion of the PSL results shown in the Results (Section 4.4.2) was collected using 60 s scans.

4.2.10 Deconvolution of average transfer function of scanning AAC

To determine the aerodynamic size distribution of an aerosol using a scanning AAC upstream of a particle detector, the particle concentration ($N_{det}(t_i)$) that it classifies at time t_i during the scan is determined by:

$$N_{det}(t_i) = \int \eta(\tau)\, \bar{\Omega}_{AAC}(\tau, t_i)\, dN(\tau), \tag{4.49}$$

where $\eta(\tau)$ is the counting efficiency of the downstream particle detector and $N(\tau)$ is the particle concentration of the aerosol source, both at particle relaxation time τ. This relationship is similar to the methodology used to deconvolute measurements of the steady-state DMA [229], scanning DMA [261] or steady-state AAC (developed in Chapter 3). During scanning operation, $\bar{\Omega}_{AAC}(\tau, t_i)$ is the average transfer function of the scanning AAC over the counting time of the particle detector at time t_i. During steady-state operation, the transfer function of the AAC is constant over the counting time of the particle detector. Therefore, the instantaneous ($\Omega_{AAC,ss}$) and average ($\bar{\Omega}_{AAC,ss}$) transfer function of the steady-state AAC are the same and Equation 4.49 becomes the same as that used for the deconvolution of the steady-state AAC in Section A.2.

As shown in Section B.8, Equation 4.49 can be expanded and rearranged to isolate the spectral density of the aerosol in terms of particle relaxation time (i.e. $dN(\tau)/d\log\tau$) as follows:

$$\left.\frac{dN(\tau)}{d\log\tau}\right|_{\bar{\tau}^*_{sc,i}} = \frac{N_{det}(t_i)\ln(10)}{\eta(\bar{\tau}^*_{sc,i})\,\beta^*_{sc,i}}, \tag{4.50}$$

where $\beta^*_{sc,i}$ is the non-dimensional deconvolution parameter of the average transfer function of the scanning AAC at time t_i as follows:

[8] This ratio accounts for the standard 15 s retrace time for each consecutive SMPS scan.

$$\beta^*_{\mathrm{sc},i} = \int \frac{\bar{\Omega}_{\mathrm{AAC}}(\tau, t_i)}{\tau} \mathrm{d}\tau. \tag{4.51}$$

This integral (Equation 4.51) is solved for the idealized, average transfer function of the scanning AAC based on limited trajectory theory (i.e. Equation 4.41) in Section B.9 and for the non-idealized, average transfer function of the scanning AAC with balanced flows based on particle streamline theory (i.e. Equation 4.42) in Section B.10. These solutions are also summarized in Table 4.6. The simple form of these solutions allows for direct implementation on the microprocessor of the AAC, thus allowing real-time data inversion and avoiding the need for an external computer during measurements. Similar to inversions for other aerosol classifiers, such as the DMPS [132], SMPS [261] and steady-state AAC (in Section 3.3.2), the inversion parameters for the scanning AAC were derived assuming the concentration of the aerosol is constant over the width of its average transfer function ($\bar{\Omega}_{\mathrm{sc}}$). To avoid this assumption and also allow faster scans, future work could investigate the possibility of using higher-order inversion schemes, such as the Twomey algorithm used by Collins et al. [37] or the L-curve algorithm used by Talukdar and Swihart [234] or Kanaparthi et al. [118] to improve the inversion of SMPS data.

It is interesting, but slightly counter-intuitive, that the deconvolution parameter based on particle streamline theory is the same for the scanning AAC (shown by Equation 4.53), as the one previously determined for the steady-state AAC in Section A.3.2 and summarized in Section 3.3.2. As previously shown, the instantaneous transfer function of the steady-state ($\Omega_{\mathrm{AAC,ss}}$) and scanning ($\Omega_{\mathrm{AAC,sc}}$) AAC have the same shape (as summarized in Table 4.1 and shown in Figure 4.1), and thus the same area underneath them. Since these transfer functions (i.e. $\Omega_{\mathrm{AAC,ss}}$ and $\Omega_{\mathrm{AAC,sc}}$) are the same, the smearing of $\Omega_{\mathrm{AAC,sc}}$ over to the counting time of the particle detector (i.e. resulting in $\bar{\Omega}_{\mathrm{AAC,sc}}$) must maintain the same weighting of the average transfer function relative to particle relaxation time to achieve the same deconvolution parameter, as defined by Equation 4.51. This fact is slightly counter-intuitive and not immediately obvious by visual inspection. For example, the average transfer functions ($\bar{\Omega}_{\mathrm{AAC,sc}}$) shown in Figure 4.3 have deconvolution parameters (i.e. $\int \bar{\Omega}_{\mathrm{AAC,sc}}/\tau \, \mathrm{d}\tau$) that are independent[9] of their counting times (t_{c}).

Figure 4.4a shows that the deconvolution parameter (β^*_{sc}) based on idealized limited trajectory or particle streamline theory have excellent agreement (agree within 6.7% or less). Based on this idealized theory, the deconvolution parameter only depends on the dimensions (i.e. $r_1 = 56$ mm, $r_2 = 60$ mm and $L = 206$ mm for the current commercial AAC) and flows (i.e. Q_{a} and Q_{sh}, which are reflected in β) of the classifier. The effects of particle losses

[9]This statement of independence neglects that the non-idealized parameters (λ_Ω and μ_Ω) change based on the average setpoint of the scanning AAC over t_{c} (i.e. $\bar{\tau}^*_{\mathrm{sc}}$ as defined by Equation 4.45).

Table 4.6 Deconvolution of the average transfer function of the scanning AAC.

Parameter	Limited Trajectory (LT) Theory	Particle Streamline (PS) Theory with Balanced (B) Classifier Flows	Appx. Eqn	
			LT	PS
β_{sc}^*	$c_{f11}\left[\mathcal{EI}\left(c_{\tau 13}\, c_{f12}\right) - \mathcal{EI}\left(c_{\tau \min}\, c_{f12}\right)\right] + c_{f13} \ln\left(\frac{c_{\tau 13}}{c_{\tau \min}}\right) + c_{f31} \ln\left(\frac{c_{\tau 23}}{c_{\tau 13}}\right) + c_{f23} \ln\left(\frac{c_{\tau \max}}{c_{\tau 23}}\right) + c_{f21}\left[\mathcal{EI}\left(c_{\tau \max}\, c_{f22}\right) - \mathcal{EI}\left(c_{\tau 23}\, c_{f22}\right)\right]$ (4.52)	$\lambda_\Omega\, \mu_\Omega \left[\ln\left(\frac{1+\frac{\beta}{\mu_\Omega}}{1-\frac{\beta}{\mu_\Omega}}\right) + \frac{\mu_\Omega}{\beta} \ln\left(1 - \left(\frac{\beta}{\mu_\Omega}\right)^2\right)\right]$ (4.53)	B.168	B.212

Where $\mathcal{EI}(x)$ is the Exponential Integral Function defined by Equation B.101, and the boundary constants ($c_{\tau \min}$, $c_{\tau 13}$, $c_{\tau 23}$ and $c_{\tau \max}$) and other constants (c_{f11}, c_{f12}, c_{f13}, c_{f21}, c_{f22} and c_{f23}) for β_{sc}^* based on limited trajectory theory are defined in Table B.2 and by Equation B.38 (c_{f31}).

and transfer function broadening on the deconvolution parameter are shown in Figures 4.4b and 4.4c at two different samples flow rates ($Q_a = 0.3$ or 1.5 L/min, respectively). These figures are based on particle streamline theory and use the non-idealized parameters for the AAC previously determined in Section 3.4. The white boundaries show the classification range of the current commercial version of the AAC based on the non-dimensional parameter of classifier flow (β as defined by Equation 4.32) and its average setpoint ($\bar{\tau}_{sc}^*$).

At the minimum sample flow of the AAC ($Q_a = 0.3$ L/min), the difference between the idealized ($\beta_{sc,PS,B,I}^*$) and non-idealized ($\beta_{sc,PS,B,NI}^*$) deconvolution parameter based on particle streamline theory increases with decreasing particle relaxation time, as shown in Figure 4.4b. This trend agrees with expectations as the particle losses and transfer function broadening in the AAC increase as the particles become smaller.

At the maximum sample flow of the AAC ($Q_a = 1.5$ L/min), a portion of its classification range results in non-physical results for $\beta_{sc,PS,B,NI}^*$, as shown in Figure 4.4c. This region produces non-physical results as the factor of β/μ_Ω becomes greater than or equal to one, which implies the AAC transfer function spans to zero or negative particle relaxation times. This non-physical result is likely not due to the theory, but a result of extrapolating the non-idealized parameters previously determined in Chapter 3 at $\beta = 0.1$ to higher β values. This inference is supported by the non-physical results starting at $\beta > 0.46$ and the smallest particle size where μ_Ω is the largest. This outcome highlights that the non-idealized

parameters previously determined should only be used at β values close to 0.1 (as shown by the consistent results in Figure 4.4b, which spans from $\beta = 0.02$ to 0.15). Therefore, future work is required to characterise these non-idealized parameters at other flow conditions.

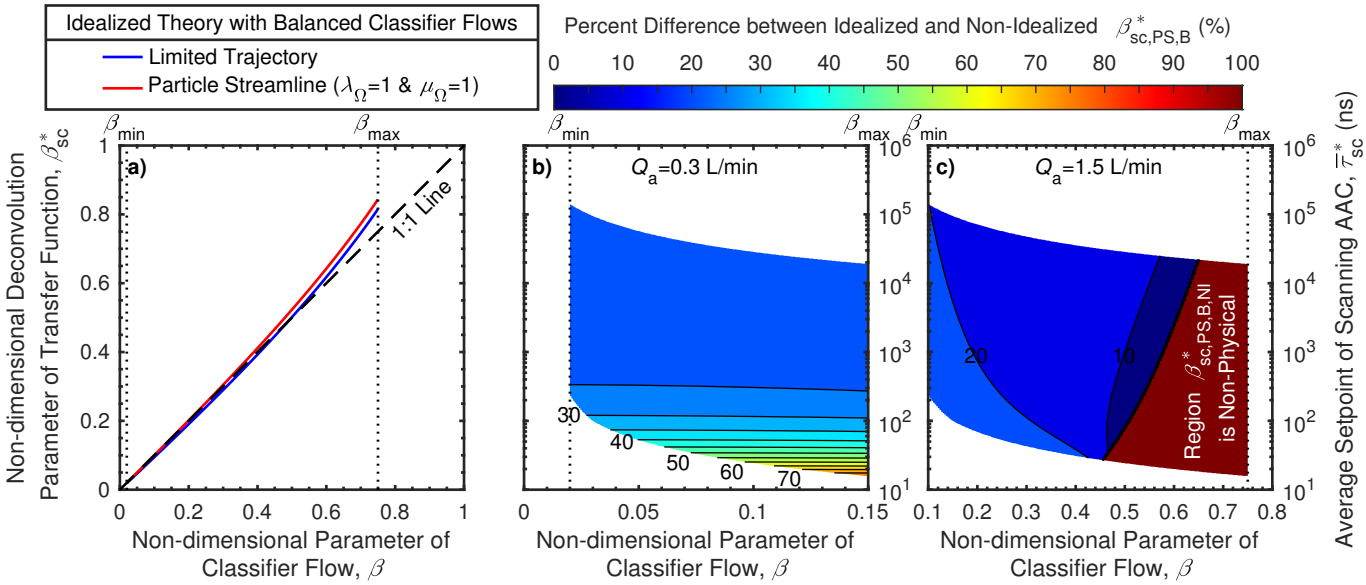

Fig. 4.4 A comparison of the non-dimensional deconvolution parameter (β^*_{sc}) of the average transfer function of the scanning AAC, where subplot a) compares the parameters based on idealized limited trajectory or particle streamline theory, while subplots b) and c) compare the idealized and non-idealized[3] deconvolution parameters based on particle streamline theory at two sample flows ($Q_a = 0.3$ or 1.5 L/min).

Finally, the spectral density of the aerosol ($dN/d\log\tau$ defined in Equation 4.50) can be calculated in terms of aerodynamic diameter ($dN/d\log d_a$) by the chain rule as shown in Section B.8. This conversion requires the factor $d\log\tau/d\log d_a$, which was previously determined for the inversion of the steady-state AAC in Section A.4, specifically Equation A.47.

4.2.11 Effects of delay time downstream of the AAC

In addition to the residence time (t_f) of the particles in the AAC classifier, the time for the particles to travel from the classifier outlet to the downstream particle detector and be detected must also be considered. This time, henceforth referred to as the delay time (t_d), is defined as:

$$t_d = t_t + t_{det}, \tag{4.54}$$

where t_t is the residence time or plumbing delay of the classified particles in the tubing between the classifier outlet and detector inlet, and t_{det} is the response time of the particle

detector, including the transport time of the particles within the detector. Since the equipment and its configuration downstream of the DMA in the SMPS configuration are the same as that downstream of the scanning AAC, the same theory developed for these effects in the SMPS can be applied. Assuming plug flow in the tube, t_t can be estimated by:

$$t_t = \frac{L_t}{\bar{V}_t} = \frac{\pi d_t^2 L_t}{4Q_s}, \tag{4.55}$$

where Q_s is the sample volumetric flow rate of the AAC, while L_t and d_t are the length and inner diameter of the tube, respectively, and $\bar{V}_t$ is the average flow velocity within the tube. The validity of assuming uniform flow in the downstream tubing and particle detector is discussed in Section 4.6. However, it has been shown at sufficiently fast scan times in the SMPS, the viscous flow significantly smears the arrival times of the classified particles to the detection region of the downstream particle detector [220, 37].

While the delay time t_d for a given flowrate, tube length and particle detector can be estimated by calculating t_t (Equation 4.55) and based on the specifications of the detector, it is best to determine this value experimentally. The delay time can be determined by completing a bidirectional scan (i.e. consecutive up and down scan) of a stable, monodispersed aerosol. If the delay time is correct, the measurements of the up and down scan will be the same. If the delay time is too short, the mode measured by the up scan will appear smaller in particle relaxation time/size than the down scan. While if the delay time is too long, the mode measured by the up scan will appear larger in particle relaxation time/size than the down scan.

This method is referred to as the up-down agreement (UDA) approach by Collins et al. [36] and is one of three methods they used to determine the delay time of the SMPS. The transit time approach introduces a step-change in particle concentration and measures the time for it to travel through the system and be detected. The PSL approach introduces particles of known sizes (such as PSL particles) and shifts the measurements to the correct size by changing the delay time [36]. Each of these three methods often provides different delay times, which propagate into the measurement error [36]. This work only uses the UDA approach to determine the delay time for the scanning AAC, and its limitations are discussed further in Section 4.6.

Finally, the time (t_r) the particle detector reports its concentration measurement (N_{det}) relative to the start of the scan ($t = 0$) is related to the measurement time of the scan (t_m) by:

$$t_m = t_r - t_c - t_d, \tag{4.56}$$

where t_c is the counting time of the particle detector. As previously discussed in Section 4.2.9 (and also Section B.7.3), the measurements collected during the AAC scan are only valid from $t_m = t_f$ to $t_m = t_{sc}$.

4.3 Experimental setup

The theory and practical implementation of the scanning AAC were validated by measuring PSL particles with known sizes. It was also validated by comparing the aerodynamic size distributions of three different aerosols it measured to those measured by stepping the steady-state AAC, as previously developed in Chapter 3. The experimental setup used to collect these measurements, using the AAC (Cambustion Ltd., Cambridge, UK) in stepping or scanning operation, is shown in Figure 4.5. For both measurement modes of the three aerosol sources, a 3775 Condensation Particle Counter (CPC; TSI Inc., Shoreview, MN, USA) was used as the particle detector. However, due to equipment availability, a 3752 CPC (TSI Inc.) was used as the particle detector for the PSL measurements. These detectors use the same operating principle [8], with the 3752 CPC being a newer version of the 3775 CPC.

For either stepping or scanning operation, the AAC controlled the CPC, logged its measurements at 1 Hz (i.e. detector counting time of 1 s) and completed the inversion of the data in real-time. As developed in Chapter 3, the steady-state AAC stepped its setpoint in aerodynamic diameter ($d^*_{a,ss}$) and the corresponding concentration of the classified particles ($N_{det}(d^*_{a,ss})$) was measured by the CPC. This approach limited its measurements to when the AAC had stabilized at a setpoint. Thus no measurements were collected while changing setpoints or during the time required for particles at the new setpoint to travel through the classifier and reach the detection region of the downstream particle detector. The scanning AAC continuously varied its average setpoint in aerodynamic diameter ($\bar{d}^*_{a,ss}$) by following the required speed profile for the classifier (i.e. Equation 4.7). The corresponding concentration of the classified particles (N_{det}) was measured by the CPC and logged by the AAC as a function of the reported time (t_r). This raw data was converted to a similar form as that from the steady-state AAC (i.e. $N_{det}(d^*_a)$), by determining the measurement time (t_m) that corresponds to the reported time (t_r) using Equation 4.56, and then Equation 4.45 to determine the corresponding average setpoint of the scanning AAC ($\bar{\tau}^*_{sc}$). The equivalent aerodynamic diameter of this setpoint ($\bar{d}^*_{a,sc}$) was determined using Equation 1.1.

The steady-state and scanning measurements were collected consecutively, with both an up and down scan completed in each measurement mode. This approach allowed the same equipment to be used for both measurement modes and thus avoided other sources of disagreement, such as the agreement between different AACs or CPCs, and different particle

losses within the instruments or sample tubing. All of the measurements collected used a 25 cm tube of conductive silicone with a 6 mm diameter between the AAC outlet and CPC inlet.

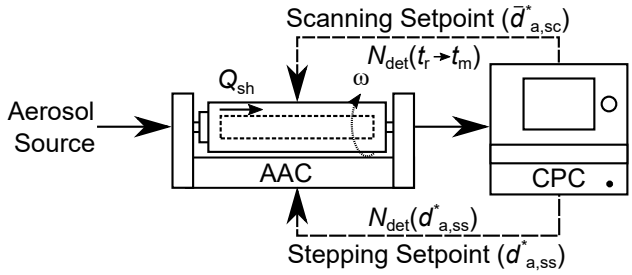

Fig. 4.5 Experimental setup used to validate the deconvolution theory of the scanning AAC.

4.3.1 Aerosol sources

The experimental setups used to generate the four different aerosols, DOS (di-octyl sebacate), NaCl, soot and PSL particles, are shown in Figures 4.6a to 4.6d, respectively. The first three aerosol sources (i.e. DOS, NaCl and soot) were used to compare the measurements of the steady-state and scanning AAC. For all three of these aerosol sources, a rotating disk diluter (Cambustion Ltd.) was used to dilute the aerosol sample. The dilution ratios used for the DOS, NaCl and soot aerosol sources were 130, 200 and 350, respectively. These dilutions were selected to maintain the concentration of the classified particles at any AAC setpoint below 5×10^4 particles per cm^3, thus increasing the accuracy of the 3775 CPC measurements by allowing it to operate in its single particle counting mode [246]. The disk diluter was not used for the PSL measurements, as the concentrations of the particles classified by the scanning AAC were all within the higher single counting limit ($< 1 \times 10^5$ particles per cm^3) of the 3752 CPC [250].

Since the aerosol instruments only required 0.3 or 1.5 L/min of sample flow, spills were used to exhaust excess flow. Aerosol sources generated with a liquid (i.e. DOS, NaCl and PSL) used liquid traps to remove excess liquid mobilized during atomization. Those sources where the liquid was distilled water (i.e. NaCl and PSL) also used a silica bead dryer to remove any water on the particles from atomization. To reduce the drying demand on the dryer, it was positioned after the spill on the diluted sample to minimize the particle concentration and flow rate passing through it.

Except for one size of PSL particles, the atomizer shown in Figure 4.6a, b or d was a Collison nebulizer (BGI Inc., Butler, NJ, USA) operating with HEPA-filtered air at 10 psig. A medicinal nebuliser (Aeroneb Go, Philips, Eindhoven, Netherlands) was used to produce the bigger droplets required to atomize the largest PSL size of 2.02 µm (Figure 4.6d). The

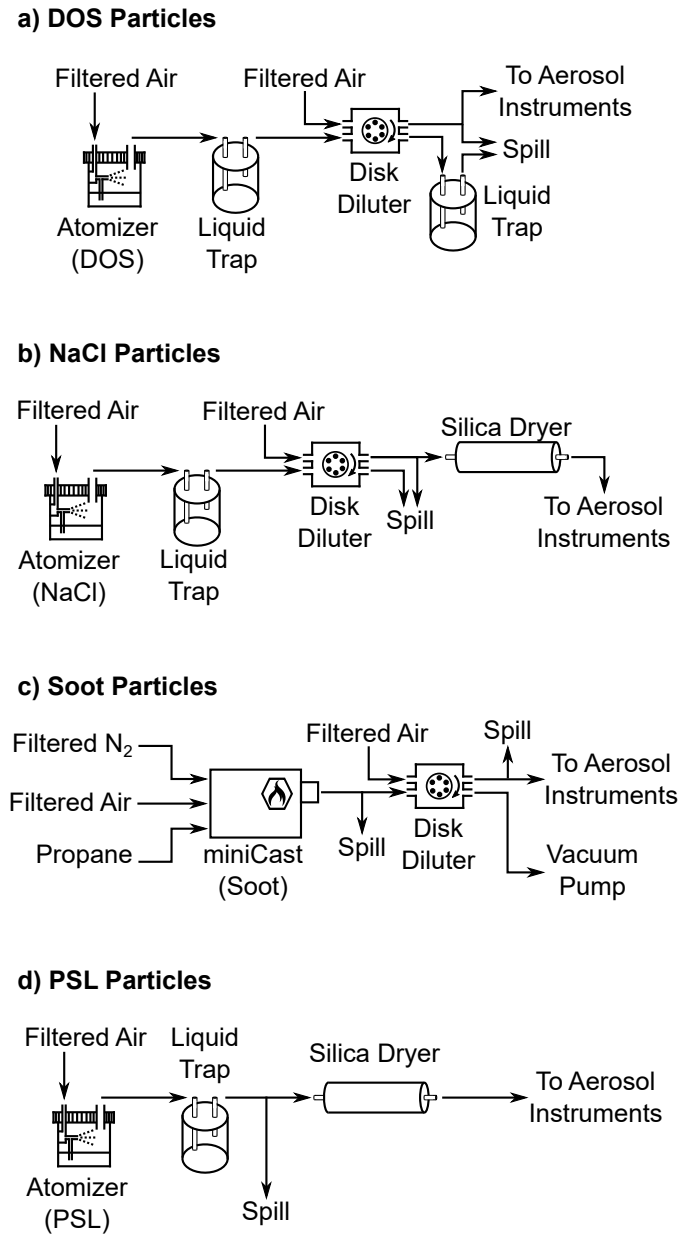

Fig. 4.6 The experimental setup used to generate each of the four aerosols used to validate the deconvolution theory of the scanning AAC.

soot particles (Figure 4.6c) were produced using a miniCast 4202 (Jing Ltd., Zollikofen, Switzerland) in autonomous mode (i.e. internal flow controllers) with the filtered air, filtered nitrogen and propane supplied at 2 bar. All of the aerosol sources were generated at positive pressure (i.e. above atmospheric pressure). However, due to the higher flowrates generated by the miniCast, a spill was required immediately downstream of its outlet. Therefore, the

vacuum pump incorporated within the disk dilutor was used to pull a portion of the aerosol sample generated by the miniCast for dilution.

To limit the transient characteristics of the aerosol source affecting the agreement between the steady-state and scanning AAC results, each of the aerosol sources was operated for at least half an hour before collecting measurements. This warm-up time was increased to an hour for the miniCast. Furthermore, the external effects on the aerosol sources, such as temperature, were monitored, and pilot pressure regulators (11400-2G-PE100; Norgren GmbH, Alphen, Germany) were utilized to improve the stability of the gas pressures used to generate all four aerosols shown in Figure 4.6.

Despite these efforts and as later discussed in Section 4.4.1, the agreement of the measurements was still limited by the stability of each aerosol source. This stability was independently quantified by bypassing the AAC in Figure 4.5 and using the CPC to measure the total number concentration (N_{tot}) of each aerosol source over 2 hours. To operate the CPC in the same measurement mode during these stability measurements, the dilution ratio of the disk dilutor was increased to 3000, 500 and 5000 for the DOS, NaCl and soot sources, respectively.

4.4 Validation of size distribution deconvolution

4.4.1 Agreement with steady-state AAC

The agreement between the aerodynamic size distributions measured by stepping and scanning the AAC for all three aerosol sources (i.e. DOS, NaCl and soot particles) was generally within a few percent but did vary by up to 11.3%, as shown in Figure 4.7. This agreement was based on fitting[10] the parameters of a lognormal distribution to each of the measured size distributions, specifically the Count Median Diameter (CMD), Geometric Standard Deviation (GSD) and total number concentration of the particles (N_{tot}).

However, the agreement between measurements of the steady-state and scanning AAC was limited by the stability of each aerosol source. As previously mentioned, the stability of each aerosol source was independently quantified by using the CPC to directly measure the total number concentration (N_{tot}) of each aerosol source over 2 hours. The most stable source was DOS with a standard deviation of 0.8% and a maximum variation of $\pm$2.8% in its total number concentration of particles over 2 hours. This high stability resulted in the size distributions (i.e. CMD, GSD and N_{tot}) of DOS measured by the steady-state and scanning AAC agreeing within 2.0% or better. Furthermore, these agreements were consistent when

[10]The lognormal distribution was fitted to each measured size distributions using least-squares minimization.

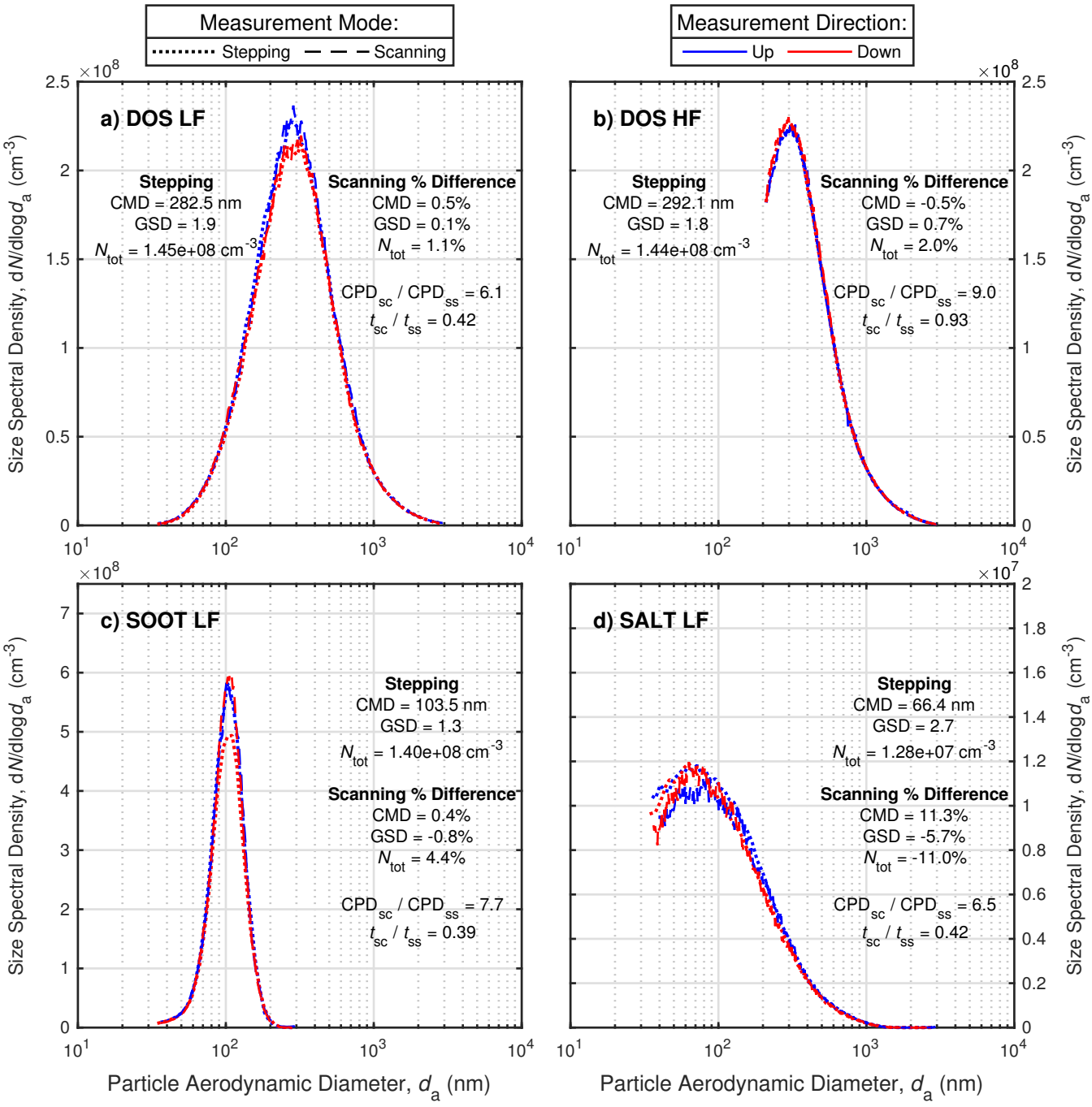

Fig. 4.7 Comparison of particle size distributions from different aerosol sources measured by stepping or scanning the AAC, where a) and b) show the AAC measurements of the DOS particles at low and high classifier flows, respectively, while c) and d) show the AAC measurements at low classifier flows of the soot and salt particles, respectively.

operating the AAC at either low (LF: $Q_a = 0.3$ and $Q_{sh} = 3$ L/min) or high (HF: $Q_a = 1.5$ and $Q_{sh} = 15$ L/min) classifier flows, as shown in Figures 4.7a and 4.7b, respectively.

After the 1 hour warm-up, the soot produced by the miniCAST had periods of relative stability (standard deviation of 4.0% in its total number concentration of particles over 2 hours). However, over 2 hours, its concentration shifted four times to a new mean that varied by greater than 10% from the previous one. These shifts occurred over 30 s or less, and therefore are hypothesized to be due to sudden changes in demand on the shared nitrogen, air and propane systems in the laboratory. However, no changes were noticed on the pressure gauges of the regulators. An example of this concentration shift occurred between the up and down scan of the steady-state AAC, as shown in Figure 4.7c. This result is independent of the scanning theory developed in this chapter, and further supports that the stability of the sources limited the agreement of the measurements. Despite this concentration shift, the CMD and GSD of the size distributions of the soot particles measured by the steady-state and scanning AAC agreed within 0.8% or better, as shown in Figure 4.7c.

The mean number concentration of the salt particles continuously shifted over 2 hours. This trend is reflected by a standard deviation of 16.2% in its total number concentration of particles over 2 hours, but a short-term standard deviation (i.e. based on a 600 s moving average) of only 1.5%. This instability is likely due to the concentration of salt in the water of the Collison nebulizer changing over time from its atomization jet draining to its fluid reservoir. This trend agrees with the AAC results, with each consecutive measurement of size distribution, using either the stepping or scanning AAC, shifting slightly in amplitude. As shown in Figure 4.7d, this source instability results in the largest disagreement between the measurements of the steady-state and scanning AAC of 11.3%, -5.7% and -11.0% for the CMD, GSD and N_{tot}, respectively.

Due to these stability limitations, consecutive measurements and their repeatability from the same polydispersed aerosol source are not reported. This exclusion is intentional as the stability of these aerosol sources dominates this repeatability, and thus, is not representative of the agreement between the steady-state and scanning AAC measurements. To determine the repeatability of measurements using the scanning AAC, PSL particles of known sizes were measured multiple times, as discussed in the next section.

All of the measurements using the steady-state AAC were collected at 32 classes per decade (CPD). The DOS, NaCl and soot measurements using the scanning AAC were collected with scan times (t_{sc}) of 600 s, 630 s and 300 s, respectively. Based on the particle size range of the scans, these scan times resulted in scan constants (τ_{sc}) of 85.4 s, 125.6 s, 89.9 s and 107.5 s for the DOS LF, DOS HF, NaCl and soot measurements, respectively. Therefore, the scan time and associated CPD of the measurements of the three aerosol sources

using the scanning AAC were 1.1 to 2.6 times faster[11] and 6.1 to 9.0 times higher[12] classes per decades than those of the steady-state AAC, as shown in Figure 4.7.

4.4.2 Validation using PSL particles

For further validation, six different sizes of PSL particles (from 100 nm to 2.02 µm) were also measured with the scanning AAC. A minimum of two up scans and two down scans were collected at each size of PSL particles. Based on the known density of the PSL particles (i.e. 1050 kg/m^3) and the conversion theory developed for the steady-state AAC in Section A.5, the aerodynamic size distribution measured by the scanning AAC for each PSL particle size was converted to its equivalent mobility distribution. As shown in Figure 4.8, all of the measured CMDs agree within 8.7% of the stated particle sizes or 5.7% if the uncertainty in the stated sizes is considered. The grey shaded area in Figure 4.8 illustrates these sizing uncertainties in the PSL particles, while the error bars illustrate the repeatability[13] of the CMDs measured by the scanning AAC. The measured CMDs, including between the up and down scans, are highly repeatable (average of 0.2%), thus validating the delay times determined by the UDA method.

The agreement of these PSL measurements is not only a function of the scanning inversion, but the uncertainty of the flow, speed and geometry of the classifier. Therefore, the PSL results are biased by these other sources of uncertainty and can be corrected through calibration. For example, Tavakoli et al. [240] and Kinney et al. [129] accounted for these biases by determining the effective length of the AAC (prototype) and DMA classifier based on PSL measurements. These scanning PSL results are similar to those of Johnson et al. [105], which found the measurements of the steady-state AAC agreed within 4.7% for nine PSL particle sizes between 29 nm and 2.02 µm and observed a similar positive bias.

It should be noted that the narrowness of the size distributions produced by the PSL particles may conflict with the data inversion of the scanning AAC. Specifically, the assumption (as mentioned in Section 4.2.10 and discussed in Section B.8) that the concentration of the aerosol is constant over the width of the average transfer function of the scanning AAC may not be valid. However, this assumption is also used in the inversion of other aerosol classifiers, such as the DMPS [132], SMPS [261] and steady-state AAC (i.e. Chapter 3). Therefore, these classifiers also suffer from similar issues when measuring narrow size distributions,

[11] This ratio is based on the average times (t_{ss}) to complete the up or down scan using the steady-state AAC. The down scan of the steady-state AAC was 1% to 8% faster than its up scan due to its higher capacity to decelerate than accelerate.

[12] The CPD of the measurements collected using the scanning AAC also depend on the counting time (t_c) of the detector as shown in Equation 4.46. For this data, the CPC was operated with a counting time of 1 s.

[13] The repeatability was estimated assuming a 95% confidence interval and using a t-distribution.

such as PSL particles. However for typical SMPS measurements, Stolzenburg and McMurry [230] recently showed that although this assumption causes significant errors in the width (i.e. GSD) of the distribution measured, it only has a minor effect ($< 1\%$) on the measured CMD and amplitude (i.e. N_{tot}). These conclusions likely also apply to the AAC given the results and understanding of previous research that use the AAC to measure a narrow size distribution generated using PSL particles [240, 105] or by using another aerosol classifier in tandem, as done by Tavakoli and Olfert [239], and Chapters 3, 5 and 6 of this current work. Therefore, this assumption within the inversion likely does not significantly affect the CMD measured by the steady-state or scanning AAC, including the PSL results shown in this chapter.

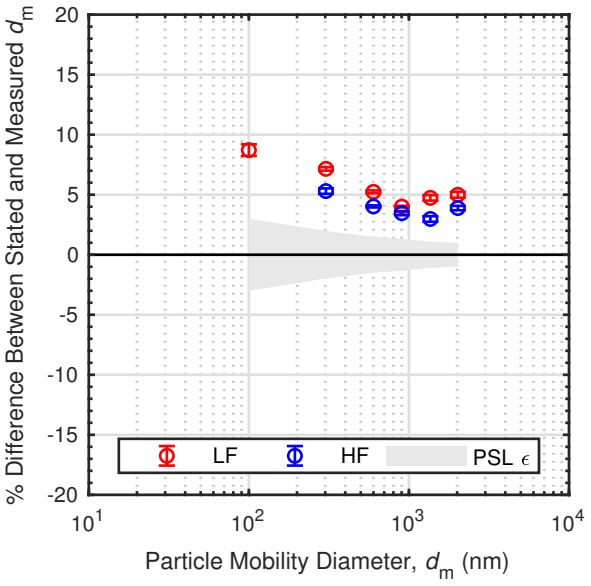

Fig. 4.8 Agreement between PSL calibration particles and the mobility equivalent CMDs of the size distributions measured by the scanning AAC. The error bars depict the repeatability of the measurements (assuming a 95% confidence interval), while the shaded region represents the uncertainty in the PSL sizes based on manufacturer specifications.

4.5 Uniform versus viscous axial flow

Similar to the SMPS theory developed by Wang and Flagan [261], all of the theory developed for the scanning AAC in this chapter assumes uniform flow in the axial direction of the classifier. This assumption is equivalent to assuming all of the particles have the same residence time in the classifier, as highlighted by Section 4.2.4. However, in reality, the axial

flow in the AAC classifier is viscous and varies as a function of radial position due to no-slip boundary conditions at the walls of the classifier. Therefore, particles closer to the classifier walls will have lower axial velocities, and thus longer residence times. This varying velocity profile does not affect the steady-state transfer function of the DMA [133, 86] or AAC [238]. However, it does distort the transfer function of the SMPS as the ratio of the mean residence time of the particles in the classifier to the scan constant (i.e. t_f/τ_{sc}) increases [36, 47, 167]. For example at $t_f/\tau_{sc} = 3.11$, the median electrical mobility and particle counts (i.e. area under transfer function of DMA during scanning) measured by the SMPS vary by 46% and 55%, respectively, from those predicted by assuming uniform axial flow [167]. However as the t_f to τ_{sc} ratio approaches zero, the transfer function of the SMPS accounting for viscous flow converges to that of the steady-state DMA [36, 47, 167].

For this work, the experimental results of the polydispersed aerosols were collected with $t_f/\tau_{sc} = 0.01$ to 0.06, while those of the PSL particles were collected with $t_f/\tau_{sc} = 0.01$ to 0.13. Therefore, the effect of viscous axial flow on these results is likely insignificant. For reference, at a t_f/τ_{sc} of 0.16 the median electrical mobility and particle counts measured by the SMPS only shift by 2% or less [36, 167]. Furthermore, given the acceleration/deceleration limitations of the AAC classifier (as discussed in Section 4.2.3), typical AAC scans are less likely to achieve t_f to τ_{sc} ratios where the effects of viscous axial flow need to be considered for measurement accuracy.

However, the t_f to τ_{sc} ratios the AAC can achieve increase as its scanning range is narrowed or shifted to lower classifier speeds. For example, scanning the AAC based on its maximum[6] acceleration/deceleration between 20 and 100 rad/s at low classifier flows ($Q_a = 0.3$ L/min and $Q_{sh} = 3$ L/min) results in t_f/τ_{sc} of 0.66 or 1.30 for the up or down scan, respectively. At standard gas conditions and a detector counting time (t_c) of 1 s, this up scan measures the aerodynamic size distribution between 624 and 2433 nm particles at 19 CPD in 27 s, while the down scan measures the aerodynamic size distribution between 798 and 2207 nm particles at 10 CPD in 14 s. These scan times (i.e. 27 and 14 s) also approach the residence time of the particles in the classifier (i.e. 5.5 s), which would likely further affect the measurements.

Therefore, the effect of viscous axial flow on the transfer function of the scanning AAC needs to be investigated in future work. Given the difference in classifier dimensions between the AAC and DMA, the threshold value for t_f/τ_{sc} that corresponds to appreciable effects of viscous axial flow is likely different between the instruments. Furthermore, some aspects of their classification methods are reversed. For example, increasing the total gas flow in the classifier shifts the measurement range to smaller particle sizes in the DMA, but larger particle sizes in the AAC. Also, continuously increasing the voltage in the DMA

classifies progressively larger particles, while continuously increasing the speed of the AAC classifies progressively smaller particles. Therefore, the difference in distortions observed in the transfer function between the up and down scan of the SMPS at fast scan times [36, 47, 167] may appear during the opposite scans of the AAC (i.e. during the down and up scan, respectively).

4.6 Delay time

The delay times (t_d) of the scanning AAC were determined by minimizing the difference between consecutive up and down scans. This method is similar to the up-down agreement (UDA) approach described by Collins et al. [36] for the SMPS. For the polydispersed aerosol measurements using the 3775 CPC, the delay times were 7 s and -0.1 s at low and high flows, respectively. The slightly negative delay time at high-flow is due to internal software and communication timings between the AAC and CPC. For the PSL particle measurements using the 3752 CPC, the delay times varied from 6.9 to 9.7 and 3.0 to 4.2 s at low and high flows, respectively.

This variation in delay times for the PSL results is likely due to its scans being collected more quickly than the scans of the polydispersed aerosols (i.e. τ_{sc} approximately halved), and assuming the delay time is a constant rather than a distribution [36]. Viscous flow also occurs in the plumbing between the classifier outlet and the detection region of the particle detector. This flow profile smears the detection times of the particles classified at each measurement time (t_m). Russell et al. [220] showed this effect is significant in the SMPS at high ratios of mixing time to scan constant (τ_{sc}). Since the downstream plumbing and particle detector are the same in the SMPS or scanning AAC, previous theory for this smearing effect in the SMPS can be readily adapted to the scanning AAC.

Russell et al. [220] combined a fixed delay time with a model of a continuously stirred tank reaction to represent the distribution of detection times and derive an "effective transfer function" for the DMA. Collins et al. [37] found similar outcomes, but simplified the approach by assuming an exponential decay to remove the effect of the mixing within the detector first, then inverting the data based on the DMA response. Kanaparthi et al. [118] also accounted for these smearing effects from downstream flows. They took a more comprehensive approach by incorporating these effects, as well as the impacts of the plumbing delay and counting times, directly into the arrival time transfer function of the SMPS. All three studies found as the ratio of mixing/smearing time (where higher values correspond to greater non-ideal flows) to scan constant increased, the size distributions measured by the SMPS were broader and had lower amplitudes.

Assuming a constant mixing time for a particular detector and flow rate, its ratio to the constant (τ_{sc}) of each AAC scan varies by 188% and 76% for the PSL measurements at low and high flow, respectively. These variations are higher than the 26% observed in the same ratio for measurements of the polydispersed aerosols at low or high flow. Therefore, this higher variation likely drives the higher variance in the delay time of the PSL measurements. For example, the 6.9 s and 9.7 s delay times at low-flow correspond to 300 s and 90 s scans, respectively. If only 60 s scans of PSL at low-flow are considered, the variance in the mixing time to scan constant reduces by 34% and the variance in the delay time reduces by 60% (8.3 to 9.3 s).

Assuming the same mixing time as Russell et al. [220] and Collins et al. [37] of 1.5 s, its ratio to the scan constant varied from 0.012 to 0.036 for the experimental results in this chapter. Although this range is at the lower end of the 0.035 to 0.345 range tested by Collins et al. [37] for the SMPS, they still observed a slight broadening of the distribution at 0.035 due to flow mixing downstream of the DMA. Therefore, it is unlikely this downstream flow effect had any appreciable impact on the measurements of the scanning AAC in this work. However, this effect still manifested in the variation of the delay times corresponding to the PSL measurements.

This result supports the conclusion of Collins et al. [36] that the delay time determined by the UDA approach masks the smearing effects of the downstream flow and thus deviates from the true delay time. If the downstream plumbing is minimized, the mixing time in the detector usually dominates and varies significantly between different detectors [220, 37]. Therefore, the delay time for the scanning AAC must be determined for any significant change in the scanning constant (τ_{sc}), downstream plumbing, flow rate or particle detector. This requirement could be relaxed in the future by following similar approaches as those previously discussed (i.e. Russell et al. [220], Collins et al. [37], Kanaparthi et al. [118]) and accounting for the smearing effects of the flow downstream of the AAC within or before the data inversion. However, similar to the viscous flow effects in the classifier, additional testing is required with AAC scans significantly faster than those in this work to amplify these flow effects and investigate their impact on the measurements. Computation fluid dynamic (CFD) simulations would also be valuable to verify the transfer function of the scanning AAC and capture the smearing effects from non-uniform axial flows, as well as the flow effects from the classifier inlet and outlet geometries.

4.7 Conclusions

To accelerate size distribution measurements using the AAC, this chapter develops the theory to continuously scan, rather than step, the AAC setpoint upstream of a particle detector. This theory shows that if the angular speed of the AAC is varied following an exponential function, the proportional change in the centrifugal force field over the residence time of particles in the classifier is independent of their inlet time. Based on this speed profile and assuming uniform axial flow, the transfer function of the scanning AAC is derived by limited trajectory theory and found to be the same shape as that of the steady-state AAC. This outcome is used to adapt the parameterized transfer function of the steady-state AAC based on particle streamline theory, which accounts for non-idealized particle and flow behaviours within the classifier, to the scanning AAC. For both forms of the transfer function, the effect of the counting time of the particle detector downstream of the scanning AAC is quantified by determining the average transfer function over this time. The inversion of these average transfer functions is then determined, and the inversion parameter based on particle streamline theory and assuming uniform axial flow is found to be the same for either the steady-state or scanning AAC.

This scanning theory and its implementation are validated by the high agreement of the experimental results. Specifically, the high agreement (11.3% or better in terms of CMD, GSD and N_{tot}) of the measurements of the scanning AAC compared to those of the steady-state AAC of three different aerosol sources (DOS, NaCl and soot) with varying GSDs (1.3 to 2.7) and CMDs (66.4 nm to 292.1 nm). If the stability of the aerosol source is considered, the agreement between the stepping and scanning measurements using the AAC improves to 2.0% or better. This validation is further supported by the high agreement (within 8.7%) of scanning measurements of PSL particles (six sizes between 100 nm to 2.02 µm).

For the experimental results shown in this chapter, the measurements of the scanning AAC were 1.1 to 2.6 times faster and collected at 6.1 to 9.0 times higher CPD than those of the stepping AAC. This approach also leverages the high transmission efficiency and true monodispersity of the particles classified by the AAC. As a result, the measured distribution does not need to be corrected for multiply-charged particles, unlike those measured by electrostatic instruments, such as the SMPS or ELPI.

However, the minimum scan time of the AAC is limited by the acceleration/deceleration its classifier can achieve. Therefore, when measuring a similar size range (approximately 30 to 700 nm), the up, down or combined scan of the AAC is 3.2, 2.0 and 1.8 times longer, respectively, than the equivalent, standard SMPS scan, while at a similar or higher CPD (64 vs 49 or 196). One key advantage of the scanning AAC is the broad range and upper limit of its particle sizing, scanning in ten minutes or less from approximately 30 to 2900

nm at low-flow and from approximately 200 to 6800 nm at high-flow. To further accelerate these measurements, future work could investigate if the transfer function of the AAC can be determined if the classifier is scanned at the maximum acceleration rather than scanned exponentially. However, it is likely that an analytical solution for this approach is not possible, and numerical methods would need to be used, significantly complicating the inversion process.

For typical AAC scans across broad size ranges, the assumption of uniform axial flow is likely valid given the maximum acceleration and deceleration the classifier can achieve. However, future work is required to consider the viscous flows within the classifier and downstream plumbing/detector, and as the scan time is reduced, quantify the smearing of the particle residence and detection times.

Chapter 5

Measuring the Bipolar Charge Distribution of Spherical Particles

5.1 Introduction

This chapter[1] addresses Objective 2a and develops the AAC methodology to measure the bipolar charge distribution of spherical particles by using an AAC and DMA in tandem. This new approach overcomes some significant limitations of previous methodologies used for the same purpose, which are primarily based on electrostatic classification techniques (as summarized in Section 2.3). Similar to the most common approach of using a TDMA, the AAC-DMA system can determine the size-resolved charge fractions over a broad range of particle sizes with high statistical confidence compared to the previously described trajectory or deposition methods. The AAC-DMA system improves on the TDMA approach by leveraging the classification properties of the AAC. As established in Chapter 3, the AAC transmission efficiency is 2.6 to 5.1 times higher than a neutraliser-DMA system and produces a truly monodispersed aerosol independent of particle charge state [240], thus avoiding any multiple charging artefacts introduced during electrostatic classification.

Also since the AAC does not require the particles to be charged during classification, the charge fractions from an aerosol source can be directly measured using the same approach and data inversion by simplify bypassing the candidate charger. This aspect of the AAC also allows uncharged particles to be easily generated by using an ESP in tandem. In contrast, methodologies with upstream electrostatic classification (such as the TDMA) require the aerosol to be charged, classified, re-neutralised and then passed through an ESP, thus significantly reducing the concentration of the classified, uncharged particles. Therefore,

[1] This chapter is based on an article by Johnson et al. [106] published by Elsevier in the Journal of Aerosol Science on 07/02/2020, available online: https://doi.org/10.1016/j.jaerosci.2020.105526.

relative to the TDMA approach, the AAC-DMA system has a higher measurement signal across a larger range of particle sizes from the same aerosol source, and thus, can resolve more particle charge states.

5.1.1 Outline of chapter

To recognize these advantages and enhance measurements of bipolar charge distributions, this work develops the methodology to operate the AAC and DMA in tandem. This approach is then used to measure the charge fractions of 40 to 596 nm spherical particles neutralised by a new ^{85}Kr, old ^{85}Kr or x-ray neutraliser. The effects on the charge fractions of the particles using different sample flow rates (0.6 L/min or 1.2 L/min) and ions escaping from the neutraliser outlet are also investigated. For all of these cases, the resulting bipolar charge fractions are compared with those from widely-utilized charging theory. While this chapter focuses on bipolar charge distributions, the AAC development currently highlighted could also characterise the charging of particles with low charge states (i.e. 10 or less) produced by mechanisms other than bipolar charging.

5.2 Experimental setup

5.2.1 Simplified experimental setup

To simplify the description of this new methodology, the minimum experimental setup required to characterise particle charging fractions produced by a candidate charger[2] using a tandem AAC-DMA system is first discussed, as shown in Figure 5.1. An Aerodynamic Aerosol Classifier (AAC; Cambustion Ltd., Cambridge, UK), at a constant setpoint, is used to select a narrow range of particle aerodynamic diameters from a polydispersed aerosol. The aerodynamically monodispersed aerosol is then electrically charged by passing it through the candidate charger. The sample flow is then passed through an electrostatic precipitator (ESP). At a high voltage (V_{ESP}), the ESP captures any charged particles in the aerosol sample by generating a sufficiently large electric field to induce an electrostatic force on the charged particles that dominates their motion. This force causes the charged particles to be captured by the electrodes of the ESP, while allowing the uncharged particles to pass through unaffected.

The ESP outlet is directly connected to either the DMA classifier inlet (flow path A) or the condensation particle counter (CPC, Agarwal and Sem [8]) inlet (flow path B) depending

[2]This experimental setup can also be used to characterise the particle charging fractions produced by aerosol generation methods by removing the candidate charger from the setup.

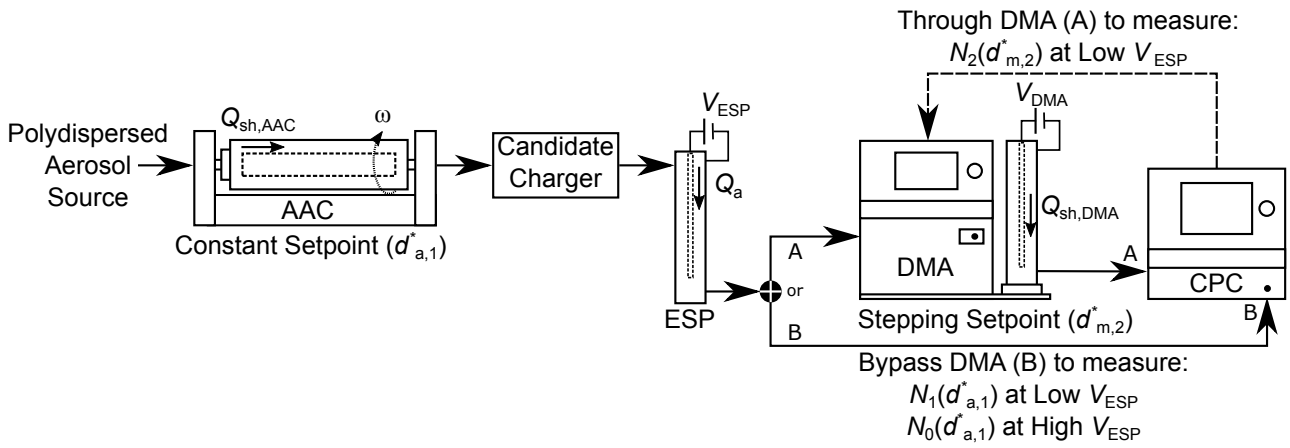

Fig. 5.1 Minimum experimental setup required to characterise the aerosol charge distribution generated by a candidate charger using a tandem AAC-DMA system (for explanation purposes only).

on the desired measurement[3]. The different particle electrical mobilities produced by each charge state are resolved using flow path A by stepping the DMA voltage (i.e. a step-scan) and measuring the particle number concentration ($N_2(d^*_{m,2})$) at each DMA mobility setpoint using the downstream CPC. It should be noted that the DMA is operated without its standard neutraliser.

To determine both the negative and positive charge fractions of the particles, a positive or negative polarity DMA voltage is utilized, respectively. At the start and end of each DMA step-scan, the sample is switched to flow path B and the ESP is operated at low or high voltage (order of single volts and multiple kilovolts, respectively), while the downstream CPC quantifies the number concentrations of all of the particles ($N_1(d^*_{a,1})$) or those which are uncharged ($N_0(d^*_{a,1})$), respectively. The high ESP voltage setting is determined by the potential difference required to capture all of the charged particles, while remaining a safe margin below the electrical breakdown voltage between the inner and outer electrodes. When measuring $N_2(d^*_{m,2})$ and $N_1(d^*_{a,1})$ the AAC classified particles are still passed through the ESP with a low voltage to avoid changes in particle losses from impaction and diffusion within the ESP, while capturing any ions that escape from the candidate charger.

5.2.2 Actual experimental setup

The actual experimental setup used to characterise the particle charging fractions produced by each candidate charger is shown in Figure 5.2. This test setup builds on the methodol-

[3]To switch between flow path A and flow path B, the conductive tubing is physically moved to avoid changes in particle losses in the sampling lines, for example via valves or other flow-switching devices.

ogy previously described for the minimum experimental setup (i.e. Figure 5.1) to address additional testing considerations. To avoid any particle charge developed during aerosol generation interfering with the charge states produced by the candidate charger [100], an ESP was used upstream of the AAC (ESP 1) to first establish an uncharged particle source. The high transmission efficiency of the AAC (previously quantified in Section 3.4) helped compensate for the charged portion of polydispersed aerosol captured by ESP 1. ESP 1 was a custom instrument, while ESP 2 was a commercial device (Cambustion Ltd). Other instrumentation was also utilized in parallel to further characterise the aerosol. The results from this other instrumentation will be discussed in future studies.

To meet the sample flow requirements of this setup, HEPA filtered compressed air (i.e. make-up air) was added downstream of the AAC using a mass flow controller (Alicat Scientific, Tucson, AZ, USA). This flow arrangement allowed the AAC to be operated where its transfer function had been previously characterised, as summarized in Chapter 3 (i.e. at 0.3 and 3 L/min sample and sheath flows, respectively).

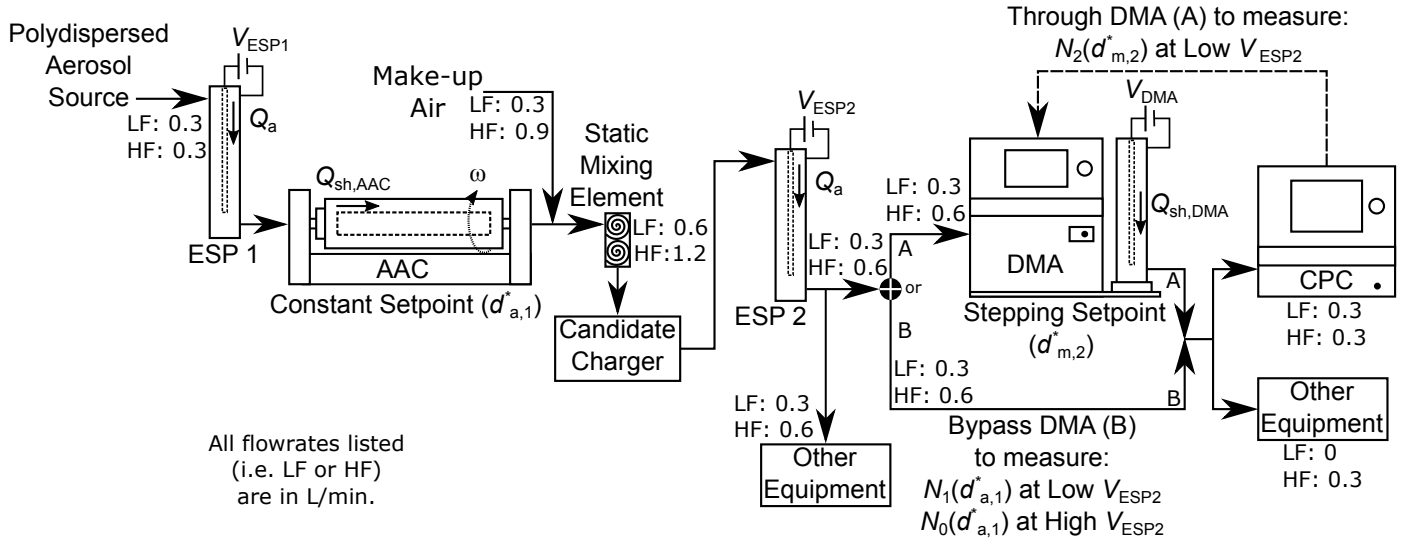

Fig. 5.2 Actual experimental setup used by this work to characterise the aerosol charge distribution generated by the candidate charger using the tandem AAC-DMA system.

Due to the challenges of developing a new methodology and instrument availability, this research was completed as two separate experimental campaigns. This approach allowed the AAC-DMA inversion process to be developed and validated between the campaigns, and a more complete dataset to be collected. The first and second campaign took place from November to December 2017 and February to March 2019, respectively, and studied the particle charging produced with sample flow rates of 1.2 L/min (high flow- HF) and 0.6 L/min

(low flow- LF) through the candidate chargers, respectively. The exact same equipment and configuration were utilized for both campaigns with some minor exceptions. The first campaign used a Collison nebulizer (BGI Inc., Waltham, MA, USA), a 3080 Electrostatic Classifier with a 3081 DMA (TSI Inc., Shoreview, MN, USA) and a 3776 CPC (TSI Inc.), while the second campaign utilized a custom 1-jet impaction nebulizer, a 3082 Electrostatic Classifier with a 3081 DMA (TSI Inc.) and a 3752 CPC (TSI Inc.). To produce the low flow condition, the second campaign removed the other equipment sampling in parallel to the CPC and lowered the sample flow rate of the additional equipment sampling in parallel at the outlet of ESP 2 from 0.6 L/min to 0.3 L/min.

5.2.3 Aerosol sources

The polydispersed aerosol was generated at several litres per minute by atomizing pure DOS (di-octyl sebacate) using a Collison nebulizer (BGI Inc.), custom 1-jet impaction nebulizer or TSI 9302 constant output nebulizer (TSI Inc.). Similar to the testing for the steady-state AAC (i.e. Section 3.2.3), the TSI constant output atomizer was operated with a 6 ml/hr supply of DOS using a syringe pump (Harvard Apparatus Holliston, MA, USA: Model 22) to produce a smaller size distribution. This atomization setup was only used to collect the 40 nm setpoint of the charging data. After atomization a liquid trap was used to remove excess liquid, then a rotating disk diluter (Cambustion Ltd.) was used control the particle concentration to ensure $N_2(d^*_{\mathrm{m},2})$, $N_1(d^*_{\mathrm{a},1})$ and $N_0(d^*_{\mathrm{a},1})$ were measured in the same CPC measurement mode (i.e. below the coincidence correction modes of the 3776 and 3752 CPCs). Since the experimental system only required 0.3 L/min, two spills (at slightly below atmospheric pressure) were used, one upstream and the other downstream of the rotating disk diluter, to extract the flow differences.

When initially switching between flow path A and B during the first campaign, it was discovered that the particle allocation between different sample paths (such as DMA/CPC vs other instrumentation) was a function of the tube positions. This effect was due to inadequate mixing between the make-up air and AAC-classified particles despite the combined flows passing through significant tube lengths (approximately 58 cm of 6 mm conductive tubing) and components (Candidate Charger and ESP 2) before being subdivided. Passing the combined sample through a static mixing element made of metal overcame this effect. For more details regarding this effect, refer to Walker et al. [260]. To avoid uneven particle losses, all of the aerosol sample paths had the same flow rates and tube lengths.

5.2.4 Test matrix and candidate chargers

The first campaign measured the particle charging fractions at seven different AAC aerodynamic diameter setpoints ($d^*_{a,1}$), spaced logarithmically between 40 to 596 nm. Due to the larger particles produced by the Collison nebulizer, the 60 nm setpoint at high-flow was originally the smallest size characterised during the first campaign. However later in the same campaign, this test range was expanded down to 40 nm by switching from the Collison nebulizer to the TSI constant output atomizer. Both atomization methods were also utilized in the second campaign (i.e. low-flow measurements), and thus the 60 nm point was not included in these measurements.

The 596 nm upper limit was determined by the maximum mobility setpoint of the DMA[4], while the 40 nm lower limit was determined by the polydispersed aerosol size distribution. If an aerosol source with a smaller distribution was used, the 25 nm AAC lower setpoint limit[5] would become the limiting factor. At each AAC aerodynamic diameter setpoint ($d^*_{a,1}$), at least two scans stepping both a positive and negative DMA classifier voltage were completed. To limit aerosol source and system instabilities affecting the results, a step-scan was only accepted if the $N_1(d^*_{a,1})$ and $N_0(d^*_{a,1})$ measurements before and after each step-scan agreed within 10%.

To validate the AAC-DMA inversion and particle charge fraction measurements, this work used a new[6] ^{85}Kr 10 mCi radioactive bipolar charger (TSI Inc.: Model 3077A) as the candidate charger. Similarly, DOS particles were selected as the polydispersed aerosol source due to their spherical morphology and known density (914 kg/m^3). These results were then compared against charge fractions of particles produced by an old[7] ^{85}Kr 10 mCi radioactive bipolar charger (TSI Inc.: Model 3077A) and x-ray bipolar charger (TSI Inc.: Model 3087). Unless otherwise stated, all ^{85}Kr neutralisers tested included the insert installed in the charger inlet, as recommended by TSI, to promote charging the aerosol to a steady-state charge distribution [248].

[4] Accounting for the need for the DMA to step across the width of the AAC transfer function, i.e. above and below the largest and smallest AAC setpoint used, respectively.

[5] It is important to note that this lower limit is in terms of particle aerodynamic diameter. Therefore, as the particle density increases, the equivalent mobility diameter selected by the AAC decreases. For example, a 25 nm aerodynamic diameter particle with a density of 2000 kg/m^3 in air at standard conditions has a mobility diameter of 12.9 nm.

[6] The isotope reference date of the charger was within 6 months of testing.

[7] The isotope reference date of the charger was more than one half-life (i.e. 10.756 years) from testing.

5.3 Theory

5.3.1 Tandem AAC-DMA convolution

To determine the fractions of total particles at each charge state, the likelihood that the particles pass through each classifier must be considered. Chapter 3 of this work and Karlsson and Martinsson [120] demonstrated that the AAC and DMA transfer functions (Ω), respectively, can be represented by a triangle when operated with balanced flows[8]:

$$\Omega = \lambda_\Omega \frac{\mu_\Omega^2}{2\beta}\left[\left|\tilde{x} - \left(1+\frac{\beta}{\mu_\Omega}\right)\right| + \left|\tilde{x} - \left(1-\frac{\beta}{\mu_\Omega}\right)\right| - 2|\tilde{x}-1|\right] = \lambda_\Omega\,\Omega_\mathrm{B}, \tag{5.1}$$

where $\tilde{x}$ is the non-dimensional[9] particle relaxation time ($\tilde{\tau}$) or electrical mobility ($\tilde{Z}_\mathrm{p}$) domain for the AAC or DMA transfer function, respectively. The idealized transfer function width is quantified by the non-dimensional classifier flow parameter β, which is the ratio of the classifier sample flow (Q_a) to sheath flow (Q_sh) for balanced flow operation. Non-ideal particle behaviour within either classifier, such as losses due to impaction and broadening of the transfer function due to diffusion, is quantified by the transmission efficiency (λ_Ω, with a value between 0 and 1) and transfer function width factor (μ_Ω) determined experimentally by Karlsson and Martinsson [120] for the DMA and in Section 3.4 for the AAC. The transmission efficiency scales the area under the transfer function (i.e. Ω scales linearly with λ_Ω), while the width factor scales the full width at half maximum (FWHM) of the transfer function. Therefore, the transfer functions of either the AAC or DMA considering broadening only can be described by Ω_B as shown in Equation 5.1.

Utilizing these transfer functions within the tandem AAC-DMA inversion, the theoretical particle number concentration ratio between upstream ($N_1(d^*_{\mathrm{a},1})$) and downstream ($N_2(d^*_{\mathrm{m},2})$) of the DMA can be predicted by:

$$\frac{N_2(d^*_{\mathrm{m},2})}{N_1(d^*_{\mathrm{a},1})} = \frac{\sum_{n=n_\mathrm{min}}^{n_\mathrm{max}} \int \eta\,\Omega_\mathrm{AAC}\,f_n\,\Omega_{\mathrm{DMA},n}\,\mathrm{d}d_\mathrm{m}}{\int \eta\,\Omega_\mathrm{AAC}\,\mathrm{d}\tau}, \tag{5.2}$$

where η is the counting efficiency of the particle counter as a function of particle size, f_n is the fraction of particles with n elemental charges, and n_min and n_max are the minimum and

[8] The classifier sheath inlet and outlet flows are the same, and the classifier sample inlet and outlet flows are also the same.

[9] The particle property divided by the classifier setpoint (i.e. centroid of transfer function), AAC with setpoint τ^*: $\tilde{\tau} = \frac{\tau}{\tau^*}$, DMA with setpoint Z^*_p: $\tilde{Z}_\mathrm{p} = \frac{Z_\mathrm{p}}{Z^*_\mathrm{p}}$.

maximum charge states considered, respectively. While this equation correctly considers the fraction of particles with no charge (i.e. f_0), these particles do not pass through the DMA (i.e. $\Omega_{\mathrm{DMA},0} = 0$), and thus have no effect on the particle number concentration ratio (N_2/N_1). Furthermore, since the AAC produces a monodispersed aerosol [240], the non-ideal particle behaviour within the DMA is approximately constant and independent of its mobility setpoint (i.e. only a function of the AAC setpoint, $\lambda_{\Omega,\mathrm{DMA}}(d^*_{\mathrm{a},1})$ and $\mu_{\Omega,\mathrm{DMA}}(d^*_{\mathrm{a},1})$).

To calculate the integral in the numerator of Equation 5.2, the AAC and DMA transfer function must be converted to the same particle property domain. Particle mobility diameter was chosen as the common domain, as this particle property is the main consideration for transfer function broadening and losses due to diffusion, thereby limiting iterative effects within the AAC-DMA inversion process. Both the AAC and DMA transfer functions can be converted to the particle mobility domain (d_{m}) by iteratively solving the following relationship[10]:

$$d_{\mathrm{m}} = \sqrt{\frac{18\tau\mu}{C_c(d_{\mathrm{m}})\rho_{\mathrm{eff}}}} = \frac{neC_c(d_{\mathrm{m}})}{3\pi\mu Z_{\mathrm{p}}}, \tag{5.3}$$

where τ is the particle relaxation time selected by the AAC, μ is the surrounding gas viscosity, C_c is the Cunningham slip correction, ρ_{eff} is the particle effective density, e is the elemental charge (1.60×10^{-19}C), and Z_{p} is the particle electrical mobility selected by the DMA.

Substituting Equation 5.1 into Equation 5.2 and assuming the particle charge fractions (f_n) and counting efficiency (η) are constant over the width of the AAC transfer function, and that the AAC and DMA transmission efficiencies ($\lambda_{\Omega,\mathrm{AAC}}$ and $\lambda_{\Omega,\mathrm{DMA}}$) are constant over the widths of their respective transfer functions, Equation 5.2 simplifies to:

$$\frac{N_2(d^*_{\mathrm{m},2})}{N_1(d^*_{\mathrm{a},1})} = \lambda_{\Omega,\mathrm{DMA}} \frac{\sum_{n=n_{\min}}^{n_{\max}} f_n \int \Omega_{\mathrm{B,AAC}}\, \Omega_{\mathrm{B,DMA},n}\, \mathrm{d}d_{\mathrm{m}}}{\int \Omega_{\mathrm{B,AAC}}\, \mathrm{d}\tau}. \tag{5.4}$$

This simplification demonstrates that the measured ratio of particle number concentrations (N_2/N_1) is independent of the AAC transmission efficiency ($\lambda_{\Omega,\mathrm{AAC}}$). It also highlights that the particle charge fractions (f_n) scale inversely with the DMA transmission efficiency ($\lambda_{\Omega,\mathrm{DMA}}$). To account for the difference between the actual and theoretical/idealized DMA transmission efficiency ($\lambda_{\Omega,\mathrm{DMA}}$ and $\lambda_{\Omega,\mathrm{DMA,I}}$, respectively) an array of constants ($f_{n,\mathrm{I}}$) is assigned as follows:

$$f_n\, \lambda_{\Omega,\mathrm{DMA}} = f_{n,\mathrm{I}}\, \lambda_{\Omega,\mathrm{DMA,I}}. \tag{5.5}$$

[10]This relationship is a rearranged variation of a subset of Equation 1.1, which is based on Hinds [84].

The theoretical/idealized DMA transmission efficiency ($\lambda_{\Omega,\mathrm{DMA,I}}$) was estimated following Karlsson and Martinsson [120]. Utilizing Equations 5.3 to convert the transfer functions to the particle mobility diameter domain, and substituting Equation 5.5 into Equation 5.4 gives:

$$\frac{N_2(d^*_{\mathrm{m},2})}{N_1(d^*_{\mathrm{a},1})} = \lambda_{\Omega,\mathrm{DMA,I}} \quad \frac{\sum_{n=n_{\min}}^{n_{\max}} \boldsymbol{f_{n,\mathrm{I}}} \int \Omega_{\mathrm{B,AAC}}\, \Omega_{\mathrm{B,DMA},n}\, \mathrm{d}d_{\mathrm{m}}}{\int \Omega_{\mathrm{B,AAC}}\, \mathrm{d}\tau}, \tag{5.6}$$

where in the numerator $\Omega_{\mathrm{B,AAC}}$ is a function of $d_{\mathrm{m}}(\tau, \boldsymbol{\rho_{\mathrm{eff}}}, \mu)$, β_{AAC} and $\boldsymbol{\mu_{\Omega,\mathrm{f}}} \cdot \mu_{\Omega,\mathrm{AAC}}$, and $\Omega_{\mathrm{B,DMA},n}$ is a function of $d_{\mathrm{m}}(Z_{\mathrm{p}}, n, e, \mu)$, β_{DMA} and $\mu_{\Omega,\mathrm{DMA}}$. The transfer function broadening for the DMA ($\mu_{\Omega,\mathrm{DMA}}$) and AAC ($\mu_{\Omega,\mathrm{AAC}}$) was estimated following Birmili et al. [19] and Section 3.4.2, respectively. The **emboldened fitting parameters** shown in Equation 5.6 and summarized in Table 5.1 indicate the parameters used to fit the theoretical tandem AAC-DMA convolution to the experimental particle number concentration results (N_2/N_1) using least-squares minimization. Therefore, the degrees of freedom in the tandem AAC-DMA inversion were the number of charge states considered, neglecting the uncharged fraction, plus two (i.e. ρ_{eff} and $\mu_{\Omega,\mathrm{f}}$). For example, the 40 and 596 nm particles had 4 and 14 degrees of freedom within the inversion, respectively, and were fitted using 25 and 54 points on average, respectively. This inversion process was started using initial guesses. For example, the initial guesses used for the tandem AAC-DMA inversion characterising DOS particles with a 78 nm AAC aerodynamic diameter setpoint (i.e. 84 nm mobility diameter) were ρ_{eff} equals 914 kg/m^3, $\mu_{\Omega,\mathrm{f}}$ equals 1 and $f_{n,\mathrm{I}}$ equals 0.17%, 4.11%, 27.12%, 20.71%, 2.31%, 0.08% for charge states -3 to -1 and +1 to +3, respectively.

As listed in Table 5.1, these and all other initial guesses for $f_{n,\mathrm{I}}$ (i.e. the particle charge fractions neglecting the deviations between the actual and theoretical DMA transmission efficiency) were determined based on the charging models of Wiedensohler [266] and Gunn and Woessner [75]. Following standard practice, such as for SMPS measurements [247, 249], Wiedensohler [266] was used to estimate the charge fractions of particles with two or less absolute charge states, while Gunn and Woessner [75] was used to estimate the charge fractions of particles with three or more absolute charge states. For consistency between these bipolar charging models and also following standard practice [247, 249], the positive to negative ion mobility ratio of 0.875 was used with the charging model of Gunn and Woessner [75]. While both of these bipolar charging models assume an equal concentration of positive and negative ions, the charging model of Gunn and Woessner [75] does not consider the mass of the ions, unlike the charging model of Wiedensohler [266].

Table 5.1 Parameters used to fit the theoretical convolution of the tandem AAC-DMA to the experimental results.

Parameter	Effect on Fit	Implementation	Initial Guess
$f_{n,\mathrm{I}}$	Amplitude	Independent parameter for each charge state	Following Wiedensohler [266] and Gunn and Woessner [75]
$\mu_{\Omega,\mathrm{f}}$	Width	Constant parameter across all charge states	1 (i.e. ideal agreement)
ρ_{eff}	Horizontal location*	Constant parameter across all charge states	DOS†: ρ_{eff}=914 kg/m^3

*The position of the aerodynamically classified particles in the particle mobility diameter domain.
†The DOS particles have a spherical morphology, and thus have a constant effective density (i.e. independent of their size)

To maintain the independence of the fitting parameters, the width fit parameter ($\mu_{\Omega,\mathrm{f}}$) could only be applied through one of the two classifier transfer functions. For example, a DMA and an AAC operating in tandem with broad and narrow transfer functions, respectively, could have the same overlap between their transfer functions (i.e. area under the tandem AAC-DMA transfer function) as ones operating with narrow and broad transfer functions, respectively. The width fit parameter was applied through the AAC rather than the DMA transfer function due to the higher variability in the width of the AAC transfer function across its setpoint range, as previously shown in Figure 3.4b. However, since the width of both the AAC and DMA transfer functions affect their overlap, the fitted $\mu_{\Omega,\mathrm{f}}$ captures the combined deviation of the actual AAC and DMA transfer function widths from their expected values previously determined in Chapter 3 and by Birmili et al. [19], respectively.

5.3.2 Determining the particle charge fractions

To satisfy physical constraints, the particle charge fractions (f_n), including the uncharged fraction (f_0), must sum to one as follows:

$$f_0 + \sum_{n=n_{\min}}^{-1} f_n + \sum_{n=1}^{n_{\max}} f_n = 1. \tag{5.7}$$

After applying the convolution fit to the experimental data (i.e. determining $f_{n,\mathrm{I}}$ values using Equation 5.6), the actual DMA transmission efficiency can be found by isolating f_n in Equation 5.5, substituting it into Equation 5.7 and rearranging as follows:

$$\lambda_{\Omega,\mathrm{DMA}} = \frac{\lambda_{\Omega,\mathrm{DMA,I}}\left[\sum_{n=n_{\min}}^{-1} f_{n,\mathrm{I}} + \sum_{n=1}^{n_{\max}} f_{n,\mathrm{I}}\right]}{1-f_0}. \tag{5.8}$$

Finally, the charge fraction (f_n) at each n charge state, accounting for the actual DMA transmission efficiency, can be found by substituting Equation 5.8 into Equation 5.5 and rearranging as follows:

$$f_n = f_{n,\mathrm{I}} \frac{1-f_0}{\sum_{n=n_{\min}}^{-1} f_{n,\mathrm{I}} + \sum_{n=1}^{n_{\max}} f_{n,\mathrm{I}}}. \tag{5.9}$$

The uncharged fraction (f_0) does not need to be corrected for the actual DMA transmission efficiency as it is measured without passing through the DMA classifier as follows:

$$f_0 = \frac{N_0(d^*_{\mathrm{a},1})}{N_1(d^*_{\mathrm{a},1})}. \tag{5.10}$$

5.4 Tandem AAC-DMA convolution

An example of the convolution theory (dashed line calculated using Equation 5.6 with the initial guesses summarized in Table 5.1) and convolution fit (solid line) to the experimental tandem AAC-DMA results (circles) at each of the first campaign's seven AAC aerodynamic diameter setpoints ($d^*_{\mathrm{a},1}$) is shown in Figure 5.3. The two colours of series depict the positively and negatively charged particle results. The convolution fits for the high-flow conditions through the charger (i.e. campaign 1) are shown due to the higher discrepancies between the convolution initial guesses (dashed line) and convolution fit (solid line) than the low-flow conditions (i.e. campaign 2), as well as having one additional AAC setpoint (i.e. 60 nm). This higher discrepancy, which is likely due to the particles not reaching a steady-state charge distribution as discussed later in detail, highlights the ability of the convolution fit (solid line) to capture the experimental results (circles). These results also demonstrate the ability of the tandem AAC-DMA system to resolve up to 13 charge states (i.e. each as a separate peak) across a wide range of particle sizes (40 to 596 nm) from the same aerosol source. The peaks become closer together as the particle charge state increases as each increment in charge state is smaller in proportion to its overall charge state and resulting electrical mobility.

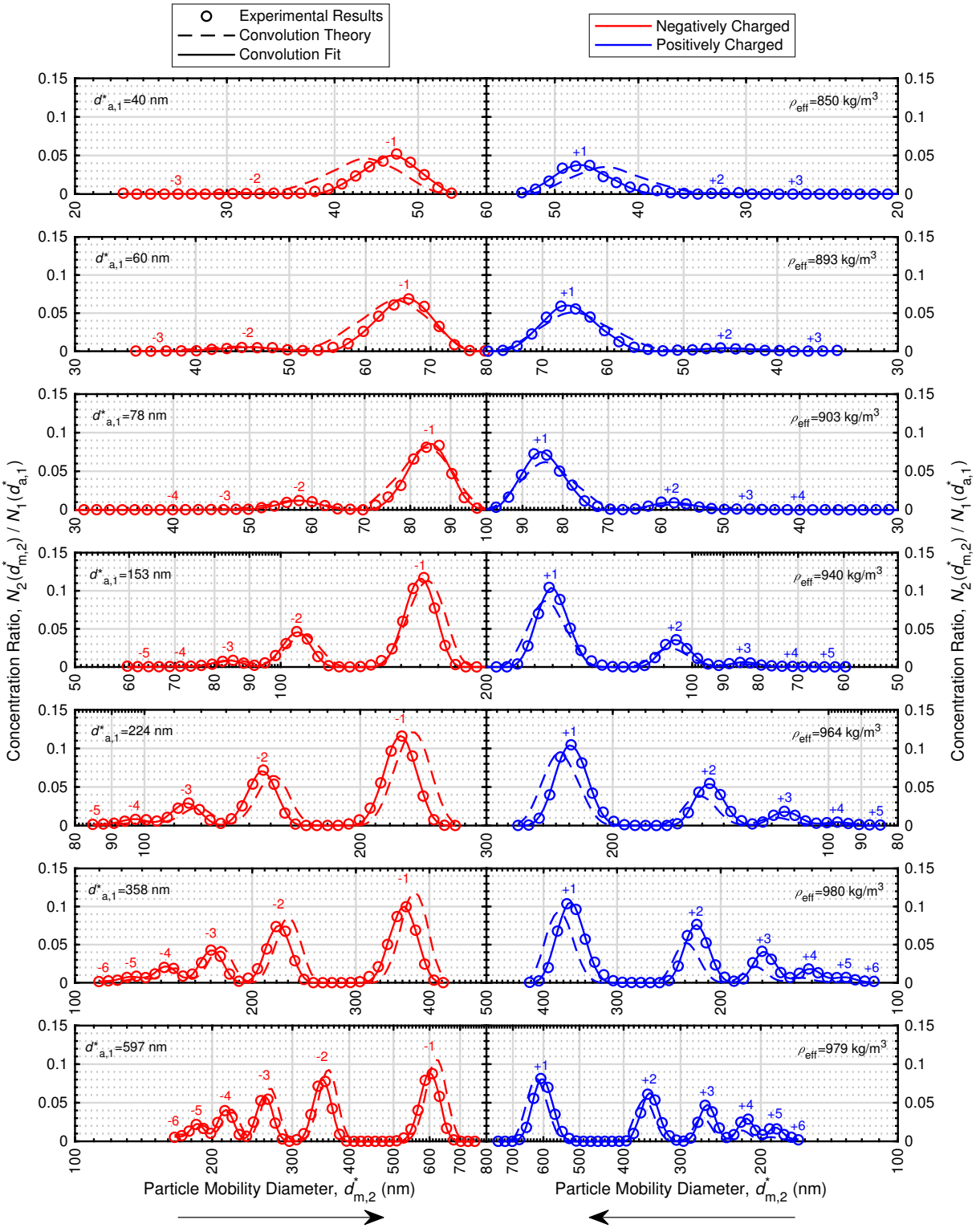

Fig. 5.3 Tandem AAC-DMA experimental measurements at high-flow (i.e. Campaign 1) compared to the theoretical convolution (i.e. initial guesses) and fitted convolution.

5.5 Experimental validation of tandem AAC-DMA

The particle charge fractions measured at low-flow (0.6 L/min) through the new ^{85}Kr charger by the tandem AAC-DMA system at one AAC aerodynamic diameter setpoint (224 nm) are shown in Figure 5.4. These measured charge fractions were highly repeatable[11], within 0.012, as depicted by the vertical error bars. Furthermore, these results predominantly agree within their repeatability limits with the theoretical charge fractions estimated following Wiedensohler [266] and Gunn and Woessner [75] as previously outlined in the Section 5.3.1.

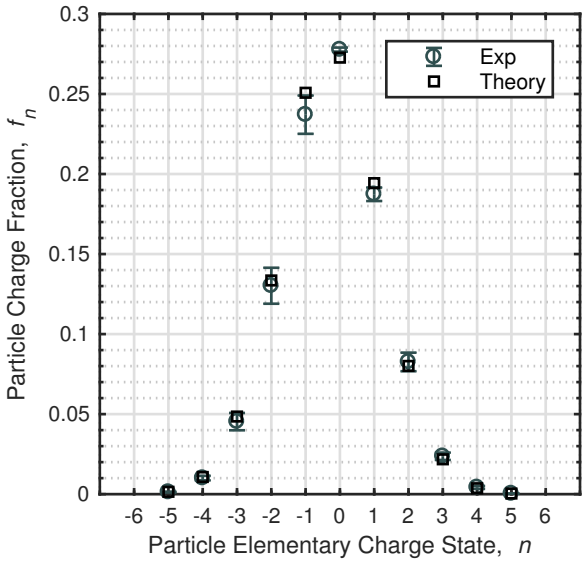

Fig. 5.4 95% confidence interval of charge fractions measured by the tandem AAC-DMA system for particles with 224 nm aerodynamic diameters compared to theory [266, 75].

The particle charge fractions measured at low-flow (0.6 L/min) through the new ^{85}Kr charger by the tandem AAC-DMA system at six different particle sizes (i.e. average of at least three step-scans for both particle polarities at each AAC aerodynamic setpoint) are shown in Figure 5.5. The high agreement between the measured and theoretical charge fractions (charge fraction differences within -0.022 to 0.023) validate this new methodology with an average absolute difference of 0.007.

The average percent differences for the other fitting parameters of the tandem AAC-DMA convolution relative to theory at the low-flow charger conditions are shown in Figure 5.6. The largest measured percent difference in particle effective density was 9.45%. This maximum

[11] Based on a 95% confidence interval (CI) using a t-distribution and the measurement repeatability of at least five positive and negative DMA classifier voltage step-scans.

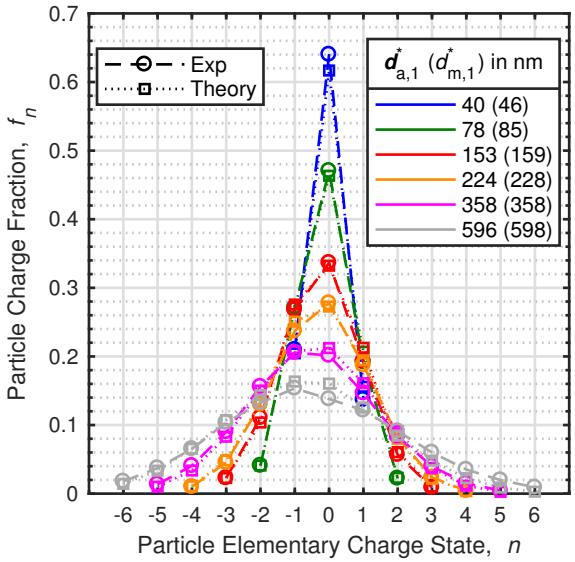

Fig. 5.5 Particle charge fractions measured at low-flow by the tandem AAC-DMA system compared to theory [266, 75].

density disagreement agrees within the estimated uncertainty of 11.5% in the particle effective density measured by the tandem AAC-DMA system, which was determined by propagating[12] the previously determined accuracies of 3% for the DMA [129] and 4.7% for the AAC [105].

With the exception of one data point, the DMA transmission efficiency ($\lambda_{\Omega,\mathrm{DMA}}$) calculated from the convolution fit (i.e. Equation 5.8) also agrees within 10% of the expected values previously determined by Karlsson and Martinsson [120] experimentally. These expected values also account for particle losses due to diffusion during DMA classification, which becomes more significant as particle size decreases [120]. Therefore, as expected the largest DMA transmission efficiency deviation (15.4%) is at the smallest particle size (i.e. 40 nm), and the remaining percent differences decrease as particle size increases before stabilizing above 150 nm.

As previously discussed, since the width of both the AAC and DMA transfer functions affect their overlap (i.e. the area under the tandem AAC-DMA transfer function), fitting the transfer function width parameter ($\mu_{\Omega,\mathrm{f}}$) within the theoretical AAC transfer function captures the combined deviation of the actual AAC and DMA transfer function widths from the expected values previously determined in Chapter 3 and by Birmili et al. [19], respectively.

[12] Neglecting the effects of the Cunningham Slip Correction, the uncertainty (u) in the effective density is $u_{\rho_{\mathrm{eff}}}/\rho_{\mathrm{eff}} = \sqrt{4(u_{d_\mathrm{a}}/d_\mathrm{a})^2 + 4(u_{d_\mathrm{m}}/d_\mathrm{m})^2}$.

The broadening of these transfer functions is also a strong function of particle diffusion, which becomes more dominant as particle size decreases, as previously shown in Figure 3.4b. The percent difference from theory in the tandem classifier broadening varies by 8% to 13% at the smaller particle sizes and decreases to within 5% at the larger particle sizes. This progression generally agrees with the expected transfer function broadening trend caused by particle diffusion.

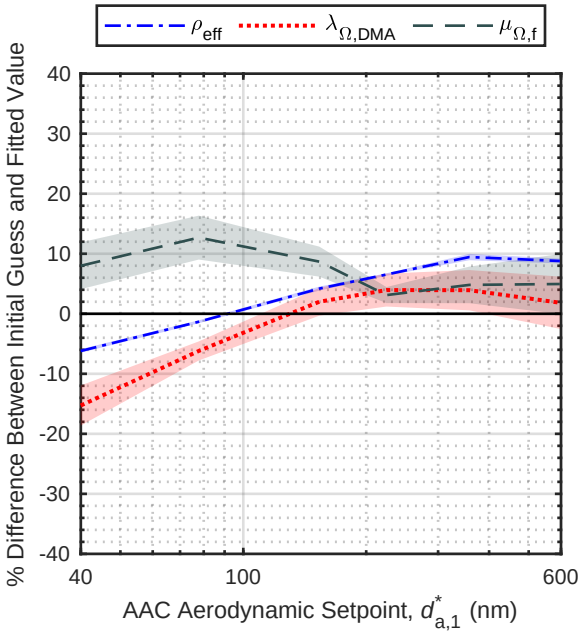

Fig. 5.6 Differences between theory (as described in Table 5.1) and fitted values of the tandem AAC-DMA inversion at low-flow conditions. Each shaded area represents the repeatability of the corresponding fitted parameter, assuming a t-distribution and 95% confidence interval.

The agreement of the convoluted parameters, such as particle density and charge fractions, as well as the classifier transfer function broadening and transmission efficiency, with expected values further demonstrates the ability of the tandem AAC-DMA system to accurately measure multiple parameters simultaneously.

5.6 Effects of flow rate on particle charge fractions

At high-flow conditions (1.2 L/min) through the new ^{85}Kr charger, theory [266, 75] predicts higher negative single charge and uncharged fractions, and lower positive charge fractions (focused on charge states plus two to five) than the measured charge fractions as shown in Figure 5.7a. Furthermore, this trend becomes more prevalent as particle size increases and is

drastically different than the charge fractions measured at low-flow conditions (0.6 L/min) as shown in Figure 5.7b.

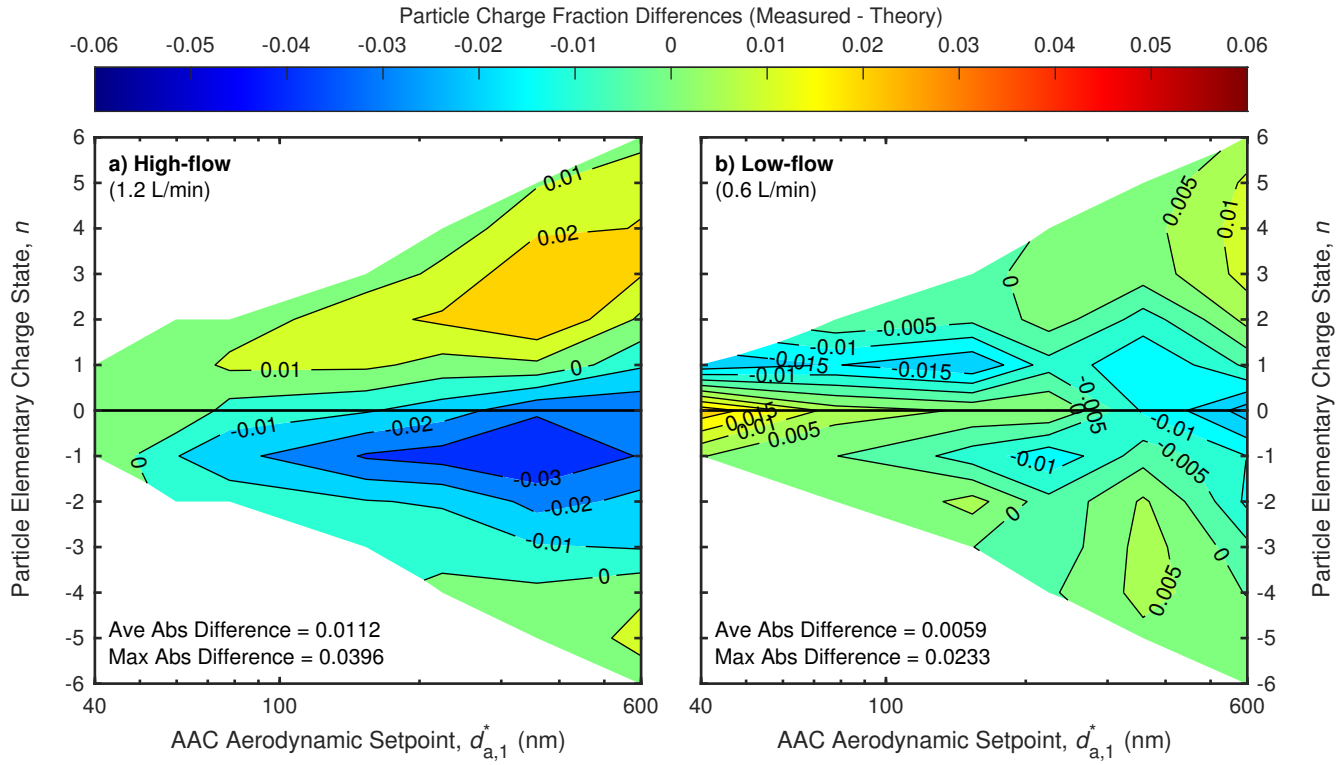

Fig. 5.7 Differences between particle charge fractions measured by the tandem AAC-DMA system at a) high-flow and b) low-flow through the new ^{85}Kr charger compared to theory [266, 75].

This disagreement between theory and the measured charged fractions at the higher sample flow (1.2 L/min) is likely due to the charging process not reaching a steady-state. To reach a steady-state charge distribution, there must be sufficient ion concentrations and minimum exposure time to those ions for a particular particle size and maximum concentration [4, 88, 181, 182, 41, 92]. Furthermore, the particle concentrations through the charger at high-flow (4.95×10^2 to 3.08×10^4 particles per cm^3 depending on the particle size) were the same or lower than the particle concentration through the charger at low-flow (2.69×10^3 to 3.19×10^4 particles per cm^3).

This observation of not reaching a steady-state charge distribution at high-flow was also reported by Yang et al. [277], who characterised the charging of ammonium sulfate particles with similar or lower concentrations (5×10^2 to 3×10^3 particles per cm^3). They found the same neutraliser (TSI 3077A ^{85}Kr, 370 MBq) with the inlet insert was close to theoretical values for 100 to 900 nm particles at low flow (0.3 L/min), but when the flow

rate was increased to (0.93 L/min) the +1 charge fraction of the particles became lower than predicted by theory [277]. While their observation that the particle charging diverges from the steady-state distribution as the flow rate increases agrees with this work, their lower +1 charge fraction at high-flow (0.93 L/min) disagrees, as shown by the higher +1 charge fraction in Figure 5.7a. However these studies are not directly comparable, given the results of Yang et al. [277] were collected using an aerosol source of positively charged particles at 0.93 L/min, and the results shown herein were collected using an uncharged aerosol source at 1.2 L/min.

Lower activity (41 MBq or 74 MBq) ^{85}Kr neutralisers have also been shown in multiple studies to not attain a steady-state charge distribution for smaller particles ($<$ 50 nm) at flow rates of 0.9 L/min or greater [39, 82], or based on some non-dimensional parameter, which considers the concentration of ions and particles, and their interaction time [41, 92]. These charging discrepancies at smaller particle sizes may also be partly attributed to the charging model of Wiedensohler [266] consistently underestimating the particle-ion collision kernel during the charging of sub 10 nm particles [152].

5.7 Effects of free-ions on particle charge fractions

The inference that the charging process did not reach a steady-state at the higher sample flow (1.2 L/min) is supported by the measured charge fractions at one AAC setpoint (d_{a}^{*} =224 nm) while varying the exposure time of the particles to the free-ions downstream of the neutraliser, as shown in Figure 5.8. Previous studies have identified that ions escape the neutraliser and travel downstream with the particles [263, 88, 12, 242, 82]. Due to the difference in mobility between the positive and negative ions, the negative ions are preferentially lost, and the proportion of positive ions increases [263, 88, 242].

This conclusion is supported by ion current measurements taken downstream of the new ^{85}Kr neutraliser using HEPA filtered air (i.e. no particles) with different flow rates (0.3, 1.2 or 1.5 L/min) and tube lengths[13] (8, 33 or 200 cm) all being net[14] positive. As expected, the net concentration of positive ions downstream of the neutraliser increased as flow rate increased. For example with the 8 cm tube length, the net concentration of positive ions[15] downstream of the neutraliser increased by 21% (3.69×10^5 vs 3.06×10^5 ions per cm^3) or

[13]The 8 cm length reflects the shortest tube length possible with the instrument arrangement and was used for all of the measurements in this work unless otherwise stated. The 33 cm length reflects the length of tubing recommended by TSI [247] between the neutraliser outlet and inlet of the 3082 DMA column.

[14]Net refers to the charge summation of ions that reach the electrometer. For example, a net positive ion current indicates that the ions in the sampled air have a higher total of positive charges than negative.

[15]Assuming one elemental charge per ion.

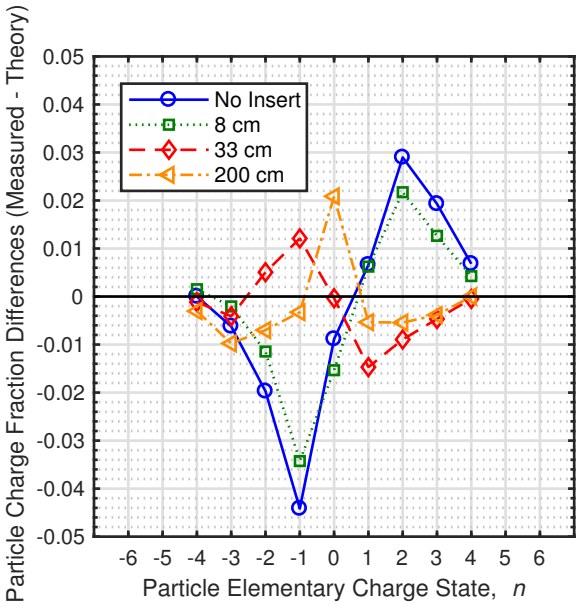

Fig. 5.8 Differences between charge fractions measured by the AAC-DMA system compared to theory [266, 75] for particles with 224 nm aerodynamic diameters, while varying the downstream capture distance of ions escaping from the new ^{85}Kr charger at high-flow.

24% (3.78×10^5 vs 3.06×10^5 ions per cm^3) as the flow rate was increased from 0.3 L/min to 1.2 or 1.5 L/min, respectively. Also as expected, the ion concentration became increasingly positive as the tube length increased due to more negative ions being preferentially lost. For example, the increase in net concentration of positive ions[15] as the flow rate increased from 0.3 to 1.5 L/min was 24% or 199% with a tube length of 8 or 33 cm, respectively[16]. Despite this increase in the proportion of positive ions, the net concentration of positive ions[15] decreased by 97% or more for all three flow rates as the tube length increased from 8 to 200 cm due to the increase losses of ions of both polarities.

However, there is disagreement between previous studies regarding the effects of these predominantly positive ions downstream of the neutraliser on the particle charge fractions. Hoppel and Frick [88] concluded that due to these ions the particle charge distribution will continue to change downstream of the neutraliser and thus a true steady-state could never be reached. However, Alonso et al. [12] concluded that the free-ions will only affect the particle charge distribution if a steady-state is not achieved before exiting the neutraliser. This outcome is supported by the findings of He and Dhaniyala [82], which found the effects

[16]The corresponding measurement for the 200 cm long tube was not included, as the net concentration of positive ions at 0.3 L/min with this tube length was low (0.2 fA), and an order of magnitude less than the 5 fA accuracy [245] of the aerosol electrometer (TSI Inc.: 3068B) used.

of the free-ions on the negative to positive charge fraction of 17 nm particles were significant downstream of a low activity ^{85}Kr neutraliser (74 MBq), but not a ^{210}Po or x-ray neutraliser. Interestingly, these results were also consistent with their findings of whether the particles achieved a steady-state charge distribution from these neutralisers [82]. Finally, Tigges et al. [242] concluded at reasonably high ratios of ion to particle concentrations ($\geq$ 100), which is also a consideration for attaining a steady-state charge distribution, the effect of the free-ions downstream of the neutraliser is negligible for typical SMPS measurements (<5% change in the fraction of singly-charged particles).

Based on the differences in the measured charge fractions as shown in Figure 5.8, the free-ions downstream of the neutraliser at high-flow (i.e. 1.2 L/min) do significantly affect the particle charge fractions, shifting the single charge states by up to 0.034 (16% difference) and double charge states by up to 0.021 (21% difference). These results support the conclusions of Hoppel and Frick [88] and Alonso et al. [12], as well as the findings of He and Dhaniyala [82] at the smaller particle size of 17 nm. Although, it is still unclear if the free-ions had an effect as a true steady-state can never be reached as per Hoppel and Frick [88], or because the particles had not achieved a steady-state charge distribution before leaving the neutraliser as per Alonso et al. [12].

However, these results disagree with the previously discussed conclusions of Tigges et al. [242]. Based on the previous characterisation of the TSI 3077A ^{85}Kr neutraliser by de La Verpilliere et al. [41] and of a similar activity (10 mCi) ^{85}Kr source by Liu and Pui [156], the ion concentration inside the new ^{85}Kr neutraliser was estimated to be 9×10^6 ions per cm^3. Therefore, despite operating at conditions typical for SMPS measurements, with a flow rate of 1.2 L/min and maximum concentration of 3.08×10^4 particles per cm^3 (equivalent to a minimum ion to particle concentration ratio of 292), the effects of free-ions downstream of the neutraliser were significant.

5.8 Effects of charger inlet insert on particle charge fractions

These measurements also show without the inlet insert on the new ^{85}Kr neutraliser the charge fractions deviate slightly further from theory. Yang et al. [277] also found deviations from theory for the same neutraliser with and without the inlet insert in place, specifically that without the insert particles larger than 700 nm were charged to lower +1 charge fractions than predicted by theory. While the observation that the inlet insert affects the charge fractions agrees with this work, their lower +1 charge fraction disagrees, as shown by the 0.0066

higher +1 charge fraction in Figure 5.8. However these studies are not directly comparable, given the results of Yang et al. [277] were collected using an aerosol source of positively charged particles (100-900 nm) at 0.3 L/min, and the results shown herein were collected using uncharged, 224 nm particles at 1.2 L/min.

The effect of the inlet insert on the charge fractions of the particles is likely due to it increasing the residence time of the particles in the ^{85}Kr neutraliser. For example, Yang et al. [277] found the inlet insert increases the residence time of at least 50% of the particles in the ^{85}Kr neutraliser by approximately 41 times at 0.93 L/min and approximately 6 times at 2 L/min.

5.9 Differences in particle charge fractions between chargers

Using the tandem AAC-DMA system, the particle charge fractions resulting from the new ^{85}Kr charger[6], old ^{85}Kr charger[7], or x-ray charger at three AAC setpoints ($d^*_{a,1} = 78$ nm, 224 nm or 596 nm) are shown in Figure 5.9. The flow rate through each charger was either low-flow (LF: 0.6 L/min) or high-flow (HF: 1.2 L/min).

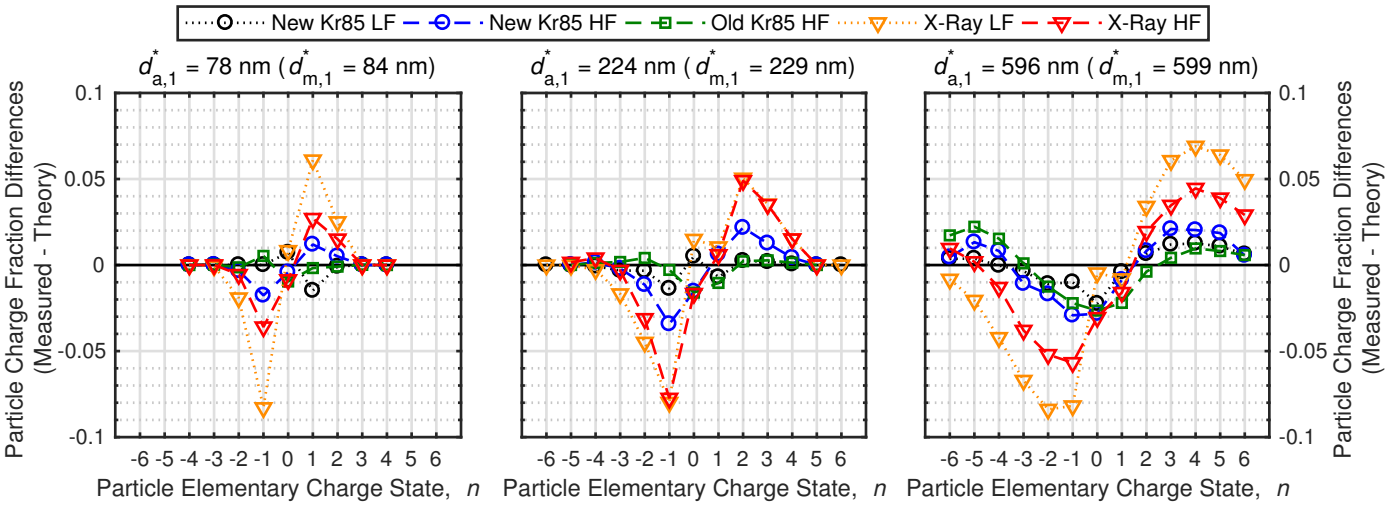

Fig. 5.9 Differences between charge fractions measured by the AAC-DMA system compared to theory [266, 75] for different bipolar chargers.

All three ^{85}Kr charging datasets agree within a 0.034 fraction of charging theory [266, 75], with the charging fractions measured at low-flow through the new ^{85}Kr agreeing within 0.004 on average with theory (disagreement range of -0.022 to 0.013). The charge fractions

measured at high-flow through the new and old ^{85}Kr agree within 0.009 (disagreement range of -0.034 to 0.022) and 0.006 (disagreement range of -0.027 to 0.022) on average with theory, respectively. These results are counter-intuitive as it was expected that the old ^{85}Kr would perform worst at high flow, not marginally better, than the new ^{85}Kr charger. The results indicate the difference in activity level between the ^{85}Kr chargers had no significant effects on the charge distribution of the particles at high-flow. These results agree with He and Dhaniyala [82] which found that an old (22 years old, equivalent to more than two ^{85}Kr half-lives) and new ^{85}Kr (TSI 3077) charger produced similar charging efficiencies for sub 50 nm particles. However, the results disagree with Jiang et al. [101] which found an old ^{85}Kr (approximately one-half life) produced different single charged fractions for 70 nm particles than ^{85}Kr chargers with activities exceeding 70 MBq.

At both high and low sample flows, the x-ray charger deviated significantly from the ^{85}Kr chargers and from theory [266, 75], producing significantly higher fractions of positively charged particles and considerably lower fractions of negatively charged particles relative to theory. These results agree with Mamakos [166] which found that a soft x-ray charger yields systemically higher fractions of positively charged, soot particles (70 to 309 nm) at multiple charge states compared to ^{85}Kr charging, and Tigges et al. [243] which found that soft x-ray also produced more positively charged particles than radioactive sources. This conclusion is further supported by Jiang et al. [101], which found a soft x-ray charger using 70 nm DOS particles produced a higher ratio of positively to negatively charged particles than predicted by theory.

However, Yang et al. [277] found a soft x-ray charger reached the predicted steady-state charging fractions at different tested flow rates (0.3 to 4.0 L/min) and particle sizes (100 to 900 nm). A possible explanation for the discrepancy in results and a note of caution comes from Wiedensohler et al. [270] which states that “a brand-new soft x-ray charger performed well, according to the specific bipolar charge equilibrium. However, a device with working hours even below the recommended lifetime showed a significant degradation in its performance. An investigation of the long-term performance has to be done in future." The x-ray source used in the current work was manufactured in 2011, and its number of operating hours is unknown.

These results indicate that care must be taken in assuming the validity of the SMPS system using standard inversion procedures when using the present model of x-ray charger. Others have shown that these discrepancies in charge fractions are due to the different ion mobilities produced by x-ray chargers relative to radioactive neutralisers [243]. This difference is accounted for within newer SMPS inversions by increasing the positive-to-negative ion

mobility ratio from 0.875 to 0.975 and using different coefficients to estimate the charging fractions produced by x-ray chargers [249].

5.10 Conclusions

Considering the agreement between the experimental results collected using the new ^{85}Kr charger at low-flow and widely-utilized charging theory [75, 266] for the convolution fit (i.e. N_2/N_1), charge fractions, and other fitting parameters, the proposed methodology of using a tandem AAC-DMA system to measure particle charge fractions is strongly supported. The tandem AAC-DMA overcomes limitations of the TDMA methodology for characterising particle charge distributions, specifically avoiding multiply-charged particles from the upstream DMA and its low transmission efficiency of singly-charged particles due to neutralisation limitations.

The advantages of the AAC-DMA system and inversion method allow the charge fractions of particles with up to 13 charge states (i.e. -6 to +6) to be accurately measured. While the charge fractions of the particles at low-flow (0.6 L/min) through the new ^{85}Kr charger agreed well (average absolute difference of 0.007) with charging theory [75, 266], a systematic disagreement (up to 0.04 difference or 33% difference) between the measured charge fractions and theory was found at high sample flow (1.2 L/min) through the new ^{85}Kr charger. This trend becomes more prevalent as particle size increases and is likely due to the charging process not reaching a steady-state. At these charging conditions, theory predicts higher negative single charge and uncharged fractions, and lower positive charge fractions (focused on charge states plus two to five) than measured. The tandem AAC-DMA methodology also has the sensitivity to detect other charging phenomena, such as the effects of free-ions downstream of the charger, the inlet insert on the ^{85}Kr charger and different particle chargers (x-ray, old ^{85}Kr and new ^{85}Kr). It was found that regardless of flow rate, a soft x-ray charger produced charge fractions which deviated significantly from theory, producing higher fractions of positively charged particles and lower fractions of negatively charged particles relative to theory. These charge fraction discrepancies have been shown by others to be due to the different ion mobilities produced by x-ray chargers relative to radioactive neutralisers.

All of these results indicate that care must be taken in using charging methods for aerosol characterisation, such as standard SMPS measurements. Particularly, consideration must be given to the type of charger (i.e. its geometry, activity and flow rate), and the interaction time with free-ions downstream of the charger to ensure the aerosol is charged to the expected charge distribution.

Chapter 6

Measuring the Bipolar Charge Distribution of Non-Spherical Particles

6.1 Introduction

This chapter[1] addresses Objective 2b and develops the AAC methodology to measure the bipolar charge distributions of non-spherical particles by using an AAC-DMA-DMA system. This new approach expands upon the one developed for spherical particles in Chapter 5, and also overcomes significant limitations of previous methodologies used to study the bipolar charging of non-spherical particles. As summarized in Section 2.4, these previous approaches are primarily based on electrostatic classification techniques.

6.1.1 Challenges with electrostatic classification of non-spherical particles

Similar to applications with spherical particles, electrostatic classifiers are limited by their ability to produce an aerosol of homogeneous, non-spherical particles, which has narrow ranges of particle mass, mobility and relaxation time simultaneously. For example, spherical or non-spherical particles classified by the DMA are only similar in electrical mobility (Z_p), and due to different charge states (n) have a range of mechanical mobilities (B) and masses (m), as shown by the following relationship[2] between these particle properties:

$$\tau = mB = m\frac{Z_\mathrm{p}}{ne}, \tag{6.1}$$

[1] This chapter is based on an article by Johnson et al. [107] published by Elsevier in the Journal of Aerosol Science on 23/11/2020, available online: https://doi.org/10.1016/j.jaerosci.2020.105705.

[2] This relationship is a subset of Equation 1.1, which is based on Hinds [84].

where e is the elemental charge (1.60×10^{-19} C) and τ is the relaxation time of the particle. The significance of these multiple charging artefacts during electrostatic classification is highlighted by the example TDMA results shown in Figure 6.1a and previously discussed in Section 2.5.2. As a quick overview, this issue is caused by larger particles with higher charge behaving the same way in an external electric field (i.e. have the same electrical mobility) as smaller particles with lower charge. The labels at the top of Figure 6.1a denote the charge state n_1 or n_2 of each particle after classification by the upstream or downstream DMA (i.e. $n_1 \rightarrow n_2$), respectively. Therefore, the singly-charged particles classified by the upstream DMA (i.e. particles with the mobility size intended for classification) are denoted by the $1 \rightarrow n_2$ labels, while the remaining labels highlight the artefacts from multiply-charged particles also classified by the upstream DMA.

To reduce the potential biases introduced by multiply-charged particles, previous charging studies of non-spherical particles have utilized a wide range of approaches. The trajectory or deposition approaches (previously summarized in Section 2.4) can account for this effect as the larger, multiply-charged particles are also identified during visual processing. However, these manual methodologies are labour-intensive, making it challenging to collect and analyse representative samples. Some electrostatic studies, such as TDMA measurements by Maricq [169] and DMA-ESP measurements by Matsoukas and Friedlander [179], largely focused on particles smaller than 100 nm, where the fraction of multiply-charged particles is negligible. For example, only 3% of 60 nm particles neutralised to a steady-state charge distribution are estimated to be multiply-charged [266]. This charging aspect is leveraged by two-stage aerosol generators, which use a DMA to select small, singly-charged particles (< 40 nm), then a condensation chamber to grow these solid particles to the size of interest. While Uin et al. [252] demonstrated this approach generates an aerosol of homogeneous particles, it is limited to spherical particles, each with a multi-phase composition formed of specific materials. Alternatively, expanding the approach of Gupta and McMurry [76] from spherical particles to non-spherical particles,, Kulkarni et al. [142] used a ^{210}Po neutraliser with low activity (500 µCi) to narrow the charge distribution of CNTs upstream of the TDMA. This narrowing reduces the ratio of multiply-charged to singly-charged particles before classification by the upstream DMA.

Others [215, 172, 142] have used or discussed the advantages of characterising particles only larger than the mode of the aerosol, as the concentration of larger particles that can potentially become multiply-charged is greatly reduced. By controlling the mean diameter of the aerosol particles, Maricq [172] was able to limit the proportion of multiply-charged particles classified by the upstream DMA to less than 10% from the PAO oil and soot sources. However, this approach limits the charging measurements to specific size ranges or operating

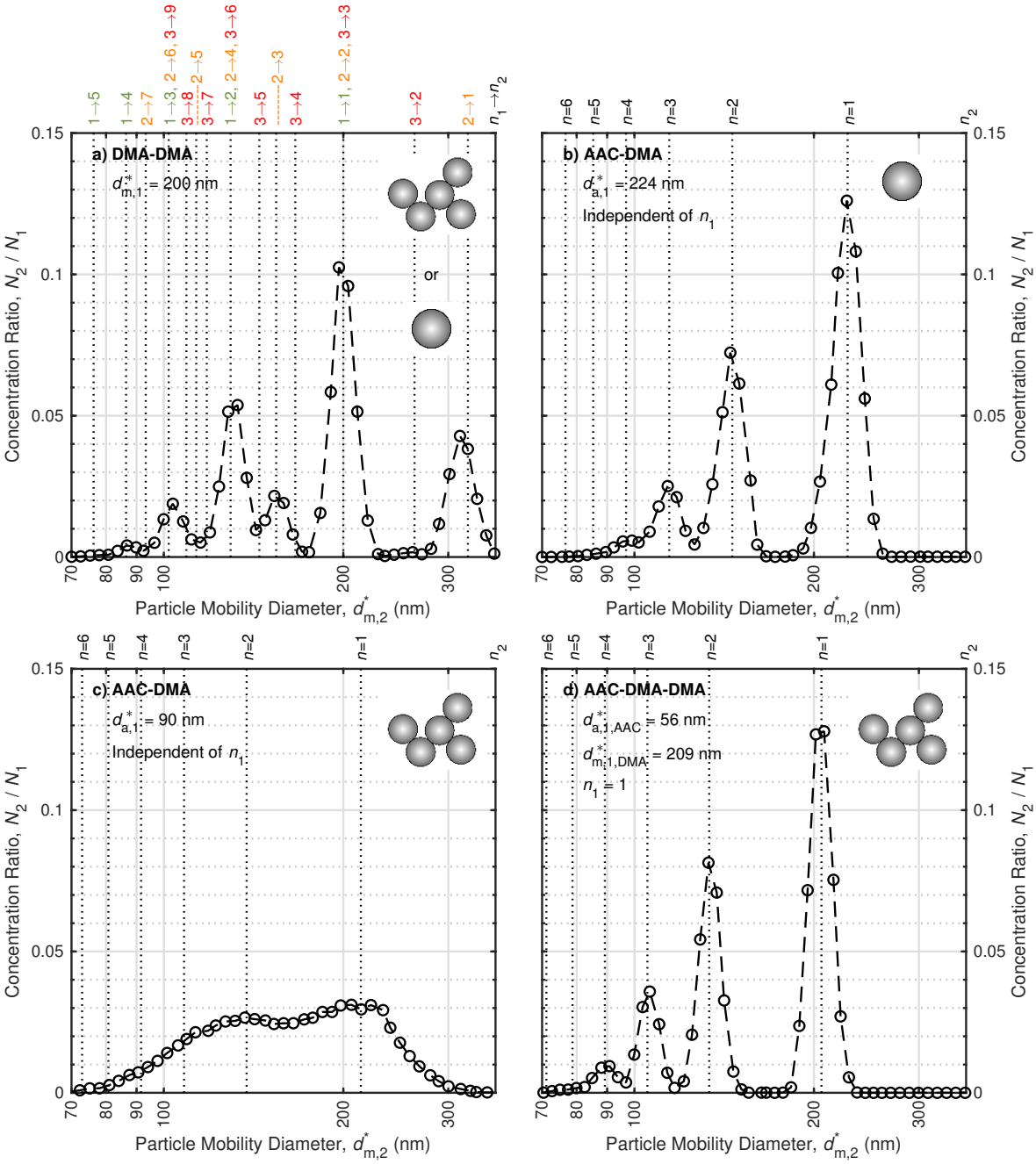

Fig. 6.1 Ratio of particle number concentrations, where N_1 is the particle concentration classified by different combinations of upstream classifiers at constant setpoints ($d^*_{m,1}$ for upstream DMA setpoint and $d^*_{a,1}$ for AAC setpoint), while N_2 is the particle concentration classified by the downstream DMA at different mobility diameter setpoints ($d^*_{m,2}$). The four subplots depict results from different upstream classifiers as follows: a) DMA classifying spherical or non-spherical particles; b) AAC classifying spherical particles; c) AAC classifying non-spherical particles; and d) AAC and DMA in tandem classifying non-spherical particles.

conditions of the aerosol source. Furthermore, some aerosol sources are not as easy to modify or control, as mentioned by Maricq [172] for particles from a diesel engine with a multiply-charged proportion as high as 20%.

Following similar reasoning, other charging studies remove particles larger than those of interest using inertial or aerodynamic separation methods. Romay-Novas and Pui [218] demonstrated using a micro-orifice impactor in series with a DMA to reduce the effects of multiple charging (to 6% or less) and produce a nearly monodispersed aerosol of spherical particles. Following a similar approach for non-spherical particles, both Kulkarni et al. [142] and Ku et al. [140] used an inertial impactor to reduce the effects of multiply-charged particles in their measurements of charged fraction using a DMA-ESP-CPC. While impactors are robust and straightforward, their resolution is limited (by particle diffusion and flow effects), and it is difficult to change their cutoff diameter quickly (i.e. need to alter its geometry or flow conditions). Furthermore, these inertial separation approaches require the relationship between the aerodynamic and mobility diameters of the particles to be known [142], which is more complex for non-spherical particles.

In addition to these approaches, many charging studies also post-correct the measurements to reduce the bias introduced by any remaining multiply-charged particles. Rogak and Flagan [215] used the size distribution of each aerosol and the average charge fractions predicted by Kousaka et al. [138] to estimate the fraction of multiply-charged particles and correct their measurements of uncharged fractions. Building on this approach, Kulkarni et al. [142] used a SMPS to measure the particle size distribution downstream of the DMA-ESP setup. Based on the size distribution, the proportion of multiply-charged particles was estimated by the ratio of areas under the peaks larger than the upstream DMA setpoint (e.g. $3 \rightarrow 2$ or $2 \rightarrow 1$ peak in Figure 6.1a) to those areas under the peaks at smaller sizes. This correction shifted the measured charged fractions by up to 5%, highlighting the significant effect of multiply-charged particles given this correction was after the use of a low-activity neutraliser and impactor.

Similarly, Maricq [171] and Mamakos [166] corrected the charge fractions measured using a TDMA for multiply-charged particles by selecting progressive setpoints for the upstream DMA (i.e. doubling its classifier voltage) so that the doubly-charged particles at one setpoint aligned with the singly-charged particles at another setpoint. Maricq [172] also corrected TDMA measurements for multiple charging effects, but based on the area under the $2 \rightarrow 1$ peak. Rather than collecting a separate measurement of size distribution, this study scanned the downstream DMA a small amount above the setpoint of the upstream DMA. However, all of these corrections methods assumed that the multiply-charged particles only consisted of doubly-charged particles, and thus their proportion was overestimated [215, 142].

For example, Kulkarni et al. [142] discusses a case where this correction overestimates the fraction of multiply-charged particles by approximately 30%.

Kim et al. [127] avoided this overestimation by assuming the charge distribution of the aerosol followed a Boltzmann distribution and developing an inversion to correct the charge fractions measured using a TDMA. This approach was then adopted by Maricq [173] to correct the charge distribution measurements of soot produced from a flame or diesel engine. To avoid the assumption of a Boltzmann charge distribution, Xiao et al. [276] developed an iterative process to remove the effect of multiply-charged particles by using the charge distribution estimated from the previous iteration.

6.1.2 Challenges with aerodynamic classification of non-spherical particles

The AAC classifies particles by their aerodynamic diameter, a property which is independent of particle charge [240]. As a result, the AAC requires no controls or corrections to limit the effect of multiple charging during particle classification. Figure 6.1b shows that by using the AAC to select homogeneous, spherical particles, individual peaks corresponding to each charge state produced by the charger of interest may be resolved using a downstream DMA. Using this approach, Chapter 5 measured the bipolar charge distribution (up to six charge states) of spherical, DOS particles between 40 and 600 nm using different neutralisers and operating conditions. Relative to the TDMA, Chapter 5 also demonstrated that the AAC-DMA approach leverages the high-transmission efficiency of the AAC (quantified in Chapter 3) and simplifies generating an aerosol of uncharged particles to avoid biasing the charging process of interest.

However, significant challenges are introduced when the AAC-DMA approach is applied to non-spherical particles. The aerodynamic diameter of a particle is a function of its mass and drag. Spherical particles with a consistent composition have a constant effective density, resulting in a unique relationship between their aerodynamic, mobility and geometric diameters. In contrast, the density of non-spherical particles often varies with particle size [197]. For example, a small, non-spherical particle with a low mass and drag could have the same aerodynamic diameter, but different mobility diameter, than a large, non-spherical particle with a high mass and drag. This effect is shown in Figure 6.2, which compares the aerodynamic and mobility size distributions of aerosols with spherical or non-spherical particles. As expected, the widths of the size distributions corresponding to the spherical particles are approximately the same. However, the aerodynamic size distribution of the

non-spherical particles is significantly narrower than their mobility distribution as particles at one aerodynamic diameter had a range of mobility diameters (or vice versa).

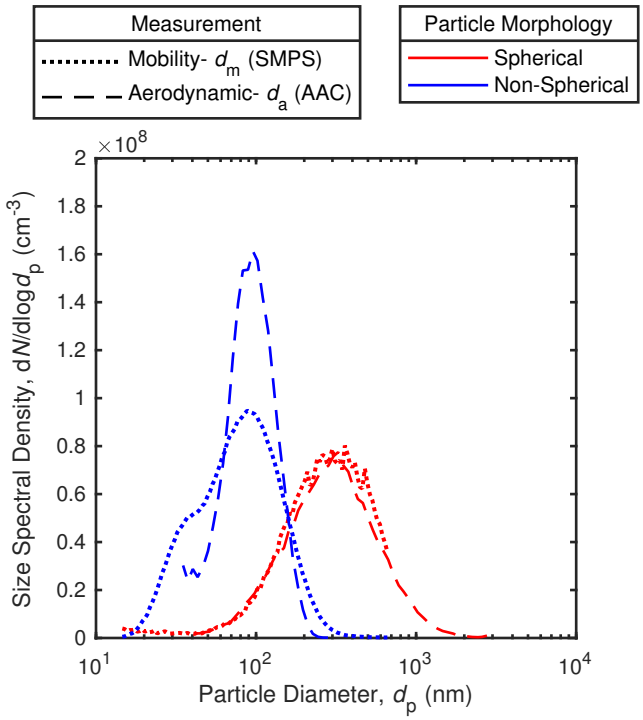

Fig. 6.2 Mobility (d_m measured by SMPS) and aerodynamic (d_a measured by AAC) size distributions of spherical (DOS) and non-spherical (soot) particles.

While Chapter 5 demonstrated spherical particles classified by the AAC are homogeneous, non-spherical particles classified by the AAC are only similar in relaxation time (τ) and due to varying effective densities (ρ_{eff}) also have a range of mechanical mobilities (B) and masses (m). This aspect is shown by the following relationship[3] between these particle properties:

$$\tau = mB = m\frac{Z_p}{ne} = \frac{C_c(d_a)\,\rho_o\,d_a^2}{18\mu} = \frac{C_c(d_m)\,\rho_{eff}\,d_m^2}{18\mu}, \tag{6.2}$$

where d_m and d_a are the mobility and aerodynamic diameters of the particle, respectively (and are often used to describe the setpoints of the DMA and AAC, respectively), while C_c is the Cunningham slip correction, μ is the surrounding gas viscosity and ρ_o is unit density (1000 kg/m^3).

This effect is further illustrated by measurements of non-spherical particles using a tandem AAC-DMA, as shown in Figure 6.1c. The AAC selected particles with a narrow range of aerodynamic diameters around 90 nm; however, these classified particles had a

[3]This relationship is a subset of Equation 1.1, which is based on Hinds [84].

variety of mobility diameters as shown by the broad peaks, which blended together. This broadening introduces significant challenges during data deconvolution to determine the charge fractions of the particles, especially at higher charges states.

6.1.3 Outline of chapter

The challenges of using either electrostatic or aerodynamic classification for charging studies stems from the fact that the classified particles are not homogeneous. To overcome these challenges, this chapter will first demonstrate that using an AAC-DMA in tandem can select homogeneous, non-spherical particles. These particles have similar mobility diameters (d_{m}), aerodynamic diameters (d_{a}) and masses (m), simultaneously. At a high-level, the advantages of this approach are illustrated in Figure 6.1d. The AAC is used to overcome multiple charging effects from the upstream DMA, while the upstream DMA is used to overcome the broadness in the mobility domain of the non-spherical particles classified by the AAC (due to their effective density varying with particle size). The second part of this chapter will measure the bipolar charge distribution (up to ± 8 charge states) of this homogeneous, flame-generated soot ($d_{\mathrm{m}} = 80$ to 433 nm) using another DMA downstream to distinguish each charge peak. Finally, these results are compared to previous charging studies of non-spherical particles and widely-utilized charging theory.

6.2 Experimental setup

6.2.1 Generating homogeneous, non-spherical particles

The experimental setup used to generate an aerosol of homogeneous, non-spherical particles (i.e. similar mass and mobility, simultaneously) is shown in Figure 6.3a. Soot aggregates produced from a miniCast 4202 (Jing Ltd., Zollikofen, Switzerland) were used to demonstrate this approach; however, other non-spherical particles in the submicron range could have also been tested. Similar to the testing for the scanning AAC (i.e. Section 4.3.1), the miniCast was operated using its internal flow controllers with filtered air, filtered nitrogen and propane at 2 bar. A catalytic stripper (Catalytic Instruments GmbH & Co.KG, Rosenheim, Germany: Model CS015) operating at 350°C was used to remove any semi-volatile components from the aggregates. Next, an AAC (Cambustion Ltd., Cambridge, UK) was used to select particles with a narrow range of aerodynamic diameters and a neutraliser was used to charge the AAC classified particles as a prerequisite for classification by the DMA (labelled as ^{85}Kr Neutraliser 1 and DMA 1 in Figure 6.3a, respectively).

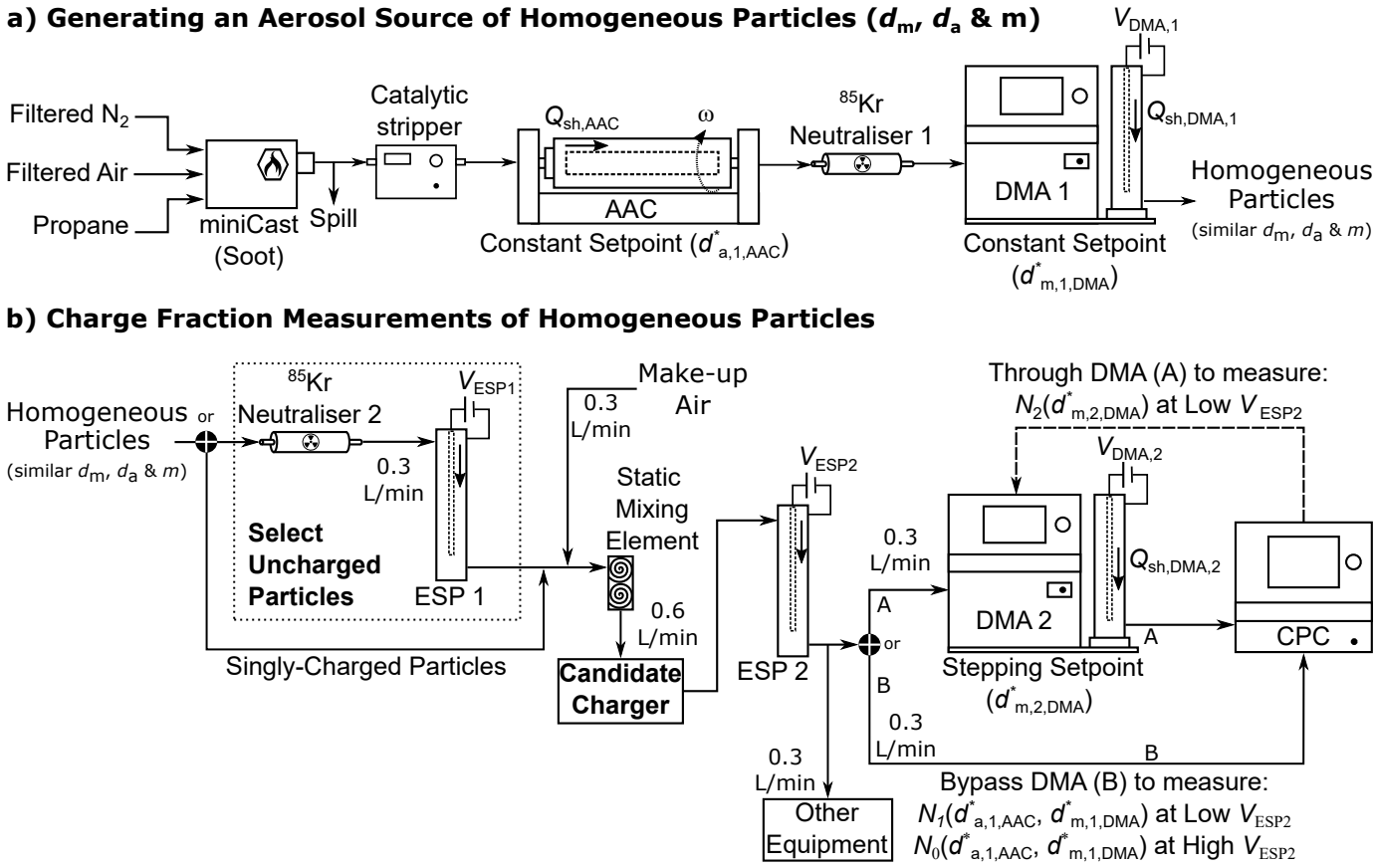

Fig. 6.3 Experimental setup used to a) generate homogeneous particles (i.e. similar d_m, d_a and m) using a tandem AAC-DMA and b) measure the charge fractions of these homogeneous particles using a downstream DMA and CPC.

DMA 1 was set to classify particles sufficiently larger than the mode of those classified by the AAC, thus reducing the proportion of multiply-charged particles. This approach is similar to the inertial separation approaches previously discussed for the TDMA and DMA-ESP methodologies. However, the AAC is used as the inertia separator instead of an impactor. Unlike most inertia classification methods, the resolution and setpoint of the AAC can be dynamically changed based on the speed and sheath flow rate of its classifier [238]. This flexibility, as well as the size range of the AAC, simplify removing non-spherical particles larger than those of interest (i.e. those that could potentially become multiply-charged and introduce measurement biases).

The setpoints of the AAC and DMA 1 were determined by experimentally validating the removal of multiply-charged particles. This check was accomplished by having DMA 2 measure over a larger range during the first measurement at each setpoint combination and looking for any evidence of multiply-charged artefacts, such as standalone peaks larger than

the setpoint of DMA 1 as shown in Figure 6.1a. The tandem-classified particles were also collected on clean silicon substrates placed on the ground electrode of a custom ESP. Images of the particle-loaded substrates were then captured using a scanning electron microscope (SEM: Leo Gemini 1530VP FEG-SEM) with an accelerating voltage of 10 kV.

Furthermore, since both the AAC and DMA act as high-resolution, band-pass filters, their implementation in a tandem configuration selects a narrow range of non-spherical particles in terms of both relaxation time (τ) and electrical mobility (Z_p), respectively. Combining these band-pass filters also selects particles that have a narrow range of masses (m), as shown by Equation 6.2. Importantly, the AAC removes larger particles which would otherwise become multiply-charged particles and be classified by the upstream DMA, complicating applications which require a homogeneous particle source. For particles composed of a homogeneous or semi-homogeneous material, these narrow ranges of equivalent diameters and mass likely result in a narrow range of morphologies. It is unlikely for particles to have different shapes while having similar properties across these other domains. Therefore, the AAC-DMA can be used to generate an aerosol of non-spherical particles with homogeneous properties (i.e. similar particle masses, mobilities and relaxation times). This aspect was indirectly demonstrated by Tavakoli and Olfert [239] using an AAC-DMA to measure the mass, dynamic shape factor and effective density of soot aggregates or DOS particles. It is also supported by the example results from each approach of aerosol classification shown in Figure 6.1.

Based on the same concepts, using a Centrifugal Particle Mass Analyser (CPMA; Olfert and Collings [198]) or Aerosol Particle Mass Analyser (APM; Ehara et al. [50]) in tandem with an AAC would also be capable of selecting homogeneous, non-spherical particles. However, different electrostatic based classifiers in series would only select homogeneous particles in unique circumstances given both instruments classify particles based on their charge. For example, a tandem CPMA-DMA system would only select homogeneous particles if the effective density of the aerosol resulted in the multiply-charged particles from DMA classification (i.e. in terms of electrical mobility) not overlapping with multiples of the CPMA setpoint (i.e. mass-to-charge).

While the tandem AAC-DMA generates an aerosol of homogeneous, non-spherical particles, it does come at a cost. Similar to other inertia separation methods used to limit multiple charging effects from the DMA, the classified particles are limited to specific ranges of properties as the DMA setpoint must be sufficiently larger than that of the AAC to avoid multiple charging effects. This limitation is a function of the effective density and charge distributions of the aerosol. As a result, only specific ranges of particle equivalent diameters and masses can be used to produce an aerosol of homogeneous, non-spherical particles. For

example, the AAC classified particles shown in Figure 6.1c that are singly-charged have average aerodynamic and mobility diameters of 90 and 214 nm, respectively. However, to generate homogeneous particles, the tandem AAC-DMA must select particles from the upper portion of this distribution. This restriction is reflected in Figure 6.1d, where the AAC and DMA setpoints are further offset at 56 and 209 nm, respectively.

Also by introducing a DMA to classify non-spherical particles, many of the advantages of using the AAC to select homogeneous, spherical particles, as previously demonstrated in Chapter 5, are reduced in the AAC-DMA approach. The high transmission efficiency of the AAC (quantified in Chapter 3) is restricted by the low transmission efficiency of the neutraliser-DMA system in tandem. This transmission efficiency is further reduced if an uncharged, homogeneous source of non-spherical particles is required. Due to the operating principles of the DMA, particles must be charged, classified by the DMA, re-neutralised and passed through an ESP to generate an aerosol of uncharged particles. This approach is similar to previous charging studies [1, 158, 226, 217, 225, 83, 78, 280, 271, 209, 82, 279] that used a DMA to generate an aerosol of uncharged, monodispersed particles.

6.2.2 Measuring the bipolar charge of non-spherical particles

The experimental setup used to measure the bipolar charge distribution of the homogeneous particles is shown in Figure 6.3b. This section of the experimental setup is similar to the one used in Chapter 5 for the charging of spherical particles (Section 5.2). A neutraliser and ESP (labelled as ^{85}Kr Neutraliser 2 and ESP 1 in Figure 6.3b) were used to condition the aerosol to comprise only uncharged particles and thereby avoid biasing the charging process of interest. At three of the seven particle sizes characterised (as shown in Table 6.1) ^{85}Kr Neutraliser 2 and ESP 1 were bypassed due to low measurement signals. Given the particle concentrations at these three data points were low (< 526 cm^{-3}) and consisted of only singly-charged particles, it is unlikely this pre-existing charge on the particles affected the results of the candidate charger.

Having selected the uncharged particles (or bypassed ^{85}Kr Neutraliser 2 and ESP 1), the remainder of the experimental setup was operated following the same procedures as the spherical charging setup described in Section 5.2. Briefly, the homogeneous particles were then passed through the candidate charger, which for these measurements was a new[4] ^{85}Kr 10 mCi radioactive neutraliser (TSI Inc., Shoreview, MN, USA: Model 3077A). ESP 2 (Cambustion Ltd.), DMA 2 and a CPC (TSI Inc.: Model 3752) were then used to quantify the bipolar charge distribution produced by the candidate charger. To determine

[4]Within six months of the isotope reference date.

Table 6.1 Test matrix outlining properties of the soot aggregates that were characterized for bipolar charging.

$d^*_{a,1,AAC}$ (nm)	$d^*_{m,1,DMA}$ (nm)	Ave ρ_{eff} (kg/m^3)	ESP 1 Bypassed
35	80	397	Yes
35	95	325	Yes
56	150	297	No
56	209	184	No
89	302	181	No
89	362	134	No
89	433	99	Yes

the uncharged fraction, DMA 2 was bypassed, and the total ($N_1(d^*_{a,1,AAC}, d^*_{m,1,DMA})$) and uncharged ($N_0(d^*_{a,1,AAC}, d^*_{m,1,DMA})$) particle concentrations were measured by the CPC with ESP 2 at a low[5] (single volts) or high (multiple kilovolts) voltage, respectively. To measure the charge fractions, DMA 2 stepped through the electrical mobility domain of the particles (referred to as a step-scan), while the CPC recorded their corresponding concentration (N_2) at each DMA setpoint ($d^*_{m,2,DMA}$). Since the particles had similar mechanical mobilities, each charge state appeared at a different electrical mobility in the measured distribution. The positive or negative charge fractions of the aerosol were measured by operating DMA 2 with a negative or positive classification voltage, respectively. The uncharged fraction was measured at the start and end of each DMA 2 step-scan. This set of measurements was repeated at least three times for each combination of AAC-DMA 1 setpoints shown in Table 6.1, as well as for both particle polarities.

The effective particle densities listed in Table 6.1 are 1.4 to 2.4 times lower than the effective densities reported for "average" soot by Olfert and Rogak [197] at similar equivalent mobility diameters. These differences highlight that this approach[6] limits the specific ranges of particle properties (i.e. equivalent diameters and masses) that can be used to generate homogeneous particles, as previously highlighted in Section 6.2.1. Therefore, the charging characteristics reported in this chapter are specific to the low-density aggregates tested and cannot be used to describe average aggregates from the same soot source. However, the subset of low-density particles represent a more open structure and thus have the greatest deviation from spherical morphologies for that aerosol source. Consequently, the data collected by this

[5]Unless measuring the uncharged concentration of particles, a low voltage was maintained on ESP 2 to trap any ions that escape the candidate charger and avoid downstream charging effects biasing the results, as demonstrated in Section 5.7.

[6]This limitation to specific ranges of particle properties also applies to other inertial separation methods used to reduce multiple charging effects during electrostatic classification, such as impaction.

work provides an estimate for the upper bound of average aggregates from the same soot source.

The total particle concentration (N_1) measured at the start and end of each DMA 2 step-scan was also used to verify the stability of the aerosol source. To avoid this stability biasing the results, only DMA 2 step-scans where N_1 was stable within 10% were included in the results. The DMAs were both manufactured by TSI Inc, with DMA 1 consisting of a 3080 Electrostatic Classifier with a 3081 Column and DMA 2 consisting of a 3082 Electrostatic Classifier with a 3081 Column. Following standard practice, all three aerosol classifiers (i.e. AAC, DMA 1 and DMA 2) were operated with constant sheath-to-sample flow ratios of 10:1 for high-resolution classification. Please see Section 5.2 for further details given the significant overlap between the approaches for determining the bipolar charging of spherical (Chapter 5) and non-spherical particles (this chapter).

6.3 Theory

6.3.1 AAC-DMA-DMA convolution

Expanding the theory developed for the tandem AAC-DMA in Section 5.3.1 to the AAC-DMA-DMA, the theoretical ratio of particle concentrations upstream (N_2) and downstream (N_1) of DMA 2 can be predicted by:

$$\frac{N_2(d^*_{\mathrm{m,2,DMA}})}{N_1(d^*_{\mathrm{a,1,AAC}},\, d^*_{\mathrm{m,1,DMA}})} = \frac{\sum_{n_1=n_{\min}}^{n_{\max}} \sum_{n_2=n_{\min}}^{n_{\max}} \int \eta\, \Omega_{\mathrm{AAC}}\, f_{n_1}\, \Omega_{\mathrm{DMA1},n_1}\, f_{n_2}\, \Omega_{\mathrm{DMA2},n_2}\, \mathrm{d}d_{\mathrm{m}}}{\sum_{n_1=n_{\min}}^{n_{\max}} \int \eta\, \Omega_{\mathrm{AAC}}\, f_{n_1}\, \Omega_{\mathrm{DMA1},n_1}\, \mathrm{d}d_{\mathrm{m}}}, \quad (6.3)$$

where Ω_x is the transfer function of classifier x, η is the counting efficiency function of the particle detector, $n_{\min}$ and $n_{\max}$ are the minimum and maximum charge states considered, respectively, and f_{n_1} and f_{n_2} are the charge fractions of charge state n upstream and downstream of the candidate charger, respectively. However, with effective removal of larger particles using the AAC, all of the particles classified by DMA 1 are singly-charged (i.e. $n_1 = 1$), resulting in Equation 6.3 simplifying to:

$$\frac{N_2}{N_1} = \frac{\sum_{n_2=n_{\min}}^{n_{\max}} \int \eta\, \Omega_{\mathrm{AAC}}\, f_1\, \Omega_{\mathrm{DMA1},1}\, f_{n_2}\, \Omega_{\mathrm{DMA2},n_2}\, \mathrm{d}d_{\mathrm{m}}}{\int \eta\, \Omega_{\mathrm{AAC}}\, f_1\, \Omega_{\mathrm{DMA1},1}\, \mathrm{d}d_{\mathrm{m}}}. \quad (6.4)$$

This simplification highlights the advantages of physically removing multiple charging effects from the upstream DMA, rather than accounting for this effect through complex post-processing. While the transfer function of the AAC is narrow in particle relaxation time, it is likely broad in mobility diameter (d_m) for non-spherical particles due their distribution of effective densities. This aspect was previously demonstrated in Figures 6.1c and 6.2. Therefore, assuming the transfer function of the AAC (Ω_AAC), as well as the counting efficiency (η) of the detector and charge fractions (f_1 and f_{n_2}) of the particles, are constant over the narrow width of the DMA transfer functions in the mobility domain, Equation 6.4 simplifies to a TDMA inversion as follows:

$$\frac{N_2}{N_1} = \frac{\sum_{n_2=n_\mathrm{min}}^{n_\mathrm{max}} f_{n_2} \int \Omega_{\mathrm{DMA1},1}\, \Omega_{\mathrm{DMA2},n_2}\, \mathrm{d}d_\mathrm{m}}{\int \Omega_{\mathrm{DMA1},1}\, \mathrm{d}d_\mathrm{m}}. \tag{6.5}$$

Based on the non-idealized transfer function of the DMA operating with balanced flows[7] determined by Karlsson and Martinsson [120], which uses the transmission efficiency (λ_Ω) and transfer function broadening factor (μ_Ω) to account for non-ideal behaviour (such as particles losses and diffusion), Equation 6.5 becomes:

$$\frac{N_2}{N_1} = \frac{\sum_{n_2=n_\mathrm{min}}^{n_\mathrm{max}} f_{n_2} \int \lambda_{\Omega,\mathrm{DMA1}}\, \Omega_{\mathrm{B,DMA1},1}\, \lambda_{\Omega,\mathrm{DMA2}}\, \Omega_{\mathrm{B,DMA2},n_2}\, \mathrm{d}d_\mathrm{m}}{\int \lambda_{\Omega,\mathrm{DMA1}}\, \Omega_{\mathrm{B,DMA1},1}\, \mathrm{d}d_\mathrm{m}}, \tag{6.6}$$

where $\Omega_\mathrm{B,DMA}$ is the transfer function of the DMA considering non-idealized broadening only and was adapted from Karlsson and Martinsson [120] as follows:

$$\Omega_\mathrm{B,DMA} = \frac{\mu_\Omega^2}{2\beta}\left[\left|\tilde{Z}_\mathrm{p} - \left(1+\frac{\beta}{\mu_\Omega}\right)\right| + \left|\tilde{Z}_\mathrm{p} - \left(1-\frac{\beta}{\mu_\Omega}\right)\right| - 2|\tilde{Z}_\mathrm{p} - 1|\right]. \tag{6.7}$$

β is the non-dimensional classifier flow parameter based on the ratio of sample to sheath flow when the DMA is operated with balanced flows[7], while $\tilde{Z}_\mathrm{p}$ is the non-dimensional electrical mobility (i.e. the electrical mobility Z_p of the particle normalized by the DMA setpoint Z_p^*).

Similar to previous assumptions, assuming the transmission efficiency ($\lambda_\mathrm{\Omega,DMA}$) of the DMA is constant over the narrow width of its transfer function Equation 6.6 simplifies to:

$$\frac{N_2}{N_1} = \lambda_\mathrm{\Omega,DMA2} \frac{\sum_{n_2=n_\mathrm{min}}^{n_\mathrm{max}} f_{n_2} \int \Omega_{\mathrm{B,DMA1},1}\, \Omega_{\mathrm{B,DMA2},n_2}\, \mathrm{d}d_\mathrm{m}}{\int \Omega_{\mathrm{B,DMA1},1}\, \mathrm{d}d_\mathrm{m}}. \tag{6.8}$$

[7] The sample flows entering and exiting the classifier are the same.

This equation highlights that the transmission efficiency of DMA 2 ($\lambda_{\Omega,\mathrm{DMA2}}$) inversely scales the charge fractions (f_{n_2}) measured downstream of the candidate charger. Similar to AAC-DMA inversion in Chapter 5, the difference between the actual and theoretical/idealized transmission efficiency of the DMA ($\lambda_{\Omega,\mathrm{DMA2}}$ and $\lambda_{\Omega,\mathrm{DMA2,I}}$, respectively) can be accounted for by assigning an array of constants ($f_{n_2,\mathrm{I}}$) as follows:

$$f_{n_2}\,\lambda_{\Omega,\mathrm{DMA2}} = f_{n_2,\mathrm{I}}\,\lambda_{\Omega,\mathrm{DMA2,I}}. \tag{6.9}$$

Based on this substitution (i.e. Equation 6.9), Equation 6.8 becomes:

$$\frac{N_2}{N_1} = \lambda_{\Omega,\mathrm{DMA2,I}} \frac{\sum_{n_2=n_{\min}}^{n_{\max}} \boldsymbol{f_{n_2,\mathrm{I}}} \int \Omega_{\mathrm{B,DMA1},1}\,\Omega_{\mathrm{B,DMA2},n_2}\,\mathrm{d}d_{\mathrm{m}}}{\int \Omega_{\mathrm{B,DMA1},1}\,\mathrm{d}d_{\mathrm{m}}}. \tag{6.10}$$

where $\Omega_{\mathrm{B,DMA1},1}$ is a function of $d_{\mathrm{m}}(Z_{\mathrm{p,DMA1}}, e, \mu)$, β_{DMA1} and $\boldsymbol{\mu_{\Omega,\mathrm{DMA1}}}$, while $\Omega_{\mathrm{B,DMA2},n_2}$ is a function of $d_{\mathrm{m}}(\boldsymbol{Z^*_{\mathrm{p},12}} \cdot Z_{\mathrm{p,DMA2}}, \boldsymbol{n_{\mathrm{f}}}_2, e, \mu)$, β_{DMA2} and $\boldsymbol{\mu_{\Omega,\mathrm{DMA2}}}$. The **emboldened fitting parameters**, shown in Equation 6.10 and summarized in Table 6.2, highlight the parameters used to fit the theoretical convolution of the TDMA to the measured ratio of particle concentrations (N_2/N_1) using least-squares minimization. Equation 6.10 also reflects that uncharged particles do not pass through DMA (i.e. do not affect N_2/N_1) and that the losses and transfer function broadening in DMA 2 are a function of $d^*_{\mathrm{m},1,\mathrm{DMA}}$ as the aerosol is already monodisperse.

Table 6.2 Parameters used to fit the theoretical convolution of the TDMA to the experimental results.

Parameter	Effect on Fit	Implementation	Initial Guess
$f_{n_2,\mathrm{I}}$	Amplitude	Independent parameter for each charge state	Following Wiedensohler [266] and Gunn and Woessner [75]
$\mu_{\Omega,\mathrm{DMA}}$	Width	Constant parameter across all charge states	Following Birmili et al. [19]
$Z^*_{\mathrm{p},12}$	Horizontal location	Constant parameter across all charge states	1 (i.e. ideal agreement)
n_{f}	Horizontal spacing	Constant parameter across all charge states	1 (i.e. ideal spacing)

The parameters of $f_{n_2,\mathrm{I}}$ and $\mu_{\Omega,\mathrm{DMA}}$ are similar to those used by the AAC-DMA inversion in Chapter 5 to capture the height and width of the distribution peaks measured by DMA 2, respectively. This TDMA inversion assumes the broadening of the DMA transfer function is

the same in both DMA 1 and 2 (i.e. $\mu_{\Omega,\mathrm{DMA1}} = \mu_{\Omega,\mathrm{DMA2}} = \mu_{\Omega,\mathrm{DMA}}$). In contrast, the AAC-DMA inversion used in Chapter 5 applied the width factor only through the AAC transfer function (due to its higher variability with classifier setpoint) to maintain the independence of the fitting parameters. The parameter of $Z^*_{\mathrm{p},12}$ accounts for disagreements in the setpoints of DMA 1 and 2, and performs a similar function as the effective density parameter used in Chapter 5 to align the AAC and DMA setpoints. However, this current work introduced one additional fitting parameter, n_f, to account for non-linear agreement between the setpoints of DMA 1 and 2 (i.e. the agreement between the similar classifiers is not constant over their measurement ranges). This disagreement manifested in the spacing between the distribution peaks measured by the DMA 2, which became more prevalent at peaks that corresponded to higher charge states ($|n_2| > 5$) as DMA 2 measured across a larger range. Therefore, the primary function of $Z^*_{\mathrm{p},12}$ is to align the singly-charged setpoints of DMA 1 and 2, while n_f aligns the peaks of the multiply-charged particles by changing the spacing between them. To avoid redundancy with the linear parameter of $Z^*_{\mathrm{p},12}$, n_f was applied as a power to charge state n_2 of the particles, and thus had a larger effect on the position of peaks which corresponded to higher charge states.

The degrees of freedom of this inversion is the number of charge states considered (neglecting the uncharged fraction) plus three (i.e. $\mu_{\Omega,\mathrm{DMA}}$, $Z^*_{\mathrm{p},12}$ and n_f). For example, at the smallest (80 nm) and largest (433 nm) DMA 1 setpoints of this work, the degrees of freedom of the inversion were 11 and 19, by considering up to 4 and 8 charge states, respectively. The inversions of these measurements were well-defined by fitting against 35 and 52 data points, respectively. These degrees of freedom correspond to one more than utilized for the AAC-DMA inversion in Chapter 5, although both inversions are implemented in the same way based on initial guesses from previous studies. The charging models of Wiedensohler [266] and Gunn and Woessner [75] were applied as outlined in Section 5.3.1 for the initial guess of $f_{n_2,\mathrm{I}}$. Birmili et al. [19] was followed as the initial guess for the broadening of the DMA transfer function, while the initial guess for the agreement between the setpoints between DMA 1 and 2 was assumed to be ideal. For example at the smallest DMA 1 setpoint (80 nm), the initial guesses were $\mu_{\Omega,\mathrm{DMA}} = 0.93$, $Z^*_{\mathrm{p},12} = 1$ and $n_\mathrm{f} = 1$, while $f_{n_2,\mathrm{I}}$ equals 0.001%, 0.13%, 3.73%, 26.81%, 20.46%, 2.10%, 0.06%, 0.0004% for charge states -4 to -1 and +1 to +4, respectively.

The remaining theory to determine the charge fractions (f_n) of the non-spherical particles from the fitted values of $f_{n_2,\mathrm{I}}$ is the same approach as outlined in Section 5.3.2 for spherical particles. This theory also determines the difference between the actual and theoretical transmission efficiency of DMA 2 ($\lambda_{\Omega,\mathrm{DMA2}}$ and $\lambda_{\Omega,\mathrm{DMA2,I}}$, respectively).

6.3.2 Additional considerations for the convolution

The validity of the convolution assuming the AAC transfer function is constant over the width of the DMA transfer function in the mobility domain depends on the aerosol source, specifically its effective density and charge distributions. This assumption was validated for this work by also completing the inversion without this assumption (i.e. based on a simplified form of Equation 6.4). The charge fractions determined from this more complicated inversion, without any optimization, agreed within 0.0048 to those determined from the simplified inversion (i.e. based on Equation 6.10). The more complicated inversion also provided other insights that the AAC transfer function was a secondary factor in the inversion of the data. For example, the effective density determined by the inversion through aligning the AAC and DMA transfer functions in the mobility domain could vary by up to approximately 20% with negligible effects on the measured charge fractions.

Applications of the AAC-DMA-DMA convolution are also less flexible than those of the AAC-DMA convolution developed in Chapter 5 for spherical particles. Specific to the application of charging characterisation, the latter approach for spherical particles can also be used to measure the charge distribution of an aerosol source by bypassing the candidate charger and following the same convolution process. However since the DMA requires particles to be charged, measuring the charge distribution of non-spherical particles directly from their source with the AAC-DMA-DMA requires a more complicated inversion with a back-propagation. This more advanced inversion is similar to those used by the previous TDMA studies of Kim et al. [127] and Maricq [169, 170, 171, 173] to measure the charging of soot produced from different combustion processes.

6.4 Generating homogeneous, non-spherical particles

The effectiveness of using a tandem AAC-DMA to generate an aerosol of homogeneous, non-spherical particle is highlighted by the SEM images[8] shown in Figure 6.4. Each row of images within the figure shows the soot aggregates classified at a different combination of AAC-DMA 1 setpoints (as previously summarized in Table 6.1), while each column shows the aggregates at a near and far-field scale to demonstrate their individual morphology and uniformity, respectively.

Based on the verified removal of multiply-charged artefacts previously discussed and neglecting possible effects from flow alignment which may affect the drag of non-spherical particles during their classification [45, 72], all of the particles shown in the same image

[8]The SEM images shown in Figure 6.4 were captured by Xiao Zhang at the University of Cambridge.

within Figure 6.4 have narrow ranges of aerodynamic and mobility diameters, as well as masses. Furthermore, since the aggregates likely consisted of nearly homogeneous material (i.e. elemental carbon), these narrow ranges of equivalent diameters and mass results in a narrow range of particle morphologies. These SEM images demonstrate that it is unlikely for particles to have different shapes while having similar properties across these other domains. While some minor discrepancies between particle morphologies are observed in the SEM images at the larger classifier setpoints, this discrepancy is hypothesized to be due to the SEM images only capturing a 2D projection of the aggregates. Therefore, the AAC-DMA can be used to generate an aerosol of homogeneous particles across multiple properties of the particles.

It is also interesting to note that the 56-209 nm and 89-302 nm setpoint combinations have approximately the same effective density of 180 kg/m^3 (as previously listed in Table 6.1), but have different equivalent diameters, masses and morphologies as shown in Figure 6.4d versus Figure 6.4e. This fact demonstrates that careful selection of the AAC-DMA setpoints allows the possible isolation of particular properties of the homogeneous, non-spherical particles.

6.5 Tandem DMA convolution

The generation of homogeneous particles is further supported by the electrical mobility measurements of the tandem-classified particles using DMA 2, as shown in Figure 6.5. Each subplot row of Figure 6.5 represents a different combination of AAC-DMA 1 setpoints (as previously summarized in Table 6.1). These results illustrate the effectiveness of using the AAC to remove larger particles and avoid DMA 1 classifying multiply-charged particles, while using DMA 1 to overcome the broadness in the mobility domain of the non-spherical particles classified by the AAC. These results are in sharp contrast to the examples shown in Figure 6.1a and Figure 6.1c, which demonstrate these significant effects.

Figure 6.5 also illustrates the convolution theory (dashed line calculated using Equation 6.10 with the initial guesses outlined in Table 6.2) and convolution fit (solid line) to the experimental results (circles) collected using the AAC-DMA-DMA at each of the seven setpoint combinations outlined in Table 6.1. These results demonstrate the ability of the convolution to capture the experimental results and that the AAC-DMA-DMA can resolve up to 17 charge states (i.e. -8 to +8) of non-spherical particles.

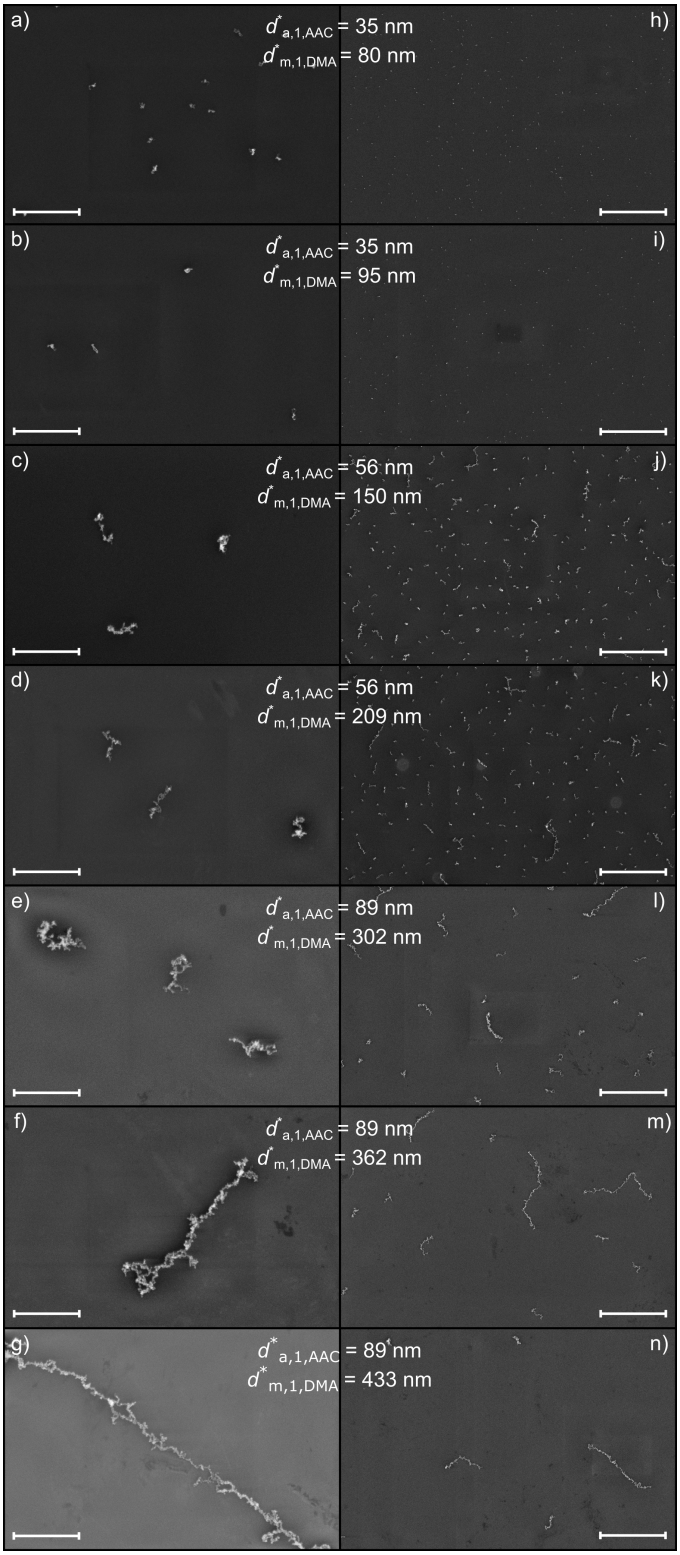

Fig. 6.4 SEM images of particles classified at each setpoint combination of the AAC and the upstream DMA (DMA 1) with a 1 µm or 5 µm scale (images a to g or h to n, respectively).

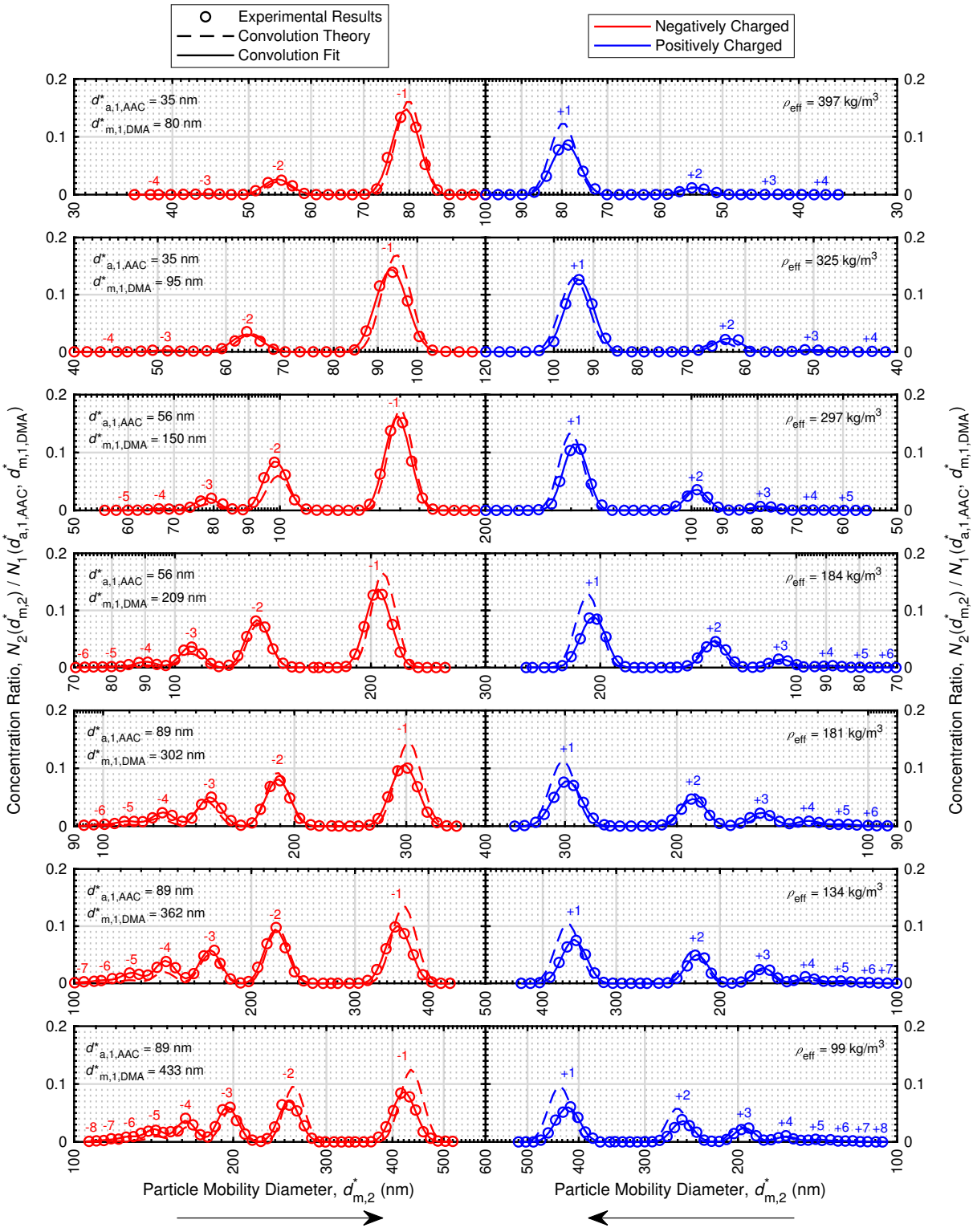

Fig. 6.5 AAC-DMA-DMA experimental measurements of low-density soot aggregates compared to the theoretical convolution (i.e. initial guesses) and fitted convolution, where the results of the positively and negatively charged particles are depicted by different colors.

6.6 Bipolar charging of non-spherical particles

As previously discussed in Section 6.2.2, homogeneous, non-spherical particles classified by the tandem AAC-DMA (with no multiple charging effects) are not representative of "average" non-spherical particles from the same source, but rather those that deviate the most from spherical particles. The measured charge distribution of these low-density soot aggregates relative to theory [266, 75] is shown in Figure 6.6a. These results demonstrate that the aggregates become more charged than predicted by theory, which overestimates the uncharged fraction (by 0.042 to 0.069) and, to a lesser extent, the single charge fractions (by up to 0.037), while underestimating the proportion of multiply-charged particles (by up to 0.135 cumulatively at one particle size or up to 0.039 at one multiple charge state and size). These discrepancies with theory are approximately three times higher (in terms of average and maximum absolute differences in charge fractions) than the charge distribution of spherical particles measured in Section 5.5 and reshown in Figure 6.6b to allow a direct comparison.

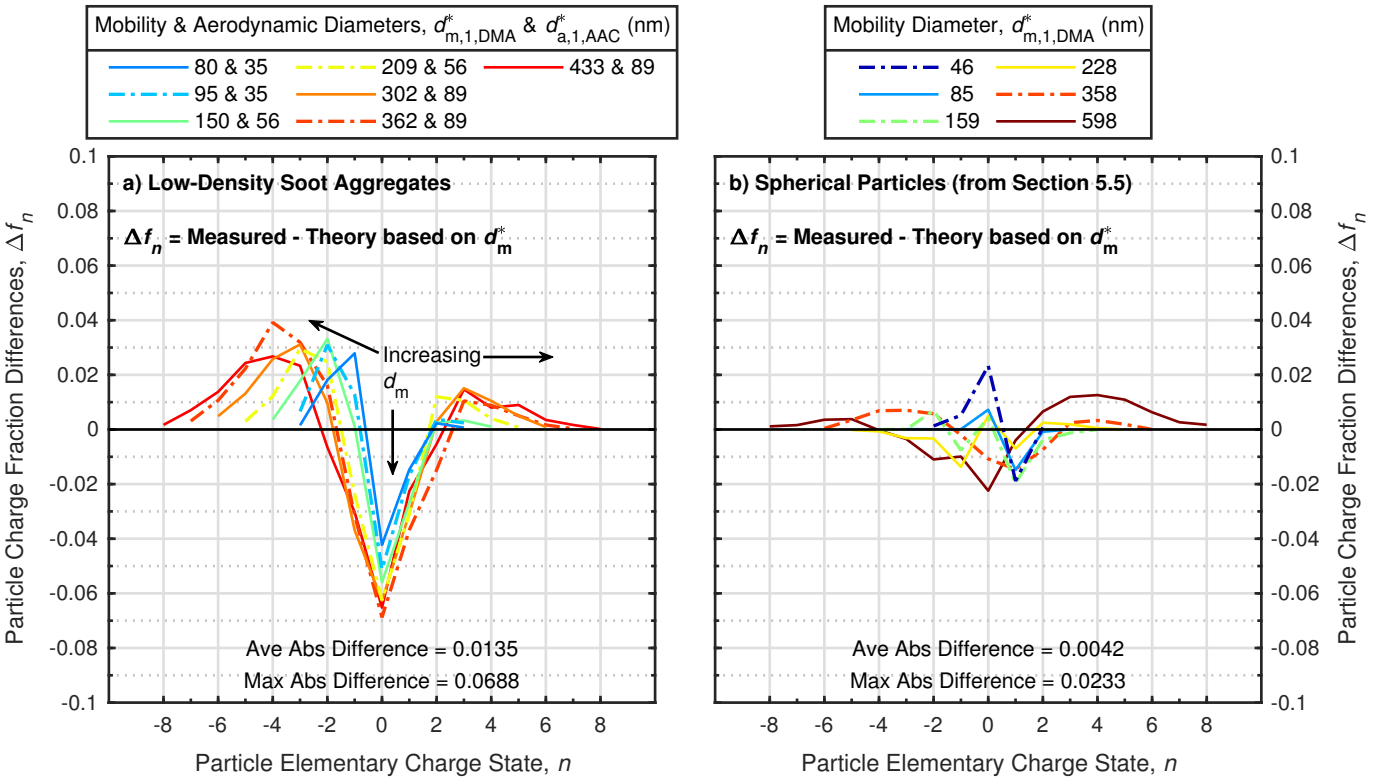

Fig. 6.6 Differences between charging theory [75, 266] based on the setpoint of the upstream DMA ($d^*_{m,1,DMA}$) and measured charge fractions of a) low-density soot aggregates or b) DOS particles after being neutralised using a ^{85}Kr charger.

Both the non-spherical data from this chapter and spherical data from Section 5.5 were collected within days of each other using the same ^{85}Kr neutraliser operating at 0.6 L/min flow. Furthermore, due to the transmission efficiency trade-offs previously discussed (i.e. AAC-DMA-DMA vs AAC-DMA), the particle concentration that passed through the neutraliser was lower for the low-density soot aggregates ($6.3 \times 10^1 - 4.0 \times 10^3$ particles per cm^{-3}) than the spherical particles ($2.7 \times 10^3 - 3.2 \times 10^4$ particles per cm^{-3}). This lower concentration should only improve the convergence of the charge distribution of the aggregates to a steady-state charge distribution and the resulting agreement with charging theory.

However, the discrepancy between theory and the measured charging of the aggregates was expected and is largely due to their morphology. The lower uncharged fraction of the low-density soot aggregates (differences of -0.042 to -0.069) agrees well with the -0.012 to -0.045, -0.022 to -0.061 or -0.044 to -0.085 differences reported by Xiao et al. [276] for neutralised (using ^{210}Po) diesel (d_m=30 and 230 nm, fractal dimension of 1.75), silver ($d_\mathrm{m} = 50$ to 350 nm, mass-mobility exponent of 2.07 from 100°C sintering) or silver-chain ($d_\mathrm{m} = 100$ to 300 nm, fractal dimension of 1.78 with no sintering) aggregates, respectively. These results also have excellent agreement with the -0.045 to -0.064 or -0.001 to -0.056 differences reported by Ku et al. [140] for the uncharged fraction of high aspect (> 10) particles (CNF with $d_\mathrm{m} = 400$, 600 or 700 nm or MWCNT with $d_\mathrm{m} = 188$ to 594 nm, respectively) neutralised using ^{210}Po. Tanaka et al. [235] and Kulkarni et al. [142], also found that the uncharged fraction of neutralised CNFs ($d_\mathrm{m} \approx 25$ to 170 nm and aspect ratios of 4.6 to 39.4) and neutralised CNTs ($d_\mathrm{m} = 100$ to 1000 nm and aspect ratios of ≈ 3), respectively, were lower, with differences of -0.01 to -0.13 relative to those of NaCl particles and 0.015 to -0.089 relative to theory, respectively. Rogak and Flagan [215] also observed lower uncharged fractions of titanium oxide agglomerates relative to spherical particles ($d_\mathrm{m} = 40$ to 794 nm), but to a lesser extent than the other studies, with differences of -0.01 to -0.03 between the ^{85}Kr neutralised aerosols.

The increased charging of the aggregates relative to spheres of equivalent mobilities, which is qualitatively reflected in the larger width of the charging differences shown in Figure 6.6a versus Figure 6.6b, also agrees with previous charging studies. The higher proportion of multiple charging for non-spherical particles, which further increases with particle size, was also observed by Drayton [45], Maricq [172] and Xiao et al. [276] as summarized in Table 6.3. These previous studies, with the exception of Drayton [45] (which only measured the positive charge fractions), also observed that the proportion of multiple charging was preferentially negative, as previously highlighted by Figure 6.6a. The high agreement of the measured uncharged fractions and charge distribution trends with previous studies provides some insights into the charging differences of average non-spherical particles

measured by other studies with higher uncertainty (due to multiple-charging effects) versus low-density aggregates (i.e. upper boundary of morphology deviation) characterised by this work with lower uncertainty.

Table 6.3 Ratios of doubly-charged fractions of non-spherical to spherical particles from different studies.

Study	d_m (nm)	Agglomerate	Neutralizer	$\frac{f_{-2}(\text{Non}-\text{Spherical})}{f_{-2}(\text{Spherical})}$	$\frac{f_{+2}(\text{Non}-\text{Spherical})}{f_{+2}(\text{Spherical})}$
Current Study	80 to 430	Low-Density Soot (Burner)	^{85}Kr	1.60 to 0.96	1.16 to 0.84
Drayton [45]	80 to 205	Titanium Oxide	^{85}Kr	N/A	2.06 to 0.88
Maricq [172]*	80 to 430	Soot (Burner or Diesel)	^{210}Po	1.66 to 1.01	1.61 to 0.96
Xiao et al. [276]	75 to 270	Soot (Diesel)	^{210}Po	1.57 to 1.40	1.00 to 0.73

*Results shown were calculated based on the fitted parameters for bipolar charging of soot provided by this study.

Mamakos [166] also found higher charging of aggregates by characterising the positive charge fraction ratios (i.e. f_{+2}/f_{+1} and f_{+3}/f_{+1}) of soot produced by a miniCast and neutralised using ^{85}Kr. This aerosol source and neutraliser are the same as the ones used in this work. For soot aggregates with mobility diameters below 150 nm, Mamakos' results agree within 0.006 and 0.008 of the f_{+2}/f_{+1} and f_{+3}/f_{+1} calculated from the results of this work, respectively. For larger soot aggregates ($d_m > 150$ nm), this agreement decreases by two orders of magnitude to within 0.111 and 0.104 for f_{+2}/f_{+1} and f_{+3}/f_{+1}, respectively. This significant increase in discrepancy at larger sizes is likely due to the differences in the charging of average soot aggregates measured by Mamakos [166] versus the low-density aggregates (i.e. upper boundary of morphology deviation) characterised by this work. Multiple-charging effects in the upstream DMA of the TDMA approach used by Mamakos [166], which would become more prevalent as particle size increases, may also contribute to this discrepancy. Finally, the soot aggregates between the studies are also slightly different, as the current approach also passed the particles through a catalytic stripper and ESP to generate an aerosol of uncharged, non-volatile particles.

The higher charging of aggregates was also recorded by Ahlberg and Hansson [9] and Dua et al. [46] measuring the neutralised (using ^{85}Kr and ^{204}Tl, respectively) charge fractions of singlets, doublets and triplets formed of 364 nm and 500 nm PSL particles, respectively. Both studies observed that the aggregate morphologies obtained higher charges than predicted by the Boltzmann distribution. Ahlberg and Hansson [9] accounted for this discrepancy in charging by using a capacitance (rather than volume) equivalent diameter (known as the Smoluchowski diameter) with the Boltzmann distribution.

In contrast, a few studies have observed limited effect of particle morphology on its charging. Gopalakrishnan et al. [72] found both their measurements and simulations were

relatively insensitive to particle morphology by comparing the single-to-double charge ratios of gold spheres (52 and 73 nm) or rods ($d_m \approx 30$ to 70 nm) neutralised by ^{210}Po. However, this discrepancy could be explained by the smaller range of particle sizes (i.e. sub 100 nm) range investigated by Gopalakrishnan et al. [72] compared to the other studies previously discussed. Although further investigation is required, this hypothesis is supported by the bipolar charging of spherical and non-spherical trending towards convergence at smaller particle sizes as shown in Figure 6.6a. Matsoukas and Friedlander [179] also observed no significant differences in the charged fraction of flame-generated aggregates ($d_m = 10$ to 200 nm) to spheres of zinc nitrate (30 to 200 nm), both neutralised using ^{85}Kr. However, only considering the charged fraction of an aerosol does not fully capture the degree of broadening of its charge distribution, and thus can be misleading [276].

In addition to the agreement with a vast majority of the previously discussed charging studies, the methodology of using an AAC-DMA-DMA is further supported by the high agreement (within 10%) of the other inversion parameters with theory, as shown in Figure 6.7. Each shaded area on the figure represents the repeatability of the corresponding fitted parameter, assuming a t-distribution and 95% confidence interval. As expected, the setpoints of DMA 1 and 2 had excellent agreement (average and maximum disagreement of 2.5% and 3.9%, respectively) and are highly repeatable as shown by the narrow width of the corresponding shaded area. This agreement between the DMAs is similar to the 3% uncertainty in DMA classification previously determined by Kinney et al. [129]. The non-linear agreement between the DMAs as the setpoint of DMA 2 was stepped over a range was also close to ideal, with n_f varying from 1 to 0.97. As expected, n_f deviates slightly from 1 at the larger particle sizes due to DMA 2 measuring across a larger range (and farther from the setpoint of DMA 1) to characterise the higher charge states. Finally, the transmission efficiency ($\lambda_{\Omega,\mathrm{DMA}}$) and broadening factor ($\mu_{\Omega,\mathrm{DMA}}$) of the DMA agree within 10% of values previously determined by Karlsson and Martinsson [120] and Birmili et al. [19], respectively.

6.7 Equivalent charging diameter of low-density soot aggregates

Previous studies have shown that these differences in the bipolar charging of non-spherical particles are due to their morphology affecting their capacitance [9, 263]. This aspect was demonstrated on a macro-scale by Brown and Hemingway [25] arranging steel balls in different configurations and measuring the capacitance (i.e. ability to hold charge) of the "agglomerate". This demonstration is supported by theory developed by Cheng & Yeh, which

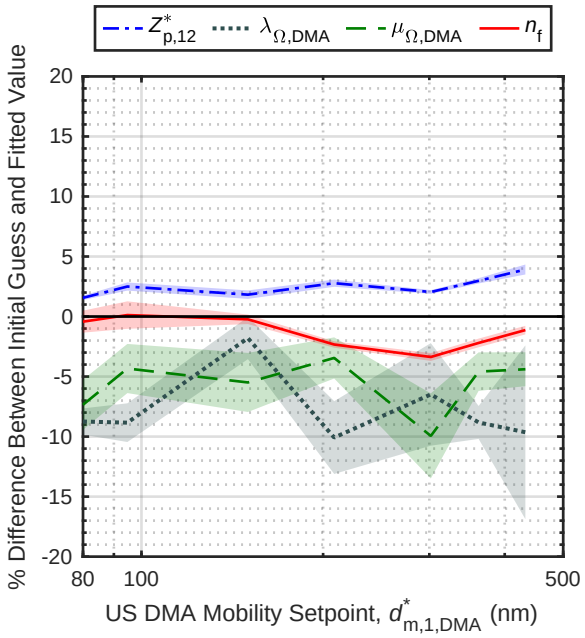

Fig. 6.7 Differences between theory ($\mu_{\Omega,DMA}$: Birmili et al. [19] and $\lambda_{\Omega,DMA}$: Karlsson and Martinsson [120]) and fitted parameters of the TDMA inversion (as described in Table 6.2). Each shaded area represents the repeatability of the corresponding fitted parameter, assuming a t-distribution and 95% confidence interval.

predicted that the charge distribution of an aerosol should broaden as the number of primary particles in an aggregate increase [31] and that the charging of a fibre is likely proportional to its length [32]. Mayya [180] took this theory one step further by proposing the capacitance of an aggregate scales with the size of its primary particles times their number to the inverse power of its fractal dimension. This theory also concluded that the capacitance of a particle is "equivalent to the rate of absorption [of bipolar ions] per unit concentration" during charging, which is related to its Smoluchowski diameter.

To capture these effects of particle morphology (i.e. change in capacitance) on its charging, the concept of a charging equivalent diameter was introduced in the early 1980s [9, 262]. Wen et al. [262] developed a theory that predicted the higher charging of non-spherical particles by approximating their morphology as a prolate spheroid. This theory determined that for a prolate spheroid with an aspect ratio between 10 to 100, its charging equivalent diameter is roughly 0.25 times its length. Han and Gentry [80] also developed a charging model for non-spherical particles based on a simplified spheroid geometry, which predicted the charging of a flake-shaped particle is equivalent to its surface-area equivalent diameter.

A model developed by Filippov [54] also supported that the discrepancy between the charging of spherical and non-spherical particles is based on differences in their capacitance,

and similar to Mayya [180], suggested the equivalent charging diameter is proportional to the radius of gyration of the aggregate. More recently, Gopalakrishnan et al. [73] expanded these theories to the transition regime using Brownian dynamics, and also predicted that non-spherical particles become more charged than spherical particles. Their model predicted that as a non-dimensional factor related to the particle morphology decreases (based on the Smoluchowski radius/capacity and projected area of the aggregate), the uncharged and multiply-charged fractions of non-spherical particles decrease and increase, respectively.

To simplify the approach of these theories, the charging equivalent diameter of the aggregates studied in this work was estimated by minimizing the least-squares difference between the experimental data and the spherical charging models of Wiedensohler [266] and Gunn and Woessner [75]. Similar approaches were first suggested by Wen et al. [262] and Ahlberg and Hansson [9], and slight variations of it have been widely used by other experiment-based charging studies, such as Rogak and Flagan [215], Drayton [45], Kulkarni et al. [142] and Ku et al. [140].

To preferentially weight the lower charge states ($|n| \leq 3$), which are a primary consideration for electrostatic methodologies with bipolar charging, one equivalent diameter was determined[9] based on the entire charge distribution at each combination of AAC-DMA 1 setpoints. The results of this approach are shown in Figure 6.8 and further demonstrate that the low-density aggregates gain more charge (i.e. their charge is equivalent to a “larger" particle) than spherical particles of similar mobilities. This figure also demonstrates that the charging results of this work are an estimate for the upper bound, with the bipolar charging of average aggregates from the same soot source falling somewhere between this upper limit and the lower limit for the charging of spherical particles (i.e. 1:1 line). These boundaries highlight the challenges of measuring the charging of non-spherical particles, and that future work is required to characterise this region. The AAC-DMA-DMA approach of this chapter, without limiting the setpoints of the classifiers to avoid multiple charging effects, could be used for this objective. While this approach would also have multiple-charging effects, it is hypothesized that their effects would be reduced and the data easier to deconvolute compared to previous TDMA approaches due to the additional particle characterisation by the AAC.

As expected, equivalent charging diameter is predicted to converge to mobility diameter at smaller particle sizes (< 68 nm), as the number of primary particles in each aggregate decrease and its corresponding morphology converges to a sphere. This progression of morphology is demonstrated in the SEM images (i.e. by comparing Figures 6.4a to 6.4g). This convergence was also observed by Drayton [45] as the mobility diameter of neutralised agglomerates of titanium oxide decreased to approximately 40 nm.

[9]The validity of this approach is discussed at the end of this section.

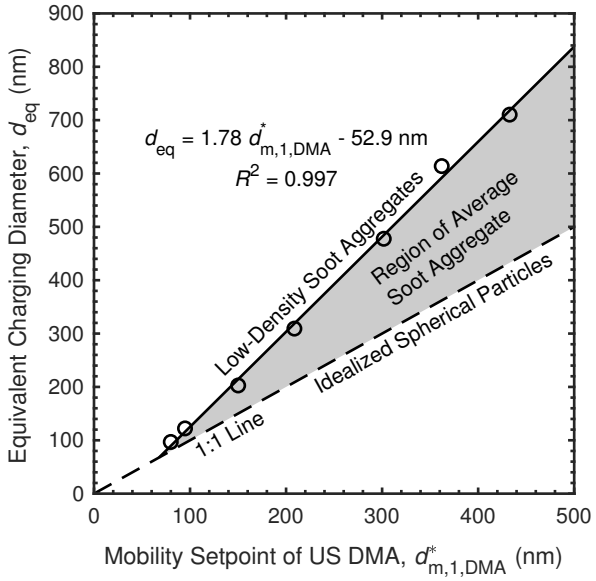

Fig. 6.8 Equivalent charging diameters of low-density soot aggregates based on fitted equivalent diameters that minimize the least-squares summation between the measured charge fractions and those predicted by theory [75, 266].

As shown in Figure 6.8, the relationship between the equivalent charging and mobility diameters was found to be linear with a slope of 1.78. It is hypothesized that this relationship will switch from a linear form to a constant offset at larger particle sizes to reflect that the aggregate morphologies usually follow a fractal relation (i.e. are bigger but are formed of a repeating structure). However, additional testing is required with particles larger than those in this current work to investigate this possible effect.

It is interesting to note that the seven equivalent charging diameters shown in Figure 6.8 correspond to three AAC setpoints, as shown in Table 6.1. Different combinations of AAC and DMA setpoints select particles with different aerodynamic and mobility diameters, which correspond to different particle masses, effective densities, and ultimately, morphologies. This charging independence from aerodynamic diameter indicates that the aggregates characterised by this work likely represent the upper bound (i.e. highest deviation from spherical particles) of average particles from the same soot source.

Drayton [45] also found that agglomerates obtained higher charge than spheres with a charging equivalent diameter ratio of 1.25 for neutralised aggregates of titanium oxide ($d_m = 20$ to 215 nm). This equivalent charging ratio has also been shown to increase with the aspect ratio of a particle. For two types of single-wall CNTs (both with aspect ratios of

≈ 3), Kulkarni et al. [142] found the charging equivalent ratio was 2.85 ($d_m = 400$ to 700 nm) or 4.34 ($d_m = 400$ to 1000 nm). Building on this work, Ku et al. [140] characterised particles with higher aspect ratios (≈ 10), and found the equivalent charging factors were 1.76 to 5.01 for CNF ($d_m = 400$ to 700 nm) and 1.72 to 1.89 for MWCNT ($d_m = 280$ to 600 nm). Finally, Tanaka et al. [235] found the equivalent charging diameter of CNFs ($d_m = 20$ to 90 nm and aspect ratios of 4.6 to 39.4) was approximately double the estimate generated by the prolate spheroid theory of Wen et al. [262].

Rogak and Flagan [215] found a charging equivalent factor of 1.1 for titanium oxide agglomerates ($d_m = 40$ to 794 nm) neutralised using ^{85}Kr. While the uncharged fractions measured by Rogak and Flagan [215] agree relatively well (but on the lower end) with the results of this chapter and other studies previously discussed, this low equivalent charging factor of 1.1 is likely underestimated by only considering the uncharged fraction of the aggregates as it does not capture the broadening of the charge distribution [276]. This underestimation was also previously discussed for the results of Matsoukas and Friedlander [179], and may also exist in the equivalent charging factors reported Ku et al. [140] and Kulkarni et al. [142] as these values were also based on measurements of uncharged fractions.

Finally, Figure 6.9a demonstrates that one equivalent charging diameter at each combination of AAC-DMA 1 setpoints can capture the same trends observed experimentally across the entire charge distribution, as shown in Figure 6.6a. The agreement between these figures is shown in Figure 6.9b and demonstrates that using the equivalent diameter with the charging theory [266, 75] reduces the differences between the experimental results of the low-density aggregate charging and theory (average and maximum absolute differences of 0.0035 and 0.0229, respectively) to similar differences (average and maximum absolute differences of 0.0042 and 0.0233, respectively) previously determined in Section 5.5 for spherical particles with the same theory, as shown in Figure 6.6b.

6.8 Effects of aggregate charging on electrostatic mobility measurements

To provide insights into the effect of these upper charging discrepancies, the relationship established for equivalent charging diameter in Figure 6.8 was propagated through the standard inversion for the SMPS. This quantification only considers an aerosol source that follows a lognormal size distribution and the error introduced by the discrepancy between the charge fractions of the low-density aggregates (i.e. those measured by this work or the upper boundary) versus those commonly used in the inversion and multiple charge correction

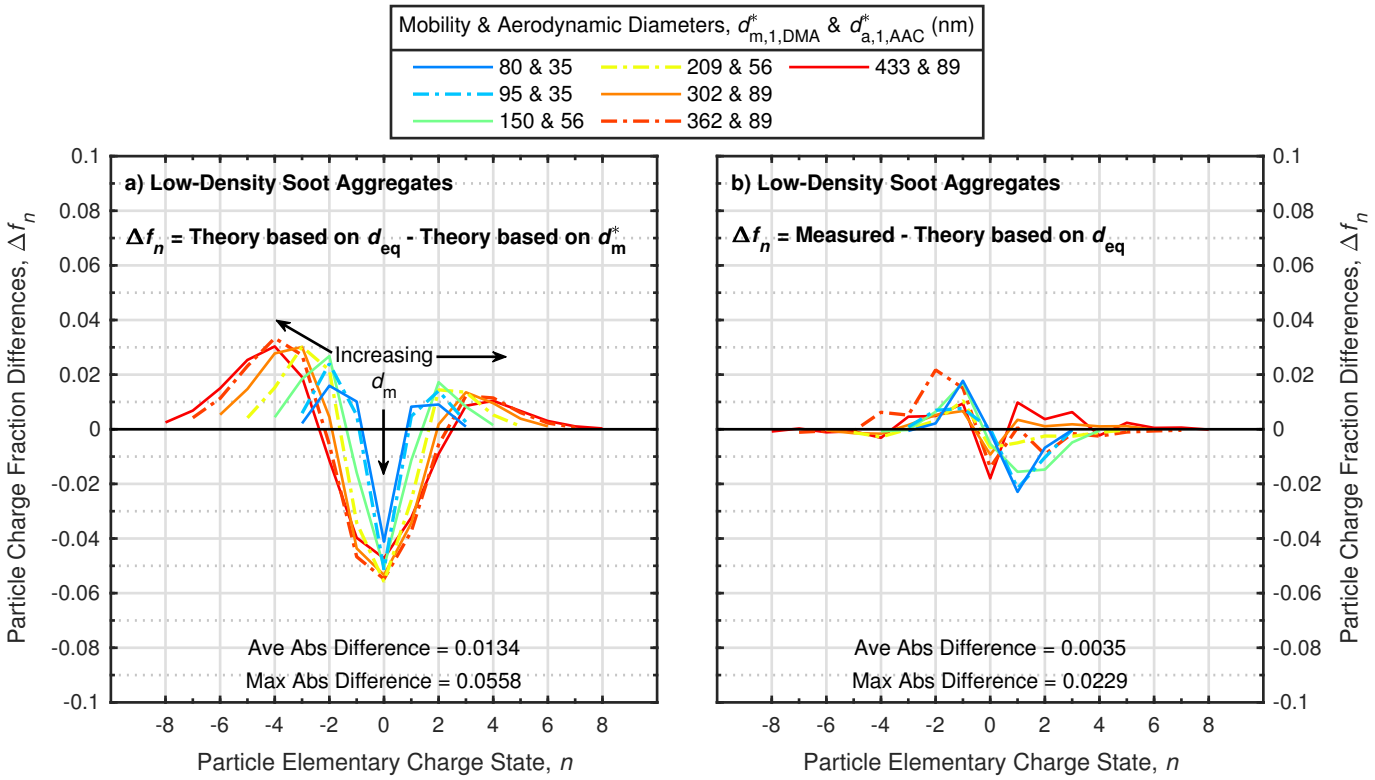

Fig. 6.9 Differences between charge fractions (f_n) from theory [75, 266] based on the equivalent charging diameter (d_{eq}) and a) theory [75, 266] based on the setpoint of the upstream DMA ($d^*_{m,1,DMA}$) or b) measured.

of the raw SMPS measurements (i.e. estimates based on Wiedensohler [266] and Gunn and Woessner [75]).

The examples considered are limited to aerosols with GMDs of 100, 200 or 400 nm (to align with the particle sizes characterised in this work) and geometric standard deviations (GSD) of 1.2, 1.7 or 2.5. This lower GSD of 1.2 avoids introducing significant errors[10] from the SMPS inversion assuming the aerosol size distribution is constant over the width of the DMA transfer function [230].

For the nine different combinations of the example GMDs and GSDs, and considering an aerosol source that only consists of low-density aggregates, the charging discrepancies would cause the lognormal parameters reported by the SMPS to vary by up to 16.9%. Specifically, the SMPS errors in terms of GMD, GSD and total particle concentration (N_{tot}) would be -16.9% to -2.1%, -5.2% to 13.9% and -2.9% to 8.7%, respectively. The GMD becomes more under-reported as the GMD or GSD of the aerosol increases, while the GSD becomes

[10] A GSD of 1.2 or greater limits the errors from this inversion assumption to 0.26% or less in terms of the measured CMD and GSD, and 0.94% or less for the reported number concentration.

less under-reported or more over-reported as the GMD of the aerosol increases or the GSD of the aerosol decreases. The N_{tot} becomes less under-reported or more over-reported as the GMD or GSD of the aerosol decreases. Since these error estimates are based on the charging of low-density aggregates rather than average aggregates from the same soot source, these values represent an upper estimate of measurement errors from the SMPS due to these charging discrepancies. Finally, the magnitude of these error estimates (up to 16.9%) agrees with the 10-15% distortion in size distributions estimated by Maricq [172] and the 15% under-reporting in total particle concentration estimated by Xiao et al. [276] for soot aggregates.

6.9 Conclusions

Previous methodologies for measuring the bipolar charge distribution of an aerosol, which are usually based on electrostatic or aerodynamic classification, are limited by their ability to produce an aerosol of homogeneous particles. To overcome these challenges, this chapter demonstrated using a tandem AAC-DMA to select non-spherical particles which have narrow ranges of different equivalent diameters (i.e. aerodynamic and mobility diameters) and mass, simultaneously.

This approach was validated by the SEM images, which highlighted the uniformity of the tandem-classified particles and visualized their change in morphology at different setpoint combinations of the AAC and DMA. Electrical mobility distributions of the tandem-classified particles also supported this new methodology and sharply contrasted with those collected after classification of the non-spherical particles by the AAC or DMA alone. This approach is further supported by the agreement of these size distributions with the theoretical inversion of the AAC-DMA-DMA. This inversion determined that the setpoints of the upstream and downstream DMA agreed within 3.9%, while the transmission efficiency and broadening factor of the DMA transfer function both agreed within 10% of theory.

While this new approach produces an aerosol of homogeneous particles, the AAC setpoint must be sufficiently lower than the DMA setpoint to avoid introducing multiply-charged particles during DMA classification, thus limiting the homogeneous particle source to a subset of particle equivalent diameters and masses. This subset of particles is not representative of "average" non-spherical particles from the same source, but rather those that deviate the most from spherical particles. Therefore, characterising this subset of homogeneous, non-spherical particles estimates the upper bound due to this deviation in morphology.

To quantify this upper boundary for bipolar charging, an AAC-DMA-DMA was used to measure up to 17 charge states (i.e. -8 to +8) of size-resolved, soot aggregates with

mobility diameters between 80 and 433 nm. The low-density soot aggregates obtained higher charges than predicted by theory and were preferentially negatively-charged. Relative to the measurements, theory overestimated the uncharged fraction (by 0.042 to 0.069) and, to a lesser extent, the single charge fractions (by up to 0.037) of the soot aggregates. It also underestimated the proportion of multiply-charged aggregates by up to 0.039 at one multiple charge state and size, or by up to 0.123 or 0.034 cumulatively at one particle size for negative or positive multiply-charged particles, respectively.

The equivalent charging diameters of the low-density soot aggregates was found to be linearly related to their mobility diameters ($d_{\mathrm{eq}} = 1.78 d_{\mathrm{m}} - 52.9$ nm), with the two equivalent diameters predicted to converge at smaller particle sizes ($d_{\mathrm{m}} < 68$ nm). This charging independence from aerodynamic diameter indicates that the low-density aggregates characterised by this work likely represent the upper bound (i.e. highest deviation from spherical particles) of average particles from the same source of flame soot. These results also demonstrated that one equivalent charging diameter at each combination of AAC-DMA 1 setpoints was able to capture the same trends observed experimentally across the entire charge distribution. Furthermore, this equivalent charging diameter reduced the differences between the experimental results of the low-density aggregate charging and theory (average and maximum absolute differences of 0.0035 and 0.0229, respectively) to similar differences (average and maximum absolute differences of 0.0042 and 0.0233, respectively) previously determined for spherical particles with the same charging theory.

The high-agreement of the measured uncharged fractions and charge distribution trends with previous studies provides some insights into the charging differences of average non-spherical particles measured by other studies with higher uncertainty (due to multiple-charging effects) versus low-density aggregates (i.e. upper boundary of morphology deviation) characterised by this work with lower uncertainty. The higher uncertainties in previous studies due to multiple charging effects and the restricted range of particle properties currently studied highlight the challenges of characterising the bipolar charging of non-spherical particles. Therefore, future work building on the demonstrated AAC-DMA-DMA approach is required to address these gaps.

Chapter 7

Conclusions

7.1 Project conclusions

The overall objective of this dissertation was to develop state-of-the-art methodologies for characterising the aerodynamic size and bipolar charge distributions of an aerosol by advancing the development and knowledge of a relatively new aerosol instrument, the Aerodynamic Aerosol Classifier (AAC). The AAC classifies aerosol particles based on their relaxation time, and due to its novel operating principle provides the opportunity to overcome challenges of previous methodologies used for similar sizing and charging measurements. To recognize these advantages, this thesis is the first to develop and validate different instrument configurations with the AAC, including the associated theory and required data inversions, for these applications.

To gain insights into the practical implementation of the AAC and account for non-ideal particle and flow behaviours within the classifier, its transfer function was first characterised (for setpoints from 32 nm to 3 µm) by using tandem AACs and comparing the experimental results to the theoretical tandem deconvolution. These results show that the AAC transmission efficiency (λ_Ω) is 2.6 to 5.1 times higher than a combined ^{85}Kr radioactive neutraliser and Differential Mobility Analyser (DMA) system. However, the width factor of the AAC transfer function (μ_Ω) is 1.3 to 1.9 times higher than predicted by theory. Using this characterised transfer function, the deconvolution theory to accurately measure the aerodynamic size distribution of an aerosol $(\mathrm{d}N/\mathrm{d}\log d_\mathrm{a})$ by stepping the AAC setpoint ($d^*_{\mathrm{a},i}$) whilst in series with a particle detector (such as a Condensation Particle Counter, CPC) was developed as follows:

$$\left.\frac{\mathrm{d}N(d_\mathrm{a})}{\mathrm{d}\log d_\mathrm{a}}\right|_{d^*_{\mathrm{a},i}} = \frac{N_\mathrm{det}(d^*_{\mathrm{a},i})\ln(10)}{\eta(d^*_{\mathrm{a},i})\left.\frac{\mathrm{d}\log d_\mathrm{a}}{\mathrm{d}\log\tau}\right|_{d^*_{\mathrm{a},i}}\beta^*_i}, \tag{7.1}$$

where N_det is the number concentration of the particles classified by the AAC and η is the counting efficiency of the particle counter downstream of the AAC, both at AAC setpoint $d^*_{\mathrm{a},i}$, while β^*_i is the deconvolution parameter. This transfer function characterisation and stepping deconvolution were validated by comparing size distributions measured with an AAC-CPC system against parallel measurements taken with other commercial aerosol instruments from the same aerosol sources.

The stepping AAC was demonstrated to overcome the low classification resolutions and set measurement ranges (which focus on larger particles) of previous methodologies for aerodynamic sizing by leveraging the high transmission efficiency, independence from particle charging, and adjustable classification range and resolution of the AAC. However, this approach requires the AAC setpoint to be stepped and stabilised before each measurement, which forces trade-offs between measurement time and step resolution. To overcome this trade-off, this thesis then developed and validated novel theory, which allows the speed of the AAC classifier to be continuously varied (following an exponential function), rather than stepped. The transfer function of the scanning AAC was derived by limited trajectory theory and was found to be the same shape as that of the steady-state AAC. This outcome was then used to adapt the parameterized transfer function of the steady-state AAC based on particle streamline theory, which accounts for non-idealized particle and flow behaviours within the classifier, to the scanning AAC. The average of these transfer functions over the counting time of the particle detector downstream of the scanning AAC was then quantified, and the corresponding deconvolution parameters determined.

For sufficiently long scan times, the deconvolution parameter (β^*) based on particle streamline theory for either the steady-state/stepping AAC (β^*_ss) or scanning AAC (β^*_sc) was found to be the same, as follows:

$$\beta^*_\mathrm{ss} = \beta^*_\mathrm{sc} = \lambda_\Omega\,\mu_\Omega\left[\ln\left(\frac{1+\frac{\beta}{\mu_\Omega}}{1-\frac{\beta}{\mu_\Omega}}\right) + \frac{\mu_\Omega}{\beta}\ln\left(1-\left(\frac{\beta}{\mu_\Omega}\right)^2\right)\right], \tag{7.2}$$

where β is the non-dimensional flow parameter of the AAC based on its aerosol sample flow to sheath flow ratio and the same deconvolution equation (i.e. Equation 7.1) was found for the scanning AAC. This deconvolution theory and the practical implementation of the scanning AAC was validated by the high agreement (within 11.3%) of its measurements compared to those of the stepping AAC of three different aerosol sources (DOS, NaCl

and Soot). If the stability of the aerosol source is considered, this agreement improved to 2.0% or better. This validation was further supported by the high agreement (within 8.7%) of scanning measurements of PSL particles (six sizes between 100 nm to 2.02 µm). This scanning approach was demonstrated to reduce the AAC measurement time (1.1 to 2.6 times faster), while increasing the resolution of the measured distribution (6.1 to 9.0 times higher classes per decade).

In addition to these advances in aerosol sizing, this thesis also developed and validated a new method to measure the bipolar charge distribution of spherical particles. This approach uses an AAC in series with a DMA and CPC and overcomes significant limitations of the commonly used tandem DMA system, such as multiply-charged particle artefacts and low measurement signals. It was demonstrated that the AAC-DMA system could resolve more particle charge fractions (demonstrated to ± 6) across a larger range of particle sizes from the same aerosol source. The tandem AAC-DMA methodology also has the sensitivity to detect other charging phenomena and was shown to capture the effects of different sample flow rates through the charger, free-ions downstream of the charger, the inlet insert on the ^{85}Kr charger and different particle chargers (x-ray, old ^{85}Kr and new ^{85}Kr).

The charge fractions of the spherical particles at low-flow (0.6 L/min) through the new ^{85}Kr charger agreed well (average absolute difference of 0.007) with widely-used charging theory. However, significant deviations from theory (up to a 0.044 difference in charge fractions) were found with a higher sample flow rate (1.2 L/min), with different exposure times to free-ions downstream of the charger, or with the inlet insert on the new ^{85}Kr charger. It was found that regardless of flow rate, a soft x-ray charger resulted in charge fractions which deviated significantly from theory (up to a 0.084 difference in charge fractions), producing higher and lower fractions of positively and negatively charged particles relative to theory, respectively.

However, a large portion of naturally occurring and human-made particles have non-spherical morphologies, which greatly complicate charging studies using previous methodologies (which are predominantly electrostatic techniques) or the AAC-DMA approach developed in this work. These challenges stem from the fact that the classified particles are not homogeneous prior to charging. It was demonstrated that generating an aerosol of homogeneous particles, which has narrow ranges of particle mass, mobility and relaxation time simultaneously, with either a DMA or AAC is challenging. Particles classified by the DMA are often not homogeneous (or monodispersed) due to multiply-charged particles. While the AAC overcomes this challenge for spherical particles (as demonstrated and leveraged for the charging of spherical particles in this work), homogeneity is not achieved with non-spherical particles due to their effective density varying with particle size. To

address this gap, this thesis demonstrated using an AAC and DMA in tandem to generate an aerosol of homogeneous, non-spherical particles. This approach was validated using images from a scanning electron microscope (SEM) and electrical mobility measurements of the tandem-classified particles to highlight their homogeneity.

To limit the effects of multiple charging during classification by the upstream DMA in this approach, only a subset of DMA and AAC setpoints are permitted. While this subset is not representative of "average" non-spherical particles from the same aerosol source, this subset of low-density particles deviates the most from spherical morphology, and thus, provides insights into the upper bound of other particle properties, such as charging. Using this approach to select homogeneous particles, the bipolar charge distribution of low-density soot aggregates was then measured using another DMA downstream. This AAC-DMA-DMA approach was demonstrated to measure up to 17 individual charge states (i.e. -8 to +8) after neutralisation (with ^{85}Kr) of size-resolved, soot aggregates with mobility diameters between 80 and 433 nm. The low-density soot aggregates obtained higher charges than predicted by theory, which overestimated the uncharged fraction (by 0.042 to 0.069) and, to a lesser extent, the single charge fractions (by up to 0.037) of the low-density soot aggregates, while underestimating their proportion of multiple charging (by up to 0.135 cumulatively at one particle size or up to 0.039 at one multiple charge state and size). These charging discrepancies represent an upper bound of the bipolar charging of average aggregates from the same source of flame soot.

The charging discrepancies of the spherical and non-spherical particles identified by this work are likely due to the simplifying assumptions made by the widely-utilized charging theory. The spherical charging results demonstrated that assuming the steady-state charge distribution is reached may not be valid for instances of common aerosol applications and that this theory neglects the effects of free-ions downstream of the charger. The non-spherical charging results highlighted that this theory neglects the morphology of non-spherical particles. Therefore, rigorous measurement of particle charge distributions and utilization of more comprehensive charging models are necessary for accurate aerosol characterisation, such as standard SMPS measurements.

The AAC applications developed and validated in this dissertation are intended to support the aerosol community. It is hoped that others will use these new methodologies to further characterise the sizing and bipolar charging of aerosols, leading to a greater understanding of aerosol science. To support this progression, the approaches developed in this work of stepping or scanning the AAC for aerodynamic sizing have been directly incorporated within the commercial version of the instrument. It is also hoped that others will build upon the

foundational AAC theory established in this work and continue to develop the AAC to further advance aerosol methodologies.

7.2 Future work

Through developing these new AAC methodologies, additional knowledge gaps were identified. The AAC inversions developed in this work for measuring the aerodynamic size distribution of an aerosol are generalized and valid across the entire measurement range of the AAC. However, the accuracy of these measurements at particular operating conditions or for different particle properties could be improved by further characterizing the AAC performance. For example, characterising the AAC transfer function using tandem AACs (as developed in Chapter 3) with spherical particles between 3 to 6 µm, across its entire measurement range with non-spherical particles or at different ratios of classifier flows (i.e. $\beta \neq 10$) would improve the accuracy of size distributions measurements using the stepping or scanning AAC at similar conditions. These AAC sizing methodologies could also be further validated by comparisons against an ELPI+ (i.e. a high-resolution version of the classic ELPI) or an APS. Furthermore, the discrepancy between the theoretical and actual width of the AAC transfer function identified by this work (and hypothesized to be due to flow effects within the classifier) also provides an opportunity to further optimize the AAC and improve its classification resolution.

To accelerate measurements with the scanning AAC, the arrival time theory to account for viscous flows within the classifier and downstream plumbing/detector could be developed (as discussed in Sections 4.5 and 4.6). Similarly, higher-order inversion schemes (such as the Twomey or L-curve algorithm) and different speed profiles for the classifier could also be investigated to accelerate measurements of the scanning AAC further.

The advantages of the tandem AAC-DMA system for measuring the bipolar charging of spherical particles could also be used to investigate the charging effects of different particle compositions and additional charging conditions (i.e. flow rates, particle and ion concentrations). These results would provide further insights into the requirements for reaching a steady-state charge distribution and support the validation of new charging theory and models. The AAC-DMA-DMA system also overcomes challenges of previous methodologies for measuring the bipolar charging of non-spherical particles. However, this approach has lower transmission efficiencies (due to charging limitations) and, to avoid multiple charging artefacts, is restricted to a subset of particle properties (which represent an upper bound rather than an average particle from the same aerosol source). These constraints

highlight the challenges of measuring the bipolar charging of non-spherical particles and the opportunity to build upon the methodologies developed in this thesis for this purpose.

References

[1] Adachi, M., Kousaka, Y., and Okuyama, K. (1985). Unipolar and bipolar diffusion charging of ultrafine aerosol particles. *Journal of Aerosol Science*, 16(2):109–123.

[2] Adachi, M., Liu, B. Y. H., and Pui, D. Y. H. (1991). Development of an Automatic System for Measuring Particle Charge and Size distributions in a clean room. *Particle & Particle Systems Characterization*, 8(1-4):200–208.

[3] Adachi, M., Okuyama, K., and Kousaka, Y. (1987). Simple Evaluation Method of Bipolar Diffusion Charging of Aerosol Particles and Its Application to Smoke Detectors. *Aerosol Science and Technology*, 7(2):217–229.

[4] Adachi, M., Okuyama, K., Kozuru, H., Kousaka, Y., and Pui, D. Y. H. (1989). Bipolar Diffusion Charging of Aerosol Particles Under High Particle/Ion Concentration Ratios. *Aerosol Science and Technology*, 11(2):144–156.

[5] Adachi, M., Okuyana, K., and Kousaka, Y. (1983). Electrical neutralization of charged aerosol particles by bipolar ions. *Journal of Chemical Engineering of Japan*, 16(3):229–235.

[6] Adachi, M., Okuyana, K., Kousaka, Y., and Takahasi, T. (1980). Electrical Charging of Uncharged Aerosol Particles Under at Bipolar Ion Concentrations. *Journal of Chemical Engineering of Japan*, 13(1):55–60.

[7] Adachi, M., Pui, D. Y. H., and Liu, B. Y. H. (1993). Aerosol Charge Neutralization by a Corona Ionizer. *Aerosol Science and Technology*, 18(1):48–58.

[8] Agarwal, J. K. and Sem, G. J. (1980). Continuous flow, single-particle-counting condensation nucleus counter. *Journal of Aerosol Science*, 11(4):343–357.

[9] Ahlberg, M. S. and Hansson, H.-C. (1983). Equilibrium charge distribution of multiplets of monodisperse latex spheres. *Journal of Aerosol Science*, 14(4):499–505.

[10] Ahn, K.-H. and Chung, H. (2010). Aerosol electrical mobility spectrum analyzer. *Journal of Aerosol Science*, 41(4):344–351.

[11] Ahn, K. H., Sohn, S. H., Jung, C. H., and Choi, M. (2001). In situ measurement of nano particle size distribution and charge characteristics in H2/O2/TEOS diffusion flame. *Scripta Materialia*, 44(8-9):1889–1892.

[12] Alonso, M., Alguacil, F. J., Nomura, T., and Kousaka, Y. (2001). Examination of after-charging effects downstream of an aerosol neutralizer. *Journal of Aerosol Science*, 32(2):287–294.

[13] Alonso, M., Kousaka, Y., Nomura, T., Hashimoto, N., and Hashimoto, T. (1997). Bipolar charging and neutralization of nanometer-sized aerosol particles. *Journal of Aerosol Science*, 28(8):1479–1490.

[14] Babick, F., Hillemann, L., Stintz, M., Dillenburger, T., Pitz, M., Hellmann, A., Antonyuk, S., Ripperger, S., Huber, F. J. T., Will, S., Wernet, R., Seipenbusch, M., Gensch, M., Weber, A., Kiesler, D., Kruis, E., Friehmelt, R., and Sachweh, B. (2018). Multiparameter Characterization of Aerosols. *Chemie Ingenieur Technik*, 90(7):923–936.

[15] Balachandran, W., Kulon, J., Koolpiruck, D., Dawson, M., and Burnel, P. (2003). Bipolar charge measurement of pharmaceutical powders. *Powder Technology*, 135-136:156–163.

[16] Baron, P. A. (1986). Calibration and Use of the Aerodynamic Particle Sizer (APS 3300). *Aerosol Science and Technology*, 5(1):55–67.

[17] Bau, S. and Witschger, O. (2013). A modular tool for analyzing cascade impactors data to improve exposure assessment to airborne nanomaterials. *Journal of Physics: Conference Series*, 429(1):12002.

[18] Baxter, K., Jones, C., and Fletcher-Wood, G. (2008). High sensitivity sensor for continuous direct measurement of bipolar charged aerosols. *Journal of Physics: Conference Series*, 142:12045.

[19] Birmili, W., Stratmann, F., Wiedensohler, A., Covert, D., Russell, L. M., and Berg, O. (1997). Determination of Differential Mobility Analyzer Transfer Functions Using Identical Instruments in Series. *Aerosol Science and Technology*, 27(2):215–223.

[20] Biskos, G., Mastorakos, E., and Collings, N. (2004). Monte-Carlo simulation of unipolar diffusion charging for spherical and non-spherical particles. *Journal of Aerosol Science*, 35(6):707–730.

[21] Biskos, G., Reavell, K., and Collings, N. (2005a). Description and theoretical analysis of a differential mobility spectrometer. *Aerosol Science and Technology*, 39(6):527–541.

[22] Biskos, G., Reavell, K., and Collings, N. (2005b). Electrostatic characterisation of corona-wire aerosol chargers. *Journal of Electrostatics*, 63(1):69–82.

[23] Bricard, J., Madelaine, G., and Pourprix, M. (1976). Contribution a l'etude de la charge electrique des aerosols: Description de l'appareillage—I. *Journal of Aerosol Science*, 7(1):37 – 42.

[24] Brown, R. C. (1997). Tutorial review: Simultaneous measurement of particle size and particle charge. *Journal of Aerosol Science*, 28(8):1373–1391.

[25] Brown, R. C. and Hemingway, M. A. (1995). Electric charge distribution and capacitance of agglomerates of spherical particles: Theory and experimental simulation. *Journal of Aerosol Science*, 26(8):1197–1206.

[26] Buckley, A. J., Wright, M. D., and Henshaw, D. L. (2008). A Technique for Rapid Estimation of the Charge Distribution of Submicron Aerosols under Atmospheric Conditions. *Aerosol Science and Technology*, 42(12):1042–1051.

[27] Burtscher, H., Reis, A., and Schmidt-Ott, A. (1986). Particle charge in combustion aerosols. *Journal of Aerosol Science*, 17(1):47–51.

[28] Cambustion (2018). Aerodynamic Aerosol Classifier (AAC)- User Manual (Original Instructions) Version 1.13.

[29] Chein, H. and Lundgren, D. A. (1993). A Virtual Impactor with Clean Air Core for the Generation of Aerosols with Narrow Size Distributions. *Aerosol Science and Technology*, 18(4):376–388.

[30] Chen, B. T., Cheng, Y. S., and Yeh, H. C. (1990). A Study of Density Effect and Droplet Deformation in the TSI Aerodynamic Particle Sizer. *Aerosol Science and Technology*, 12(2):278–285.

[31] Cheng, Y.-S. and Yeh, H.-C. (1981). Equilibrium bipolar charge distribution of aerosols consisting of chains of uniform spheres. *Journal of Colloid and Interface Science*, 84(2):444–450.

[32] Cheng, Y.-S. and Yeh, H.-C. (1983). Theoretical equilibrium bipolar charge distributions of chain aggregates with uniform spheres. *Journal of Aerosol Science*, 14(4):489–494.

[33] Clement, C. F. and Harrison, R. G. (1992). The charging of radioactive aerosols. *Journal of Aerosol Science*, 23(5):481–504.

[34] Cohen, A. J., Brauer, M., Burnett, R., Anderson, H. R., Frostad, J., Estep, K., Balakrishnan, K., Brunekreef, B., Dandona, L., Dandona, R., Feigin, V., Freedman, G., Hubbell, B., Jobling, A., Kan, H., Knibbs, L., Liu, Y., Martin, R., Morawska, L., Pope III, C. A., Shin, H., Straif, K., Shaddick, G., Thomas, M., van Dingenen, R., van Donkelaar, A., Vos, T., Murray, C. J. L., and Forouzanfar, M. H. (2017). Estimates and 25-year trends of the global burden of disease attributable to ambient air pollution: an analysis of data from the Global Burden of Diseases Study 2015. *The Lancet*, 389(10082):1907–1918.

[35] Cohen, B. S., Xiong, J. Q., Fang, C.-P., and Li, W. (1998). Deposition of Charged Particles on Lung Airways. *Health Physics*, 74(5):554–560.

[36] Collins, D. R., Cocker, D. R., Flagan, R. C., and Seinfeld, J. H. (2004). The Scanning DMA Transfer Function. *Aerosol Science and Technology*, 38(8):833–850.

[37] Collins, D. R., Flagan, R. C., and Seinfeld, J. H. (2002). Improved Inversion of Scanning DMA Data. *Aerosol Science and Technology*, 36(1):1–9.

[38] Conner, W. D. (1966). An Inertial-Type Particle Separator for Collecting Large Samples. *Journal of the Air Pollution Control Association*, 16(1):35–38.

[39] Covert, D., Wiedensohler, A., and Russell, L. (1997). Particle Charging and Transmission Efficiencies of Aerosol Charge Neutralizes. *Aerosol Science and Technology*, 27(2):206–214.

[40] Dahneke, B. and Flachsbart, H. (1972). An aerosol beam spectrometer. *Journal of Aerosol Science*, 3(5):345–349.

[41] de La Verpilliere, J. L., Swanson, J. J., and Boies, A. M. (2015). Unsteady bipolar diffusion charging in aerosol neutralisers: A non-dimensional approach to predict charge distribution equilibrium behaviour. *Journal of Aerosol Science*, 86(Supplement C):55–68.

[42] DeCarlo, P. F., Slowik, J. G., Worsnop, D. R., Davidovits, P., and Jimenez, J. L. (2004). Particle morphology and density characterization by combined mobility and aerodynamic diameter measurements. Part 1: Theory. *Aerosol Science and Technology*, 38(12):1185–1205.

[43] Dickau, M., Johnson, T. J., Thomson, K., Smallwood, G., and Olfert, J. S. (2015). Demonstration of the CPMA-Electrometer System for Calibrating Black Carbon Particulate Mass Instruments. *Aerosol Science and Technology*, 49(3):152–158.

[44] Dodd, E. E. (1953). The Statistics of Liquid Spray and Dust Electrification by the Hopper and Laby Method. *Journal of Applied Physics*, 24(1):73–80.

[45] Drayton, P. (1997). Experimental and theoretical studies of aerosol agglomerates.

[46] Dua, S. K., Mayya, Y. S., and Kotrappa, P. (1980). Equilibrium charge distribution on doublets and triplets of uniform 0.500 μm diameter polystyrene spheres—an experimental study. *Journal of Aerosol Science*, 11(4):415–419.

[47] Dubey, P. and Dhaniyala, S. (2008). Analysis of Scanning DMA Transfer Functions. *Aerosol Science and Technology*, 42(7):544–555.

[48] Dubey, P. and Dhaniyala, S. (2011). A New Approach to Calculate Diffusional Transfer Functions of Scanning DMAs. *Aerosol Science and Technology*, 45(8):1031–1040.

[49] Eggersdorfer, M. L., Gröhn, A. J., Sorensen, C. M., McMurry, P. H., and Pratsinis, S. E. (2012). Mass-mobility characterization of flame-made ZrO2 aerosols: Primary particle diameter and extent of aggregation. *Journal of Colloid and Interface Science*, 387(1):12–23.

[50] Ehara, K., Hagwood, C., and Coakley, K. J. (1996). Novel method to classify aerosol particles according to their mass-to-charge ratio - aerosol particle mass analyser. *Journal of Aerosol Science*, 27(2):217–234.

[51] Emets, E. P., Kascheev, V. A., and Poluektov, P. P. (1991). Simultaneous measurement of aerosol particle charge and size distributions. *Journal of Aerosol Science*, 22(3):389–394.

[52] Enghoff, M. B. and Svensmark, J. (2017). Measurement of the charging state of 4–70nm aerosols. *Journal of Aerosol Science*, 114:13–20.

[53] Fierz, M., Houle, C., Steigmeier, P., and Burtscher, H. (2011). Design, Calibration, and Field Performance of a Miniature Diffusion Size Classifier. *Aerosol Science and Technology*, 45(1):1–10.

[54] Filippov, A. V. (1994). Charge distribution among non-spherical particles in a bipolar ion environment. *Journal of Aerosol Science*, 25(4):611–615.

[55] Finlay, W. H. (2001). *The mechanics of inhaled pharmaceutical aerosols: an introduction*. Academic Press, San Diego, USA.

[56] Fissan, H., Hummes, D., Stratmann, F., Büscher, P., Neumann, S., Pui, D. Y. H., and Chen, D. (1996). Experimental Comparison of Four Differential Mobility Analyzers for Nanometer Aerosol Measurements. *Aerosol Science and Technology*, 24(1):1–13.

[57] Fjeld, R., Gauntt, R. O., and McFarland, A. R. (1981). Aerosol charging by bipolar ions of unequal current densities: experiments in low electric fields. *Journal of Colloid and Interface Science*, 83(1):82–89.

[58] Fjeld, R. A., Deyuan Wu, and McFarland, A. R. (1988). Bipolar charging of particles in the 1 to 10 μm diameter size range. In *Conference Record of the 1988 IEEE Industry Applications Society Annual Meeting*, pages 1728–1732 vol.2.

[59] Fjeld, R. A., Wu, D., and McFarland, A. R. (1990). Evaluation of continuum regime theories for bipolar charging of particles in the 0.3-13 μm diameter size range. *IEEE Transactions on Industry Applications*, 26(3):523–528.

[60] Flagan, R. C. (1998). History of Electrical Aerosol Measurements. *Aerosol Science and Technology*, 28(4):301–380.

[61] Flagan, R. C. (2004). Opposed Migration Aerosol Classifier (OMAC). *Aerosol Science and Technology*, 38(9):890–899.

[62] Flanagan, V. P. V. and O'Connor, T. C. (1961). Ionization equilibrium in aerosols. *Geofisica pura e applicata*, 50(1):148–154.

[63] Foot, E., Clark, J., and Withers, P. (2000). A comparison of two techniques for the measurement of particle size and mobility in an electric field. *Journal of Aerosol Science*, 31(1):610–611.

[64] Forster, P., Ramaswamy, V., Artaxo, P., Berntsen, T., Betts, R., Fahey, D. W., Haywood, J., Lean, J., Lowe, D. C., Myhre, G., Nganga, J., Prinn, R., Raga, G., Schulz, M., van Dorland, R., Bodeker, G., Boucher, O., Collins, W. D., Conway, T. J., Dlugokencky, E., Elkins, J. W., Etheridge, D., Foukal, P., Fraser, P., Geller, M., Joos, F., Keeling, C. D., Kinne, S., Lassey, K., Lohmann, U., Manning, A. C., Montzka, S., Oram, D., O'Shaughnessy, K., Piper, S., Plattner, G.-K., Ponater, M., Ramankutty, N., Reid, G., Rind, D., Rosenlof, K., Sausen, R., Schwarzkopf, D., Solanki, S. K., Stenchikov, G., Stuber, N., Takemura, T., Textor, C., Wang, R., Weiss, R., and Whorf, T. (2007). Changes in Atmospheric Constituents and in Radiative Forcing. In Solomon, S., Qin, D., Manning, M., Chen, Z., Marquis, M., Averyt, K. B., Tignor, M., and Miller, H. L., editors, *Climate Change 2007: The Physical Science Basis. Contribution of Working Group I to the 4th Assessment Report of the Intergovernmental Panel on Climate Change*. Cambridge Univ. Press, Cambridge, UK, and New York.

[65] Forsyth, B., Liu, B. Y. H., and Romay, F. J. (1998). Particle Charge Distribution Measurement for Commonly Generated Laboratory Aerosols. *Aerosol Science and Technology*, 28(6):489–501.

[66] Fuchs, N. A. (1963). On the stationary charge distribution on aerosol particles in a bipolar ionic atmosphere. *Geofisica pura e applicata*, 56(1):185–193.

[67] Gagné, S., Leppä, J., Petäjä, T., McGrath, M. J., Vana, M., Kerminen, V.-M., Laakso, L., and Kulmala, M. (2012). Aerosol charging state at an urban site: new analytical approach and implications for ion-induced nucleation. *Atmospheric Chemistry and Physics*, 12(10):4647–4666.

[68] Gauntt, R. O., Fjeld, R. A., and Mcfarland, A. R. (1984). Bipolar Charging of Near-Micrometer Sized Aerosol. *IEEE Transactions on Industry Applications*, IA-20(6):1636–1641.

[69] Giechaskiel, B., Bonnel, P., Perujo, A., and Dilara, P. (2019). Solid Particle Number (SPN) Portable Emissions Measurement Systems (PEMS) in the European Legislation: A Review. *International Journal of Environmental Research and Public Health*, 16(23):4819.

[70] Gillespie, T. and Langstroth, G. O. (1952). An Instrument for Determining the Electric Charge Distribution in Aerosols. *Canadian Journal of Chemistry*, 30(12):1056–1068.

[71] Glover, W. and Chan, H.-K. (2004). Electrostatic charge characterization of pharmaceutical aerosols using electrical low-pressure impaction (ELPI). *Journal of Aerosol Science*, 35(6):755–764.

[72] Gopalakrishnan, R., McMurry, P. H., and Hogan, C. J. (2015). The Bipolar Diffusion Charging of Nanoparticles: A Review and Development of Approaches for Non-Spherical Particles. *Aerosol Science and Technology*, 49(12):1181–1194.

[73] Gopalakrishnan, R., Meredith, M. J., Larriba-Andaluz, C., and Hogan, C. J. (2013a). Brownian dynamics determination of the bipolar steady state charge distribution on spheres and non-spheres in the transition regime. *Journal of Aerosol Science*, 63:126–145.

[74] Gopalakrishnan, R., Thajudeen, T., Ouyang, H., and Hogan, C. J. (2013b). The unipolar diffusion charging of arbitrary shaped aerosol particles. *Journal of Aerosol Science*, 64(Supplement C):60–80.

[75] Gunn, R. and Woessner, R. H. (1956). Measurements of the systematic electrification of aerosols. *Journal of Colloid Science*, 11(3):254–259.

[76] Gupta, A. and McMurry, P. H. (1989). A Device for Generating Singly Charged Particles in the 0.1–1.0-μm Diameter Range. *Aerosol Science and Technology*, 10(3):451–462.

[77] Gysel, M., McFiggans, G. B., and Coe, H. (2009). Inversion of tandem differential mobility analyser (TDMA) measurements. *Journal of Aerosol Science*, 40(2):134–151.

[78] Han, B., Hudda, N., Ning, Z., Kim, H.-J., Kim, Y.-J., and Sioutas, C. (2009). A novel bipolar charger for submicron aerosol particles using carbon fiber ionizers. *Journal of Aerosol Science*, 40(4):285–294.

[79] Han, B., Shimada, M., Okuyama, K., and Choi, M. (2003). Classification of monodisperse aerosol particles using an adjustable soft X-ray charger. *Powder Technology*, 135-136:336–344.

[80] Han, R.-J. and Gentry, J. W. (1991). Unipolar and bipolar charging of platelets. *Journal of Aerosol Science*, 22:S227 – S230.

[81] He, M. and Dhaniyala, S. (2013). A multiple charging correction algorithm for scanning electrical mobility spectrometer data. *Journal of Aerosol Science*, 61:13–26.

[82] He, M. and Dhaniyala, S. (2014). Experimental characterization of flowrate-dependent bipolar diffusion charging efficiencies of sub-50 nm particles. *Journal of Aerosol Science*, 76:175–187.

[83] Hernandez-Sierra, A., Alguacil, F. J., and Alonso, M. (2003). Unipolar charging of nanometer aerosol particles in a corona ionizer. *Journal of Aerosol Science*, 34(6):733–745.

[84] Hinds, W. C. (1999). *Aerosol technology: properties, behavior, and measurement of airborne particles*. Wiley-Interscience Publication, Hoboken, NJ, 2nd ed. edition.

[85] Hochrainer, D. (1971). A new centrifuge to measure the aerodynamic diameter of aerosol particles in the submicron range. *Journal of Colloid and Interface Science*, 36(2):191–194.

[86] Hoppel, W. A. (1978). Determination of the aerosol size distribution from the mobility distribution of the charged fraction of aerosols. *Journal of Aerosol Science*, 9(1):41–54.

[87] Hoppel, W. A. and Frick, G. M. (1986). Ion—Aerosol Attachment Coefficients and the Steady-State Charge Distribution on Aerosols in a Bipolar Ion Environment. *Aerosol Science and Technology*, 5(1):1–21.

[88] Hoppel, W. A. and Frick, G. M. (1990). The Nonequilibrium Character of the Aerosol Charge Distributions Produced by Neutralizers. *Aerosol Science and Technology*, 12(3):471–496.

[89] Huang, Y., Seinfeld, J. H., and Flagan, R. C. (2020). Diffusional transfer function for the scanning electrical mobility spectrometer (SEMS). *Aerosol Science and Technology*, 54(10):1157–1168.

[90] Hummes, D., Neumann, S., Fissan, H., and Stratmann, F. (1996). Experimental Determination of the Transfer Function of a Differential Mobility Analyzer (DMA) in the nanometer size range. *Particle & Particle Systems Characterization*, 13(5):327–332.

[91] Hussin, A., Scheibel, H. G., Becker, K. H., and Porstendörfer, J. (1983). Bipolar diffusion charging of aerosol particles—I: experimental results within the diameter range 4–30 nm. *Journal of Aerosol Science*, 14(5):671–677.

[92] Ibarra, I., Rodríguez-Maroto, J., and Alonso, M. (2020). Bipolar charging and neutralization of particles below 10 nm, the conditions to reach the stationary charge distribution, and the effect of a non-stationary charge distribution on particle sizing. *Journal of Aerosol Science*, 140:105479.

[93] International Civil Aviation Organization (2020). ICAO Doc 9501: Environmental Technical Manual- Volume II Procedures for the Emissions Certification of Aircraft Engines. Technical report.

[94] International Organization for Standardization (2002). ISO 16183:2002 Heavy-duty engines- Measurement of gaseous emissions from raw exhaust gas and of particulate emissions using partial flow dilution systems under transient test conditions.

[95] International Organization for Standardization (2009). ISO 15900:2009 Determination of particle size distribution — Differential electrical mobility analysis for aerosol particles.

[96] Jantunen, M. J. and Reist, P. C. (1983). General field charging theory for aerosol particle charging and neutralizing in unipolar and bipolar ion fields. *Journal of Aerosol Science*, 14(2):127–133.

[97] Järvinen, A., Aitomaa, M., Rostedt, A., Keskinen, J., and Yli-Ojanperä, J. (2014). Calibration of the new electrical low pressure impactor (ELPI+). *Journal of Aerosol Science*, 69:150–159.

[98] Järvinen, A., Heikkilä, P., Keskinen, J., and Yli-Ojanperä, J. (2017). Particle charge-size distribution measurement using a differential mobility analyzer and an electrical low pressure impactor. *Aerosol Science and Technology*, 51(1):20–29.

[99] Jayne, J. T., Leard, D. C., Zhang, X., Davidovits, P., Smith, K. A., Kolb, C. E., and Worsnop, D. R. (2000). Development of an Aerosol Mass Spectrometer for Size and Composition Analysis of Submicron Particles. *Aerosol Science and Technology*, 33(1-2):49–70.

[100] Ji, J. H., Bae, G. N., and Hwang, J. (2004). Characteristics of aerosol charge neutralizers for highly charged particles. *Journal of Aerosol Science*, 35(11):1347–1358.

[101] Jiang, J., Kim, C., Wang, X., Stolzenburg, M. R., Kaufman, S. L., Qi, C., Sem, G. J., Sakurai, H., Hama, N., and McMurry, P. H. (2014). Aerosol Charge Fractions Downstream of Six Bipolar Chargers: Effects of Ion Source, Source Activity, and Flowrate. *Aerosol Science and Technology*, 48(12):1207–1216.

[102] Joe, Y.-H., Shim, J., Shin, I.-K., Yook, S.-J., and Park, H.-S. (2018). A Study on Electrical Charge Distribution of Aerosol Using Gerdien Ion Counter. *Aerosol and Air Quality Research*, 18(12):2922–2928.

[103] John, W. and Davis, J. W. (1974). The measurement of the charge distribution on monodisperse aerosols. *Atmospheric Environment (1967)*, 8(10):1029–1034.

[104] Johnson, T. J., Irwin, M., Symonds, J. P. R., Olfert, J. S., and Boies, A. M. (2018a). Measuring aerosol size distributions with the aerodynamic aerosol classifier. *Aerosol Science and Technology*, 52(6):655–665.

[105] Johnson, T. J., Nishida, R. T., Irwin, M., Symonds, J. P. R., Olfert, J. S., and Boies, A. M. (2018b). Agreement Between Different Aerosol Classifiers Using Spherical Particles. In *Cambridge Particle Meeting*, Cambridge, UK, June 15, 2018.

[106] Johnson, T. J., Nishida, R. T., Irwin, M., Symonds, J. P. R., Olfert, J. S., and Boies, A. M. (2020). Measuring the bipolar charge distribution of nanoparticles: Review of methodologies and development using the Aerodynamic Aerosol Classifier. *Journal of Aerosol Science*, 143:105526.

[107] Johnson, T. J., Nishida, R. T., Zhang, X., Symonds, J. P. R., Olfert, J. S., and Boies, A. M. (2021a). Generating an Aerosol of Homogeneous, Non-Spherical Particles and Measuring their Bipolar Charge Distribution. *Journal of Aerosol Science*, 153(0021-8502):105705.

[108] Johnson, T. J., Symonds, J. P. R., and Olfert, J. S. (2013). Mass-Mobility Measurements Using a Centrifugal Particle Mass Analyzer and Differential Mobility Spectrometer. *Aerosol Science and Technology*, 47(11):1215–1225.

[109] Johnson, T. J., Symonds, J. P. R., Olfert, J. S., and Boies, A. M. (2021b). Accelerated measurements of aerosol size distributions by continuously scanning the aerodynamic aerosol classifier. *Aerosol Science and Technology*, 55(2):119–141.

[110] Johnston, A. M. (1983). A semi-automatic method for the assessment of electric charge carried by airborne dust. *Journal of Aerosol Science*, 14(5):643–655.

[111] Johnston, A. M., Vincent, J. H., and Jones, A. D. (1985). Measurements of electric charge for workplace aerosols. *The Annals of occupational hygiene*, 29(2):271–284.

[112] Johnston, A. M., Vincent, J. H., and Jones, A. D. (1987). Electrical Charge Characteristics of Dry Aerosols Produced by a Number of Laboratory Mechanical Dispensers. *Aerosol Science and Technology*, 6(2):115–127.

[113] Jung, H. and Kittelson, D. B. (2005a). Characterization of Aerosol Surface Instruments in Transition Regime. *Aerosol Science and Technology*, 39(9):902–911.

[114] Jung, H. and Kittelson, D. B. (2005b). Measurement of Electrical Charge on Diesel Particles. *Aerosol Science and Technology*, 39(12):1129–1135.

[115] Jung, T., Burtscher, H., and Schmidt-Ott, A. (1988). Multiple charging of ultrafine aerosol particles by aerosol photoemission (APE). *Journal of Aerosol Science*, 19(4):485–490.

[116] Kallinger, P., Steiner, G., and Szymanski, W. W. (2012). Characterization of four different bipolar charging devices for nanoparticle charge conditioning. *Journal of Nanoparticle Research*, 14(6):944.

[117] Kallinger, P. and Szymanski, W. W. (2015). Experimental determination of the steady-state charging probabilities and particle size conservation in non-radioactive and radioactive bipolar aerosol chargers in the size range of 5–40 nm. *Journal of Nanoparticle Research*, 17(4):171.

[118] Kanaparthi, M. A., Cevaer, S. D., and Dhaniyala, S. (2018). Towards near real-time SEMS size distribution measurements under up-scan operation. *Journal of Aerosol Science*, 126:217–230.

[119] Karasev, V. V., Ivanova, N. A., Sadykova, A. R., Kukhareva, N., Baklanov, A. M., Onischuk, A. A., Kovalev, F. D., and Beresnev, S. A. (2004). Formation of charged soot aggregates by combustion and pyrolysis: charge distribution and photophoresis. *Journal of Aerosol Science*, 35(3):363–381.

[120] Karlsson, M. N. A. and Martinsson, B. G. (2003). Methods to measure and predict the transfer function size dependence of individual DMAs. *Journal of Aerosol Science*, 34(5):603–625.

[121] Kasper, G. and Shaw, D. T. (1982). Comparative Size Distribution Measurements on Chain Aggregates. *Aerosol Science and Technology*, 2(3):369–381.

[122] Keskinen, J., Pietarinen, K., and Lehtimäki, M. (1992). Electrical low pressure impactor. *Journal of Aerosol Science*, 23(4):353–360.

[123] Khain, A., Rosenfeld, D., and Pokrovsky, A. (2005). Aerosol impact on the dynamics and microphysics of deep convective clouds. *Quarterly Journal of the Royal Meteorological Society*, 131(611):2639–2663.

[124] Kielser, D. and Kruis, F. (2017). High resolution measurement of aerodynamic focusing behaviour of nanoparticles in different gases and gas- mixtures using a Differential Aerodynamic Particle Sizer (DAPS). In *2017 European Aerosol Conference*, Zurich, Switzerland, August 29, 2017.

[125] Kim, H., Kim, J., Yang, H., Suh, J., Kim, T., Han, B., Kim, S., Kim, D. S., Pikhitsa, P. V., and Choi, M. (2006). Parallel patterning of nanoparticles via electrodynamic focusing of charged aerosols. *Nature Nanotechnology*, 1(2):117–121.

[126] Kim, J. H. J., Mulholland, G. G. W., Kukuck, S. R. S., and Pui, D. D. Y. H. (2005a). Slip Correction Measurements of Certified PSL Nanoparticles Using a Nanometer Differential Mobility Analyzer (Nano-DMA) for Knudsen Number From 0.5 to 83. *Journal of Research of the National Institute of Standards and Technology*, 110(1):31–54.

[127] Kim, S. H., Woo, K. S., Liu, B. Y. H., and Zachariah, M. R. (2005b). Method of measuring charge distribution of nanosized aerosols. *Journal of Colloid and Interface Science*, 282(1):46–57.

[128] Kimoto, S., Mizota, K., Kanamaru, M., Okuda, H., Okuda, D., and Adachi, M. (2009). Aerosol Charge Neutralization by a Mixing-Type Bipolar Charger using Corona Discharge at High Pressure. *Aerosol Science and Technology*, 43(9):872–880.

[129] Kinney, P. D., Pui, D. Y. H., Bryner, N. P., and Mulholland, G. W. (1991). Use of the electrostatic classification method to size 0.1 micrometer SRM particles - A feasibility study. *Journal of Research of the National Institute of Standards and Technology*, 96(2):147–176.

[130] Kittelson, D. B., Pui, D. Y. H., and Moon, K. C. (1986). Electrostatic Collection of Diesel Particles. In *SAE Technical Paper*. SAE International.

[131] Kittelson, D. B., Reinertsen, J., and Michalski, J. (1991). Further Studies of Electrostatic Collection and Agglomeration of Diesel Particles. In *SAE Technical Paper*. SAE International.

[132] Knutson, E. O. (1976). Extended Electric Mobility Method for Measuring Aerosol Particle Size and Concentration. In Liu, B. Y. H., editor, *Fine Particles*, pages 739–762. Academic Press, London, UK.

[133] Knutson, E. O. and Whitby, K. T. (1975). Aerosol classification by electric mobility: apparatus, theory, and applications. *Journal of Aerosol Science*, 6(6):443–451.

[134] Koh, S. (2007). Strategies for Controlled Placement of Nanoscale Building Blocks. *Nanoscale research letters*, 2(11):519–545.

[135] Kojima, H. (1978). Measurements of equilibrium charge distribution on aerosols in bipolar ionic atmosphere. *Atmospheric Environment (1967)*, 12(12):2363–2368.

[136] Kojima, H. and Sekikawa, T. (1973). An Attempt for Obtaining the Aerosol Size Distribution. *Journal of the Meteorological Society of Japan. Ser. II*, 51(5):287–293.

[137] Kousaka, Y., Adachi, M., Okuyama, K., Kitada, N., and Motouchi, T. (1983). Bipolar Charging of Ultrafine Aerosol Particles. *Aerosol Science and Technology*, 2(4):421–427.

[138] Kousaka, Y., Okuyama, K., and Adachi, M. (1985). Determination of Particle Size Distribution of Ultra-Fine Aerosols Using a Differential Mobility Analyzer. *Aerosol Science and Technology*, 4(2):209–225.

[139] Kousaka, Y., Okuyama, K., Adachi, M., and Ebie, K. (1981). Measurement of Electric Charge of Aerosol Particles Generated by Various Methods. *Journal of Chemical Engineering of Japan*, 14(1):54–58.

[140] Ku, B. K., Deye, G. J., Kulkarni, P., and Baron, P. A. (2011). Bipolar diffusion charging of high-aspect ratio aerosols. *Journal of Electrostatics*, 69(6):641–647.

[141] Kulkarni, P., Baron, P. A., and Willeke, K., editors (2011). *Aerosol measurement: principles, techniques, and applications.* Wiley, Hoboken, N.J., 3rd ed. edition.

[142] Kulkarni, P., Deye, G. J., and Baron, P. A. (2009). Bipolar diffusion charging characteristics of single-wall carbon nanotube aerosol particles. *Journal of Aerosol Science*, 40(2):164–179.

[143] Kulon, J. and Balachandran, W. (2001). The measurement of bipolar charge on aerosols. *Journal of Electrostatics*, 51-52:552–557.

[144] Kulon, J., Hrabar, S., Machowski, W., and Balachandran, W. (2001). A bipolar charge measurement system for aerosol characterization. *IEEE Transactions on Industry Applications*, 37(2):472–479.

[145] Kwon, S. B., Sakurai, H., Seto, T., and Kim, Y. J. (2006). Charge neutralization of submicron aerosols using surface-discharge microplasma. *Journal of Aerosol Science*, 37(4):483–499.

[146] Laakso, L., Gagné, S., Petäjä, T., Hirsikko, A., Aalto, P. P., Kulmala, M., and Kerminen, V.-M. (2007). Detecting charging state of ultra-fine particles: instrumental development and ambient measurements. *Atmospheric Chemistry and Physics*, 7(5):1333–1345.

[147] Lee, H.-K. and Ahn, K.-H. (2017). Charging Effect on the 80-200 nm Size Atmospheric Aerosols during a Lightning Event. *Aerosol and Air Quality Research*, 17(10):2624–2630.

[148] Lee, H. M., Kim, C. S., Shimada, M., and Okuyama, K. (2005a). Bipolar diffusion charging for aerosol nanoparticle measurement using a soft X-ray charger. *Journal of Aerosol Science*, 36(7):813–829.

[149] Lee, H. M., Kim, C. S., Shimada, M., and Okuyama, K. (2005b). Effects of Mobility Changes and Distribution of Bipolar Ions on Aerosol Nanoparticle Diffusion Charging. *Journal of Chemical Engineering of Japan*, 38(7):486–496.

[150] Lelieveld, J., Evans, J. S., Fnais, M., Giannadaki, D., and Pozzer, A. (2015). The contribution of outdoor air pollution sources to premature mortality on a global scale. *Nature*, 525(7569):367–371.

[151] Leppä, J., Mui, W., Grantz, A. M., and Flagan, R. C. (2017). Charge distribution uncertainty in differential mobility analysis of aerosols. *Aerosol Science and Technology*, 51(10):1168–1189.

[152] Li, L., Chahl, H. S., and Gopalakrishnan, R. (2020). Comparison of the predictions of Langevin Dynamics-based diffusion charging collision kernel models with canonical experiments. *Journal of Aerosol Science*, 140:105481.

[153] Li, W., Li, L., and Chen, D.-R. (2006). Technical Note: A New Deconvolution Scheme for the Retrieval of True DMA Transfer Function from Tandem DMA Data. *Aerosol Science and Technology*, 40(12):1052–1057.

[154] Liebhaber, F. B., Juozaitis, A., Willeke, K., Baron, P., Talaska, G., and Chen, C.-C. (1994). Technique for assessing the electrical charge levels of aerosols. *American Industrial Hygiene Association Journal*, 55(7):610–618.

[155] Lissowski, P. (1940). Das Laden von Aerosolteilchen in einer bipolaren Ionenatmosphäre. *Acta physicochimica URSS*, 13(2).

[156] Liu, B. Y. H. and Pui, D. Y. H. (1974a). Electrical neutralization of aerosols. *Journal of Aerosol Science*, 5(5):465–472.

[157] Liu, B. Y. H. and Pui, D. Y. H. (1974b). Equilibrium bipolar charge distribution of aerosols. *Journal of Colloid and Interface Science*, 49(2):305–312.

[158] Liu, B. Y. H., Pui, D. Y. H., and Lin, B. Y. (1986). Aerosol Charge Neutralization by a Radioactive Alpha Source. *Particle & Particle Systems Characterization*, 3(3):111–116.

[159] Liu, P., Ziemann, P. J., Kittelson, D. B., and McMurry, P. H. (1995). Generating Particle Beams of Controlled Dimensions and Divergence: I. Theory of Particle Motion in Aerodynamic Lenses and Nozzle Expansions. *Aerosol Science and Technology*, 22(3):293–313.

[160] Magnusson, M. H., Ohlsson, B. J., Björk, M. T., Dick, K. A., Borgström, M. T., Deppert, K., and Samuelson, L. (2014). Semiconductor nanostructures enabled by aerosol technology. *Frontiers of Physics*, 9(3):398–418.

[161] Mai, H. and Flagan, R. C. (2018). Scanning DMA Data Analysis I. Classification Transfer Function. *Aerosol Science and Technology*, 52(12):1382–1399.

[162] Mai, H., Kong, W., Seinfeld, J. H., and Flagan, R. C. (2018). Scanning DMA data analysis II. Integrated DMA-CPC instrument response and data inversion. *Aerosol Science and Technology*, 52(12):1400–1414.

[163] Maisels, A., Kruis, F. E., and Fissan, H. (2002). Mixing selectivity in bicomponent, bipolar aggregation. *Journal of Aerosol Science*, 33(1):35–49.

[164] Makar, P. A., Gong, W., Milbrandt, J., Hogrefe, C., Zhang, Y., Curci, G., Žabkar, R., Im, U., Balzarini, A., Baró, R., Bianconi, R., Cheung, P., Forkel, R., Gravel, S., Hirtl, M., Honzak, L., Hou, A., Jiménez-Guerrero, P., Langer, M., Moran, M. D., Pabla, B., Pérez, J. L., Pirovano, G., San José, R., Tuccella, P., Werhahn, J., Zhang, J., and Galmarini, S. (2015). Feedbacks between air pollution and weather, Part 1: Effects on weather. *Atmospheric Environment*, 115:442–469.

[165] Maltoni, G. G., Melandri, C., Prodi, V., Tarroni, G., Zaiacomo, A., Bompane, G. F., and Formignani, M. (1973). An improved parallel plate mobility analyzer for aerosol particles. *Journal of Aerosol Science*, 4(6):447–455.

[166] Mamakos, A. (2016). Methodology to quantify the ratio of multiple-to single-charged fractions acquired in aerosol neutralizers. *Aerosol Science and Technology*, 50(4):363–372.

[167] Mamakos, A., Ntziachristos, L., and Samaras, Z. (2008). Differential mobility analyser transfer functions in scanning mode. *Journal of Aerosol Science*, 39(3):227–243.

[168] Maricq, M. M. (2004). Size and charge of soot particles in rich premixed ethylene flames. *Combustion and Flame*, 137(3):340–350.

[169] Maricq, M. M. (2005). The dynamics of electrically charged soot particles in a premixed ethylene flame. *Combustion and Flame*, 141(4):406–416.

[170] Maricq, M. M. (2006a). A comparison of soot size and charge distributions from ethane, ethylene, acetylene, and benzene/ethylene premixed flames. *Combustion and Flame*, 144(4):730–743.

[171] Maricq, M. M. (2006b). On the electrical charge of motor vehicle exhaust particles. *Journal of Aerosol Science*, 37(7):858–874.

[172] Maricq, M. M. (2008a). Bipolar Diffusion Charging of Soot Aggregates. *Aerosol Science and Technology*, 42(4):247–254.

[173] Maricq, M. M. (2008b). Thermal equilibration of soot charge distributions by coagulation. *Journal of Aerosol Science*, 39(2):141–149.

[174] Marple, V. A. (2004). History of Impactors—The First 110 Years. *Aerosol Science and Technology*, 38(3):247–292.

[175] Marple, V. A., Rubow, K. L., and Behm, S. M. (1991). A Microorifice Uniform Deposit Impactor (MOUDI): Description, Calibration, and Use. *Aerosol Science and Technology*, 14(4):434–446.

[176] Marra, J., Voetz, M., and Kiesling, H.-J. (2010). Monitor for detecting and assessing exposure to airborne nanoparticles. *Journal of Nanoparticle Research*, 12(1):21–37.

[177] Martinsson, B. G., Karlsson, M. N. A., and Frank, G. (2001). Methodology to Estimate the Transfer Function of Individual Differential Mobility Analyzers. *Aerosol Science and Technology*, 35(4):815–823.

[178] Matsoukas, T. (1997). The Coagulation Rate of Charged Aerosols in Ionized Gases. *Journal of Colloid and Interface Science*, 187(2):474–483.

[179] Matsoukas, T. and Friedlander, S. K. (1991). Dynamics of aerosol agglomerate formation. *Journal of Colloid and Interface Science*, 146(2):495–506.

[180] Mayya, Y. S. (1990). Theory of diffusion charging of fractal aerosol aggregates. *Journal of Colloid and Interface Science*, 140(1):185–191.

[181] Mayya, Y. S. and Holländer, W. (1995). Ion Densities and Particle Charges for Alpha Ionization in an Aerosol Atmosphere: Columnar Recombination Corrections. *Aerosol Science and Technology*, 23(4):628–640.

[182] Mayya, Y. S. and Sapra, B. K. (1996). Variation of the aerosol charge neutralization coefficient in the entire particle size range. *Journal of Aerosol Science*, 27(8):1169–1178.

[183] Mazumder, M. K. and Kirsch, K. J. (1977). Single particle aerodynamic relaxation time analyzer. *Review of Scientific Instruments*, 48(6):622–624.

[184] McMurry, P. H., Wang, X., Park, K., and Ehara, K. (2002). The relationship between mass and mobility for atmospheric particles: A new technique for measuring particle density. *Aerosol Science and Technology*, 36(2):227–238.

[185] Megaw, W. J. and Wells, A. C. (1969). Production of Monodisperse Sub-micron Aerosols of which Each Particle carries a Specified Number of Electronic Charges. *Nature*, 224:689–690.

[186] Melandri, C., Tarroni, G., Prodi, V., Zaiacomo, T. D., Formignani, M., and Lombardi, C. C. (1983). Deposition of charged particles in the human airways. *Journal of Aerosol Science*, 14(5):657–669.

[187] Metayer, Y., Houlaki, S., and Madelaine, G. (1984). Charge distribution on submicronic aerosol particles in a bipolar ionic atmosphere. *Journal of Aerosol Science*, 15(3):258–261.

[188] Millikan, R. A. (1910). The Isolation of an Ion, A Precision Measurement of Its Charge, and the Correction of Stokes's Law. *Science*, 32(822):436–448.

[189] Modesto-Lopez, L. B., Kettleson, E. M., and Biswas, P. (2011). Soft X-ray charger (SXC) system for use with electrospray for mobility measurement of bioaerosols. *Journal of Electrostatics*, 69(4):357–364.

[190] Moon, K.-C. (1984). *Charging mechanism of submicron diesel particles*. PhD thesis, University of Minnesota, Ann Arbor.

[191] Nie, Y., Wang, Y., and Biswas, P. (2017). Mobility and Bipolar Diffusion Charging Characteristics of Crumpled Reduced Graphene Oxide Nanoparticles Synthesized in a Furnace Aerosol Reactor. *The Journal of Physical Chemistry C*, 121(19):10529–10537.

[192] Nishida, R. T., Johnson, T. J., Hassim, J. S., Graves, B. M., Boies, A. M., and Hochgreb, S. (2020). A simple method for measuring fine-to-ultrafine aerosols using bipolar charge equilibrium. *ACS Sensors*, 5(2):447–453.

[193] Nishida, R. T., Yamasaki, N. M., Schriefl, M. A., Boies, A. M., and Hochgreb, S. (2019). Modelling the effect of aerosol polydispersity on unipolar charging and measurement in low-cost sensors. *Journal of Aerosol Science*, 130:10–21.

[194] NIST (2019). NIST Digital Library of Mathematical Functions. http://dlmf.nist.gov/, Release 1.0.25 of 2019-12-15.

[195] Nolan, P. J. and Kennan, E. L. (1948). Condensation Nuclei from Hot Platinum: Size, Coagulation Coefficient and Charge-Distribution. *Proceedings of the Royal Irish Academy. Section A: Mathematical and Physical Sciences*, 52:171–190.

[196] Okuda, T., Yoshida, T., Gunji, Y., Okahisa, S., Kusdianto, K., Gen, M., Sato, S., and Lenggoro, I. W. (2015). Preliminary Study on the Measurement of the Electrostatic Charging State of PM2.5 Collected on Filter Media. *Asian Journal of Atmospheric Environment*, 9(2):137–145.

[197] Olfert, J. and Rogak, S. (2019). Universal relations between soot effective density and primary particle size for common combustion sources. *Aerosol Science and Technology*, 53(5):485–492.

[198] Olfert, J. S. and Collings, N. (2005). New method for particle mass classification - the Couette centrifugal particle mass analyzer. *Journal of Aerosol Science*, 36(11):1338–1352.

[199] Olfert, J. S., Reavell, K. S., Rushton, M. G., and Collings, N. (2006). The experimental transfer function of the Couette centrifugal particle mass analyzer. *Journal of Aerosol Science*, 37(12):1840–1852.

[200] Onischuk, A. A., di Stasio, S., Karasev, V. V., Baklanov, A. M., Makhov, G. A., Vlasenko, A. L., Sadykova, A. R., Shipovalov, A. V., and Panfilov, V. N. (2003). Evolution of structure and charge of soot aggregates during and after formation in a propane/air diffusion flame. *Journal of Aerosol Science*, 34(4):383–403.

[201] Ouf, F.-X. and Sillon, P. (2009). Charging Efficiency of the Electrical Low Pressure Impactor's Corona Charger: Influence of the Fractal Morphology of Nanoparticle Aggregates and Uncertainty Analysis of Experimental Results. *Aerosol Science and Technology*, 43(7):685–698.

[202] Park, S. H., Lee, K. W., Shimada, M., and Okuyama, K. (2005). Coagulation of bipolarly charged ultrafine aerosol particles. *Journal of Aerosol Science*, 36(7):830–845.

[203] Pollak, L. W. and Metnieks, A. L. (1962a). On the validity of Boltzmann's distribution law for the charges of aerosol particles in electrical equilibrium. *Geofisica pura e applicata*, 53(1):111–132.

[204] Pollak, L. W. and Metnieks, A. L. (1962b). The approach to charge equilibrium in a stored aerosol during aging. *Geofisica pura e applicata*, 51(1):225–236.

[205] Pope, C. A. (2000). Review: Epidemiological Basis for Particulate Air Pollution Health Standards. *Aerosol Science and Technology*, 32(1):4–14.

[206] Porstendörfer, J., Hessin, A., and Scheibel, H. G. (1983). Experimental results on charging probability for positively and negatively charged particles in the diameter size range between 4 and 30 nm. *Journal of Aerosol Science*, 14(3):276–279.

[207] Porstendörfer, J., Hussin, A., Scheibel, H. G., and Becker, K. H. (1984). Bipolar diffusion charging of aerosol particles—II. Influence of the concentration ratio of positive and negative ions on the charge distribution. *Journal of Aerosol Science*, 15(1):47–56.

[208] Pui, D. Y. H., Fruin, S., and McMurry, P. H. (1988). Unipolar Diffusion Charging of Ultrafine Aerosols. *Aerosol Science and Technology*, 8(2):173–187.

[209] Qi, C. and Kulkarni, P. (2013). Miniature Dual-Corona Ionizer for Bipolar Charging of Aerosol. *Aerosol Science and Technology*, 47(1):81–92.

[210] Rao, N. P., de la Mora, J. F., and McMurry, P. H. (1992). High-resolution aerodynamic spectrometry of submicron particles: sheathed variable-cut impactors vs other devices. *Journal of Aerosol Science*, 23(1):11–26.

[211] Reischl, G. P., Mäkelä, J. M., Karch, R., and Necid, J. (1996). Bipolar charging of ultrafine particles in the size range below 10 nm. *Journal of Aerosol Science*, 27(6):931–949.

[212] Reischl, G. P., Scheibel, H. G., and Porstendörfer, J. (1983). The bipolar charging of aerosols: Experimental results in the size range below 20-nm particle diameter. *Journal of Colloid and Interface Science*, 91(1):272–275.

[213] Renninger, R. G., Mazumder, M. K., and Testerman, M. K. (1981). Particle sizing by electrical single particle aerodynamic relaxation time analyzer. *Review of Scientific Instruments*, 52(2):242–246.

[214] Rich, T. A., Pollak, L. W., and Metnieks, A. L. (1959). Estimation of average size of submicron particles from the number of all and uncharged particles. *Geofisica pura e applicata*, 44(1):233–241.

[215] Rogak, S. N. and Flagan, R. C. (1992). Bipolar diffusion charging of spheres and agglomerate aerosol particles. *Journal of Aerosol Science*, 23(7):693–710.

[216] Romay, F. J., Liu, B. Y. H., and Pui, D. Y. H. (1994). A Sonic Jet Corona Ionizer for Electrostatic Discharge and Aerosol Neutralization. *Aerosol Science and Technology*, 20(1):31–41.

[217] Romay, F. J. and Pui, D. Y. H. (1992). On the Combination Coefficient of Positive Ions with Ultrafine Neutral Particles in the Transition and Free-Molecule Regimes. *Aerosol Science and Technology*, 17(2):134–147.

[218] Romay-Novas, F. J. and Pui, D. Y. H. (1988). Generation of Monodisperse Aerosols in the 0.1–1.0-μm Diameter Range Using a Mobility Classification–Inertial Impaction Technique. *Aerosol Science and Technology*, 9(2):123–131.

[219] Rowland, M., Cavecchi, A., Thielmann, F., Kulon, J., Shur, J., and Price, R. (2019). Measuring The Bipolar Charge Distributions of Fine Particle Aerosol Clouds of Commercial PMDI Suspensions Using a Bipolar Next Generation Impactor (bp-NGI). *Pharmaceutical Research*, 36(15):1–14.

[220] Russell, L. M., Flagan, R. C., and Seinfeld, J. H. (1995). Asymmetric Instrument Response Resulting from Mixing Effects in Accelerated DMA-CPC Measurements. *Aerosol Science and Technology*, 23(4):491–509.

[221] Saari, S., Arffman, A., Harra, J., Rönkkö, T., and Keskinen, J. (2018). Performance evaluation of the HR-ELPI + inversion. *Aerosol Science and Technology*, 52(9):1037–1047.

[222] SAE (2020). ARP6320: Procedure for the Continuous Sampling and Measurement of Non-Volatile Particle Emissions from Aircraft Turbine Engines.

[223] Sahu, M., Park, J., and Biswas, P. (2012). In Situ Charge Characterization of TiO2 and Cu–TiO2 Nanoparticles in a Flame Aerosol Reactor. *Journal of Nanoparticle Research*, 14(2):678.

[224] Servaas, T. E. and Krider, E. (1977). The steady-state charged fraction of 0.01 um particles. *Journal of Aerosol Science*, 8(2):91–99.

[225] Shimada, M., Han, B., Okuyama, K., and Otani, Y. (2002). Bipolar Charging of Aerosol Nanoparticles by a Soft X-ray Photoionizer. *Journal of Chemical Engineering of Japan*, 35(8):786–793.

[226] Stober, J., Schleicher, B., and Burtscher, H. (1991). Bipolar Diffusion Charging of Particles in Noble Gases. *Aerosol Science and Technology*, 14(1):66–73.

[227] Stöber, W. and Flachsbart, H. (1971). High resolution aerodynamic size spectrometry of quasi-monodisperse latex spheres with a spiral centrifuge. *Journal of Aerosol Science*, 2(2):103–116.

[228] Stolzenburg, M. (1988). *An ultrafine aerosol size distribution measuring system*. PhD thesis, University of Minnesota, Ann Arbor.

[229] Stolzenburg, M. R. and McMurry, P. H. (2008). Equations Governing Single and Tandem DMA Configurations and a New Lognormal Approximation to the Transfer Function. *Aerosol Science and Technology*, 42(6):421–432.

[230] Stolzenburg, M. R. and McMurry, P. H. (2018). Accuracy of recovered moments for narrow mobility distributions obtained with commonly used inversion algorithms for mobility size spectrometers. *Aerosol Science and Technology*, 52(6):614–625.

[231] Stommel, Y. G. and Riebel, U. (2004). A new corona discharge-based aerosol charger for submicron particles with low initial charge. *Journal of Aerosol Science*, 35(9):1051–1069.

[232] Swanson, J. and Kittelson, D. (2008). A Method to Measure Static Charge on a Filter Used for Gravimetric Analysis. *Aerosol Science and Technology*, 42(9):714–721.

[233] Takahashi, K. and Kudo, A. (1973). Electrical charging of aerosol particles by bipolar ions in flow type charging vessels. *Journal of Aerosol Science*, 4(3):209–216.

[234] Talukdar, S. S. and Swihart, M. T. (2003). An Improved Data Inversion Program for Obtaining Aerosol Size Distributions from Scanning Differential Mobility Analyzer Data. *Aerosol Science and Technology*, 37(2):145–161.

[235] Tanaka, Y., Higashi, H., Manirakiza, E., Seto, T., Otani, Y., and Hirasawa, M. (2014). Charge Neutralization of Aerosol Carbon Nanofibers. *Journal of Chemical Engineering of Japan*, 47(8):644.

[236] Tang, J., Verrelli, E., and Tsoukalas, D. (2009). Assembly of charged nanoparticles using self-electrodynamic focusing. *Nanotechnology*, 20(36):365605.

[237] Tardos, G. I., Snaddon, R. W. L., and Dietz, P. W. (1984). Electrical Charge Measurements on Fine Airborne Particles. *IEEE Transactions on Industry Applications*, IA-20(6):1578–1583.

[238] Tavakoli, F. and Olfert, J. S. (2013). An Instrument for the Classification of Aerosols by Particle Relaxation Time: Theoretical Models of the Aerodynamic Aerosol Classifier. *Aerosol Science and Technology*, 47(8):916–926.

[239] Tavakoli, F. and Olfert, J. S. (2014). Determination of particle mass, effective density, mass–mobility exponent, and dynamic shape factor using an aerodynamic aerosol classifier and a differential mobility analyzer in tandem. *Journal of Aerosol Science*, 75:35–42.

[240] Tavakoli, F., Symonds, J. P. R., and Olfert, J. S. (2014). Generation of a Monodisperse Size-Classified Aerosol Independent of Particle Charge. *Aerosol Science and Technology*, 48(3):i–iv.

[241] Thomas, J. W. and Rimberg, D. (1967). A simple method for measuring the average charge on a monodisperse aerosol. *Staub-Reinhalt, Luft*, 27:18–22.

[242] Tigges, L., Jain, A., and Schmid, H.-J. (2015a). On the bipolar charge distribution used for mobility particle sizing: Theoretical considerations. *Journal of Aerosol Science*, 88:119–134.

[243] Tigges, L., Wiedensohler, A., Weinhold, K., Gandhi, J., and Schmid, H.-J. (2015b). Bipolar charge distribution of a soft X-ray diffusion charger. *Journal of Aerosol Science*, 90(Supplement C):77–86.

[244] Tsai, C.-J., Lin, J.-S., Deshpande, C. G., and Liu, L.-C. (2005). Electrostatic Charge Measurement and Charge Neutralization of Fine Aerosol Particles during the Generation Process. *Particle & Particle Systems Characterization*, 22(5):293–298.

[245] TSI (2006). Model 3068B Aerosol Electrometer- Users Manual Revision A.

[246] TSI (2007). Model 3775 Condensation Particle Counter: Operation and Service Manual Revision D.

[247] TSI (2009). Series 3080 Electrostatic Classifiers- Operation and Service Manual Revision J.

[248] TSI (2014). Aerosol Neutralization Issue Model 3077(A): Application Note 3007-001.

[249] TSI (2016). Electrostatic Classifier Model 3082 Scanning Mobility Particle Sizer (SMPS) Spectrometer Model 3938- Operation and Service Manual Revision C.

[250] TSI (2017). Condensation Particle Counter Model 3752- Operation Manual Revision B.

[251] Tu, G., Song, Q., and Yao, Q. (2016). Relationship between particle charge and electrostatic enhancement of filter performance. *Powder Technology*, 301:665–673.

[252] Uin, J., Tamm, E., and Mirme, A. (2009). Electrically Produced Standard Aerosols in a Wide Size Range. *Aerosol Science and Technology*, 43(8):847–853.

[253] Vemury, S. and Pratsinis, S. E. (1996). Charging and coagulation during flame synthesis of silica. *Journal of Aerosol Science*, 27(6):951–966.

[254] Vijayakumar, R. and Whitby, K. T. (1984). Bipolar Steady State Charge Fraction of Ultrafine Aerosols. *Aerosol Science and Technology*, 3(1):25–30.

[255] Vincent, J. H. (1985). On the practical significance of electrostatic lung deposition of isometric and fibrous aerosols. *Journal of Aerosol Science*, 16(6):511–519.

[256] Vincent, J. H., Johnston, A. M., Jones, A. D., and McLachlan, C. Q. (1985). Measurement of Electric Charge on Airborne Dusts in Textile Industry Workplaces. *Textile Research Journal*, 55(8):469–477.

[257] Vincent, J. H., Johnston, W. B., Jones, A. D., and Johnston, A. M. (1981). Static Electrification of Airborne Asbestos - A Study of Its Causes, Assessment and Effects on Deposition in the Lungs of Rats. *Am. Ind. Hyg. Assoc. J.*, 42:711.

[258] Vishnyakov, V. I., Kiro, S. A., Oprya, M. V., and Ennan, A. A. (2016). Charge distribution of welding fume particles after charging by corona ionizer. *Journal of Aerosol Science*, 94:9–21.

[259] Vomela, R. A. and Whitby, K. T. (1967). The charging and mobility of chain aggregate smoke particles. *Journal of Colloid and Interface Science*, 25(4):568–576.

[260] Walker, D., Johnson, T. J., Nishida, R. T., Symonds, J. P. R., Reavell, K., Bainschab, M., and Bergmann, A. (2018). Uniformity of Particle Concentration after Mixing Aerosol Flows. In *10th International Aerosol Conference*, St. Louis, USA. September 7, 2018.

[261] Wang, S. C. and Flagan, R. C. (1990). Scanning Electrical Mobility Spectrometer. *Aerosol Science and Technology*, 13(2):230–240.

[262] Wen, H. Y., Reischl, G. P., and Kasper, G. (1984a). Bipolar diffusion charging of fibrous aerosol particles—I. charging theory. *Journal of Aerosol Science*, 15(2):89–101.

[263] Wen, H. Y., Reischl, G. P., and Kasper, G. (1984b). Bipolar diffusion charging of fibrous aerosol particles—II. charge and electrical mobility measurements on linear chain aggregates. *Journal of Aerosol Science*, 15(2):103–122.

[264] Whitby, K. T. and Peterson, C. M. (1965). Electrical Neutralization and Particle Size Measurement of Dye Aerosols. *Industrial & Engineering Chemistry Fundamentals*, 4(1):66–72.

[265] WHO (2016). Ambient air pollution: A global assessment of exposure and burden of disease. Technical report, World Health Organization (WHO).

[266] Wiedensohler, A. (1988). An approximation of the bipolar charge distribution for particles in the submicron size range. *Journal of Aerosol Science*, 19(3):387–389.

[267] Wiedensohler, A. and Fissan, H. J. (1988). Aerosol charging in high purity gases. *Journal of Aerosol Science*, 19(7):867–870.

[268] Wiedensohler, A. and Fissan, H. J. (1991). Bipolar Charge Distributions of Aerosol Particles in High-Purity Argon and Nitrogen. *Aerosol Science and Technology*, 14(3):358–364.

[269] Wiedensohler, A., Lütkemeier, E., Feldpausch, M., and Helsper, C. (1986). Investigation of the bipolar charge distribution at various gas conditions. *Journal of Aerosol Science*, 17(3):413–416.

[270] Wiedensohler, A., Wiesner, A., Weinhold, K., Birmili, W., Hermann, M., Merkel, M., Müller, T., Pfeifer, S., Schmidt, A., Tuch, T., Velarde, F., Quincey, P., Seeger, S., and Nowak, A. (2018). Mobility particle size spectrometers: Calibration procedures and measurement uncertainties. *Aerosol Science and Technology*, 52(2):146–164.

[271] Wild, M., Meyer, J., and Kasper, G. (2012). A fast and accurate method of using electrical mobility scans for the direct measurement of aerosol charge distributions. *Journal of Aerosol Science*, 52(Supplement C):69–79.

[272] Wilson, J. C. and Liu, B. Y. H. (1980). Aerodynamic particle size measurement by laser-doppler velocimetry. *Journal of Aerosol Science*, 11(2):139–150.

[273] Withers, P. B., Foot, E. V. J., and Clark, J. M. (1998). The measurement of particle size and mobility in an electric field. *Journal of Aerosol Science*, 29(2):S1243 – S1244.

[274] Woessner, R. H. and Gunn, R. (1956). Measurements related to the fundamental processes of aerosol electrification. *Journal of Colloid Science*, 11(1):69–76.

[275] Wong, J., Lin, Y.-W., Kwok, P. C. L., Niemelä, V., Crapper, J., and Chan, H.-K. (2015). Measuring Bipolar Charge and Mass Distributions of Powder Aerosols by a Novel Tool (BOLAR). *Molecular Pharmaceutics*, 12(9):3433–3440.

[276] Xiao, K., Swanson, J. J., Pui, D. Y. H., and Kittelson, D. B. (2012). Bipolar Diffusion Charging of Aggregates. *Aerosol Science and Technology*, 46(7):794–803.

[277] Yang, H., Dhaniyala, S., and He, M. (2018). Performance of Bipolar Diffusion Chargers: Experiments with Particles in the Size Range of 100 to 900 nm. *Aerosol Science and Technology*, 52(2):182–191.

[278] Yli-Ojanperä, J., Ukkonen, A., Järvinen, A., Layzell, S., Niemelä, V., and Keskinen, J. (2014). Bipolar Charge Analyzer (BOLAR): A New Aerosol Instrument for Bipolar Charge Measurements. *J. Aerosol Sci.*, 77:16–30.

[279] Yoon, Y. H., Bong, C., and Kim, D. S. (2015). Evaluation of the performance of a soft X-ray charger for the bipolar charging of nanoparticles. *Particuology*, 18:165–169.

[280] Yun, K. M., Lee, S. Y., Iskandar, F., Okuyama, K., and Tajima, N. (2009). Effect of X-ray energy and ionization time on the charging performance and nanoparticle formation of a soft X-ray photoionization charger. *Advanced Powder Technology*, 20(6):529–536.

[281] Zhao, B., Liou, K.-N., Gu, Y., Li, Q., Jiang, J. H., Su, H., He, C., Tseng, H.-L. R., Wang, S., Liu, R., Qi, L., Lee, W.-L., and Hao, J. (2017). Enhanced PM2.5 pollution in China due to aerosol-cloud interactions. *Scientific Reports*, 7(1):4453.

Appendix A

Theory for Measuring Size Distributions using the Steady-State AAC

A.1 Transfer function of steady-state AAC

Tavakoli and Olfert [238] determined the non-diffusing (ND) transfer function (Ω_{ND}) of Aerodynamic Aerosol Classifier (AAC) using particle streamline theory to be:

$$\Omega_{\mathrm{ND}}(\tilde{\tau},\beta,\delta)=\frac{1}{2\beta\,(1-\delta)}\left[|\tilde{\tau}-(1+\beta)|+|\tilde{\tau}-(1-\beta)|-|\tilde{\tau}-(1+\beta\,\delta)|-|\tilde{\tau}-(1-\beta\,\delta)|\right], \tag{A.1}$$

where β and δ are non-dimensional parameters for the classifier flows defined as:

$$\beta=\frac{Q_{\mathrm{s}}+Q_{\mathrm{a}}}{Q_{\mathrm{sh}}+Q_{\mathrm{exh}}}, \tag{A.2}$$

$$\delta=\frac{Q_{\mathrm{s}}-Q_{\mathrm{a}}}{Q_{\mathrm{s}}+Q_{\mathrm{a}}}, \tag{A.3}$$

and $\tilde{\tau}$ is the non-dimensional particle relaxation time expressed as:

$$\tilde{\tau}=\frac{\tau}{\tau^{*}}. \tag{A.4}$$

Q_{a} is the aerosol flow rate entering the classifier, Q_{s} is the classified aerosol flow rate leaving the classifier, Q_{sh} is the sheath flow rate entering the classifier and Q_{exh} is the sheath flow rate leaving the classifier. τ^{*} is the particle relaxation time corresponding to the peak of the AAC transfer function and was determined by Tavakoli and Olfert [238] to be:

$$\tau^* = \frac{Q_{\text{sh}} + Q_{\text{exh}}}{\pi\omega^2(r_1 + r_2)^2 L}, \tag{A.5}$$

where ω is the rotational speed, r_1 is the inner radius, r_2 is the outer radius and L is the effective length of the classifier.

A.1.1 Idealized transfer function with balanced flows

However for balanced (B) classifier flows (i.e. $Q_{\text{exh}} = Q_{\text{sh}}$ and $Q_{\text{a}} = Q_{\text{s}}$), $\beta = Q_{\text{a}}/Q_{\text{sh}}$ and $\delta = 0$, and Ω_{ND} (Equation A.1) simplifies to:

$$\Omega_{\text{ND,B}}(\tilde{\tau}, \beta) = \frac{1}{2\beta}\left[|\tilde{\tau} - (1+\beta)| + |\tilde{\tau} - (1-\beta)| - 2|\tilde{\tau} - 1|\right]. \tag{A.6}$$

Assuming $\tilde{\tau} \leq 1$ (thus also $\tilde{\tau} < (1+\beta)$) and $\tilde{\tau} \geq (1-\beta)$, $\Omega_{\text{ND,B}}$ (Equation A.6) becomes:

$$\begin{aligned} \Omega_{\text{ND,B}}(\tilde{\tau}, \beta) &= \frac{1}{2\beta}\left[-(\tilde{\tau} - (1+\beta)) + (\tilde{\tau} - (1-\beta)) + 2(\tilde{\tau} - 1)\right] \\ \Omega_{\text{ND,B}}(\tilde{\tau}, \beta) &= 1 + \frac{1}{\beta}(\tilde{\tau} - 1), \end{aligned} \tag{A.7}$$

and assuming $\tilde{\tau} > 1$ (thus also $\tilde{\tau} > (1-\beta)$) and $\tilde{\tau} \leq (1+\beta)$, $\Omega_{\text{ND,B}}$ (Equation A.6) becomes:

$$\begin{aligned} \Omega_{\text{ND,B}}(\tilde{\tau}, \beta) &= \frac{1}{2\beta}\left[-(\tilde{\tau} - (1+\beta)) + (\tilde{\tau} - (1-\beta)) - 2(\tilde{\tau} - 1)\right] \\ \Omega_{\text{ND,B}}(\tilde{\tau}, \beta) &= 1 + \frac{1}{\beta}(1 - \tilde{\tau}). \end{aligned} \tag{A.8}$$

Combining Equations A.7 and A.8 to represent each side of the triangular transfer function of the AAC operating with balanced flows and neglecting particle diffusion forms the following piecewise function (i.e. the idealized transfer function):

$$\Omega_{\text{ND,B}}(\tilde{\tau}, \beta) = \begin{cases} 1 + \frac{1}{\beta}(\tilde{\tau} - 1) & \text{if } (1-\beta) \leq \tilde{\tau} \leq 1 \\ 1 + \frac{1}{\beta}(1 - \tilde{\tau}) & \text{if } 1 < \tilde{\tau} \leq (1+\beta) \\ 0 & \text{elsewhere} \end{cases}. \tag{A.9}$$

Using the definition of $\tilde{\tau}$ (Equation A.4) to convert $\Omega_{\text{ND,B}}$ (Equation A.9) to the τ domain becomes:

$$\Omega_{\mathrm{ND,B}}(\tau,\,\tau^*,\,\beta) = \begin{cases} 1+\frac{1}{\beta}\,(\frac{\tau}{\tau^*}-1) & \text{if } (1-\beta)\,\tau^* \le \tau \le \tau^* \\ 1+\frac{1}{\beta}\,(1-\frac{\tau}{\tau^*}) & \text{if } \tau^* < \tau \le (1+\beta)\,\tau^*\,. \\ 0 & \text{elsewhere} \end{cases} \tag{A.10}$$

Full width at half maximum (FWHM) of transfer function

The full width at half maximum (FWHM) is often used to quantify the classification resolution of an instrument (i.e the width of its transfer function). The maximum height ($h_{\mathrm{max,I}}$) of the idealized (I) transfer function ($\Omega_{\mathrm{ND,B}}$ defined in Equation A.9) can be found at $\tilde{\tau} = 1$ as follows:

$$h_{\mathrm{max,I}} = \Omega_{\mathrm{ND,B}}(\tilde{\tau}=1,\,\beta) = 1+\frac{1}{\beta}\,(1-1) = 1. \tag{A.11}$$

Therefore, the height of the idealized transfer function at the half maximum is 0.5. The particle relaxation time which corresponds to the lower boundary of the FWHM (i.e. $\tilde{\tau}_{\mathrm{L,I}} < 1$) can be found by solving Equation A.9 for this value as follows:

$$0.5 = 1+\frac{1}{\beta}\,(\tilde{\tau}_{\mathrm{L,I}}-1) \rightarrow \boldsymbol{\tilde{\tau}_{\mathrm{L,I}} = 1-0.5\beta}, \tag{A.12}$$

and similarly the upper boundary of the FWHM (i.e. $\tilde{\tau}_{\mathrm{U,I}} > 1$) is:

$$0.5 = 1+\frac{1}{\beta}\,(1-\tilde{\tau}_{\mathrm{U,I}}) \rightarrow \boldsymbol{\tilde{\tau}_{\mathrm{U,I}} = 1+0.5\beta}. \tag{A.13}$$

Therefore, the full width at half maximum of the idealized transfer function ($\mathrm{FWHM_I}$) in the $\tilde{\tau}$ domain can be determined from the difference in Equations A.13 and A.12 as follows:

$$\mathrm{FWHM_I}(\beta) = \tilde{\tau}_{\mathrm{U,I}} - \tilde{\tau}_{\mathrm{L,I}} = \beta, \tag{A.14}$$

or converting to the τ domain as:

$$\mathrm{FWHM_I}(\tau^*,\,\beta) = \beta\,\tau^*. \tag{A.15}$$

Area under transfer function

The lower x-axis intercept of the idealized triangular transfer function (i.e. $\tilde{\tau}_{\mathrm{L,int,I}} < 1$) can be found from setting Equation A.9 equal to zero and solving as follows:

$$1+\frac{1}{\beta}\,(\tilde{\tau}_{\mathrm{L,int,I}}-1) = 0 \rightarrow \boldsymbol{\tilde{\tau}_{\mathrm{L,int,I}} = (1-\beta)}, \tag{A.16}$$

and similarly solving for the upper x-axis intercept (i.e. $\tilde{\tau}_{\mathrm{U,int,I}} > 1$) as follows:

$$1 + \frac{1}{\beta}\left(1 - \tilde{\tau}_{\mathrm{U,int,I}}\right) = 0 \rightarrow \boldsymbol{\tilde{\tau}_{\mathrm{U,int,I}} = (1+\beta)}. \tag{A.17}$$

Therefore, the maximum width $(w_{\mathrm{max,I}})$ of the idealized triangular transfer function in the $\tilde{\tau}$ domain can be found from the difference in Equations A.17 and A.16 as follows:

$$w_{\mathrm{max,I}} = \tilde{\tau}_{\mathrm{U,int,I}} - \tilde{\tau}_{\mathrm{L,int,I}} = 2\beta. \tag{A.18}$$

Furthermore, the area under the idealized triangular transfer function (A_{I}) can be found from Equations A.11 and A.18 as follows:

$$A_{\mathrm{I}} = 0.5\, h_{\mathrm{max,I}}\, w_{\mathrm{max,I}} = \beta, \tag{A.19}$$

or converting to the τ domain as:

$$A_{\mathrm{I}} = 0.5\, h_{\mathrm{max,I}}\, w_{\mathrm{max,I}} = \beta\, \tau^{*}. \tag{A.20}$$

A.1.2 Non-idealized transfer function with balanced flows

To capture non-ideal (NI) behavior within the instrument, such as particle diffusion and losses, the idealized AAC transfer function (Equation A.10) can be parameterized by introducing scaling factors that still maintain its triangular shape. This parameterization is similar to the one developed by Martinsson et al. [177] to characterize the transfer function of the Differential Mobility Analyzer (DMA). A transfer function width factor (μ_Ω) is introduced to scale the FWHM of the AAC transfer function (Equation A.15) in the τ domain as follows:

$$\mathrm{FWHM_{NI}}(\tau^*, \beta, \mu_\Omega) = \frac{\beta\, \tau^*}{\mu_\Omega}, \tag{A.21}$$

and a transmission efficiency (λ_Ω) is introduced to scale the area under the AAC transfer function (Equation A.20) in the τ domain as follows:

$$A_{\mathrm{NI}} = \lambda_\Omega\, \beta\, \tau^*. \tag{A.22}$$

From the definitions of $\mathrm{FWHM_I}$ and $w_{\mathrm{max,I}}$ (Equations A.14 and A.18, respectively), the FWHM of the triangular transfer function is related to its base width (w_{max}) by:

$$w_{\mathrm{max}} = 2\mathrm{FWHM}. \tag{A.23}$$

Substituting Equation A.23 into an equation for the area of a triangle (similar to Equation A.20), and isolating h_{max}, results in:

$$h_{\mathrm{max}} = \frac{A}{\mathrm{FWHM}}. \tag{A.24}$$

Therefore, substituting the definitions of $\mathrm{FWHM_{NI}}$ and A_{NI} (Equations A.21 and A.22, respectively) into the defintion of h_{max} (Equation A.24), the maximum height of the scaled AAC transfer function shifts from the idealized maximum of 1 to:

$$h_{\mathrm{max,NI}} = \frac{A_{\mathrm{NI}}}{\mathrm{FWHM_{NI}}} = \lambda_\Omega\, \mu_\Omega, \tag{A.25}$$

and the non-idealized transfer function of the AAC $(\Omega_{\mathrm{ND,B,NI}})$ shifts from the idealized representation (Equation A.9 or Equation A.10, repsectively) to:

$$\Omega_{\mathrm{ND,B,NI}}(\tilde{\tau}, \beta, \lambda_\Omega, \mu_\Omega) = \begin{cases} \lambda_\Omega\, \mu_\Omega\, [1 + \frac{\mu_\Omega}{\beta}\, (\tilde{\tau} - 1)] & \text{if } (1 - \frac{\beta}{\mu_\Omega}) \leq \tilde{\tau} \leq 1 \\ \lambda_\Omega\, \mu_\Omega\, [1 + \frac{\mu_\Omega}{\beta}\, (1 - \tilde{\tau})] & \text{if } 1 < \tilde{\tau} \leq (1 + \frac{\beta}{\mu_\Omega})\,, \\ 0 & \text{elsewhere} \end{cases} \tag{A.26}$$

or

$$\Omega_{\mathrm{ND,B,NI}}(\tau,\,\tau^*,\,\beta,\,\lambda_\Omega,\,\mu_\Omega) = \begin{cases} \lambda_\Omega\,\mu_\Omega\,[1+\frac{\mu_\Omega}{\beta}\,(\frac{\tau}{\tau^*}-1)] & \text{if } (1-\frac{\beta}{\mu_\Omega})\,\tau^* \le \tau \le \tau^* \\ \lambda_\Omega\,\mu_\Omega\,[1+\frac{\mu_\Omega}{\beta}\,(1-\frac{\tau}{\tau^*})] & \text{if } \tau^* < \tau \le (1+\frac{\beta}{\mu_\Omega})\,\tau^*\,, \\ 0 & \text{elsewhere} \end{cases} \tag{A.27}$$

in the $\tilde{\tau}$ or τ domain, respectively. These piecewise functions (Equations A.26 or A.27) can also be represented in the same form as the original AAC transfer function [238] in the $\tilde{\tau}$ domain as:

$$\Omega_{\mathrm{ND,B,NI}}(\tilde{\tau},\,\beta,\,\lambda_\Omega,\,\mu_\Omega) = \frac{\lambda_\Omega\,\mu_\Omega^2}{2\beta}\left[\left|\tilde{\tau}-\left(1+\frac{\beta}{\mu_\Omega}\right)\right|+\left|\tilde{\tau}-\left(1-\frac{\beta}{\mu_\Omega}\right)\right|-2\,|\tilde{\tau}-1|\right]. \tag{A.28}$$

A.2 Inversion of transfer function for steady-state AAC with balanced flows

Similar to the process developed by Stolzenburg and McMurry [229] for the DMA (but in terms of particle relaxation time rather than electrical mobility), the particle number concentration (N_{det}) that passes through the steady-state AAC operating at setpoint τ_i^* can be determined from:

$$N_{\text{det}}(\tau_i^*) = \int \eta(\tau)\,\Omega(\tau,\,\tau_i^*)\,\mathrm{d}N(\tau), \tag{A.29}$$

where $\eta(\tau)$ is the counting efficiency of the particle detector downstream of the AAC and $N(\tau)$ is the particle number concentration of the aerosol source at particle relaxation time τ, while $\Omega(\tau,\,\tau_i^*)$ is the transfer function of the AAC at setpoint τ_i^*. Applying the chain rule to the integrand from Equation A.29:

$$\frac{\mathrm{d}N(\tau)}{\mathrm{d}\tau} = \frac{\mathrm{d}N(\tau)}{\mathrm{d}\log\tau}\frac{\mathrm{d}\log\tau}{\mathrm{d}\tau}. \tag{A.30}$$

Furthermore, the derivative of $\log(\tau)$ with respect to τ is equivalent to:

$$\frac{\mathrm{d}\log\tau}{\mathrm{d}\tau} = \frac{1}{\ln(10)}\frac{1}{\tau}. \tag{A.31}$$

Therefore, substituting Equation A.31 into Equation A.30, and isolating $\mathrm{d}N(\tau)$:

$$\frac{\mathrm{d}N(\tau)}{\mathrm{d}\tau} = \frac{\mathrm{d}N(\tau)}{\mathrm{d}\log\tau}\frac{1}{\ln(10)}\frac{1}{\tau} \rightarrow \boldsymbol{\mathrm{d}N(\tau) = \mathrm{d}\tau\frac{\mathrm{d}N(\tau)}{\mathrm{d}\log\tau}\frac{1}{\ln(10)}\frac{1}{\tau}}. \tag{A.32}$$

Substituting Equation A.32 into Equation A.29 and assuming η and $\mathrm{d}N/\mathrm{d}\log\tau$ are constant over the narrow width of the AAC transfer function (due to being operated at a sufficient resolution) becomes:

$$\begin{aligned} N_{\text{det}}(\tau_i^*) &= \int \eta(\tau)\,\Omega(\tau,\,\tau_i^*)\frac{\mathrm{d}N(\tau)}{\mathrm{d}\log\tau}\frac{1}{\ln(10)}\frac{1}{\tau}\mathrm{d}\tau \\ N_{\text{det}}(\tau_i^*) &= \eta(\tau_i^*)\frac{\mathrm{d}N(\tau)}{\mathrm{d}\log\tau}\bigg|_{\tau_i^*}\frac{1}{\ln(10)}\int\frac{\Omega(\tau,\,\tau_i^*)}{\tau}\mathrm{d}\tau. \end{aligned} \tag{A.33}$$

Since the AAC transfer function is centered around τ_i^*, this value is used to estimate the constants (i.e. η and $\mathrm{d}N(\tau)/\mathrm{d}\log\tau$). Isolating the spectral density in terms of particle relaxation time (i.e. $\mathrm{d}N/\mathrm{d}\log\tau$) classified by the steady-state AAC at setpoint τ_i^* from Equation A.33:

$$\left.\frac{\mathrm{d}N(\tau)}{\mathrm{d}\log\tau}\right|_{\tau_i^*} = \frac{N_{\mathrm{det}}(\tau_i^*)\ln(10)}{\eta(\tau_i^*)\,\beta_{\mathrm{ss},i}^*}, \tag{A.34}$$

where $\beta_{\mathrm{ss},i}^*$ is the non-dimensional deconvolution parameter of the transfer function of the steady-state AAC at setpoint τ_i^* as follows:

$$\beta_{\mathrm{ss},i}^* = \int \frac{\Omega(\tau,\,\tau_i^*)}{\tau}\mathrm{d}\tau. \tag{A.35}$$

The deconvolution parameter based on the idealized or non-idealized transfer functions (Equations A.10 or A.27, respectively) of the steady-state AAC operating with balanced flows is derived in Section A.3.1 or A.3.2, respectively. These solutions $\left(\text{for } \beta_{\mathrm{ss,B,I}}^* \text{ and } \beta_{\mathrm{ss,B,NI}}^*\right)$ are summarized by Equations A.38 and A.39, respectively.

The spectral density of the aerosol can also be found in terms of aerodynamic diameter (i.e. $\mathrm{d}N/\mathrm{d}\log d_{\mathrm{a}}$) by applying the chain rule:

$$\frac{\mathrm{d}N}{\mathrm{d}\log d_{\mathrm{a}}} = \frac{\mathrm{d}N}{\mathrm{d}\log\tau}\frac{\mathrm{d}\log\tau}{\mathrm{d}\log d_{\mathrm{a}}}, \tag{A.36}$$

to Equation A.34 as follows:

$$\left.\frac{\mathrm{d}N(d_{\mathrm{a}})}{\mathrm{d}\log d_{\mathrm{a}}}\right|_{d_{\mathrm{a},i}^*} = \frac{N_{\mathrm{det}}(d_{\mathrm{a},i}^*)\ln(10)}{\eta(d_{\mathrm{a},i}^*)\left.\frac{\mathrm{d}\log d_{\mathrm{a}}}{\mathrm{d}\log\tau}\right|_{d_{\mathrm{a},i}^*}\beta_{\mathrm{ss},i}^*}, \tag{A.37}$$

where the solution for $\frac{\mathrm{d}\log d_{\mathrm{a}}}{\mathrm{d}\log\tau}$ is derived in Section A.4 and summarized by Equation A.49.

A.3 Deconvolution parameter ($\beta_{\mathrm{ss,B}}$) of steady-state AAC with balanced flows

A.3.1 Idealized transfer function

Substituting the idealized transfer function based on balanced classifier flows (Equation A.10) into Equation A.35 and determining its corresponding deconvolution parameter ($\beta^*_{\mathrm{ss,B,I}}$) as follows:

$$\begin{aligned}
\beta^*_{\mathrm{ss,B,I}} &= \int \frac{\Omega_{\mathrm{ND,B}}(\tau,\, \tau^*,\, \beta)}{\tau}\,\mathrm{d}\tau \\
&= \int_{(1-\beta)\,\tau^*}^{\tau^*} \frac{1}{\tau}\left[1+\frac{1}{\beta}\left(\frac{\tau}{\tau^*}-1\right)\right]\mathrm{d}\tau + \int_{\tau^*}^{(1+\beta)\,\tau^*} \frac{1}{\tau}\left[1+\frac{1}{\beta}\left(1-\frac{\tau}{\tau^*}\right)\right]\mathrm{d}\tau \\
&= \left[\ln(\tau)\left(1-\frac{1}{\beta}\right)+\frac{\tau}{\beta\,\tau^*}\right]\Bigg|_{(1-\beta)\,\tau^*}^{\tau^*} + \left[\ln(\tau)\left(1+\frac{1}{\beta}\right)-\frac{\tau}{\beta\,\tau^*}\right]\Bigg|_{\tau^*}^{(1+\beta)\,\tau^*} \\
\beta^*_{\mathrm{ss,B,I}} &= \ln\left(\frac{1+\beta}{1-\beta}\right)+\frac{1}{\beta}\ln\left(1-\beta^2\right).
\end{aligned} \tag{A.38}$$

A.3.2 Non-idealized transfer function

Substituting the non-idealized transfer function based on balanced classifier flows (Equation A.27) into Equation A.35 and determining its corresponding deconvolution parameter ($\beta^*_{\mathrm{ss,B,NI}}$) as follows:

$$\begin{aligned}
\beta^*_{\mathrm{ss,B,NI}} &= \int \frac{\Omega_{\mathrm{ND,B,NI}}(\tau,\, \tau^*,\, \beta,\, \lambda_\Omega,\, \mu_\Omega)}{\tau}\,\mathrm{d}\tau \\
&= \int_{\left(1-\frac{\beta}{\mu_\Omega}\right)\tau^*}^{\tau^*} \frac{\lambda_\Omega\,\mu_\Omega}{\tau}\left[1+\frac{\mu_\Omega}{\beta}\left(\frac{\tau}{\tau^*}-1\right)\right]\mathrm{d}\tau \\
&\quad + \int_{\tau^*}^{\left(1+\frac{\beta}{\mu_\Omega}\right)\tau^*} \frac{\lambda_\Omega\,\mu_\Omega}{\tau}\left[1+\frac{\mu_\Omega}{\beta}\left(1-\frac{\tau}{\tau^*}\right)\right]\mathrm{d}\tau \\
&= \lambda_\Omega\,\mu_\Omega\left[\left(\left(1-\frac{\mu_\Omega}{\beta}\right)\ln(\tau)+\frac{\mu_\Omega}{\beta}\,\frac{\tau}{\tau^*}\right)\Bigg|_{\left(1-\frac{\beta}{\mu_\Omega}\right)\tau^*}^{\tau^*}\right. \\
&\quad \left. + \left(\left(1+\frac{\mu_\Omega}{\beta}\right)\ln(\tau)-\frac{\mu_\Omega}{\beta}\,\frac{\tau}{\tau^*}\right)\Bigg|_{\tau^*}^{\left(1+\frac{\beta}{\mu_\Omega}\right)\tau^*}\right] \\
\beta^*_{\mathrm{ss,B,NI}} &= \lambda_\Omega\,\mu_\Omega\left[\ln\left(\frac{1+\frac{\beta}{\mu_\Omega}}{1-\frac{\beta}{\mu_\Omega}}\right)+\frac{\mu_\Omega}{\beta}\ln\left(1-\left(\frac{\beta}{\mu_\Omega}\right)^2\right)\right].
\end{aligned} \tag{A.39}$$

A.4 Logarithmic ratio of aerodynamic diameter to relaxation time $(\mathrm{d}\log d_\mathrm{a}/\mathrm{d}\log\tau)$

A particle's aerodynamic diameter (d_a) is related to its relaxation time (τ) by:

$$\tau = \frac{C_c(d_\mathrm{a})\,\rho_\mathrm{o}\,d_\mathrm{a}^2}{18\mu}, \tag{A.40}$$

where $C_c(d_\mathrm{a})$ is the Cunningham slip correction factor at that particle equivalent aerodynamic diameter, ρ_o is the unit density (1000 kg/m^3) and μ is the viscosity of the surrounding gas. Following ISO (2009), the Cunningham slip correction factor can be estimated from the following correlation developed by Kim et al. [126]:

$$C_c(d_\mathrm{a}) = 1 + \frac{\lambda}{d_\mathrm{a}}\left[\alpha_{c_c} + \beta_{c_c}\exp\left(-\gamma_{c_c}\frac{d_\mathrm{a}}{\lambda}\right)\right], \tag{A.41}$$

where $\alpha_{c_c} = 2\times 1.165 = 2.33$, $\beta_{c_c} = 2\times 0.483 = 0.966$ and $\gamma_{c_c} = 0.997/2 = 0.4985$. The mean free path (λ) and viscosity (μ) of the surrounding gas (assuming air) can also be estimated from Kim et al. [126] as follows:

$$\lambda = \lambda_0\left(\frac{T}{T_0}\right)^2\left(\frac{P_0}{P}\right)\left(\frac{T_0+S}{T+S}\right), \tag{A.42}$$

and

$$\mu = \mu_0\left(\frac{T}{T_0}\right)^{\frac{3}{2}}\left(\frac{T_0+S}{T+S}\right), \tag{A.43}$$

where λ_0 is the air mean free path at the reference conditions of 67.3 nm, μ_0 is the air viscosity at the reference conditions of $1.83245\,10^{-5}$ Pa·s, T is the air temperature in the classifier in K, T_0 is the reference temperature of 296.15 K, P is the air pressure in the classifier in Pa, P_0 is the reference pressure of 101325 Pa and S is the Sutherland constant for air of 110.4 K.

Substituting the definition of C_c (Equation A.41) into the relationship between τ and d_a (Equation A.40), and expanding, becomes:

$$\tau = \frac{\rho_\mathrm{o}\,d_\mathrm{a}^2}{18\mu} + \frac{\alpha_{c_c}\,\lambda\,\rho_\mathrm{o}\,d_\mathrm{a}}{18\mu} + \frac{\beta_{c_c}\,\lambda\,\rho_\mathrm{o}\,d_\mathrm{a}}{18\mu}\exp\left(-\gamma_{c_c}\frac{d_\mathrm{a}}{\lambda}\right). \tag{A.44}$$

The derivative of Equation A.44 with respect to d_a, utilizing the product law and simplifying, becomes:

$$\frac{\mathrm{d}\tau}{\mathrm{d}d_\mathrm{a}} = \frac{\rho_\mathrm{o}}{18\mu}\left[2d_\mathrm{a} + \alpha_{c_c}\,\lambda + \beta_{c_c}\,\lambda\,\exp\left(-\gamma_{c_c}\,\frac{d_\mathrm{a}}{\lambda}\right)\left(1-\frac{\gamma_{c_c}\,d_\mathrm{a}}{\lambda}\right)\right]. \tag{A.45}$$

Noting that $\frac{\mathrm{d}}{\mathrm{d}x}\log(x) = \frac{1}{\ln(10)\,x} \rightarrow \mathrm{d}\log(x) = \frac{\mathrm{d}x}{\ln(10)\,x}$, and applying this to the variables of interest (τ and d_a), then taking their ratio generates:

$$\frac{\mathrm{d}\log\tau}{\mathrm{d}\log d_\mathrm{a}} = \frac{\mathrm{d}\tau}{\mathrm{d}d_\mathrm{a}}\,\frac{\ln(10)\,d_\mathrm{a}}{\ln(10)\,\tau} = \frac{\mathrm{d}\tau}{\mathrm{d}d_\mathrm{a}}\,\frac{d_\mathrm{a}}{\tau}. \tag{A.46}$$

Substituting Equation A.45 into Equation A.46 becomes:

$$\frac{\mathrm{d}\log\tau}{\mathrm{d}\log d_\mathrm{a}} = \frac{\rho_\mathrm{o}\,d_\mathrm{a}}{18\mu\,\tau}\left[2d_\mathrm{a} + \alpha_{c_c}\,\lambda + \beta_{c_c}\,\lambda\,\exp\left(-\gamma_{c_c}\,\frac{d_\mathrm{a}}{\lambda}\right)\left(1-\frac{\gamma_{c_c}\,d_\mathrm{a}}{\lambda}\right)\right]. \tag{A.47}$$

Since $\frac{\mathrm{d}\tau}{\mathrm{d}d_\mathrm{a}}$ (Equation A.45) is a first order derivative, the following is valid $\frac{\mathrm{d}\tau}{\mathrm{d}d_\mathrm{a}} = \left(\frac{\mathrm{d}d_\mathrm{a}}{\mathrm{d}\tau}\right)^{-1}$ and thus Equation A.47 becomes:

$$\frac{\mathrm{d}\log d_\mathrm{a}}{\mathrm{d}\log\tau} = \frac{18\mu\,\tau}{\rho_\mathrm{o}\,d_\mathrm{a}}\left[2d_\mathrm{a} + \alpha_{c_c}\,\lambda + \beta_{c_c}\,\lambda\,\exp\left(-\gamma_{c_c}\,\frac{d_\mathrm{a}}{\lambda}\right)\left(1-\frac{\gamma_{c_c}\,d_\mathrm{a}}{\lambda}\right)\right]^{-1}. \tag{A.48}$$

Finally, substituting the relationship between τ and d_a (Equation A.40) into Equation A.48, and simplifying, generates the following solution:

$$\frac{\mathrm{d}\log d_\mathrm{a}}{\mathrm{d}\log\tau} = d_\mathrm{a}\,C_c(d_\mathrm{a})\left[2d_\mathrm{a} + \alpha_{c_c}\,\lambda + \beta_{c_c}\,\lambda\,\exp\left(-\gamma_{c_c}\,\frac{d_\mathrm{a}}{\lambda}\right)\left(1-\frac{\gamma_{c_c}\,d_\mathrm{a}}{\lambda}\right)\right]^{-1}, \tag{A.49}$$

which is an input to the AAC inversion in terms of aerodynamic diameter (Equation A.37).

A.5 Converting spectral density from aerodynamic diameter $(\mathrm{d}N/\mathrm{d}\log d_\mathrm{a})$ to mobility diameter $(\mathrm{d}N/\mathrm{d}\log d_\mathrm{m})$

A.5.1 Constant effective density

A particle's mobility diameter (d_m) is related to its relaxation time (τ) by:

$$\tau = m\,B = \frac{\pi}{6}\,\rho_\mathrm{eff}\,d_\mathrm{m}^3\,\frac{C_c(d_\mathrm{m})}{3\pi\,\mu\,d_\mathrm{m}} = \frac{C_c(d_\mathrm{m})\,\rho_\mathrm{eff}\,d_\mathrm{m}^2}{18\mu}, \tag{A.50}$$

where m is the particle mass, B is the particle mechanical mobility, ρ_eff is the particle effective density, μ is the viscosity of the surrounding gas and $C_c(d_\mathrm{m})$ is the Cunningham slip correction factor at that equivalent mobility diameter of the particle. Substituting the relationship between τ and d_a (Equation A.40) into the relationship between τ and d_m (Equation A.50) simplifies to:

$$\rho_\mathrm{eff}\,d_\mathrm{m}^2\,C_c(d_\mathrm{m}) = \rho_\mathrm{o}\,d_\mathrm{a}^2\,C_c(d_\mathrm{a}), \tag{A.51}$$

and can be used to convert a particle's aerodynamic diameter to its mobility diameter. The relationship between τ and d_m (Equation A.50) is the same form as the relationship between τ and d_a (Equation A.40) except in terms of particle mobility diameter (d_m) and effective density (ρ_eff) rather than particle aerodynamic diameter (d_a) and unit density ($\rho_\mathrm{o} = 1000$ kg/m^3). Therefore following the same process Section A.4 (Equations A.40 to A.49), the logarithmic derivative for the relationship between τ and d_m (Equation A.50) becomes:

$$\frac{\mathrm{d}\log\tau}{\mathrm{d}\log d_\mathrm{m}} = \frac{\rho_\mathrm{eff}\,d_\mathrm{m}}{18\mu\,\tau}\left[2d_\mathrm{m} + \alpha_{c_c}\,\lambda + \beta_{c_c}\,\lambda\,\exp\left(-\gamma_{c_c}\,\frac{d_\mathrm{m}}{\lambda}\right)\left(1 - \frac{\gamma_{c_c}\,d_\mathrm{m}}{\lambda}\right)\right], \tag{A.52}$$

and

$$\frac{\mathrm{d}\log d_\mathrm{m}}{\mathrm{d}\log\tau} = \frac{18\mu\,\tau}{\rho_\mathrm{eff}\,d_\mathrm{m}}\left[2d_\mathrm{m} + \alpha_{c_c}\,\lambda + \beta_{c_c}\,\lambda\,\exp\left(-\gamma_{c_c}\,\frac{d_\mathrm{m}}{\lambda}\right)\left(1 - \frac{\gamma_{c_c}\,d_\mathrm{m}}{\lambda}\right)\right]^{-1}. \tag{A.53}$$

Applying the chain rule between $\mathrm{d}\log d_\mathrm{a}/\mathrm{d}\log\tau$ and $\mathrm{d}\log\tau/\mathrm{d}\log d_\mathrm{m}$ (Equations A.48 and A.52, respectively) and simplifying:

$$\frac{\mathrm{d}\log d_\mathrm{a}}{\mathrm{d}\log d_\mathrm{m}} = \frac{\mathrm{d}\log d_\mathrm{a}}{\mathrm{d}\log \tau}\,\frac{\mathrm{d}\log \tau}{\mathrm{d}\log d_\mathrm{m}}$$
$$\frac{\mathrm{d}\log d_\mathrm{a}}{\mathrm{d}\log d_\mathrm{m}} = \frac{\rho_\mathrm{eff}\, d_\mathrm{m}}{\rho_\mathrm{o}\, d_\mathrm{a}}\,\frac{\left[2d_\mathrm{m} + \alpha_{c_c}\,\lambda + \beta_{c_c}\,\lambda\,\exp\left(-\gamma_{c_c}\,\frac{d_\mathrm{m}}{\lambda}\right)\left(1-\frac{\gamma_{c_c}\,d_\mathrm{m}}{\lambda}\right)\right]}{\left[2d_\mathrm{a} + \alpha_{c_c}\,\lambda + \beta_{c_c}\,\lambda\,\exp\left(-\gamma_{c_c}\,\frac{d_\mathrm{a}}{\lambda}\right)\left(1-\frac{\gamma_{c_c}\,d_\mathrm{a}}{\lambda}\right)\right]}. \tag{A.54}$$

Applying the following chain rule with $\mathrm{d}\log d_\mathrm{a}/\mathrm{d}\log d_\mathrm{m}$ (Equation A.54) simplifies to:

$$\frac{\mathrm{d}N}{\mathrm{d}\log d_\mathrm{m}} = \frac{\mathrm{d}N}{\mathrm{d}\log d_\mathrm{a}}\,\frac{\mathrm{d}\log d_\mathrm{a}}{\mathrm{d}\log d_\mathrm{m}}$$
$$\frac{\mathrm{d}N}{\mathrm{d}\log d_\mathrm{m}} = \frac{\mathrm{d}N}{\mathrm{d}\log d_\mathrm{a}}\,\frac{\rho_\mathrm{eff}\, d_\mathrm{m}}{\rho_\mathrm{o}\, d_\mathrm{a}}\,\frac{\left[2d_\mathrm{m} + \alpha_{c_c}\,\lambda + \beta_{c_c}\,\lambda\,\exp\left(-\gamma_{c_c}\,\frac{d_\mathrm{m}}{\lambda}\right)\left(1-\frac{\gamma_{c_c}\,d_\mathrm{m}}{\lambda}\right)\right]}{\left[2d_\mathrm{a} + \alpha_{c_c}\,\lambda + \beta_{c_c}\,\lambda\,\exp\left(-\gamma_{c_c}\,\frac{d_\mathrm{a}}{\lambda}\right)\left(1-\frac{\gamma_{c_c}\,d_\mathrm{a}}{\lambda}\right)\right]}, \tag{A.55}$$

where $\frac{\mathrm{d}N}{\mathrm{d}\log d_\mathrm{a}}$ is provided from the AAC inversion (Section A.2) and d_a can be converted to d_m by iteratively solving Equation A.51 with a known ρ_eff.

A.5.2 Varying effective density

The effective density (ρ_{eff}) of aerosol particles is often estimated based on a mass-mobility relationship developed by McMurry et al. [184] as follows:

$$\rho_{\text{eff}}(d_{\text{m}}) = k\, d_{\text{m}}^{d_{\text{m}}-3}, \tag{A.56}$$

where k is the mass-mobility prefactor constant, d_{m} is the mass-mobility exponent and d_{m} is the particle mobility diameter. Substituting this relationship (Equation A.56) into the relationship between d_{m} and d_{m} (Equation A.51) simplifies to:

$$k\, d_{\text{m}}^{d_{\text{m}}-1}\, C_c(d_{\text{m}}) = \rho_{\text{o}}\, d_{\text{a}}^2\, C_c(d_{\text{a}}), \tag{A.57}$$

which can be used to convert a particle's aerodynamic diameter to its equivalent mobility diameter. Substituting the definition of C_c (Equation A.41, but in terms of mobility diameter rather than aerodynamic diameter) and the mass-mobility relationship (Equation A.56) into the relationship between τ and d_{m} (Equation A.50) and expanding generates:

$$\begin{aligned} \tau &= \frac{k\, d_{\text{m}}^{d_{\text{m}}-3}\, d_{\text{m}}^2}{18\mu}\left[1+\frac{\lambda}{d_{\text{m}}}\left[\alpha_{c_c}+\beta_{c_c}\exp\left(-\gamma_{c_c}\frac{d_{\text{m}}}{\lambda}\right)\right]\right] \\ \tau &= \frac{k}{18\mu}\, d_{\text{m}}^{d_{\text{m}}-1}+\frac{k\,\alpha_{c_c}\,\lambda}{18\mu}\, d_{\text{m}}^{d_{\text{m}}-2}+\frac{k\,\beta_{c_c}\,\lambda}{18\mu}\, d_{\text{m}}^{d_{\text{m}}-2}\exp\left(-\gamma_{c_c}\frac{d_{\text{m}}}{\lambda}\right). \end{aligned} \tag{A.58}$$

The derivative of Equation A.58 with respect to d_{m}, utilizing the product law and simplifying, becomes:

$$\frac{\mathrm{d}\tau}{\mathrm{d}d_{\text{m}}} = \frac{k}{18\mu}\, d_{\text{m}}^{d_{\text{m}}-2}\left[d_{\text{m}}-1+\frac{\alpha_{c_c}\,\lambda\,(d_{\text{m}}-2)}{d_{\text{m}}}+\beta_{c_c}\,\lambda\,\exp\left(-\gamma_{c_c}\frac{d_{\text{m}}}{\lambda}\right)\left(\frac{d_{\text{m}}-2}{d_{\text{m}}}-\frac{\gamma_{c_c}}{\lambda}\right)\right]. \tag{A.59}$$

Substituting Equation A.59 into Equation A.46 (but in terms of mobility diameter rather than aerodynamic diameter) becomes:

$$\begin{aligned} \frac{\mathrm{d}\log\tau}{\mathrm{d}\log d_{\text{m}}} &= \frac{\mathrm{d}\tau}{\mathrm{d}d_{\text{m}}}\,\frac{d_{\text{m}}}{\tau} \\ \frac{\mathrm{d}\log\tau}{\mathrm{d}\log d_{\text{m}}} &= \frac{k\, d_{\text{m}}^{d_{\text{m}}-1}}{18\mu\,\tau}\left[d_{\text{m}}-1+\frac{\alpha_{c_c}\,\lambda\,(d_{\text{m}}-2)}{d_{\text{m}}}\right. \\ &\qquad \left.+\beta_{c_c}\,\lambda\,\exp\left(-\gamma_{c_c}\frac{d_{\text{m}}}{\lambda}\right)\left(\frac{d_{\text{m}}-2}{d_{\text{m}}}-\frac{\gamma_{c_c}}{\lambda}\right)\right]. \end{aligned} \tag{A.60}$$

Since $\frac{\mathrm{d}\log\tau}{\mathrm{d}\log d_\mathrm{m}}$ is a first order derivative, the following is valid $\frac{\mathrm{d}\log\tau}{\mathrm{d}\log d_\mathrm{m}} = \left(\frac{\mathrm{d}\log d_\mathrm{m}}{\mathrm{d}\log\tau}\right)^{-1}$ and thus Equation A.60 becomes:

$$\begin{aligned}\frac{\mathrm{d}\log d_\mathrm{m}}{\mathrm{d}\log\tau} = \frac{18\mu\,\tau}{k\,d_\mathrm{m}^{d_\mathrm{m}-1}}\Bigg[d_\mathrm{m} - 1 + \frac{\alpha_{c_c}\,\lambda\,(d_\mathrm{m}-2)}{d_\mathrm{m}} \\ + \beta_{c_c}\,\lambda\,\exp\left(-\gamma_{c_c}\,\frac{d_\mathrm{m}}{\lambda}\right)\left(\frac{d_\mathrm{m}-2}{d_\mathrm{m}} - \frac{\gamma_{c_c}}{\lambda}\right)\Bigg]^{-1}.\end{aligned} \tag{A.61}$$

Applying the chain rule between $\mathrm{d}\log d_\mathrm{a}/\mathrm{d}\log\tau$ and $\mathrm{d}\log\tau/\mathrm{d}\log d_\mathrm{m}$ (Equations A.48 and A.60, respectively) and simplifying:

$$\begin{aligned}\frac{\mathrm{d}\log d_\mathrm{a}}{\mathrm{d}\log d_\mathrm{m}} &= \frac{\mathrm{d}\log d_\mathrm{a}}{\mathrm{d}\log\tau}\,\frac{\mathrm{d}\log\tau}{\mathrm{d}\log d_\mathrm{m}} \\ \frac{\mathrm{d}\log d_\mathrm{a}}{\mathrm{d}\log d_\mathrm{m}} &= \frac{k\,d_\mathrm{m}^{d_\mathrm{m}-1}}{\rho_\mathrm{o}\,d_\mathrm{a}}\,\frac{\left[d_\mathrm{m} - 1 + \frac{\alpha_{c_c}\,\lambda\,(d_\mathrm{m}-2)}{d_\mathrm{m}} + \beta_{c_c}\,\lambda\,\exp\left(-\gamma_{c_c}\,\frac{d_\mathrm{m}}{\lambda}\right)\left(\frac{d_\mathrm{m}-2}{d_\mathrm{m}} - \frac{\gamma_{c_c}}{\lambda}\right)\right]}{\left[2d_\mathrm{a} + \alpha_{c_c}\,\lambda + \beta_{c_c}\,\lambda\,\exp\left(-\gamma_{c_c}\,\frac{d_\mathrm{a}}{\lambda}\right)\left(1 - \frac{\gamma_{c_c}\,d_\mathrm{a}}{\lambda}\right)\right]}.\end{aligned} \tag{A.62}$$

Applying the chain rule with $\mathrm{d}\log d_\mathrm{a}/\mathrm{d}\log d_\mathrm{m}$ (Equation A.62) simplifies to:

$$\begin{aligned}\frac{\mathrm{d}N}{\mathrm{d}\log d_\mathrm{m}} &= \frac{\mathrm{d}N}{\mathrm{d}\log d_\mathrm{a}}\,\frac{\mathrm{d}\log d_\mathrm{a}}{\mathrm{d}\log d_\mathrm{m}} \\ \frac{\mathrm{d}N}{\mathrm{d}\log d_\mathrm{m}} &= \frac{\mathrm{d}N}{\mathrm{d}\log d_\mathrm{a}}\,\frac{k\,d_\mathrm{m}^{d_\mathrm{m}-1}}{\rho_\mathrm{o}\,d_\mathrm{a}} \\ &\quad\cdot\frac{\left[d_\mathrm{m} - 1 + \frac{\alpha_{c_c}\,\lambda\,(d_\mathrm{m}-2)}{d_\mathrm{m}} + \beta_{c_c}\,\lambda\,\exp\left(-\gamma_{c_c}\,\frac{d_\mathrm{m}}{\lambda}\right)\left(\frac{d_\mathrm{m}-2}{d_\mathrm{m}} - \frac{\gamma_{c_c}}{\lambda}\right)\right]}{\left[2d_\mathrm{a} + \alpha_{c_c}\,\lambda + \beta_{c_c}\,\lambda\,\exp\left(-\gamma_{c_c}\,\frac{d_\mathrm{a}}{\lambda}\right)\left(1 - \frac{\gamma_{c_c}\,d_\mathrm{a}}{\lambda}\right)\right]},\end{aligned} \tag{A.63}$$

where $\frac{\mathrm{d}N}{\mathrm{d}\log d_\mathrm{a}}$ is provided from the AAC inversion (Section A.2) and d_a can be converted to d_m by iteratively solving Equation A.57 with known k and d_m. For a constant effective density ($k = \rho_\mathrm{eff}$ and $d_\mathrm{m} = 3$), the solution based on the mass-mobility relationship (Equation A.63) simplifies to the solution based on constant effective density (Equation A.55).

A.6 Theoretical effects of varying gas conditions on AAC classification

DeCarlo et al. [42] determined that a particle's aerodynamic diameter (d_{a}) is related to its volume equivalent diameter (d_{ve}) by:

$$\frac{d_{\mathrm{a}}}{d_{\mathrm{ve}}} = \sqrt{\frac{1}{\chi}\frac{\rho_{\mathrm{p}}}{\rho_{\mathrm{o}}}\frac{C_c(d_{\mathrm{ve}})}{C_c(d_{\mathrm{a}})}}, \tag{A.64}$$

where χ is the particle shape factor, ρ_{p} is the particle density, ρ_{o} is the unit density and C_c is the Cunningham slip correction factor. Since the volume equivalent diameter is an intrinsic particle property (i.e. does not change depending on which regime the particle is placed in), it can be used to relate the change in a particle's aerodynamic diameter from varying conditions (i.e. different temperatures, pressures and surrounding gases), such as the classifier conditions versus predefined reference conditions (0). Taking the ratio of Equation A.64 at two different conditions, assuming the shape factor is constant and that the particle does not shrink/grow due to regime changes generates:

$$\frac{d_{\mathrm{a}}}{d_{\mathrm{a},0}} = \sqrt{\frac{C_c(d_{\mathrm{ve}})}{C_c(d_{\mathrm{ve}})_0}\frac{C_c(d_{\mathrm{a},0})_0}{C_c(d_{\mathrm{a}})}}. \tag{A.65}$$

The Cunningham slip correction factor (Equation A.41) can be redefined in terms of Knudsen number (Kn) as follows:

$$C_c(\mathrm{Kn}) = 1 + \frac{\mathrm{Kn}}{2}\left[\alpha_{c_c} + \beta_{c_c}\exp\left(-\gamma_{c_c}\frac{2}{\mathrm{Kn}}\right)\right], \tag{A.66}$$

where the Knudsen number is:

$$\mathrm{Kn}(d_{\mathrm{p}}) = \frac{2\lambda}{d_{\mathrm{p}}}. \tag{A.67}$$

λ is the mean free path of the surrounding gas, d_{p} is the particle diameter of interest and Kim et al. [126] determined $\alpha_{c_c} = 2.33$, $\beta_{c_c} = 0.966$ and $\gamma_{c_c} = 0.4985$. The volume equivalent diameter Knudsen number can be related to the aerodynamic diameter Knudsen number by rearranging Equation A.67, noting that the gas mean free path is only a function of the surrounding gas conditions (not the aerosol particle size) and substituting in Equation A.64, thus at constant conditions:

$$\begin{aligned} \lambda = \text{Constant} = \frac{d_\text{a}\,\text{Kn}(d_\text{a})}{2} = \frac{d_\text{ve}\,\text{Kn}(d_\text{ve})}{2} \rightarrow \\ \text{Kn}(d_\text{ve}) = \text{Kn}(d_\text{a})\,\frac{d_\text{a}}{d_\text{ve}} = \text{Kn}(d_\text{a})\sqrt{\frac{1}{\chi}\,\frac{\rho_\text{p}}{\rho_\text{o}}\,\frac{C_c(d_\text{ve})}{C_c(d_\text{a})}}. \end{aligned} \tag{A.68}$$

Therefore, the change in the measured aerodynamic diameter is only a function of the change in Knudsen number at the conditions it was classified at versus the conditions of interest, the particle shape factor, and the ratio of particle density to unit density, as shown in Figure 3.7 of Chapter 3. Furthermore, the classifier conditions are recorded during instrument operation. Therefore, if the particle density and shape factor are known/assumed, Equations A.65 to A.68 can be iteratively solved to determine the change in the aerodynamic diameter measured at the classifier conditions to any other selected reference conditions.

A.7 Inversion of transfer function for steady-state AAC with unbalanced flows

Similar to the process developed by Stolzenburg and McMurry [229] for the DMA (but in terms of particle relaxation time rather than electrical mobility), the particle number concentration (N_{det}) that passes through the steady-state AAC operating at setpoint τ_i^* can be determined from:

$$N_{\text{det}}(\tau_i^*) = \frac{Q_{\text{a}}}{Q_{\text{s}}} \int \eta(\tau)\, \Omega(\tau,\, \tau_i^*)\, \mathrm{d}N(\tau), \tag{A.69}$$

where Q_{a} is the aerosol flow rate entering the classifier, Q_{s} is the aerosol flow rate leaving the classifier. $\eta(\tau)$ is the counting efficiency of the particle detector downstream of the AAC and $N(\tau)$ is the particle number concentration of the aerosol source at particle relaxation time τ, while $\Omega(\tau,\, \tau_i^*)$ is the transfer function of the AAC at setpoint τ_i^*. Applying the chain rule to the integrand from Equation A.69:

$$\frac{\mathrm{d}N(\tau)}{\mathrm{d}\tilde{\tau}} = \frac{\mathrm{d}N(\tau)}{\mathrm{d}\log\tau} \frac{\mathrm{d}\log\tau}{\mathrm{d}\tilde{\tau}} \rightarrow \mathrm{d}N(\tau) = \frac{\mathrm{d}N(\tau)}{\mathrm{d}\log\tau} \frac{\mathrm{d}\log\tau}{\mathrm{d}\tilde{\tau}}\, \mathrm{d}\tilde{\tau}. \tag{A.70}$$

Substituting Equation A.70 into Equation A.69:

$$N_{\text{det}}(\tau_i^*) = \frac{Q_{\text{a}}}{Q_{\text{s}}} \int \eta(\tau)\, \Omega(\tau,\, \tau_i^*) \frac{\mathrm{d}N(\tau)}{\mathrm{d}\log\tau} \frac{\mathrm{d}\log\tau}{\mathrm{d}\tilde{\tau}}\, \mathrm{d}\tilde{\tau}. \tag{A.71}$$

Using the definition of $\tilde{\tau}$ (Equation A.4) and taking its derivative:

$$\mathrm{d}\tilde{\tau} = \mathrm{d}\left(\frac{\tau}{\tau^*}\right) = \frac{1}{\tau^*}\mathrm{d}\tau, \tag{A.72}$$

as τ^* is constant when the AAC is operating at steady conditions (i.e. constant flows and classifier angular speed). Substituting the derivative of $\log(\tau)$ with respect to τ (Equation A.31) into Equation A.72:

$$\mathrm{d}\tilde{\tau} = \frac{\tau}{\tau^*} \ln(10)\, \mathrm{d}\log\tau = \tilde{\tau} \ln(10)\, \mathrm{d}\log\tau. \tag{A.73}$$

Using Equation A.73, the relaxation time derivative term in Equation A.71 becomes:

$$\begin{aligned} \frac{\mathrm{d}\log\tau}{\mathrm{d}\tilde{\tau}} &= \frac{\mathrm{d}\log\tau}{\tilde{\tau} \ln(10)\, \mathrm{d}\log\tau} \\ \frac{\mathrm{d}\log\tau}{\mathrm{d}\tilde{\tau}} &= \frac{1}{\ln(10)} \frac{1}{\tilde{\tau}}. \end{aligned} \tag{A.74}$$

Similar to Stolzenburg and McMurry [229], if the AAC is operated at a sufficient resolution to generate a narrow FWHM, $\tilde{\tau}$ can be approximated as constant (approximately one) over the particle relaxation range being classified, thus Equation A.74 becomes:

$$\frac{\mathrm{d}\log\tau}{\mathrm{d}\tilde{\tau}} \approx \frac{1}{\ln(10)}. \tag{A.75}$$

Using Equation A.75 and assuming η and $\mathrm{d}N/\mathrm{d}\log\tau$ are constant over the narrow width of the AAC transfer function (due to being operated at sufficient resolution), Equation A.71 becomes:

$$N_{\mathrm{det}}(\tau_i^*) = \frac{Q_{\mathrm{a}}}{Q_{\mathrm{s}}}\,\eta(\tau_i^*)\,\frac{\mathrm{d}N(\tau)}{\mathrm{d}\log\tau}\bigg|_{\tau_i^*}\,\frac{1}{\ln(10)}\int\Omega(\tau,\,\tau_i^*)\mathrm{d}\tilde{\tau}. \tag{A.76}$$

Since the AAC transfer function is centered around τ_i^*, this value is used to estimate the constants (i.e. η and $\mathrm{d}N(\tau)/\mathrm{d}\log\tau$). Tavakoli and Olfert [238] showed that the AAC non-diffusing transfer function in terms of particle relaxation time using particle streamline theory (Equation A.1) was the same as the DMA non-diffusing transfer function in terms of particle electrical mobility using particle streamline theory [229]. Therefore, the following solution developed by Stolzenburg and McMurry [229] applies:

$$\int\Omega_{\mathrm{ND}}(\tau,\tau_i^*)\mathrm{d}\tilde{\tau} = \beta_i\,(1+\delta_i). \tag{A.77}$$

Substituting Equation A.77 into Equation A.76 and rearranging generates the following solution to calculate the idealized size distribution of the aerosol based on particle relaxation time ($\mathrm{d}N_{\mathrm{UB}}/\mathrm{d}\log\tau$) from the primary AAC measurements when operated with unbalanced flows (UB, i.e. $\delta \neq 0$):

$$\begin{aligned} &N_{\mathrm{det}}(\tau_i^*) = \frac{Q_{\mathrm{a}}}{Q_{\mathrm{s}}}\,\eta(\tau_i^*)\,\frac{\mathrm{d}N_{\mathrm{UB}}(\tau)}{\mathrm{d}\log\tau}\bigg|_{\tau_i^*}\,\frac{1}{\ln(10)}\beta_i\,(1+\delta_i) \rightarrow \\ &\frac{\mathrm{d}N_{\mathrm{UB}}(\tau)}{\mathrm{d}\log\tau}\bigg|_{\tau_i^*} = \frac{\ln(10)\,\frac{Q_{\mathrm{s}}}{Q_{\mathrm{a}}}\,N_{\mathrm{det}}(\tau_i^*)}{\eta(\tau_i^*)\,\beta_i\,(1+\delta_i)} \end{aligned} \tag{A.78}$$

Appendix B

Theory for Measuring Size Distributions using the Scanning AAC

B.1 Simplified notation of parameter subscripts

All of the parameters in each section of this appendix and its subsections apply to a particular instance of AAC operation and theory. These different instances are categorized in Table B.1.

For readability, the title and header of each section in this appendix are used to clarify the common instances considered within the section and its subsections. This approach allows only the subscripts required to differentiate multiple instances of the same parameter within the same section to be used.

For example, consider the transfer function of the AAC denoted as Ω_{AAC}. If only one combination of instances is included within a section, such as the AAC operating at steady-state (ss) considering idealized (I), limited trajectory (LT) theory, the AAC transfer function within this section will be denoted as Ω_{AAC} rather than $\Omega_{AAC,ss,LT,I}$. To avoid the ambiguity of this reduced notation, the title and header of this section would include steady-state (ss), idealized (I) and limited trajectory (LT).

However, if different instances are considered within the same section, such as the AAC operating at steady-state (ss) or scanning (sc), with both operating modes considering idealized (I), limited trajectory (LT) theory, the AAC transfer functions within this section will be denoted as $\Omega_{AAC,ss}$ and $\Omega_{AAC,sc}$, respectively, rather than $\Omega_{AAC,ss,LT,I}$ and $\Omega_{AAC,sc,LT,I}$, respectively. Similarly, to avoid the ambiguity of this reduced notation, the title and header of this section would include idealized (I) and limited trajectory (LT). Finally, if the parameter applies to both options of a particular instance, for example it represents both balanced (B)

Table B.1 Categorized instances of AAC operation and theory.

AAC Category	Instance	Subscript Notation	Description
Operation	Steady-State	ss	AAC at a constant classifier angular speed and sheath flow (i.e. constant setpoint)
	Scanning	sc	Angular speed of the AAC classifier varies continuously with time (i.e. varying setpoint)
Transfer Function Theory	Limited Trajectory	LT	Determines the minimum and maximum particle and classifier properties that allow particles to pass through the AAC classifier
	Particle Streamline	PS	Determines the centrifugal flux function to estimate the transfer function of the AAC
Classification	Idealized	I	Neglects particle losses and broadening of AAC transfer function
	Non-Idealized	NI	Considers particle losses and broadening of AAC transfer function
Classifier Flows	Balanced	B	$Q_{sh} = Q_{exh}$ and $Q_a = Q_s$
	Unbalanced	UB	$Q_{sh} \neq Q_{exh}$ and $Q_a \neq Q_s$

and unbalanced (UB) classifier flows, no differentiation for this instance is included within the subscript of the parameter or section title/header.

B.2 Angular speed profile of AAC classifier during scanning

Note: Similar to the other sections in this appendix, this section and its subsections use simplified notation of the parameter subscripts, as outlined in Section B.1, based on the common AAC operation and theory instances included within the title and header of this section.

This section expands the scanning DMA theory developed by Wang and Flagan [261] for the electrostatic field generated by the changing voltage of the DMA classifier to the centrifugal force field generated by the changing angular speed (ω) of the AAC classifier. First, consider that the angular speed of the AAC classifier varies continuously with time (t) as follows:

$$\omega = \omega(t). \tag{B.1}$$

The centrifugal force field (E_c) generated inside the AAC classifier at time t and radial position r can then be calculated by:

$$E_c(t, r) = \omega^2(t)\, r. \tag{B.2}$$

The angular speed function ($\omega(t)$) of the classifier must produce a proportional change in the centrifugal force field (E_c) over time t, and the resulting critical particle trajectories it induces, that are independent of the times that the particles arrive at the classifier inlet (t_{in}) as follows:

$$\frac{E_c(t_{in}+t, r)}{E_c(t_{in}, r)} = j(t), \tag{B.3}$$

where j is a generic function that is only a function of t. As an initial guess, define the angular speed function ($\omega(t)$) of the classifier as:

$$\omega^2(t) = \omega_S^2\, C^{\frac{t}{\tau_{sc}}}, \tag{B.4}$$

where ω_S is the classifier speed at the start of the scan (i.e. $t = 0$), C is a constant that is any real number greater than one, and τ_{sc} is the time constant of the scan. To check if this speed profile (Equation B.4) satisfies the criteria, substitute it into Equation B.3, and simplify as follows:

$$\frac{E_c(t_{in}+t,\,r)}{E_c(t_{in},\,r)} = \frac{r\,\omega_S^2\,C^{\frac{t_{in}+t}{\tau_{sc}}}}{r\,\omega_S^2\,C^{\frac{t_{in}}{\tau_{sc}}}} = C^{\frac{t}{\tau_{sc}}} = j(t). \tag{B.5}$$

Therefore, this speed profile (Equation B.4) satisfies Equation B.3 and results in a ratio of centrifugal force fields that is independent of t_{in}. Over the scan time (t_{sc}), the classifier speed must change from ω_S to ω_E. Substituting these values into the speed profile (Equation B.4) and solving for the time constant (τ_{sc}) of the scan:

$$\omega_E^2 = \omega_S^2\,C^{\frac{t_{sc}}{\tau_{sc}}} \rightarrow \boldsymbol{\tau_{sc} = \frac{t_{sc}\ln(C)}{2\ln\left(\frac{\omega_E}{\omega_S}\right)}}. \tag{B.6}$$

Furthermore, substituting this scan constant (Equation B.6) into the speed profile (Equation B.4), and simplifying:

$$\omega^2(t) = \omega_S^2\,C^{\frac{t}{\frac{t_{sc}\ln(C)}{2\ln\left(\frac{\omega_E}{\omega_S}\right)}}} \rightarrow 2\ln\left(\frac{\omega(t)}{\omega_S}\right) = \frac{t}{\frac{t_{sc}\ln(C)}{2\ln\left(\frac{\omega_E}{\omega_S}\right)}}\ln(C) \rightarrow \boldsymbol{\omega(t) = \omega_S \exp\left(\frac{t\ln\left(\frac{\omega_E}{\omega_S}\right)}{t_{sc}}\right)}. \tag{B.7}$$

Therefore, the required angular speed of the classifier during a scan is independent of the actual value of the positive, real number constant C. It is also interesting to note that defining this angular speed function to the power of p, as follows, simplifies to the same result as the time constant (τ_{sc}) of the scan compensates for this change by scaling by a factor of $1/p$:

$$\omega_E^p = \omega_S^p\,C^{\frac{t_{sc}}{\tau_{sc}}} \rightarrow \boldsymbol{\tau_{sc} = \frac{t_{sc}\ln(C)}{p\ln\left(\frac{\omega_E}{\omega_S}\right)}}, \tag{B.8}$$

where p is a constant that is any real number. For consistency with the previous inversion studies of the scanning DMA and the centrifugal force field generated in the AAC, this work will use $C = e$ and $p = 2$, as follows:

$$\omega^2(t) = \omega_S^2 \exp\left(\frac{t}{\tau_{sc}}\right), \tag{B.9}$$

and

$$\tau_{sc} = \frac{t}{2\ln\left(\frac{\omega(t)}{\omega_S}\right)} = \frac{t_{sc}}{2\ln\left(\frac{\omega_E}{\omega_S}\right)}. \tag{B.10}$$

Therefore, the AAC completing an up scan (i.e. $\omega_E > \omega_S$) is reflected in a positive scan time constant (i.e. $\tau_{sc} > 0$), which accelerates the classifier and classifies increasingly

smaller particle relaxation times over the scan duration. A down scan (i.e. $\omega_E < \omega_S$) is reflected in a negative scan time constant (i.e. $\tau_{sc} < 0$), which decelerates the classifier and classifies increasingly larger particle relaxation times over the scan duration. The required acceleration/deceleration profile during a scan is the derivative of the speed profile (Equation B.9) as follows:

$$\frac{d\omega}{dt} = \dot{\omega} = \frac{\omega_S}{2\tau_{sc}} \exp\left(\frac{t}{2\tau_{sc}}\right). \tag{B.11}$$

The *required speed* ($\omega(t)$) and *required acceleration* ($\dot{\omega}(t)$) profiles for the AAC classifier over an example up or down scan is shown in Figure B.1, while the *acceleration/deceleration capacity* of multiple AACs (i.e. the maximum acceleration/deceleration the classifier can actually achieve) and the variation between them is shown in Figure B.2. As discussed in the main text, the acceleration/deceleration capacity varies slightly between different AACs due to small differences in drive belt tension, as well as changes in bearing friction and motor efficiency over the lifetime of the instrument. To account for this variation, the acceleration/deceleration capacities of each AAC should be periodically updated by measuring the maximum acceleration and deceleration the classifier can achieve as a function of its angular speed, such as those shown in Figure B.2.

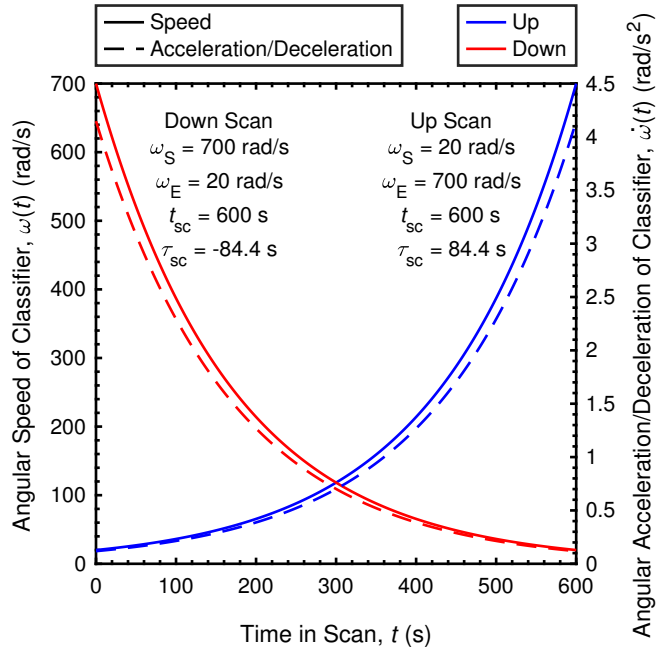

Fig. B.1 Example of the required speed and acceleration profiles for the AAC classifier during a 600 s scan from 20 rad/s to 700 rad/s.

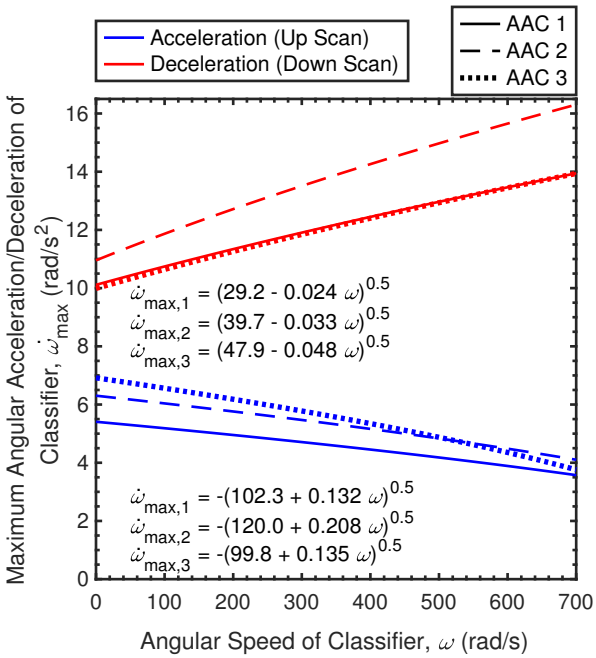

Fig. B.2 Acceleration/deceleration capacity of multiple AACs and the variation between them.

The speed of the AAC during maximum acceleration or deceleration (i.e. maximum motor or electrical brake current) is captured by a quadratic relationship with respect to time. Therefore, the maximum acceleration or deceleration the AAC achieved as a function of its angular speed (i.e. its *acceleration/deceleration capacity*) is determined by isolating time in the quadratic equation and substituting it into the derivative (with respect to time) of the quadratic equation.

B.2.1 Minimum scan time ($t_{sc,min}$)

The scan time (t_{sc}) of the AAC is limited by the angular acceleration the classifier can achieve as a function of its angular speed (i.e. acceleration/deceleration capacity of the classifier). The relationship between these parameters can be determined by substituting the required speed profile over a scan ($\omega(t)$ defined by Equation B.9) into the corresponding required acceleration profile ($\dot{\omega}(t)$ defined by Equation B.11) as follows:

$$\dot{\omega}(t) = \frac{\omega(t)}{2\tau_{sc}}. \tag{B.12}$$

Therefore, the required angular acceleration of the classifier ($\dot{\omega}(t)$) is linearly proportional to its required angular speed ($\omega(t)$) by a factor of $1/(2\tau_{sc})$, while the acceleration capacity of the classifier is proportional to the square root of its angular speed as shown in Figure B.2. This factor for required acceleration (i.e. $1/(2\tau_{sc})$) can be related to the scan time (t_{sc}) by substituting the definition of τ_{sc} (Equation B.10) into Equation B.12 and rearranging as follows:

$$\dot{\omega}(t) = \frac{\omega(t)}{2\frac{t_{sc}}{2\ln\left(\frac{\omega_E}{\omega_S}\right)}} \rightarrow \boldsymbol{t_{sc} = \frac{\omega(t)}{\dot{\omega}(t)} \ln\left(\frac{\omega_E}{\omega_S}\right)}. \tag{B.13}$$

Therefore, the minimum scan time ($t_{sc,min}$) is based on the maximum angular acceleration or deceleration ($\dot{\omega}_{max}$) the AAC can achieve during an up or down scan, respectively, as follows:

$$t_{sc,min} = \frac{\omega(t)}{\dot{\omega}_{max}(\omega(t))} \ln\left(\frac{\omega_E}{\omega_S}\right). \tag{B.14}$$

$\dot{\omega}_{max}$ is a function of classifier speed ($\omega(t)$) to reflect both the rotational energy and friction of the classifier are related to its speed and thus dominates the maximum acceleration/deceleration capacity of the AAC. An example of these acceleration and deceleration capacities for multiple AACs and the variation between them is shown in Figure B.2.

As shown in Figure B.1, the required acceleration over an up scan increases. However, the friction of the spinning classifier also increases with its speed. Therefore, the acceleration capacity of the AAC decreases as an up scan progresses (as shown in Figure B.2), while the required acceleration increases. Therefore, the minimum scan time of an up scan is the intersection of these two converging acceleration curves at the end of the up scan (i.e. $t = t_{sc}$), where the required acceleration from the scan profile is the highest and the maximum acceleration capacity of the AAC is the lowest (i.e. at highest classifier speed during scan,

$\omega = \omega_E$). Substituting these values into Equation B.14, the minimum scan time of an up scan ($t_{sc,min,up}$) is:

$$t_{sc,min,up} = \frac{\omega_E}{\dot{\omega}_{max}(\omega_E)} \ln\left(\frac{\omega_E}{\omega_S}\right), \tag{B.15}$$

where $\dot{\omega}_{max}$ is the acceleration capacity of the AAC classifier at speed ω_E.

In contrast, as shown in Figure B.1, the required deceleration over a down scan decreases. The deceleration capacity of the AAC also decreases over the down scan (as shown in Figure B.2) as the friction decreases with classifier speed. Therefore, the minimum scan time of the down scan is based on two factors. First, the maximum deceleration capacity of the AAC must meet or exceed the maximum deceleration required by the scan profile. Secondly, the maximum deceleration capacity of the AAC cannot decrease faster than the deceleration required by the scan profile. However, the required deceleration decreases linearly with classifier speed and has a zero intercept (as shown by Equation B.12), while the maximum deceleration capacity of the AAC has a nonzero intercept due to its active electric brake (as shown in Figure B.2). Since the deceleration required over a down scan is a strictly increasing function with classifier speed, both factors can be satisfied by checking the deceleration capacity of the AAC at the start of the down scan (i.e. $t = 0$), where both the required deceleration and deceleration capacity of the AAC are the highest. Substituting these values into Equation B.14, the minimum scan time of a down scan ($t_{sc,min,down}$) is:

$$t_{sc,min,down} = \frac{\omega_S}{\dot{\omega}_{max}(\omega_S)} \ln\left(\frac{\omega_E}{\omega_S}\right), \tag{B.16}$$

where $\dot{\omega}_{max}$ is the deceleration capacity of the AAC classifier at speed ω_S.

B.3 Transfer function of steady-state or scanning AAC: limited trajectory, idealized & uniform axial flow

Note: Similar to the other sections in this appendix, this section and its subsections use simplified notation of the parameter subscripts, as outlined in Section B.1, based on the common AAC operation and theory instances included within the title and header of this section.

Based on limited trajectory theory, this section completes the following two tasks in parallel:

- Rederives/verifies the limited trajectory theory developed by Tavakoli and Olfert [238] to describe the transfer function of the AAC at a constant classifier angular speed and sheath flow (i.e. one aerodynamic diameter setpoint); and
- Expands the limited trajectory theory developed by Wang and Flagan [261] to derive the transfer function for the scanning DMA to the scanning AAC (i.e. considers that the angular speed ω of the AAC classifier varies continuously with time t).

As derived in Sections 4.2.1 to 4.2.5 of the main text, a particle with relaxation time τ will migrate from radial position r_{in} to r_{out} over its residence time in the classifier (t_{f}) as follows (restatement of Equation 4.13 in main text):

$$\tau = \frac{1}{K} \ln\left(\frac{r_{\text{out}}}{r_{\text{in}}}\right). \tag{B.17}$$

For steady-state operation K equals (restatement of Equation 4.15 in main text):

$$K_{\text{ss}} = \omega^2 t_{\text{f}}, \tag{B.18}$$

while for scanning operation K equals (restatement of Equation 4.18 in main text):

$$K_{\text{sc}} = \omega_{\text{S}}^2 \, \tau_{\text{sc}} \exp\left(\frac{t_{\text{m}}}{\tau_{\text{sc}}}\right)\left[1 - \exp\left(\frac{-t_{\text{f}}}{\tau_{\text{sc}}}\right)\right], \tag{B.19}$$

where t_{f} is the particle residence time along the critical trajectory in the classifier, τ_{sc} is the time constant of the scan and t_{m} is the measurement time during the scan (defined by Equations 4.12, 4.9 and 4.17 in main text, respectively). Equation B.17 can be rearranged by isolating r_{out} as follows:

$$r_{\text{out}} = r_{\text{in}} \exp(K\tau). \tag{B.20}$$

Based on the simplified schematic of the AAC classifier geometry shown in Figure B.3, the particle with the largest relaxation time (τ_{max}) that will pass through the classifier will start at the inner radius of the classifier (i.e. $r_{in} = r_1$) and reach its outer radius (i.e. $r_{out} = r_2$) after migration time t_f.

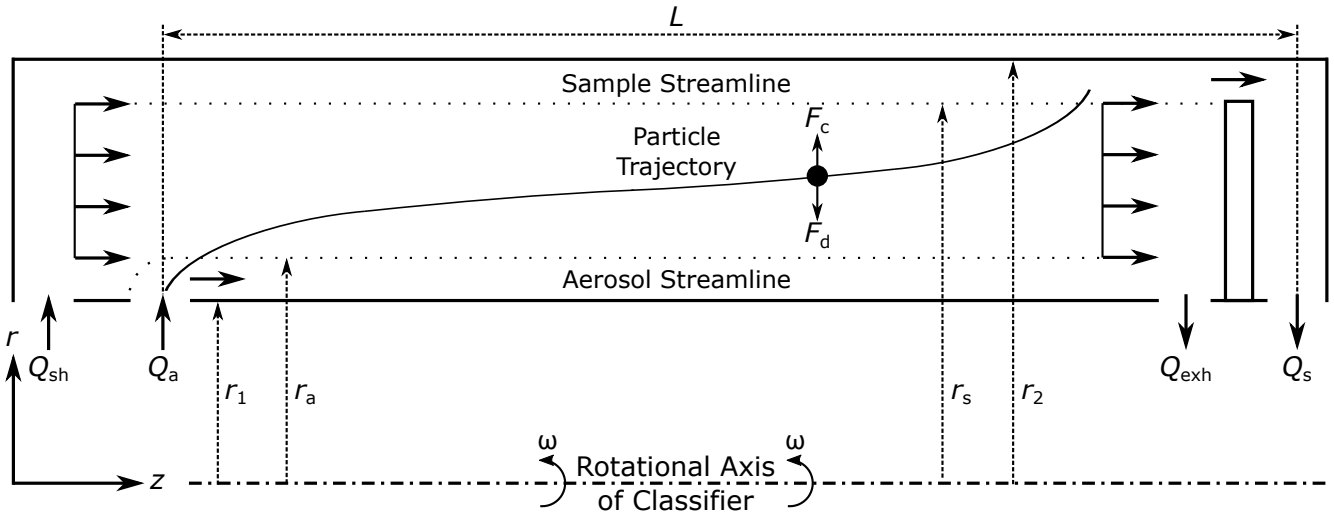

Fig. B.3 Simplified schematic of the AAC classifier.

Substituting these values (i.e. $r_{in} = r_1$ and $r_{out} = r_2$) into Equation B.17:

$$\tau_{max} = \frac{1}{K} \ln\left(\frac{r_2}{r_1}\right). \tag{B.21}$$

Based on the definitions of t_f and K_{ss} (Equation 4.12 of main text and Equation B.18, respectively), this solution (Equation B.21) agrees with Equation 5 from Tavakoli and Olfert [238] for the steady-state AAC. Since the axial flow is uniform, r_a and r_s (i.e. the radial positions within the AAC classifier at the outer edge of the aerosol streamlines and inner edge of the sample streamlines, respectively, as shown in Figure B.3) can be derived in terms of the classifier dimensions and flows by rearranging the definition of uniform axial velocity (i.e. Equation 4.11 of the main text) as follows:

$$\begin{aligned} &\frac{Q_a + Q_{sh}}{\pi(r_2^2 - r_1^2)} = \frac{Q_{sh}}{\pi(r_2^2 - r_a^2)} \rightarrow \\ &r_a = \sqrt{\frac{r_2^2\left[Q_a + Q_{sh} - Q_{sh}\left(1 - r_1^2/r_2^2\right)\right]}{Q_a + Q_{sh}}}, \end{aligned} \tag{B.22}$$

and

$$\begin{aligned} \frac{Q_a + Q_{sh}}{\pi(r_2^2 - r_1^2)} &= \frac{Q_s}{\pi(r_2^2 - r_s^2)} \rightarrow \\ r_s &= \sqrt{\frac{r_2^2\left[Q_a + Q_{sh} - Q_s\left(1 - r_1^2/r_2^2\right)\right]}{Q_a + Q_{sh}}}. \end{aligned} \tag{B.23}$$

Based on the simplified schematic of the AAC classifier geometry shown in Figure B.3, the particle with the smallest relaxation time (τ_{min}) that will pass through the classifier will start at $r_{in} = r_a$ and reach $r_{out} = r_s$ after migration time t_f. Substituting these values (i.e. Equations B.22 and B.23) into Equation B.17, and simplifying:

$$\begin{aligned} \tau_{min} &= \frac{1}{K}\ln\left(\frac{r_s}{r_a}\right) = \frac{1}{K}\ln\left(\frac{\sqrt{\frac{r_2^2}{Q_a+Q_{sh}}\left[Q_a + Q_{sh} - Q_s\left(1 - r_1^2/r_2^2\right)\right]}}{\sqrt{\frac{r_2^2}{Q_a+Q_{sh}}\left[Q_a + Q_{sh} - Q_{sh}\left(1 - r_1^2/r_2^2\right)\right]}}\right) \\ \tau_{min} &= \frac{1}{2K}\ln\left(\frac{Q_a + Q_{sh} - Q_s\left(1 - r_1^2/r_2^2\right)}{Q_a + Q_{sh} - Q_{sh}\left(1 - r_1^2/r_2^2\right)}\right). \end{aligned} \tag{B.24}$$

Based on the definitions of t_f and K_{ss} (Equation 4.12 of main text and Equation B.18, respectively), this solution (Equation B.24) agrees with Equation 7 from Tavakoli and Olfert [238] for the steady-state AAC. Therefore, the center of the AAC transfer function can be determined from[1]:

$$\tau^* = \frac{\tau_{min} + \tau_{max}}{2}. \tag{B.25}$$

For particles with relaxation times less than τ_{min} or greater than τ_{max}, the probability they will pass through the AAC classifier is zero. For particles with relaxation time greater than τ_{min} and less than τ_{max}, only a fraction of them will pass through the AAC classifier, with the magnitude depending on their starting position (r_{in}). For particles with a relaxation time greater than τ_{min}, only particles with initial position $r_{c,min} < r_{in} < r_a$ will pass through the classifier. Therefore, assuming the aerosol is uniformly distributed between the inner radius and aerosol streamline ($r_1, r_{in} < r_a$, as shown in Figure B.3), the fraction of particles between $r_{c,min}$ and r_a is:

[1]This equation assumes the transfer function is symmetric about τ^*. While this is true for the AAC transfer function derived by particle streamline theory, the AAC transfer function derived by limited trajectory is slightly skewed to the smaller particle relaxation times. This skewness is negligible for most AAC applications, however it does become noticeable as the counting time of the particle detector increases (>2 s). This difference manifests in the average transfer function of the scanning AAC derived later in Sections B.5 and B.6.

$$f_1 = \frac{r_a^2 - r_{c,min}^2}{r_a^2 - r_1^2}. \tag{B.26}$$

To determine $r_{c,min}$, assume $r_{in} = r_{c,min}$ and reaches $r_{out} = r_s$ after migration time t_f. Substituting these values into Equation B.20, and simplifying:

$$r_s = r_{c,min} \exp(\tau K) \rightarrow \boldsymbol{r_{c,min} = \frac{r_s}{\exp(\tau K)}}. \tag{B.27}$$

Substituting the definitions of r_a, r_s and $r_{c,min}$ (Equations B.22, B.23 and B.27, respectively) into the definition of f_1 (Equation B.26), and simplifying:

$$\begin{aligned} f_1 &= \frac{r_a^2 - r_{c,min}^2}{r_a^2 - r_1^2} = \frac{\frac{r_2^2}{Q_a+Q_{sh}}\left[Q_a + Q_{sh} - Q_{sh}\left(1 - r_1^2/r_2^2\right)\right] - \frac{\frac{r_2^2}{Q_a+Q_{sh}}\left[Q_a+Q_{sh}-Q_s\left(1-r_1^2/r_2^2\right)\right]}{\exp(\tau K)^2}}{\frac{r_2^2}{Q_a+Q_{sh}}\left[Q_a + Q_{sh} - Q_{sh}\left(1 - r_1^2/r_2^2\right)\right] - r_1^2} \\ f_1 &= \frac{Q_a + Q_{sh}\, r_1^2/r_2^2 - \exp(-2\tau K)\left[Q_a + Q_{sh} - Q_s\left(1 - r_1^2/r_2^2\right)\right]}{Q_a\left(1 - r_1^2/r_2^2\right)}. \end{aligned} \tag{B.28}$$

Based on the definitions of t_f and K_{ss} (Equation 4.12 of main text and Equation B.18, respectively), this solution (Equation B.28) agrees with Equation 9 from Tavakoli and Olfert [238] for the steady-state AAC. Similarly, assuming the aerosol is uniformly distributed between the inner radius and aerosol streamline ($r_1 < r_{in} < r_a$, as shown in Figure B.3), the fraction of particles between r_1 and $r_{c,max}$ is:

$$f_2 = \frac{r_{c,max}^2 - r_1^2}{r_a^2 - r_1^2}. \tag{B.29}$$

To determine $r_{c,max}$, assume $r_{in} = r_{c,max}$ and reaches $r_{out} = r_2$ after migration time t_f. Substituting these values into Equation B.20, and simplifying:

$$r_2 = r_{c,max} \exp(\tau K) \rightarrow \boldsymbol{r_{c,max} = \frac{r_2}{\exp(\tau K)}}. \tag{B.30}$$

Substituting the definitions of r_a and $r_{c,max}$ (Equations B.22 and B.30, respectively) into the definition of f_2 (Equation B.29), and simplifying:

$$f_2 = \frac{r_{c,max}^2 - r_1^2}{r_a^2 - r_1^2} = \frac{\frac{r_2^2}{\exp(\tau K_{sc})^2} - r_1^2}{\frac{r_2^2}{Q_a+Q_{sh}}\left[Q_a + Q_{sh} - Q_{sh}\left(1 - r_1^2/r_2^2\right)\right] - r_1^2} \tag{B.31}$$

$$f_2 = \frac{Q_a + Q_{sh}}{Q_a}\left(\frac{\exp(-2\tau K) - r_1^2/r_2^2}{1 - r_1^2/r_2^2}\right).$$

Based on the definitions of t_f and K_{ss} (Equation 4.12 of main text and Equation B.18, respectively), this solution (Equation B.31) agrees with Equation 11 from Tavakoli and Olfert [238] for the steady-state AAC. Finally, if the sample flowrate (Q_s) is smaller than the aerosol flowrate (Q_a), the transfer function (Ω_{AAC}) cannot be larger than:

$$f_3 = \frac{Q_s}{Q_a}. \tag{B.32}$$

Therefore, the transfer function of the steady-steady or scanning AAC (Ω_{AAC}) based on limited trajectory and assuming plug flow is:

$$\Omega_{AAC} = \max[0, \min(f_1, f_2, f_3, 1)], \tag{B.33}$$

where f_1, f_2 and f_3 are defined in Equations B.28, B.31 and B.32, respectively. This function reflects that the transfer function of the AAC cannot be greater than one (i.e. minimum function includes one) and that the transfer function outside the ranges of particle relaxation times corresponding to f_1, f_2 and f_3 is zero (i.e. maximum function includes zero). Therefore, the steady-state and scanning AAC transfer functions have the same form (i.e. same shape) independent of the measurement time. The steady-state transfer function has a constant value (K_{ss}), while the scanning transfer function has a constant value (K_{sc}) that changes based on the time the particles arrive at the classifier inlet. Please see Table 4.1 in the main text for a summary of these similar transfer functions.

B.3.1 Instantaneous setpoint of scanning AAC

The simplified form of the setpoint of the steady-state or scanning AAC can be found by substituting the definitions of τ_{min} and τ_{max} (Equations B.24 and B.21, respectively) into the definition of τ^* (Equation B.25) as follows:

$$\begin{aligned}\tau^* &= \frac{\tau_{\text{min}} + \tau_{\text{max}}}{2} \\ \tau^* &= \frac{1}{2K}\left[\ln\left(\frac{r_2}{r_1}\right) + \frac{1}{2}\ln\left(\frac{Q_{\text{a}} + Q_{\text{sh}} - Q_{\text{s}}\left(1 - r_1^2/r_2^2\right)}{Q_{\text{a}} + Q_{\text{sh}} - Q_{\text{sh}}\left(1 - r_1^2/r_2^2\right)}\right)\right].\end{aligned} \tag{B.34}$$

where $K = K_{\text{ss}}$ or $K = K_{\text{sc}}$ for the steady-state or scanning AAC, respectively. This equation determines the instantaneous setpoint of the scanning AAC as it does not account for the shift of its transfer function over the counting time of the downstream particle detector. This effect on the setpoint of the scanning AAC is considered later in Section B.7.1.

Furthermore, the instantaneous setpoint offset between steady-state and scanning operation can be found by taking the ratio of τ^*_{sc} to τ^*_{ss} (Equation B.34), while using the K constants corresponding to the steady-state and scanning AAC transfer functions as follows:

$$\frac{\tau^*_{\text{sc}}}{\tau^*_{\text{ss}}} = \frac{K_{\text{ss}}}{K_{\text{sc}}}. \tag{B.35}$$

This equation, based on the definitions of K_{ss} and K_{sc} (i.e. Equations B.18 and B.19, respectively), expands to:

$$\frac{\tau^*_{\text{sc}}}{\tau^*_{\text{ss}}} = \frac{\omega^2 t_{\text{f}}}{\omega_{\text{S}}^2\, \tau_{\text{sc}} \exp\left(\frac{t_{\text{m}}}{\tau_{\text{sc}}}\right)\left[1 - \exp\left(\frac{-t_{\text{f}}}{\tau_{\text{sc}}}\right)\right]}. \tag{B.36}$$

B.3.2 Condensed representation of transfer function for scanning AAC

To simplify derivations in the later sections of this appendix, the mathematical representation of the transfer function of the scanning AAC based on limited trajectory theory (Equation B.33) as derived in Section B.3 can be simplified by grouping the constants and reorganizing particular terms. Firstly, this transfer function can also be represented by a piecewise equation (as shown in Figure B.4) as follows:

$$\Omega_{\mathrm{AAC}} = \begin{cases} f_1 & \text{if } \tau_{\min} \leq \tau \leq \tau_{13} \\ c_{f31} & \text{if } \tau_{13} < \tau < \tau_{23} \\ f_2 & \text{if } \tau_{23} \leq \tau \leq \tau_{\max} \\ 0 & \text{elsewhere} \end{cases}, \tag{B.37}$$

where c_{f31} is a constant based on f_3 (Equation B.32):

$$c_{f31} = \min\left(f_3,\, 1\right) = \min\left(\frac{Q_{\mathrm{s}}}{Q_{\mathrm{a}}},\, 1\right), \tag{B.38}$$

and τ_{13} and τ_{23} are the particle relaxation times that correspond to the intercepts of f_1 and f_2 with the middle component of the transfer function, respectively. As shown in Figure B.4, these intercepts occur at τ^* for an AAC operating with balanced classifier flows and at some offset from τ^* for an AAC operating with unbalanced classifier flows. The offset intercept (denoted as τ_1) of f_1 and c_{f31} (Equation B.38) can be found by solving the simplified representation of f_1 (Equation B.53 as shown in Table B.2) as follows:

$$\begin{aligned} c_{f31} &= c_{f11} \exp\left[c_{f12}\, \tau_1 \exp\left(\frac{t_{\mathrm{m}}}{\tau_{\mathrm{sc}}}\right)\right] + c_{f13} \rightarrow \\ \tau_1 &= \frac{1}{c_{f12}} \ln\left(\frac{c_{f31} - c_{f13}}{c_{f11}}\right) \exp\left(\frac{-t_{\mathrm{m}}}{\tau_{\mathrm{sc}}}\right). \end{aligned} \tag{B.39}$$

Similarly, the offset intercept (denoted as τ_2) of f_2 and c_{f31} (Equation B.38) can be found by solving the simplified representation of f_2 (Equation B.57 as shown in Table B.2) as follows:

$$\begin{aligned} c_{f31} &= c_{f21} \exp\left[c_{f22}\, \tau_2 \exp\left(\frac{t_{\mathrm{m}}}{\tau_{\mathrm{sc}}}\right)\right] + c_{f23} \rightarrow \\ \tau_2 &= \frac{1}{c_{f22}} \ln\left(\frac{c_{f31} - c_{f23}}{c_{f21}}\right) \exp\left(\frac{-t_{\mathrm{m}}}{\tau_{\mathrm{sc}}}\right). \end{aligned} \tag{B.40}$$

Therefore considering both balanced or unbalanced classifier flows, the intercepts of the transfer function of the scanning AAC (denoted as τ_{13} and τ_{23}) are:

$$\tau_{13} = \min(\tau_1, \tau^*), \tag{B.41}$$

$$\tau_{23} = \max(\tau_2, \tau^*). \tag{B.42}$$

Note that all of the boundary conditions (i.e. $\tau_{\min}$, τ_{13}, τ^*, τ_{23}, $\tau_{\max}$) of the transfer function of the scanning AAC based on limited trajectory are of the form:

$$\tau_x = c_{\tau x} \exp\left(\frac{-t_m}{\tau_{sc}}\right), \tag{B.43}$$

where $c_{\tau x}$ represents the grouped constants of each boundary x shown in Figure B.4. Therefore, the transfer function of the scanning AAC based on limited trajectory can then be simplified, as shown in Table B.2 on the next page.

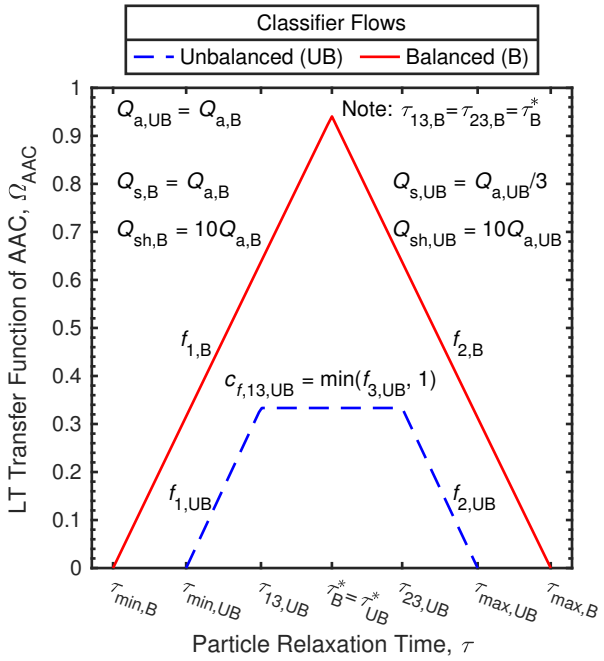

Fig. B.4 Transfer function of the AAC with balanced (B) or unbalanced (UB) classifier flows based on limited trajectory theory.

Table B.2 Constants and boundaries of the simplified mathematical representation of the transfer function of the scanning AAC based on limited trajectory theory.

Original Equation	Simplified Form	
	Equation	Constants
B.19	$K_{sc}(t_m) = c_{sc} \exp\left(\frac{t_m}{\tau_{sc}}\right)$ (B.44)	$c_{sc} = \omega_S^2 \tau_{sc} \left[1 - \exp\left(\frac{-t_f}{\tau_{sc}}\right)\right]$ (B.45)
B.21	$\tau_{max} = c_{\tau max} \exp\left(\frac{-t_m}{\tau_{sc}}\right)$ (B.46)	$c_{\tau max} = \frac{1}{c_{sc}} \ln\left(\frac{r_2}{r_1}\right)$ (B.47)
B.24	$\tau_{min} = c_{\tau min} \exp\left(\frac{-t_m}{\tau_{sc}}\right)$ (B.48)	$c_{\tau min} = \frac{1}{2c_{sc}} \ln\left(\frac{Q_a + Q_{sh} - Q_s\left(1 - r_1^2/r_2^2\right)}{Q_a + Q_{sh} - Q_{sh}\left(1 - r_1^2/r_2^2\right)}\right)$ (B.49)
B.25	$\tau^* = c_{\tau *} \exp\left(\frac{-t_m}{\tau_{sc}}\right)$ (B.50)	$c_{\tau *} = \frac{c_{\tau min} + c_{\tau max}}{2}$ (B.51) $c_{\tau *} = \frac{1}{2c_{sc}} \left[\ln\left(\frac{r_2}{r_1}\right) + \frac{1}{2} \ln\left(\frac{Q_a + Q_{sh} - Q_s\left(1 - r_1^2/r_2^2\right)}{Q_a + Q_{sh} - Q_{sh}\left(1 - r_1^2/r_2^2\right)}\right)\right]$ (B.52)
B.28	$f_1 = c_{f11} \exp\left[c_{f12}\, \tau \exp\left(\frac{t_m}{\tau_{sc}}\right)\right] + c_{f13}$ (B.53)	$c_{f11} = \frac{-\left[Q_a + Q_{sh} - Q_s\left(1 - r_1^2/r_2^2\right)\right]}{Q_a\left(1 - r_1^2/r_2^2\right)}$ (B.54) $c_{f12} = -2c_{sc}$ (B.55) $c_{f13} = \frac{Q_a + Q_{sh}\, r_1^2/r_2^2}{Q_a\left(1 - r_1^2/r_2^2\right)}$ (B.56)
B.31	$f_2 = c_{f21} \exp\left[c_{f22}\, \tau \exp\left(\frac{t_m}{\tau_{sc}}\right)\right] + c_{f23}$ (B.57)	$c_{f21} = \frac{Q_a + Q_{sh}}{Q_a\left(1 - r_1^2/r_2^2\right)} = (c_{f13} - 1)\left(\frac{r_2^2}{r_1^2}\right)$ (B.58) $c_{f22} = -2c_{sc} = c_{f12}$ (B.59) $c_{f23} = \frac{-(Q_a + Q_{sh})\left(r_1^2/r_2^2\right)}{Q_a\left(1 - r_1^2/r_2^2\right)} = -c_{f13} + 1$ (B.60)
B.39	$\tau_1 = c_{\tau 1} \exp\left(\frac{-t_m}{\tau_{sc}}\right)$ (B.61)	$c_{\tau 1} = \frac{1}{c_{f12}} \ln\left(\frac{c_{f31} - c_{f13}}{c_{f11}}\right)$ (B.62)
B.40	$\tau_2 = c_{\tau 2} \exp\left(\frac{-t_m}{\tau_{sc}}\right)$ (B.63)	$c_{\tau 2} = \frac{1}{c_{f22}} \ln\left(\frac{c_{f31} - c_{f23}}{c_{f21}}\right)$ (B.64)
B.41	$\tau_{13} = c_{\tau 13} \exp\left(\frac{-t_m}{\tau_{sc}}\right)$ (B.65)	$c_{\tau 13} = \min\left(c_{\tau 1}, c_{\tau^*}\right)$ (B.66)
B.42	$\tau_{23} = c_{\tau 23} \exp\left(\frac{-t_m}{\tau_{sc}}\right)$ (B.67)	$c_{\tau 23} = \max\left(c_{\tau 2}, c_{\tau^*}\right)$ (B.68)

B.4 Transfer function of scanning AAC: particle streamline, non-idealized, balanced flows & uniform axial flow

Note: Similar to the other sections in this appendix, this section and its subsections use simplified notation of the parameter subscripts, as outlined in Section B.1, based on the common AAC operation and theory instances included within the title and header of this section.

Based on limited trajectory theory and that the assumption of uniform axial flow is valid (i.e. sufficiently long scan times), the transfer functions of the steady-state AAC and scanning AAC have the same form, as outlined in Section B.3 and summarized in Table 4.1 of the main text. Therefore, the transfer function of the steady-state AAC based on particle streamline theory with balanced (B) flow, developed by Tavakoli and Olfert [238] and parameterized in Section 3.3.1 to capture the non-idealized particle and flow behaviour, can also describe the scanning AAC as follows:

$$\Omega_{\mathrm{AAC,B}} = \frac{\lambda_\Omega \, \mu_\Omega^2}{2\beta} \left[\left| \frac{\tau}{\tau^*_{\mathrm{sc,B}}} - \left(1 + \frac{\beta}{\mu_\Omega} \right) \right| + \left| \frac{\tau}{\tau^*_{\mathrm{sc,B}}} - \left(1 - \frac{\beta}{\mu_\Omega} \right) \right| - 2 \left| \frac{\tau}{\tau^*_{\mathrm{sc,B}}} - 1 \right| \right], \quad \text{(B.69)}$$

where λ_Ω is the AAC transmission efficiency, μ_Ω is the width factor of the transfer function and β is non-dimensional classifier flow parameter as follows (restatement of Equation 3.2 in main text):

$$\beta = \frac{Q_\mathrm{s} + Q_\mathrm{a}}{Q_\mathrm{sh} + Q_\mathrm{exh}}. \quad \text{(B.70)}$$

Russell et al. [220] used a similar approach to adapt the transfer function of the steady-state DMA developed by Knutson and Whitby [133] based on particle streamline theory to the SMPS.

B.4.1 Instantaneous setpoint of scanning AAC

The instantaneous setpoint of the scanning AAC operating with balanced classifier flows can be found by rearranging the τ^*_{sc}/τ^*_{ss} ratio (i.e. Equation B.36) as follows:

$$\begin{aligned}\tau^*_{sc,B} &= \tau^*_{ss,B}\frac{\omega_S^2\, t_f}{\omega_S^2\,\tau_{sc}\exp\left(\frac{t_m}{\tau_{sc}}\right)\left[1-\exp\left(\frac{-t_f}{\tau_{sc}}\right)\right]}\\ \tau^*_{sc,B} &= \tau^*_{ss,B}\frac{t_f}{\tau_{sc}\exp\left(\frac{t_m}{\tau_{sc}}\right)\left[1-\exp\left(\frac{-t_f}{\tau_{sc}}\right)\right]}.\end{aligned} \tag{B.71}$$

Similar to Section B.3.1, $\tau^*_{sc,B}$ represents the instantaneous setpoint of the scanning AAC as it does not account for the shift of its transfer function over the counting time of the downstream particle detector. This effect on the setpoint of the scanning AAC is considered later in Section B.7.1. Furthermore, the steady-state AAC setpoint derived by Tavakoli and Olfert [238] using particle streamline theory (i.e. Equation 19) while assuming balanced classifier flows (i.e. $Q_a = Q_s$ and $Q_{sh} = Q_{exh}$) simplifies to:

$$\tau^*_{ss,B} = \frac{2Q_{sh}}{\pi\omega^2(r_1+r_2)^2L}. \tag{B.72}$$

Therefore, the expanded solution of $\tau^*_{sc,B}$ can be found by substituting the definitions of t_f, β and $\tau^*_{ss,B}$ (Equations 4.12 of main text, B.70 and B.72, respectively) at the start of the scan ($\omega = \omega_S$) into Equation B.71 as follows:

$$\begin{aligned}\tau^*_{sc,B} &= \frac{2Q_{sh}}{\pi\omega_S^2(r_1+r_2)^2L}\frac{\frac{\pi L\left(r_2^2-r_1^2\right)}{Q_a+Q_{sh}}}{\tau_{sc}\exp\left(\frac{t_m}{\tau_{sc}}\right)\left[1-\exp\left(\frac{-t_f}{\tau_{sc}}\right)\right]}\\ \tau^*_{sc,B} &= \frac{1}{\omega_S^2\,\tau_{sc}\left[1-\exp\left(\frac{-t_f}{\tau_{sc}}\right)\right]}\frac{2(r_2^2-r_1^2)}{(\beta+1)(r_1+r_2)^2}\exp\left(\frac{-t_m}{\tau_{sc}}\right).\end{aligned} \tag{B.73}$$

B.4.2 Condensed representation of transfer function for scanning AAC

To simplify derivations in the later sections of this appendix, the mathematical representation of the transfer function of the scanning AAC based on particle streamline theory (Equation B.69) as derived in Section B.4 can be simplified by grouping the constants and reorganizing particular terms. Firstly, this transfer function can also be represented by a piecewise equation (as shown in Figure B.5) as follows:

$$\Omega_{\mathrm{AAC,B}} = \begin{cases} \lambda_\Omega \, \mu_\Omega \left[1 + \frac{\mu_\Omega}{\beta}\left(\frac{\tau}{\tau^*_{\mathrm{sc,B}}} - 1\right)\right] & \text{if } \tau_{\mathrm{min,B}} \leq \tau \leq \tau^*_{\mathrm{sc,B}} \\ \lambda_\Omega \, \mu_\Omega \left[1 + \frac{\mu_\Omega}{\beta}\left(1 - \frac{\tau}{\tau^*_{\mathrm{sc,B}}}\right)\right] & \text{if } \tau^*_{\mathrm{sc,B}} < \tau \leq \tau_{\mathrm{max,B}} \,, \\ 0 & \text{elsewhere} \end{cases} \tag{B.74}$$

where

$$\tau_{\mathrm{min,B}} = \left(1 - \frac{\beta}{\mu_\Omega}\right) \tau^*_{\mathrm{sc,B}}, \tag{B.75}$$

$$\tau_{\mathrm{max,B}} = \left(1 + \frac{\beta}{\mu_\Omega}\right) \tau^*_{\mathrm{sc,B}}. \tag{B.76}$$

Note that all of the boundary conditions (i.e. $\tau_{\mathrm{min,B}}$, $\tau^*_{\mathrm{ss,B}}$, $\tau_{\mathrm{max,B}}$) of the transfer function of the scanning AAC based on particle streamline theory are of the form:

$$\tau_{x,\mathrm{B}} = c_{\tau x,\mathrm{B}} \exp\left(\frac{-t_{\mathrm{m}}}{\tau_{\mathrm{sc}}}\right) \tag{B.77}$$

where $c_{\tau x,\mathrm{B}}$ represents the grouped constants of each boundary x shown in Figure B.5. Therefore, the transfer function of the scanning AAC based on particle streamline can then be simplified, as shown in Table B.3 on the next page.

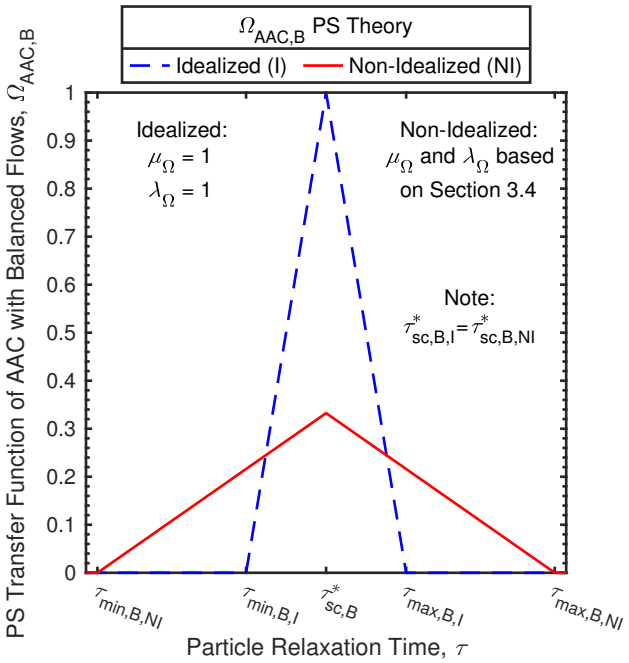

Fig. B.5 Transfer function of the AAC based on particle streamline theory considering idealized (I) or non-idealized (NI) particle behaviour.

Table B.3 Boundaries of the simplified mathematical representation of the transfer function of the scanning AAC based on particle streamline theory .

Original Equation	Simplified Form	
	Equation	Constants
B.73	$\tau^*_{sc,B} = c_{\tau*,B} \exp\left(\frac{-t_m}{\tau_{sc}}\right)$ (B.78)	$c_{\tau*,B} = \frac{1}{c_{sc}} \frac{2\left(r_2^2 - r_1^2\right)}{(\beta+1)(r_1+r_2)^2}$ (B.79) $c_{sc} = \omega_S^2 \tau_{sc} \left[1 - \exp\left(\frac{-t_f}{\tau_{sc}}\right)\right]$ (B.80)
B.75	$\tau_{min,B} = c_{\tau min,B} \exp\left(\frac{-t_m}{\tau_{sc}}\right)$ (B.81)	$c_{\tau min,B} = \left(1 - \frac{\beta}{\mu_\Omega}\right) c_{\tau*,B}$ (B.82)
B.76	$\tau_{max,B} = c_{\tau max,B} \exp\left(\frac{-t_m}{\tau_{sc}}\right)$ (B.83)	$c_{\tau max,B} = \left(1 + \frac{\beta}{\mu_\Omega}\right) c_{\tau*,B}$ (B.84)

Where c_{sc} is the same for the transfer function of the scanning AAC based on limited trajectory or particle streamline theory (i.e. Equation B.45 or B.80, respectively.)

B.5 Average transfer function of scanning AAC over t_c: limited trajectory, idealized & uniform axial flow

Note: Similar to the other sections in this appendix, this section and its subsections use simplified notation of the parameter subscripts, as outlined in Section B.1, based on the common AAC operation and theory instances included within the title and header of this section.

To determine the average transfer function of the scanning AAC over the counting time of downstream particle detector (i.e. solve the integral shown in Equation 4.33 of the main text), the piecewise notation of the transfer function based on limited trajectory theory (Equation B.37), as derived in Section B.3.2, can be represented as one equation using the Heaviside function ($\mathcal{H}(x-a)$, defined by Equation 4.34 of main text) as follows:

$$\begin{aligned}\Omega_{\mathrm{AAC}}(\tau) = &\left[\mathcal{H}(\tau-\tau_{\min})-\mathcal{H}(\tau-\tau_{13})\right]f_1 \\ &+\left[\mathcal{H}(\tau-\tau_{13})-\mathcal{H}(\tau-\tau_{23})\right]c_{f31} \\ &+\left[\mathcal{H}(\tau-\tau_{23})-\mathcal{H}(\tau-\tau_{\max})\right]f_2,\end{aligned} \tag{B.85}$$

where the values (f_1, c_{f31} and f_2) and relaxation time boundaries ($\tau_{\min}$, τ_{13}, τ_{23} and $\tau_{\max}$) are defined in Table B.2 and shown in Figure B.4. All of the relaxation time boundaries of this transfer function are of the form $\tau_x = c_{\tau x}\exp(-t_{\mathrm{m}}/\tau_{\mathrm{sc}})$ (i.e. Equation 4.35 of main text or Equation B.43). This form results in $\mathcal{H}(\tau-\tau_x) = \mathcal{H}((\tau_{\mathrm{sc}}/|\tau_{\mathrm{sc}}|)(t_{\mathrm{m}}-\tau_{\mathrm{sc}}\ln(c_{\tau x}/\tau)))$ (Equation 4.39 of the main text), and the limits of Ω_{AAC} (Equation B.85) can be converted from the particle relaxation time (τ) to measurement time (t_{m}) domain as follows:

$$\begin{aligned}\Omega_{\mathrm{AAC}}(t_{\mathrm{m}}) = &\left[\mathcal{H}\left(\frac{\tau_{\mathrm{sc}}}{|\tau_{\mathrm{sc}}|}\left(t_{\mathrm{m}}-\tau_{\mathrm{sc}}\ln\left(\frac{c_{\tau\min}}{\tau}\right)\right)\right)-\mathcal{H}\left(\frac{\tau_{\mathrm{sc}}}{|\tau_{\mathrm{sc}}|}\left(t_{\mathrm{m}}-\tau_{\mathrm{sc}}\ln\left(\frac{c_{\tau 13}}{\tau}\right)\right)\right)\right]f_1 \\ &+\left[\mathcal{H}\left(\frac{\tau_{\mathrm{sc}}}{|\tau_{\mathrm{sc}}|}\left(t_{\mathrm{m}}-\tau_{\mathrm{sc}}\ln\left(\frac{c_{\tau 13}}{\tau}\right)\right)\right)-\mathcal{H}\left(\frac{\tau_{\mathrm{sc}}}{|\tau_{\mathrm{sc}}|}\left(t_{\mathrm{m}}-\tau_{\mathrm{sc}}\ln\left(\frac{c_{\tau 23}}{\tau}\right)\right)\right)\right]c_{f31} \\ &+\left[\mathcal{H}\left(\frac{\tau_{\mathrm{sc}}}{|\tau_{\mathrm{sc}}|}\left(t_{\mathrm{m}}-\tau_{\mathrm{sc}}\ln\left(\frac{c_{\tau 23}}{\tau}\right)\right)\right)-\mathcal{H}\left(\frac{\tau_{\mathrm{sc}}}{|\tau_{\mathrm{sc}}|}\left(t_{\mathrm{m}}-\tau_{\mathrm{sc}}\ln\left(\frac{c_{\tau\max}}{\tau}\right)\right)\right)\right]f_2.\end{aligned} \tag{B.86}$$

B.5.1 Solving integral of Ω_{AAC} over t_{c} to determine $\bar{\Omega}_{\mathrm{AAC}}$

This section determines the average transfer function of the AAC ($\bar{\Omega}_{\mathrm{AAC}}$) over the counting time (t_{c}) of the particle detector by substituting Equation B.86 into Equation 4.33 of the main text and solving. To reduce the analysis, note that f_1 (Equation B.53) and f_2 (Equation B.57) have the same form as follows:

$$f_y = c_{fy1} \exp\left[c_{fy2}\,\tau \exp\left(\frac{t_{\mathrm{m}}}{\tau_{\mathrm{sc}}}\right)\right] + c_{fy3}. \tag{B.87}$$

where the corresponding coefficients for f_1 and f_2 are summarized in Table B.4.

Table B.4 Coefficients of the transfer function of the scanning AAC based on limited trajectory theory (i.e. for f_1 and f_2).

Constant	f_1	f_2
c_{fy1}	c_{f11}	c_{f21}
c_{fy2}	c_{f12}	c_{f22}
c_{fy3}	c_{f13}	c_{f23}

Expanding Equation B.86, considering its first term generically, then substituting in Equation B.87 is equivalent to:

$$\begin{aligned}
&\mathcal{H}\left(\frac{\tau_{\mathrm{sc}}}{|\tau_{\mathrm{sc}}|}\left(t_{\mathrm{m}} - \tau_{\mathrm{sc}} \ln\left(\frac{c_{\tau x}}{\tau}\right)\right)\right) f_y \\
&\quad = \mathcal{H}\left(\frac{\tau_{\mathrm{sc}}}{|\tau_{\mathrm{sc}}|}\left(t_{\mathrm{m}} - \tau_{\mathrm{sc}} \ln\left(\frac{c_{\tau x}}{\tau}\right)\right)\right)\left[c_{fy1} \exp\left[c_{fy2}\,\tau \exp\left(\frac{t_{\mathrm{m}}}{\tau_{\mathrm{sc}}}\right)\right] + c_{fy3}\right] \\
&\quad = \underbrace{\mathcal{H}\left(\frac{\tau_{\mathrm{sc}}}{|\tau_{\mathrm{sc}}|}\left(t_{\mathrm{m}} - \tau_{\mathrm{sc}} \ln\left(\frac{c_{\tau x}}{\tau}\right)\right)\right) c_{fy1} \exp\left[c_{fy2}\,\tau \exp\left(\frac{t_{\mathrm{m}}}{\tau_{\mathrm{sc}}}\right)\right]}_{\text{Term Form: } \Omega_{\mathrm{AAC,F1}}(c_{\tau x}, c_{fy1}, c_{fy2}, \tau, \tau_{\mathrm{sc}}, t_{\mathrm{m}})} \\
&\qquad + \underbrace{\mathcal{H}\left(\frac{\tau_{\mathrm{sc}}}{|\tau_{\mathrm{sc}}|}\left(t_{\mathrm{m}} - \tau_{\mathrm{sc}} \ln\left(\frac{c_{\tau x}}{\tau}\right)\right)\right) c_{fy3}}_{\text{Term Form: } \Omega_{\mathrm{AAC,F2}}(c_{\tau x}, c_{fy3}, \tau, \tau_{\mathrm{sc}}, t_{\mathrm{m}})}.
\end{aligned} \tag{B.88}$$

Therefore, substituting the two term forms (i.e. $\Omega_{\mathrm{AAC,F1}}$ and $\Omega_{\mathrm{AAC,F2}}$) identified in Equation B.88 into Equation B.86, then into the definition of $\bar{\Omega}_{\mathrm{AAC}}$ (Equation 4.33 of the main text) simplifies to the following:

$$
\begin{aligned}
\bar{\Omega}_{\mathrm{AAC}} &= \frac{1}{t_\mathrm{c}} \int_{t_\mathrm{m}}^{t_\mathrm{m}+t_\mathrm{c}} \Omega_{\mathrm{AAC}}(\tau, t'_\mathrm{m})\,\mathrm{d}t'_\mathrm{m} \\
\bar{\Omega}_{\mathrm{AAC}} &= \underbrace{\frac{1}{t_\mathrm{c}} \int_{t_\mathrm{m}}^{t_\mathrm{m}+t_\mathrm{c}} \Omega_{\mathrm{AAC,F1}}(c_{\tau\min},\, c_{f11},\, c_{f12},\, \tau,\, \tau_\mathrm{sc},\, t_\mathrm{m})\,\mathrm{d}t'_\mathrm{m}}_{\text{Term Form: } \bar{\Omega}_{\mathrm{AAC,F1}}(c_{\tau x}, c_{fy1}, c_{fy2}, \tau, \tau_\mathrm{sc}, t_\mathrm{m}, t_\mathrm{c})} \\
&\quad + \underbrace{\frac{1}{t_\mathrm{c}} \int_{t_\mathrm{m}}^{t_\mathrm{m}+t_\mathrm{c}} \Omega_{\mathrm{AAC,F2}}(c_{\tau\min},\, c_{f13},\, \tau,\, \tau_\mathrm{sc},\, t_\mathrm{m})\,\mathrm{d}t'_\mathrm{m}}_{\text{Term Form: } \bar{\Omega}_{\mathrm{AAC,F2}}(c_{\tau x}, c_{fy3}, \tau, \tau_\mathrm{sc}, t_\mathrm{m}, t_\mathrm{c})} \\
&\quad - \underbrace{\frac{1}{t_\mathrm{c}} \int_{t_\mathrm{m}}^{t_\mathrm{m}+t_\mathrm{c}} \Omega_{\mathrm{AAC,F1}}(c_{\tau 13},\, c_{f11},\, c_{f12},\, \tau,\, \tau_\mathrm{sc},\, t_\mathrm{m})\,\mathrm{d}t'_\mathrm{m}}_{\text{Term Form: } \bar{\Omega}_{\mathrm{AAC,F1}}(c_{\tau x}, c_{fy1}, c_{fy2}, \tau, \tau_\mathrm{sc}, t_\mathrm{m}, t_\mathrm{c})} \\
&\quad - \underbrace{\frac{1}{t_\mathrm{c}} \int_{t_\mathrm{m}}^{t_\mathrm{m}+t_\mathrm{c}} \Omega_{\mathrm{AAC,F2}}(c_{\tau 13},\, c_{f13},\, \tau,\, \tau_\mathrm{sc},\, t_\mathrm{m})\,\mathrm{d}t'_\mathrm{m}}_{\text{Term Form: } \bar{\Omega}_{\mathrm{AAC,F2}}(c_{\tau x}, c_{fy3}, \tau, \tau_\mathrm{sc}, t_\mathrm{m}, t_\mathrm{c})} \\
&\quad + \underbrace{\frac{1}{t_\mathrm{c}} \int_{t_\mathrm{m}}^{t_\mathrm{m}+t_\mathrm{c}} \Omega_{\mathrm{AAC,F2}}(c_{\tau 13},\, c_{f31},\, \tau,\, \tau_\mathrm{sc},\, t_\mathrm{m})\,\mathrm{d}t'_\mathrm{m}}_{\text{Term Form: } \bar{\Omega}_{\mathrm{AAC,F2}}(c_{\tau x}, c_{fy3}, \tau, \tau_\mathrm{sc}, t_\mathrm{m}, t_\mathrm{c})} \\
&\quad - \underbrace{\frac{1}{t_\mathrm{c}} \int_{t_\mathrm{m}}^{t_\mathrm{m}+t_\mathrm{c}} \Omega_{\mathrm{AAC,F2}}(c_{\tau 23},\, c_{f31},\, \tau,\, \tau_\mathrm{sc},\, t_\mathrm{m})\,\mathrm{d}t'_\mathrm{m}}_{\text{Term Form: } \bar{\Omega}_{\mathrm{AAC,F2}}(c_{\tau x}, c_{fy3}, \tau, \tau_\mathrm{sc}, t_\mathrm{m}, t_\mathrm{c})} \\
&\quad + \underbrace{\frac{1}{t_\mathrm{c}} \int_{t_\mathrm{m}}^{t_\mathrm{m}+t_\mathrm{c}} \Omega_{\mathrm{AAC,F1}}(c_{\tau 23},\, c_{f21},\, c_{f22},\, \tau,\, \tau_\mathrm{sc},\, t_\mathrm{m})\,\mathrm{d}t'_\mathrm{m}}_{\text{Term Form: } \bar{\Omega}_{\mathrm{AAC,F1}}(c_{\tau x}, c_{fy1}, c_{fy2}, \tau, \tau_\mathrm{sc}, t_\mathrm{m}, t_\mathrm{c})} \\
&\quad + \underbrace{\frac{1}{t_\mathrm{c}} \int_{t_\mathrm{m}}^{t_\mathrm{m}+t_\mathrm{c}} \Omega_{\mathrm{AAC,F2}}(c_{\tau 23},\, c_{f23},\, \tau,\, \tau_\mathrm{sc},\, t_\mathrm{m})\,\mathrm{d}t'_\mathrm{m}}_{\text{Term Form: } \bar{\Omega}_{\mathrm{AAC,F2}}(c_{\tau x}, c_{fy3}, \tau, \tau_\mathrm{sc}, t_\mathrm{m}, t_\mathrm{c})} \\
&\quad - \underbrace{\frac{1}{t_\mathrm{c}} \int_{t_\mathrm{m}}^{t_\mathrm{m}+t_\mathrm{c}} \Omega_{\mathrm{AAC,F1}}(c_{\tau\max},\, c_{f21},\, c_{f22},\, \tau,\, \tau_\mathrm{sc},\, t_\mathrm{m})\,\mathrm{d}t'_\mathrm{m}}_{\text{Term Form: } \bar{\Omega}_{\mathrm{AAC,F1}}(c_{\tau x}, c_{fy1}, c_{fy2}, \tau, \tau_\mathrm{sc}, t_\mathrm{m}, t_\mathrm{c})} \\
&\quad - \underbrace{\frac{1}{t_\mathrm{c}} \int_{t_\mathrm{m}}^{t_\mathrm{m}+t_\mathrm{c}} \Omega_{\mathrm{AAC,F2}}(c_{\tau\max},\, c_{f23},\, \tau,\, \tau_\mathrm{sc},\, t_\mathrm{m})\,\mathrm{d}t'_\mathrm{m}}_{\text{Term Form: } \bar{\Omega}_{\mathrm{AAC,F2}}(c_{\tau x}, c_{fy3}, \tau, \tau_\mathrm{sc}, t_\mathrm{m}, t_\mathrm{c})}.
\end{aligned}
\tag{B.89}
$$

All of the terms in Equation B.89 are of the form $\bar{\Omega}_{\mathrm{AAC,F1}}$ or $\bar{\Omega}_{\mathrm{AAC,F2}}$, which are solved in Sections B.5.1 and B.5.1, respectively. Therefore, substituting these solutions (i.e. Equations B.106 and B.109) into Equation B.89:

$$
\begin{aligned}
&\bar{\Omega}_{\mathrm{AAC}} = \\
&\frac{c_{f11}\,\tau_{\mathrm{sc}}}{t_{\mathrm{c}}}\Bigg\{\left[\mathcal{EI}\left(c_{f12}\,\tau\exp\left(\frac{t_{\mathrm{m}}+t_{\mathrm{c}}}{\tau_{\mathrm{sc}}}\right)\right)-\mathcal{EI}\left(c_{\tau\min}\,c_{f12}\right)\right]\mathcal{H}\left(\frac{\tau_{\mathrm{sc}}}{|\tau_{\mathrm{sc}}|}\left(t_{\mathrm{m}}+t_{\mathrm{c}}-\tau_{\mathrm{sc}}\ln\left(\frac{c_{\tau\min}}{\tau}\right)\right)\right)\\
&\qquad-\left[\mathcal{EI}\left(c_{f12}\,\tau\exp\left(\frac{t_{\mathrm{m}}}{\tau_{\mathrm{sc}}}\right)\right)-\mathcal{EI}\left(c_{\tau\min}\,c_{f12}\right)\right]\mathcal{H}\left(\frac{\tau_{\mathrm{sc}}}{|\tau_{\mathrm{sc}}|}\left(t_{\mathrm{m}}-\tau_{\mathrm{sc}}\ln\left(\frac{c_{\tau\min}}{\tau}\right)\right)\right)\Bigg\}\\
&+\frac{c_{f13}}{t_{\mathrm{c}}}\Bigg[\left(t_{\mathrm{m}}+t_{\mathrm{c}}-\tau_{\mathrm{sc}}\ln\left(\frac{c_{\tau\min}}{\tau}\right)\right)\mathcal{H}\left(\frac{\tau_{\mathrm{sc}}}{|\tau_{\mathrm{sc}}|}\left(t_{\mathrm{m}}+t_{\mathrm{c}}-\tau_{\mathrm{sc}}\ln\left(\frac{c_{\tau\min}}{\tau}\right)\right)\right)\\
&\qquad-\left(t_{\mathrm{m}}-\tau_{\mathrm{sc}}\ln\left(\frac{c_{\tau\min}}{\tau}\right)\right)\mathcal{H}\left(\frac{\tau_{\mathrm{sc}}}{|\tau_{\mathrm{sc}}|}\left(t_{\mathrm{m}}-\tau_{\mathrm{sc}}\ln\left(\frac{c_{\tau\min}}{\tau}\right)\right)\right)\Bigg]\\
&-\frac{c_{f11}\,\tau_{\mathrm{sc}}}{t_{\mathrm{c}}}\Bigg\{\left[\mathcal{EI}\left(c_{f12}\,\tau\exp\left(\frac{t_{\mathrm{m}}+t_{\mathrm{c}}}{\tau_{\mathrm{sc}}}\right)\right)-\mathcal{EI}\left(c_{\tau13}\,c_{f12}\right)\right]\mathcal{H}\left(\frac{\tau_{\mathrm{sc}}}{|\tau_{\mathrm{sc}}|}\left(t_{\mathrm{m}}+t_{\mathrm{c}}-\tau_{\mathrm{sc}}\ln\left(\frac{c_{\tau13}}{\tau}\right)\right)\right)\\
&\qquad-\left[\mathcal{EI}\left(c_{f12}\,\tau\exp\left(\frac{t_{\mathrm{m}}}{\tau_{\mathrm{sc}}}\right)\right)-\mathcal{EI}\left(c_{\tau13}\,c_{f12}\right)\right]\mathcal{H}\left(\frac{\tau_{\mathrm{sc}}}{|\tau_{\mathrm{sc}}|}\left(t_{\mathrm{m}}-\tau_{\mathrm{sc}}\ln\left(\frac{c_{\tau13}}{\tau}\right)\right)\right)\Bigg\}\\
&-\frac{c_{f13}}{t_{\mathrm{c}}}\Bigg[\left(t_{\mathrm{m}}+t_{\mathrm{c}}-\tau_{\mathrm{sc}}\ln\left(\frac{c_{\tau13}}{\tau}\right)\right)\mathcal{H}\left(\frac{\tau_{\mathrm{sc}}}{|\tau_{\mathrm{sc}}|}\left(t_{\mathrm{m}}+t_{\mathrm{c}}-\tau_{\mathrm{sc}}\ln\left(\frac{c_{\tau13}}{\tau}\right)\right)\right)\\
&\qquad-\left(t_{\mathrm{m}}-\tau_{\mathrm{sc}}\ln\left(\frac{c_{\tau13}}{\tau}\right)\right)\mathcal{H}\left(\frac{\tau_{\mathrm{sc}}}{|\tau_{\mathrm{sc}}|}\left(t_{\mathrm{m}}-\tau_{\mathrm{sc}}\ln\left(\frac{c_{\tau13}}{\tau}\right)\right)\right)\Bigg]\\
&+\frac{c_{f31}}{t_{\mathrm{c}}}\Bigg[\left(t_{\mathrm{m}}+t_{\mathrm{c}}-\tau_{\mathrm{sc}}\ln\left(\frac{c_{\tau13}}{\tau}\right)\right)\mathcal{H}\left(\frac{\tau_{\mathrm{sc}}}{|\tau_{\mathrm{sc}}|}\left(t_{\mathrm{m}}+t_{\mathrm{c}}-\tau_{\mathrm{sc}}\ln\left(\frac{c_{\tau13}}{\tau}\right)\right)\right)\\
&\qquad-\left(t_{\mathrm{m}}-\tau_{\mathrm{sc}}\ln\left(\frac{c_{\tau13}}{\tau}\right)\right)\mathcal{H}\left(\frac{\tau_{\mathrm{sc}}}{|\tau_{\mathrm{sc}}|}\left(t_{\mathrm{m}}-\tau_{\mathrm{sc}}\ln\left(\frac{c_{\tau13}}{\tau}\right)\right)\right)\Bigg]\\
&-\frac{c_{f31}}{t_{\mathrm{c}}}\Bigg[\left(t_{\mathrm{m}}+t_{\mathrm{c}}-\tau_{\mathrm{sc}}\ln\left(\frac{c_{\tau23}}{\tau}\right)\right)\mathcal{H}\left(\frac{\tau_{\mathrm{sc}}}{|\tau_{\mathrm{sc}}|}\left(t_{\mathrm{m}}+t_{\mathrm{c}}-\tau_{\mathrm{sc}}\ln\left(\frac{c_{\tau23}}{\tau}\right)\right)\right)\\
&\qquad-\left(t_{\mathrm{m}}-\tau_{\mathrm{sc}}\ln\left(\frac{c_{\tau23}}{\tau}\right)\right)\mathcal{H}\left(\frac{\tau_{\mathrm{sc}}}{|\tau_{\mathrm{sc}}|}\left(t_{\mathrm{m}}-\tau_{\mathrm{sc}}\ln\left(\frac{c_{\tau23}}{\tau}\right)\right)\right)\Bigg]\\
&+\frac{c_{f21}\,\tau_{\mathrm{sc}}}{t_{\mathrm{c}}}\Bigg\{\left[\mathcal{EI}\left(c_{f22}\,\tau\exp\left(\frac{t_{\mathrm{m}}+t_{\mathrm{c}}}{\tau_{\mathrm{sc}}}\right)\right)-\mathcal{EI}\left(c_{\tau23}\,c_{f22}\right)\right]\mathcal{H}\left(\frac{\tau_{\mathrm{sc}}}{|\tau_{\mathrm{sc}}|}\left(t_{\mathrm{m}}+t_{\mathrm{c}}-\tau_{\mathrm{sc}}\ln\left(\frac{c_{\tau23}}{\tau}\right)\right)\right)\\
&\qquad-\left[\mathcal{EI}\left(c_{f22}\,\tau\exp\left(\frac{t_{\mathrm{m}}}{\tau_{\mathrm{sc}}}\right)\right)-\mathcal{EI}\left(c_{\tau23}\,c_{f22}\right)\right]\mathcal{H}\left(\frac{\tau_{\mathrm{sc}}}{|\tau_{\mathrm{sc}}|}\left(t_{\mathrm{m}}-\tau_{\mathrm{sc}}\ln\left(\frac{c_{\tau23}}{\tau}\right)\right)\right)\Bigg\}\\
&+\frac{c_{f23}}{t_{\mathrm{c}}}\Bigg[\left(t_{\mathrm{m}}+t_{\mathrm{c}}-\tau_{\mathrm{sc}}\ln\left(\frac{c_{\tau23}}{\tau}\right)\right)\mathcal{H}\left(\frac{\tau_{\mathrm{sc}}}{|\tau_{\mathrm{sc}}|}\left(t_{\mathrm{m}}+t_{\mathrm{c}}-\tau_{\mathrm{sc}}\ln\left(\frac{c_{\tau23}}{\tau}\right)\right)\right)\\
&\qquad-\left(t_{\mathrm{m}}-\tau_{\mathrm{sc}}\ln\left(\frac{c_{\tau23}}{\tau}\right)\right)\mathcal{H}\left(\frac{\tau_{\mathrm{sc}}}{|\tau_{\mathrm{sc}}|}\left(t_{\mathrm{m}}-\tau_{\mathrm{sc}}\ln\left(\frac{c_{\tau23}}{\tau}\right)\right)\right)\Bigg]\\
&-\frac{c_{f21}\,\tau_{\mathrm{sc}}}{t_{\mathrm{c}}}\Bigg\{\left[\mathcal{EI}\left(c_{f22}\,\tau\exp\left(\frac{t_{\mathrm{m}}+t_{\mathrm{c}}}{\tau_{\mathrm{sc}}}\right)\right)-\mathcal{EI}\left(c_{\tau\max}\,c_{f22}\right)\right]\mathcal{H}\left(\frac{\tau_{\mathrm{sc}}}{|\tau_{\mathrm{sc}}|}\left(t_{\mathrm{m}}+t_{\mathrm{c}}-\tau_{\mathrm{sc}}\ln\left(\frac{c_{\tau\max}}{\tau}\right)\right)\right)\\
&\qquad-\left[\mathcal{EI}\left(c_{f22}\,\tau\exp\left(\frac{t_{\mathrm{m}}}{\tau_{\mathrm{sc}}}\right)\right)-\mathcal{EI}\left(c_{\tau\max}\,c_{f22}\right)\right]\mathcal{H}\left(\frac{\tau_{\mathrm{sc}}}{|\tau_{\mathrm{sc}}|}\left(t_{\mathrm{m}}-\tau_{\mathrm{sc}}\ln\left(\frac{c_{\tau\max}}{\tau}\right)\right)\right)\Bigg\}\\
&-\frac{c_{f23}}{t_{\mathrm{c}}}\Bigg[\left(t_{\mathrm{m}}+t_{\mathrm{c}}-\tau_{\mathrm{sc}}\ln\left(\frac{c_{\tau\max}}{\tau}\right)\right)\mathcal{H}\left(\frac{\tau_{\mathrm{sc}}}{|\tau_{\mathrm{sc}}|}\left(t_{\mathrm{m}}+t_{\mathrm{c}}-\tau_{\mathrm{sc}}\ln\left(\frac{c_{\tau\max}}{\tau}\right)\right)\right)\\
&\qquad-\left(t_{\mathrm{m}}-\tau_{\mathrm{sc}}\ln\left(\frac{c_{\tau\max}}{\tau}\right)\right)\mathcal{H}\left(\frac{\tau_{\mathrm{sc}}}{|\tau_{\mathrm{sc}}|}\left(t_{\mathrm{m}}-\tau_{\mathrm{sc}}\ln\left(\frac{c_{\tau\max}}{\tau}\right)\right)\right)\Bigg],
\end{aligned}
\tag{B.90}
$$

and grouping by common time intervals, simplifies to:

$$
\begin{aligned}
&\bar{\Omega}_{\mathrm{AAC}}(t_\mathrm{m}) = \\
&\left[\frac{c_{f11}\,\tau_\mathrm{sc}}{t_\mathrm{c}}\mathcal{EI}\left(c_{\tau\min}\,c_{f12}\right) - \frac{c_{f13}}{t_\mathrm{c}}\left(t_\mathrm{m} - \tau_\mathrm{sc}\ln\left(\frac{c_{\tau\min}}{\tau}\right)\right)\right] \\
&\quad\cdot\left[\mathcal{H}\left(\frac{\tau_\mathrm{sc}}{|\tau_\mathrm{sc}|}\left(t_\mathrm{m} - \tau_\mathrm{sc}\ln\left(\frac{c_{\tau\min}}{\tau}\right)\right)\right) - \mathcal{H}\left(\frac{\tau_\mathrm{sc}}{|\tau_\mathrm{sc}|}\left(t_\mathrm{m} + t_\mathrm{c} - \tau_\mathrm{sc}\ln\left(\frac{c_{\tau\min}}{\tau}\right)\right)\right)\right] \\
&+\left[-\frac{c_{f11}\,\tau_\mathrm{sc}}{t_\mathrm{c}}\mathcal{EI}\left(c_{f12}\,\tau\exp\left(\frac{t_\mathrm{m}}{\tau_\mathrm{sc}}\right)\right)\right] \\
&\quad\cdot\left[\mathcal{H}\left(\frac{\tau_\mathrm{sc}}{|\tau_\mathrm{sc}|}\left(t_\mathrm{m} - \tau_\mathrm{sc}\ln\left(\frac{c_{\tau\min}}{\tau}\right)\right)\right) - \mathcal{H}\left(\frac{\tau_\mathrm{sc}}{|\tau_\mathrm{sc}|}\left(t_\mathrm{m} - \tau_\mathrm{sc}\ln\left(\frac{c_{\tau13}}{\tau}\right)\right)\right)\right] \\
&+\left[\frac{c_{f11}\,\tau_\mathrm{sc}}{t_\mathrm{c}}\mathcal{EI}\left(c_{f12}\,\tau\exp\left(\frac{t_\mathrm{m}+t_\mathrm{c}}{\tau_\mathrm{sc}}\right)\right) + c_{f13}\right] \\
&\quad\cdot\left[\mathcal{H}\left(\frac{\tau_\mathrm{sc}}{|\tau_\mathrm{sc}|}\left(t_\mathrm{m} + t_\mathrm{c} - \tau_\mathrm{sc}\ln\left(\frac{c_{\tau\min}}{\tau}\right)\right)\right) - \mathcal{H}\left(\frac{\tau_\mathrm{sc}}{|\tau_\mathrm{sc}|}\left(t_\mathrm{m} + t_\mathrm{c} - \tau_\mathrm{sc}\ln\left(\frac{c_{\tau13}}{\tau}\right)\right)\right)\right] \\
&+\left[-\frac{c_{f11}\,\tau_\mathrm{sc}}{t_\mathrm{c}}\mathcal{EI}\left(c_{\tau13}\,c_{f12}\right) + \left(\frac{c_{f13}}{t_\mathrm{c}} - \frac{c_{f31}}{t_\mathrm{c}}\right)\left(t_\mathrm{m} - \tau_\mathrm{sc}\ln\left(\frac{c_{\tau13}}{\tau}\right)\right)\right] \\
&\quad\cdot\left[\mathcal{H}\left(\frac{\tau_\mathrm{sc}}{|\tau_\mathrm{sc}|}\left(t_\mathrm{m} - \tau_\mathrm{sc}\ln\left(\frac{c_{\tau13}}{\tau}\right)\right)\right) - \mathcal{H}\left(\frac{\tau_\mathrm{sc}}{|\tau_\mathrm{sc}|}\left(t_\mathrm{m} + t_\mathrm{c} - \tau_\mathrm{sc}\ln\left(\frac{c_{\tau13}}{\tau}\right)\right)\right)\right] \\
&+c_{f31}\left[\mathcal{H}\left(\frac{\tau_\mathrm{sc}}{|\tau_\mathrm{sc}|}\left(t_\mathrm{m} + t_\mathrm{c} - \tau_\mathrm{sc}\ln\left(\frac{c_{\tau13}}{\tau}\right)\right)\right) - \mathcal{H}\left(\frac{\tau_\mathrm{sc}}{|\tau_\mathrm{sc}|}\left(t_\mathrm{m} + t_\mathrm{c} - \tau_\mathrm{sc}\ln\left(\frac{c_{\tau23}}{\tau}\right)\right)\right)\right] \\
&+\left[\frac{c_{f21}\,\tau_\mathrm{sc}}{t_\mathrm{c}}\mathcal{EI}\left(c_{\tau23}\,c_{f22}\right) + \left(\frac{c_{f31}}{t_\mathrm{c}} - \frac{c_{f23}}{t_\mathrm{c}}\right)\left(t_\mathrm{m} - \tau_\mathrm{sc}\ln\left(\frac{c_{\tau23}}{\tau}\right)\right)\right] \\
&\quad\cdot\left[\mathcal{H}\left(\frac{\tau_\mathrm{sc}}{|\tau_\mathrm{sc}|}\left(t_\mathrm{m} - \tau_\mathrm{sc}\ln\left(\frac{c_{\tau23}}{\tau}\right)\right)\right) - \mathcal{H}\left(\frac{\tau_\mathrm{sc}}{|\tau_\mathrm{sc}|}\left(t_\mathrm{m} + t_\mathrm{c} - \tau_\mathrm{sc}\ln\left(\frac{c_{\tau23}}{\tau}\right)\right)\right)\right] \\
&+\left[\frac{c_{f21}\,\tau_\mathrm{sc}}{t_\mathrm{c}}\mathcal{EI}\left(c_{f22}\,\tau\exp\left(\frac{t_\mathrm{m}+t_\mathrm{c}}{\tau_\mathrm{sc}}\right)\right) + c_{f23}\right] \\
&\quad\cdot\left[\mathcal{H}\left(\frac{\tau_\mathrm{sc}}{|\tau_\mathrm{sc}|}\left(t_\mathrm{m} + t_\mathrm{c} - \tau_\mathrm{sc}\ln\left(\frac{c_{\tau23}}{\tau}\right)\right)\right) - \mathcal{H}\left(\frac{\tau_\mathrm{sc}}{|\tau_\mathrm{sc}|}\left(t_\mathrm{m} + t_\mathrm{c} - \tau_\mathrm{sc}\ln\left(\frac{c_{\tau\max}}{\tau}\right)\right)\right)\right] \\
&+\left[-\frac{c_{f21}\,\tau_\mathrm{sc}}{t_\mathrm{c}}\mathcal{EI}\left(c_{f22}\,\tau\exp\left(\frac{t_\mathrm{m}}{\tau_\mathrm{sc}}\right)\right)\right] \\
&\quad\cdot\left[\mathcal{H}\left(\frac{\tau_\mathrm{sc}}{|\tau_\mathrm{sc}|}\left(t_\mathrm{m} - \tau_\mathrm{sc}\ln\left(\frac{c_{\tau23}}{\tau}\right)\right)\right) - \mathcal{H}\left(\frac{\tau_\mathrm{sc}}{|\tau_\mathrm{sc}|}\left(t_\mathrm{m} - \tau_\mathrm{sc}\ln\left(\frac{c_{\tau\max}}{\tau}\right)\right)\right)\right] \\
&+\left[-\frac{c_{f21}\,\tau_\mathrm{sc}}{t_\mathrm{c}}\mathcal{EI}\left(c_{\tau\max}\,c_{f22}\right) + \frac{c_{f23}}{t_\mathrm{c}}\left(t_\mathrm{m} - \tau_\mathrm{sc}\ln\left(\frac{c_{\tau\max}}{\tau}\right)\right)\right] \\
&\quad\cdot\left[\mathcal{H}\left(\frac{\tau_\mathrm{sc}}{|\tau_\mathrm{sc}|}\left(t_\mathrm{m} - \tau_\mathrm{sc}\ln\left(\frac{c_{\tau\max}}{\tau}\right)\right)\right) - \mathcal{H}\left(\frac{\tau_\mathrm{sc}}{|\tau_\mathrm{sc}|}\left(t_\mathrm{m} + t_\mathrm{c} - \tau_\mathrm{sc}\ln\left(\frac{c_{\tau\max}}{\tau}\right)\right)\right)\right].
\end{aligned}
\tag{B.91}
$$

Finally, Equation B.91 can converted from the measurement time (t_m) back to the particle relaxation time (τ) domain using $\mathcal{H}(\tau - \tau_x) = \mathcal{H}\left((\tau_\mathrm{sc}/|\tau_\mathrm{sc}|)\left(t_\mathrm{m} - \tau_\mathrm{sc}\ln\left(c_{\tau x}/\tau\right)\right)\right)$ (Equation 4.39 of the main text) as follows:

$$
\begin{aligned}
\bar{\Omega}_{\mathrm{AAC}}(\tau) = &\left[\frac{c_{f11}\,\tau_{\mathrm{sc}}}{t_{\mathrm{c}}}\mathcal{EI}\left(c_{\tau\min}\,c_{f12}\right) - \frac{c_{f13}}{t_{\mathrm{c}}}\left(t_{\mathrm{m}} - \tau_{\mathrm{sc}}\ln\left(\frac{c_{\tau\min}}{\tau}\right)\right)\right] \\
&\quad\cdot\left[\mathcal{H}\left(\tau-\tau_{\min}\right) - \mathcal{H}\left(\tau-\tau_{\min,\mathrm{tc}}\right)\right] \\
&+\left[-\frac{c_{f11}\,\tau_{\mathrm{sc}}}{t_{\mathrm{c}}}\mathcal{EI}\left(c_{f12}\,\tau\exp\left(\frac{t_{\mathrm{m}}}{\tau_{\mathrm{sc}}}\right)\right)\right]\left[\mathcal{H}\left(\tau-\tau_{\min}\right) - \mathcal{H}\left(\tau-\tau_{13}\right)\right] \\
&+\left[\frac{c_{f11}\,\tau_{\mathrm{sc}}}{t_{\mathrm{c}}}\mathcal{EI}\left(c_{f12}\,\tau\exp\left(\frac{t_{\mathrm{m}}+t_{\mathrm{c}}}{\tau_{\mathrm{sc}}}\right)\right) + c_{f13}\right] \\
&\quad\cdot\left[\mathcal{H}\left(\tau-\tau_{\min,\mathrm{tc}}\right) - \mathcal{H}\left(\tau-\tau_{13,\mathrm{tc}}\right)\right] \\
&+\left[-\frac{c_{f11}\,\tau_{\mathrm{sc}}}{t_{\mathrm{c}}}\mathcal{EI}\left(c_{\tau13}\,c_{f12}\right) + \left(\frac{c_{f13}}{t_{\mathrm{c}}} - \frac{c_{f31}}{t_{\mathrm{c}}}\right)\left(t_{\mathrm{m}} - \tau_{\mathrm{sc}}\ln\left(\frac{c_{\tau13}}{\tau}\right)\right)\right] \\
&\quad\cdot\left[\mathcal{H}\left(\tau-\tau_{13}\right) - \mathcal{H}\left(\tau-\tau_{13,\mathrm{tc}}\right)\right] \\
&+c_{f31}\left[\mathcal{H}\left(\tau-\tau_{13,\mathrm{tc}}\right) - \mathcal{H}\left(\tau-\tau_{23,\mathrm{tc}}\right)\right] \\
&+\left[\frac{c_{f21}\,\tau_{\mathrm{sc}}}{t_{\mathrm{c}}}\mathcal{EI}\left(c_{\tau23}\,c_{f22}\right) + \left(\frac{c_{f31}}{t_{\mathrm{c}}} - \frac{c_{f23}}{t_{\mathrm{c}}}\right)\left(t_{\mathrm{m}} - \tau_{\mathrm{sc}}\ln\left(\frac{c_{\tau23}}{\tau}\right)\right)\right] \\
&\quad\cdot\left[\mathcal{H}\left(\tau-\tau_{23}\right) - \mathcal{H}\left(\tau-\tau_{23,\mathrm{tc}}\right)\right] \\
&+\left[\frac{c_{f21}\,\tau_{\mathrm{sc}}}{t_{\mathrm{c}}}\mathcal{EI}\left(c_{f22}\,\tau\exp\left(\frac{t_{\mathrm{m}}+t_{\mathrm{c}}}{\tau_{\mathrm{sc}}}\right)\right) + c_{f23}\right] \\
&\quad\cdot\left[\mathcal{H}\left(\tau-\tau_{23,\mathrm{tc}}\right) - \mathcal{H}\left(\tau-\tau_{\max,\mathrm{tc}}\right)\right] \\
&+\left[-\frac{c_{f21}\,\tau_{\mathrm{sc}}}{t_{\mathrm{c}}}\mathcal{EI}\left(c_{f22}\,\tau\exp\left(\frac{t_{\mathrm{m}}}{\tau_{\mathrm{sc}}}\right)\right)\right]\left[\mathcal{H}\left(\tau-\tau_{23}\right) - \mathcal{H}\left(\tau-\tau_{\max}\right)\right] \\
&+\left[-\frac{c_{f21}\,\tau_{\mathrm{sc}}}{t_{\mathrm{c}}}\mathcal{EI}\left(c_{\tau\max}\,c_{f22}\right) + \frac{c_{f23}}{t_{\mathrm{c}}}\left(t_{\mathrm{m}} - \tau_{\mathrm{sc}}\ln\left(\frac{c_{\tau\max}}{\tau}\right)\right)\right] \\
&\quad\cdot\left[\mathcal{H}\left(\tau-\tau_{\max}\right) - \mathcal{H}\left(\tau-\tau_{\max,\mathrm{tc}}\right)\right],
\end{aligned}
\tag{B.92}
$$

where τ_x is defined by Equation B.43 (restatement of Equation 4.35 in main text) and:

$$
\tau_{x,\mathrm{tc}} = c_{\tau x}\exp\left(\frac{-(t_{\mathrm{m}}+t_{\mathrm{c}})}{\tau_{\mathrm{sc}}}\right). \tag{B.93}
$$

This equation (B.93) determines the t_{c} shift on the boundary conditions ($\tau_x \to \tau_{x,\mathrm{tc}}$) of the transfer function of the scanning AAC based on limited trajectory theory, and is a restatement of Equation 4.40 of the main text. Examples of this average transfer function (i.e. based on Equation B.92) are shown in Figure 4.3 of the main text.

Analytical solution for $\bar{\Omega}_{\mathrm{AAC,F1}}$ of Equation B.89

Based on integral form 1 (i.e. $\Omega_{\mathrm{AAC,F1}}$) shown in Equation B.88:

$$\begin{aligned}\bar{\Omega}_{\mathrm{AAC,F1}} &= \frac{1}{t_c}\int_{t_m}^{t_m+t_c} \Omega_{\mathrm{AAC,F1}}\,\mathrm{d}t'_m \\ &= \frac{1}{t_c}\int_{t_m}^{t_m+t_c} \mathcal{H}\left(\frac{\tau_{sc}}{|\tau_{sc}|}\left(t'_m - \tau_{sc}\ln\left(\frac{c_{\tau x}}{\tau}\right)\right)\right) c_{fy1}\exp\left[c_{fy2}\,\tau\exp\left(\frac{t'_m}{\tau_{sc}}\right)\right]\mathrm{d}t'_m.\end{aligned} \tag{B.94}$$

Assuming τ_{sc} is greater than zero (denoted by $\bar{\Omega}_{\mathrm{AAC,F1+}}$), Equation B.94 becomes:

$$\bar{\Omega}_{\mathrm{AAC,F1+}} = \frac{1}{t_c}\int_{t_m}^{t_m+t_c} \mathcal{H}\left(t'_m - \tau_{sc}\ln\left(\frac{c_{\tau x}}{\tau}\right)\right) c_{fy1}\exp\left[c_{fy2}\,\tau\exp\left(\frac{t'_m}{\tau_{sc}}\right)\right]\mathrm{d}t'_m. \tag{B.95}$$

Applying the following substitution to Equation B.95:

$$\begin{aligned} u &= c_{fy2}\,\tau\exp\left(\frac{t'_m}{\tau_{sc}}\right) \rightarrow t'_m = \tau_{sc}\ln\left(\frac{u}{c_{fy2}\,\tau}\right) \\ \mathrm{d}u = \frac{c_{fy2}\,\tau}{\tau_{sc}}\exp\left(\frac{t'_m}{\tau_{sc}}\right)\mathrm{d}t'_m &\rightarrow \mathrm{d}t'_m = \frac{\tau_{sc}}{c_{fy2}\,\tau\exp\left(\frac{t'_m}{\tau_{sc}}\right)}\mathrm{d}u = \frac{\tau_{sc}}{u}\mathrm{d}u. \end{aligned} \tag{B.96}$$

Based on this substitution (i.e. Equation B.96), the inequality relationship defined by the Heaviside function within Equation B.95 (i.e $\mathcal{H}\left(t'_m - \tau_{sc}\ln\left(c_{\tau x}/\tau\right)\right)$ then becomes:

$$t'_m > \tau_{sc}\ln\left(\frac{c_{\tau x}}{\tau}\right) \rightarrow \tau_{sc}\ln\left(\frac{u}{c_{fy2}\,\tau}\right) > \tau_{sc}\ln\left(\frac{c_{\tau x}}{\tau}\right) \rightarrow \boldsymbol{u > c_{\tau x}\,c_{fy2}}, \tag{B.97}$$

as the base of the natural logarithm (e) is great than 1, $\ln(a) > \ln(b)$ is equivalent to $a > b$, and therefore,

$$\mathcal{H}\left(t'_m - \tau_{sc}\ln\left(\frac{c_{\tau x}}{\tau}\right)\right) = \mathcal{H}\left(u - c_{\tau x}\,c_{fy2}\right). \tag{B.98}$$

Substituting Equations B.96 and B.98 into Equation B.95 and temporarily treating the integral as indefinite:

$$\bar{\Omega}_{\mathrm{AAC,F1+}} = \frac{c_{fy1}\,\tau_{sc}}{t_c}\int \mathcal{H}\left(u - c_{\tau x}\,c_{fy2}\right)\frac{\exp(u)}{u}\mathrm{d}u. \tag{B.99}$$

Apply integration by parts to Equation B.99 as follows:

$$\begin{aligned} w = \mathcal{H}\left(u - c_{\tau x}\, c_{fy2}\right) \rightarrow \mathrm{d}w = \delta\left(u - c_{\tau x}\, c_{fy2}\right)\mathrm{d}u \\ \mathrm{d}y = \frac{\exp\left(u\right)}{u}\mathrm{d}u \rightarrow y = \mathcal{EI}\left(u\right), \end{aligned} \tag{B.100}$$

where $\mathcal{EI}$ is the Exponential Integral Function as follows:

$$\mathcal{EI}\left(x\right) = \int_{-\infty}^{x} \frac{\exp\left(x'\right)}{x'}\mathrm{d}x', \tag{B.101}$$

and δ is the Dirac delta function as follows:

$$\delta\left(x - a\right) = \begin{cases} 0 & \text{if } x \neq a \\ \infty & \text{if } x = a \end{cases}. \tag{B.102}$$

Therefore, using integration by parts based on Equation B.100, Equation B.99 becomes:

$$\bar{\Omega}_{\mathrm{AAC,F1+}} = \frac{c_{fy1}\,\tau_{\mathrm{sc}}}{t_{\mathrm{c}}}\left[\mathcal{H}\left(u - c_{\tau x}\, c_{fy2}\right)\mathcal{EI}\left(u\right) - \int \mathcal{EI}\left(u\right)\delta\left(u - c_{\tau x}\, c_{fy2}\right)\mathrm{d}u\right]. \tag{B.103}$$

Furthermore, noting that $\delta\left(u - c_{\tau x}\, c_{fy2}\right)$ vanishes everywhere except $u = c_{\tau x}c_{fy2}$, Equation B.103 becomes:

$$\begin{aligned} \bar{\Omega}_{\mathrm{AAC,F1+}} &= \frac{c_{fy1}\,\tau_{\mathrm{sc}}}{t_{\mathrm{c}}}\left[\mathcal{H}\left(u - c_{\tau x}\, c_{fy2}\right)\mathcal{EI}\left(u\right) - \mathcal{EI}\left(c_{\tau x}\, c_{fy2}\right)\int \delta\left(u - c_{\tau x}\, c_{fy2}\right)\mathrm{d}u\right] \\ \bar{\Omega}_{\mathrm{AAC,F1+}} &= \frac{c_{fy1}\,\tau_{\mathrm{sc}}}{t_{\mathrm{c}}}\left[\mathcal{EI}\left(u\right) - \mathcal{EI}\left(c_{\tau x}\, c_{fy2}\right)\right]\mathcal{H}\left(u - c_{\tau x}\, c_{fy2}\right). \end{aligned} \tag{B.104}$$

Substituting Equations B.96 and B.98 into Equation B.104 and applying the integration limits from the definition of $\bar{\Omega}_{\mathrm{AAC,F1+}}$ (i.e. t_{m} to $t_{\mathrm{m}} + t_{\mathrm{c}}$ in Equation B.95) simplifies to:

$$\bar{\Omega}_{\mathrm{AAC,F1+}} =$$
$$\frac{c_{fy1}\,\tau_{sc}}{t_c}\left[\mathcal{EI}\left(c_{fy2}\,\tau\exp\left(\frac{t'_m}{\tau_{sc}}\right)\right)-\mathcal{EI}\left(c_{\tau x}\,c_{fy2}\right)\right]\mathcal{H}\left(t'_m-\tau_{sc}\ln\left(\frac{c_{\tau x}}{\tau}\right)\right)\Bigg|_{t_m}^{t_m+t_c}$$
$$\bar{\Omega}_{\mathrm{AAC,F1+}} =$$
$$\frac{c_{fy1}\,\tau_{sc}}{t_c}\Bigg\{\left[\mathcal{EI}\left(c_{fy2}\,\tau\exp\left(\frac{t_m+t_c}{\tau_{sc}}\right)\right)-\mathcal{EI}\left(c_{\tau x}\,c_{fy2}\right)\right]\mathcal{H}\left(t_m+t_c-\tau_{sc}\ln\left(\frac{c_{\tau x}}{\tau}\right)\right)$$
$$-\left[\mathcal{EI}\left(c_{fy2}\,\tau\exp\left(\frac{t_m}{\tau_{sc}}\right)\right)-\mathcal{EI}\left(c_{\tau x}\,c_{fy2}\right)\right]\mathcal{H}\left(t_m-\tau_{sc}\ln\left(\frac{c_{\tau x}}{\tau}\right)\right)\Bigg\}. \tag{B.105}$$

As shown in Section B.5.1, this solution (Equation B.105) can be expanded to consider both $\tau_{sc}>0$ and $\tau_{sc}<0$ based on Equation B.121 (i.e. only differ by the inequality sign represented within their Heaviside functions), and thus both cases can be represented using one equation as follows:

$$\bar{\Omega}_{\mathrm{AAC,F1}} =$$
$$\frac{c_{fy1}\,\tau_{sc}}{t_c}\Bigg\{\left[\mathcal{EI}\left(c_{fy2}\,\tau\exp\left(\frac{t_m+t_c}{\tau_{sc}}\right)\right)-\mathcal{EI}\left(c_{\tau x}\,c_{fy2}\right)\right]\mathcal{H}\left(\frac{\tau_{sc}}{|\tau_{sc}|}\left(t_m+t_c-\tau_{sc}\ln\left(\frac{c_{\tau x}}{\tau}\right)\right)\right)$$
$$-\left[\mathcal{EI}\left(c_{fy2}\,\tau\exp\left(\frac{t_m}{\tau_{sc}}\right)\right)-\mathcal{EI}\left(c_{\tau x}\,c_{fy2}\right)\right]\mathcal{H}\left(\frac{\tau_{sc}}{|\tau_{sc}|}\left(t_m-\tau_{sc}\ln\left(\frac{c_{\tau x}}{\tau}\right)\right)\right)\Bigg\}. \tag{B.106}$$

Analytical solution for $\bar{\Omega}_{\mathrm{AAC,F2}}$ of Equation B.89

Based on integral form 2 (i.e. $\Omega_{\mathrm{AAC,F2}}$) shown in Equation B.88:

$$\begin{aligned}\bar{\Omega}_{\mathrm{AAC,F2}} =& \frac{1}{t_\mathrm{c}} \int_{t_\mathrm{m}}^{t_\mathrm{m}+t_\mathrm{c}} \Omega_{\mathrm{AAC,F2}} \, \mathrm{d}t'_\mathrm{m} \\ \bar{\Omega}_{\mathrm{AAC,F2}} =& \frac{1}{t_\mathrm{c}} \int_{t_\mathrm{m}}^{t_\mathrm{m}+t_\mathrm{c}} \mathcal{H}\left(\frac{\tau_\mathrm{sc}}{|\tau_\mathrm{sc}|}\left(t'_\mathrm{m} - \tau_\mathrm{sc} \ln\left(\frac{c_{\tau x}}{\tau}\right)\right)\right) c_{fy3} \, \mathrm{d}t'_\mathrm{m}.\end{aligned} \tag{B.107}$$

Assuming τ_sc is greater than zero (denoted by $\bar{\Omega}_{\mathrm{AAC,F2+}}$), Equation B.107 becomes:

$$\begin{aligned}\bar{\Omega}_{\mathrm{AAC,F2+}} =& \frac{1}{t_\mathrm{c}} \int_{t_\mathrm{m}}^{t_\mathrm{m}+t_\mathrm{c}} \mathcal{H}\left(t'_\mathrm{m} - \tau_\mathrm{sc} \ln\left(\frac{c_{\tau x}}{\tau}\right)\right) c_{fy3} \, \mathrm{d}t'_\mathrm{m} \\ =& \frac{c_{fy3}}{t_\mathrm{c}} \left(t'_\mathrm{m} - \tau_\mathrm{sc} \ln\left(\frac{c_{\tau x}}{\tau}\right)\right) \mathcal{H}\left(t'_\mathrm{m} - \tau_\mathrm{sc} \ln\left(\frac{c_{\tau x}}{\tau}\right)\right) \Bigg|_{t_\mathrm{m}}^{t_\mathrm{m}+t_\mathrm{c}} \\ \bar{\Omega}_{\mathrm{AAC,F2+}} =& \frac{c_{fy3}}{t_\mathrm{c}} \Bigg[\left(t_\mathrm{m} + t_\mathrm{c} - \tau_\mathrm{sc} \ln\left(\frac{c_{\tau x}}{\tau}\right)\right) \mathcal{H}\left(t_\mathrm{m} + t_\mathrm{c} - \tau_\mathrm{sc} \ln\left(\frac{c_{\tau x}}{\tau}\right)\right) \\ & - \left(t_\mathrm{m} - \tau_\mathrm{sc} \ln\left(\frac{c_{\tau x}}{\tau}\right)\right) \mathcal{H}\left(t_\mathrm{m} - \tau_\mathrm{sc} \ln\left(\frac{c_{\tau x}}{\tau}\right)\right) \Bigg].\end{aligned} \tag{B.108}$$

As shown in Section B.5.1, this solution (Equation B.108) can be expanded to consider both $\tau_\mathrm{sc} > 0$ and $\tau_\mathrm{sc} < 0$ based on Equation B.121 (i.e. only differ by the inequality sign represented within their Heaviside functions), and thus both cases can be represented using one equation as follows:

$$\begin{aligned}\bar{\Omega}_{\mathrm{AAC,F2}} =& \frac{c_{fy3}}{t_\mathrm{c}} \Bigg[\left(t_\mathrm{m} + t_\mathrm{c} - \tau_\mathrm{sc} \ln\left(\frac{c_{\tau x}}{\tau}\right)\right) \mathcal{H}\left(\frac{\tau_\mathrm{sc}}{|\tau_\mathrm{sc}|}\left(t_\mathrm{m} + t_\mathrm{c} - \tau_\mathrm{sc} \ln\left(\frac{c_{\tau x}}{\tau}\right)\right)\right) \\ & - \left(t_\mathrm{m} - \tau_\mathrm{sc} \ln\left(\frac{c_{\tau x}}{\tau}\right)\right) \mathcal{H}\left(\frac{\tau_\mathrm{sc}}{|\tau_\mathrm{sc}|}\left(t_\mathrm{m} - \tau_\mathrm{sc} \ln\left(\frac{c_{\tau x}}{\tau}\right)\right)\right) \Bigg].\end{aligned} \tag{B.109}$$

Reflecting an up or down scan within the Heaviside limits of $\Omega_{\mathrm{AAC,sc}}$

As mentioned in the main text, the AAC completing an up scan (i.e. $\omega_{\mathrm{E}} > \omega_{\mathrm{S}}$) is reflected in a positive scan time constant (i.e. $\tau_{\mathrm{sc}} > 0$), while a down scan (i.e. $\omega_{\mathrm{E}} < \omega_{\mathrm{S}}$) is reflected in a negative scan time constant (i.e. $\tau_{\mathrm{sc}} < 0$). This change affects the inequality that allows the Heaviside functions of the transfer function equation to be converted from the particle relaxation time (τ_x) to the measurement (t_{m}) as shown by Equation 4.39 of the main text. To quantify this effect, consider the integral of a generic function $j(x)$ times a Heaviside function with a flipping inequality sign as follows:

$$I = \int_{x_1}^{x_2} j(x)\,\mathcal{H}\left(\frac{a}{|a|}(x-a)\right)\mathrm{d}x. \tag{B.110}$$

Case 1: $a > 0$ (i.e. similar to $t_{\mathrm{sc}} > 0$)

If $a > 0$, Equation B.110 becomes:

$$I_+ = \int_{x_1}^{x_2} j(x)\,\mathcal{H}(x-a)\,\mathrm{d}x. \tag{B.111}$$

Apply integration by parts to Equation B.111 as follows:

$$\begin{aligned} u = \mathcal{H}(x-a) &\rightarrow \mathrm{d}u = \delta(x-a)\,\mathrm{d}x \\ \mathrm{d}v = j(x)\,\mathrm{d}x &\rightarrow v = \int j(x)\,\mathrm{d}x = \mathcal{J}(x), \end{aligned} \tag{B.112}$$

where $\mathcal{J}(x)$ is the integral of the generic function $j(x)$ with respect to x. Therefore, using integration by parts based on Equation B.112, Equation B.111 becomes:

$$I_+ = \mathcal{H}(x-a)\,\mathcal{J}(x)\big|_{x_1}^{x_2} - \int_{x_1}^{x_2} \mathcal{J}(x)\,\delta(x-a)\,\mathrm{d}x. \tag{B.113}$$

Furthermore, noting that $\delta(x-a)$ vanishes everywhere except $x = a$, Equation B.113 becomes:

$$\begin{aligned} I_+ &= \mathcal{H}(x-a)\,\mathcal{J}(x)\big|_{x_1}^{x_2} - \mathcal{J}(a)\int_{x_1}^{x_2} \delta(x-a)\,\mathrm{d}x \\ &= [\mathcal{J}(x) - \mathcal{J}(a)]\,\mathcal{H}(x-a)\,\big|_{x_1}^{x_2} \\ I_+ &= [\mathcal{J}(x_2) - \mathcal{J}(a)]\,\mathcal{H}(x_2-a) - [\mathcal{J}(x_1) - \mathcal{J}(a)]\,\mathcal{H}(x_1-a). \end{aligned} \tag{B.114}$$

Case 2: $a < 0$ **(i.e. similar to** $t_{sc} < 0$**)**

If $a < 0$, Equation B.110 becomes:

$$I_{-} = \int_{x_1}^{x_2} j(x)\,\mathcal{H}(a-x)\,\mathrm{d}x. \tag{B.115}$$

Apply integration by parts to Equation B.115 as follows:

$$\begin{aligned} u = \mathcal{H}(a-x) &\rightarrow \mathrm{d}u = -\delta(x-a)\,\mathrm{d}x \\ \mathrm{d}v = j(x)\,\mathrm{d}x &\rightarrow v = \int j(x)\,\mathrm{d}x = \mathcal{J}(x), \end{aligned} \tag{B.116}$$

where $\mathcal{J}(x)$ is the integral of the generic function $j(x)$ with respect to x. Therefore, using integration by parts based on Equation B.116, Equation B.115 becomes:

$$I_{-} = \mathcal{H}(a-x)\,\mathcal{J}(x)\Big|_{x_1}^{x_2} + \int_{x_1}^{x_2} \mathcal{J}(x)\,\delta(x-a)\,\mathrm{d}x. \tag{B.117}$$

Furthermore, noting that $\delta(a-x)$ vanishes everywhere except $x = a$, Equation B.117 becomes:

$$\begin{aligned} I_{-} &= \mathcal{H}(a-x)\,\mathcal{J}(x)\Big|_{x_1}^{x_2} + \mathcal{J}(a)\int_{x_1}^{x_2} \delta(x-a)\,\mathrm{d}x \\ I_{-} &= \left[\mathcal{H}(a-x)\,\mathcal{J}(x) + \mathcal{J}(a)\,\mathcal{H}(x-a)\right]\Big|_{x_1}^{x_2}. \end{aligned} \tag{B.118}$$

However, the relationship between Heaviside function with opposite inequalities (i.e. $x > a$ versus $x < a$) is:

$$\mathcal{H}(x-a) = 1 - \mathcal{H}(a-x). \tag{B.119}$$

Substituting this relationship (Equation B.119) into Equation B.118 and simplifying, as follows:

$$\begin{aligned} I_{-} &= \left[\mathcal{H}(a-x)\,\mathcal{J}(x) + \mathcal{J}(a)\,(1-\mathcal{H}(a-x))\right]\Big|_{x_1}^{x_2} \\ &= \left[\mathcal{J}(a) + (\mathcal{J}(x) - \mathcal{J}(a))\,\mathcal{H}(a-x)\right]\Big|_{x_1}^{x_2} \\ I_{-} &= \left[\mathcal{J}(x_2) - \mathcal{J}(a)\right]\mathcal{H}(a-x_2) - \left[\mathcal{J}(x_1) - \mathcal{J}(a)\right]\mathcal{H}(a-x_1). \end{aligned} \tag{B.120}$$

Case 1 or 2: $a > 0$ **or** $a < 0$

Since the solution for I (Equation B.110) for either $a > 0$ or $a < 0$ (i.e. denoted as I_+ and I_- in Equations B.114 and B.120, respectively) have the same form that only vary by the inequality sign represented by its Heaviside functions, either case ($a < 0$ or $a > 0$) can be represented by:

$$\begin{aligned} I &= \int_{x_1}^{x_2} j(x)\,\mathcal{H}\left(\frac{a}{|a|}(x-a)\right)\mathrm{d}x \\ I &= [\mathcal{J}(x_2)-\mathcal{J}(a)]\,\mathcal{H}\left(\frac{a}{|a|}(x_2-a)\right) - [\mathcal{J}(x_1)-\mathcal{J}(a)]\,\mathcal{H}\left(\frac{a}{|a|}(x_1-a)\right). \end{aligned} \tag{B.121}$$

B.6 Average transfer function of scanning AAC over t_c: particle streamline, non-idealized, balanced flows & uniform axial flow

Note: Similar to the other sections in this appendix, this section and its subsections use simplified notation of the parameter subscripts, as outlined in Section B.1, based on the common AAC operation and theory instances included within the title and header of this section.

To determine the average transfer function of the scanning AAC over the counting time of downstream particle detector (i.e. solve the integral shown in Equation 4.33 of the main text), the piecewise notation of the transfer function based on particle streamline theory (Equation B.74), as derived in Section B.4.2, can be represented as one equation using the Heaviside function ($\mathcal{H}(x-a)$, defined by Equation 4.34 of main text) as follows:

$$\begin{aligned}\Omega_{\mathrm{AAC,B}}(\tau) =& \lambda_\Omega \mu_\Omega \left[1+\frac{\mu_\Omega}{\beta}\left(\frac{\tau}{\tau^*_{\mathrm{sc,B}}}-1\right)\right]\left[\mathcal{H}\left(\tau-\tau_{\mathrm{min,B}}\right)-\mathcal{H}\left(\tau-\tau^*_{\mathrm{sc,B}}\right)\right] \\ &+\lambda_\Omega \mu_\Omega \left[1+\frac{\mu_\Omega}{\beta}\left(1-\frac{\tau}{\tau^*_{\mathrm{sc,B}}}\right)\right]\left[\mathcal{H}\left(\tau-\tau^*_{\mathrm{sc,B}}\right)-\mathcal{H}\left(\tau-\tau_{\mathrm{max,B}}\right)\right],\end{aligned} \tag{B.122}$$

where the relaxation time boundaries ($\tau_{\mathrm{min,B}}$, $\tau^*_{\mathrm{sc,B}}$ and $\tau_{\mathrm{max,B}}$) are defined in Table B.3 and shown in Figure B.5. All of the relaxation time boundaries of this transfer function are of the form $\tau_x = c_{\tau x}\exp(-t_\mathrm{m}/\tau_\mathrm{sc})$ (i.e. Equation 4.35 of main text or Equation B.77). Based on this consistent form, Equation B.122 becomes:

$$\begin{aligned}\Omega_{\mathrm{AAC,B}}(\tau,t_\mathrm{m}) =& \lambda_\Omega \mu_\Omega \left[1+\frac{\mu_\Omega}{\beta}\left(\frac{\tau}{c_{\tau*,\mathrm{B}}\exp\left(\frac{-t_\mathrm{m}}{\tau_\mathrm{sc}}\right)}-1\right)\right] \\ &\cdot\left[\mathcal{H}\left(\tau-\tau_{\mathrm{min,B}}\right)-\mathcal{H}\left(\tau-\tau^*_{\mathrm{sc,B}}\right)\right] \\ &+\lambda_\Omega \mu_\Omega \left[1+\frac{\mu_\Omega}{\beta}\left(1-\frac{\tau}{c_{\tau*,\mathrm{B}}\exp\left(\frac{-t_\mathrm{m}}{\tau_\mathrm{sc}}\right)}\right)\right] \\ &\cdot\left[\mathcal{H}\left(\tau-\tau^*_{\mathrm{sc,B}}\right)-\mathcal{H}\left(\tau-\tau_{\mathrm{max,B}}\right)\right].\end{aligned} \tag{B.123}$$

This form also results in $\mathcal{H}(\tau-\tau_{x,\mathrm{B}}) = \mathcal{H}\left(\left(\tau_\mathrm{sc}/|\tau_\mathrm{sc}|\right)\left(t_\mathrm{m}-\tau_\mathrm{sc}\ln\left(c_{\tau x,\mathrm{B}}/\tau\right)\right)\right)$ (Equation 4.39 of the main text), and the limits of $\Omega_{\mathrm{AAC,B}}$ (Equation B.123) can be converted from the particle relaxation time (τ) to the measurement time (t_m) domain as follows:

$$
\begin{aligned}
\Omega_{\mathrm{AAC,B}}(t_\mathrm{m}) =& \lambda_\Omega\,\mu_\Omega \left[1+\frac{\mu_\Omega}{\beta}\left(\frac{\tau}{c_{\tau*,\mathrm{B}}\exp\left(\frac{-t_\mathrm{m}}{\tau_\mathrm{sc}}\right)}-1\right)\right] \\
&\cdot\left[\mathcal{H}\left(\frac{\tau_\mathrm{sc}}{|\tau_\mathrm{sc}|}\left(t_\mathrm{m}-\tau_\mathrm{sc}\ln\left(\frac{c_{\tau\mathrm{min,B}}}{\tau}\right)\right)\right)-\mathcal{H}\left(\frac{\tau_\mathrm{sc}}{|\tau_\mathrm{sc}|}\left(t_\mathrm{m}-\tau_\mathrm{sc}\ln\left(\frac{c_{\tau*,\mathrm{B}}}{\tau}\right)\right)\right)\right] \\
&+\lambda_\Omega\,\mu_\Omega\left[1+\frac{\mu_\Omega}{\beta}\left(1-\frac{\tau}{c_{\tau*,\mathrm{B}}\exp\left(\frac{-t_\mathrm{m}}{\tau_\mathrm{sc}}\right)}\right)\right] \\
&\cdot\left[\mathcal{H}\left(\frac{\tau_\mathrm{sc}}{|\tau_\mathrm{sc}|}\left(t_\mathrm{m}-\tau_\mathrm{sc}\ln\left(\frac{c_{\tau*,\mathrm{B}}}{\tau}\right)\right)\right)-\mathcal{H}\left(\frac{\tau_\mathrm{sc}}{|\tau_\mathrm{sc}|}\left(t_\mathrm{m}-\tau_\mathrm{sc}\ln\left(\frac{c_{\tau\mathrm{max,B}}}{\tau}\right)\right)\right)\right] \\
\Omega_{\mathrm{AAC,B}}(t_\mathrm{m}) =& \lambda_\Omega\,\mu_\Omega\left[c_\mathrm{BL}+c_\mathrm{B1}\,\tau\exp\left(\frac{t_\mathrm{m}}{\tau_\mathrm{sc}}\right)\right] \\
&\cdot\left[\mathcal{H}\left(\frac{\tau_\mathrm{sc}}{|\tau_\mathrm{sc}|}\left(t_\mathrm{m}-\tau_\mathrm{sc}\ln\left(\frac{c_{\tau\mathrm{min,B}}}{\tau}\right)\right)\right)-\mathcal{H}\left(\frac{\tau_\mathrm{sc}}{|\tau_\mathrm{sc}|}\left(t_\mathrm{m}-\tau_\mathrm{sc}\ln\left(\frac{c_{\tau*,\mathrm{B}}}{\tau}\right)\right)\right)\right] \\
&+\lambda_\Omega\,\mu_\Omega\left[c_\mathrm{BU}-c_\mathrm{B1}\,\tau\exp\left(\frac{t_\mathrm{m}}{\tau_\mathrm{sc}}\right)\right] \\
&\cdot\left[\mathcal{H}\left(\frac{\tau_\mathrm{sc}}{|\tau_\mathrm{sc}|}\left(t_\mathrm{m}-\tau_\mathrm{sc}\ln\left(\frac{c_{\tau*,\mathrm{B}}}{\tau}\right)\right)\right)-\mathcal{H}\left(\frac{\tau_\mathrm{sc}}{|\tau_\mathrm{sc}|}\left(t_\mathrm{m}-\tau_\mathrm{sc}\ln\left(\frac{c_{\tau\mathrm{max,B}}}{\tau}\right)\right)\right)\right]
\end{aligned}
\tag{B.124}
$$

where the constants are defined in Table B.5.

Table B.5 Constants of the simplified mathematical representation of the transfer function of the scanning AAC based on particle streamline theory.

Parameter	Equation	
c_BL	$1-\frac{\mu_\Omega}{\beta}$	(B.125)
c_BU	$1+\frac{\mu_\Omega}{\beta}$	(B.126)
c_B1	$\frac{\mu_\Omega}{\beta c_{\tau*,\mathrm{B}}}$	(B.127)

B.6.1 Solving integral of $\Omega_{\mathrm{AAC,B}}$ over t_{c} to determine $\bar{\Omega}_{\mathrm{AAC,B}}$

This section determines the average transfer function of the AAC ($\bar{\Omega}_{\mathrm{AAC,B}}$) over the counting time (t_{c}) of the particle detector by substituting Equation B.124 into Equation 4.33 of the main text and solving. To reduce the analysis, note that the two terms in Equation B.124 have the same form. Expanding Equation B.124 based on its Heaviside function terms and considering its first term generically as follows:

$$\begin{aligned}
&\lambda_{\Omega}\,\mu_{\Omega}\left[c_{\mathrm{B}y}+c_{\mathrm{B}w}\,\tau\exp\left(\frac{t_{\mathrm{m}}}{\tau_{\mathrm{sc}}}\right)\right]\mathcal{H}\left(\frac{\tau_{\mathrm{sc}}}{|\tau_{\mathrm{sc}}|}\left(t_{\mathrm{m}}-\tau_{\mathrm{sc}}\ln\left(\frac{c_{\tau x,\mathrm{B}}}{\tau}\right)\right)\right)\\
&\quad=\underbrace{\lambda_{\Omega}\,\mu_{\Omega}\,c_{\mathrm{B}y}\,\mathcal{H}\left(\frac{\tau_{\mathrm{sc}}}{|\tau_{\mathrm{sc}}|}\left(t_{\mathrm{m}}-\tau_{\mathrm{sc}}\ln\left(\frac{c_{\tau x,\mathrm{B}}}{\tau}\right)\right)\right)}_{\text{Term Form: }\Omega_{\mathrm{AAC,B,F1}}(c_{\tau x,\mathrm{B}},\,c_{\mathrm{B}y},\,\tau,\,\tau_{\mathrm{sc}},\,t_{\mathrm{m}},\,\lambda_{\Omega},\,\mu_{\Omega})}\\
&\qquad+\underbrace{\lambda_{\Omega}\,\mu_{\Omega}\,c_{\mathrm{B}w}\,\tau\exp\left(\frac{t_{\mathrm{m}}}{\tau_{\mathrm{sc}}}\right)\mathcal{H}\left(\frac{\tau_{\mathrm{sc}}}{|\tau_{\mathrm{sc}}|}\left(t_{\mathrm{m}}-\tau_{\mathrm{sc}}\ln\left(\frac{c_{\tau x,\mathrm{B}}}{\tau}\right)\right)\right)}_{\text{Term Form: }\Omega_{\mathrm{AAC,B,F2}}(c_{\tau x,\mathrm{B}},\,c_{\mathrm{B}w},\,\tau,\,\tau_{\mathrm{sc}},\,t_{\mathrm{m}},\,\lambda_{\Omega},\,\mu_{\Omega})}.
\end{aligned}\tag{B.128}$$

Therefore, substituting the two term forms (i.e. $\Omega_{\mathrm{AAC,B,F1}}$ and $\Omega_{\mathrm{AAC,B,F1}}$) identified in Equation B.128 into Equation B.124, then into the definition of $\bar{\Omega}_{\mathrm{AAC}}$ (Equation 4.33 of the main text) simplifies to the following:

$$
\begin{aligned}
\bar{\Omega}_{\mathrm{AAC,B}} &= \frac{1}{t_c}\int_{t_m}^{t_m+t_c} \Omega_{\mathrm{AAC,B}}(\tau, t'_m)\,\mathrm{d}t'_m \\
\bar{\Omega}_{\mathrm{AAC,B}} &= \underbrace{\frac{1}{t_c}\int_{t_m}^{t_m+t_c} \Omega_{\mathrm{AAC,B,F1}}(c_{\tau\min,\mathrm{B}},\, c_{\mathrm{BL}},\, \tau,\, \tau_{\mathrm{sc}},\, t_m,\, \lambda_\Omega,\, \mu_\Omega)\,\mathrm{d}t'_m}_{\text{Term Form: } \bar{\Omega}_{\mathrm{AAC,B,F1}}(c_{\tau\min,\mathrm{B}}, c_{\mathrm{BL}}, \tau, \tau_{\mathrm{sc}}, t_m, \lambda_\Omega, \mu_\Omega, t_c)} \\
&\quad + \underbrace{\frac{1}{t_c}\int_{t_m}^{t_m+t_c} \Omega_{\mathrm{AAC,B,F2}}(c_{\tau\min,\mathrm{B}},\, c_{\mathrm{B1}},\, \tau,\, \tau_{\mathrm{sc}},\, t_m,\, \lambda_\Omega,\, \mu_\Omega)\,\mathrm{d}t'_m}_{\text{Term Form: } \bar{\Omega}_{\mathrm{AAC,B,F2}}(c_{\tau\min,\mathrm{B}}, c_{\mathrm{B1}}, \tau, \tau_{\mathrm{sc}}, t_m, \lambda_\Omega, \mu_\Omega, t_c)} \\
&\quad - \underbrace{\frac{1}{t_c}\int_{t_m}^{t_m+t_c} \Omega_{\mathrm{AAC,B,F1}}(c_{\tau*,\mathrm{B}},\, c_{\mathrm{BL}},\, \tau,\, \tau_{\mathrm{sc}},\, t_m,\, \lambda_\Omega,\, \mu_\Omega)\,\mathrm{d}t'_m}_{\text{Term Form: } \bar{\Omega}_{\mathrm{AAC,B,F1}}(c_{\tau*,\mathrm{B}}, c_{\mathrm{BL}}, \tau, \tau_{\mathrm{sc}}, t_m, \lambda_\Omega, \mu_\Omega, t_c)} \\
&\quad - \underbrace{\frac{1}{t_c}\int_{t_m}^{t_m+t_c} \Omega_{\mathrm{AAC,B,F2}}(c_{\tau*,\mathrm{B}},\, c_{\mathrm{B1}},\, \tau,\, \tau_{\mathrm{sc}},\, t_m,\, \lambda_\Omega,\, \mu_\Omega)\,\mathrm{d}t'_m}_{\text{Term Form: } \bar{\Omega}_{\mathrm{AAC,B,F2}}(c_{\tau*,\mathrm{B}}, c_{\mathrm{B1}}, \tau, \tau_{\mathrm{sc}}, t_m, \lambda_\Omega, \mu_\Omega, t_c)} \\
&\quad + \underbrace{\frac{1}{t_c}\int_{t_m}^{t_m+t_c} \Omega_{\mathrm{AAC,B,F1}}(c_{\tau*,\mathrm{B}},\, c_{\mathrm{BU}},\, \tau,\, \tau_{\mathrm{sc}},\, t_m,\, \lambda_\Omega,\, \mu_\Omega)\,\mathrm{d}t'_m}_{\text{Term Form: } \bar{\Omega}_{\mathrm{AAC,B,F1}}(c_{\tau*,\mathrm{B}}, c_{\mathrm{BU}}, \tau, \tau_{\mathrm{sc}}, t_m, \lambda_\Omega, \mu_\Omega, t_c)} \\
&\quad + \underbrace{\frac{1}{t_c}\int_{t_m}^{t_m+t_c} \Omega_{\mathrm{AAC,B,F2}}(c_{\tau*,\mathrm{B}},\, -c_{\mathrm{B1}},\, \tau,\, \tau_{\mathrm{sc}},\, t_m,\, \lambda_\Omega,\, \mu_\Omega)\,\mathrm{d}t'_m}_{\text{Term Form: } \bar{\Omega}_{\mathrm{AAC,B,F2}}(c_{\tau*,\mathrm{B}}, -c_{\mathrm{B1}}, \tau, \tau_{\mathrm{sc}}, t_m, \lambda_\Omega, \mu_\Omega, t_c)} \\
&\quad - \underbrace{\frac{1}{t_c}\int_{t_m}^{t_m+t_c} \Omega_{\mathrm{AAC,B,F1}}(c_{\tau\max,\mathrm{B}},\, c_{\mathrm{BU}},\, \tau,\, \tau_{\mathrm{sc}},\, t_m,\, \lambda_\Omega,\, \mu_\Omega)\,\mathrm{d}t'_m}_{\text{Term Form: } \bar{\Omega}_{\mathrm{AAC,B,F1}}(c_{\tau\max,\mathrm{B}}, c_{\mathrm{BU}}, \tau, \tau_{\mathrm{sc}}, t_m, \lambda_\Omega, \mu_\Omega, t_c)} \\
&\quad - \underbrace{\frac{1}{t_c}\int_{t_m}^{t_m+t_c} \Omega_{\mathrm{AAC,B,F2}}(c_{\tau\max,\mathrm{B}},\, -c_{\mathrm{B1}},\, \tau,\, \tau_{\mathrm{sc}},\, t_m,\, \lambda_\Omega,\, \mu_\Omega)\,\mathrm{d}t'_m}_{\text{Term Form: } \bar{\Omega}_{\mathrm{AAC,B,F2}}(c_{\tau\max,\mathrm{B}}, -c_{\mathrm{B1}}, \tau, \tau_{\mathrm{sc}}, t_m, \lambda_\Omega, \mu_\Omega, t_c)}.
\end{aligned}
\tag{B.129}
$$

All of the terms in Equation B.129 are of the form $\bar{\Omega}_{\mathrm{AAC,B,F1}}$ or $\bar{\Omega}_{\mathrm{AAC,B,F2}}$, which are solved[2] in Sections B.6.1 and B.6.1, respectively. Therefore, substituting these solutions (i.e. Equations B.136 and B.142) into Equation B.129:

[2] Assumes λ_Ω and μ_Ω are constant over the width of the scanning AAC transfer function (i.e. the AAC is operated with sufficiently high resolution and the particle detector is operated with sufficiently low counting time).

$$
\begin{aligned}
&\bar{\Omega}_{\mathrm{AAC,B}} = \\
&\frac{\lambda_\Omega\,\mu_\Omega\,c_{\mathrm{BL}}}{t_\mathrm{c}}\left[\left(t_\mathrm{m}+t_\mathrm{c}-\tau_\mathrm{sc}\ln\left(\frac{c_{\tau\mathrm{min,B}}}{\tau}\right)\right)\mathcal{H}\left(\frac{\tau_\mathrm{sc}}{|\tau_\mathrm{sc}|}\left(t_\mathrm{m}+t_\mathrm{c}-\tau_\mathrm{sc}\ln\left(\frac{c_{\tau\mathrm{min,B}}}{\tau}\right)\right)\right)\right.\\
&\qquad\left.-\left(t_\mathrm{m}-\tau_\mathrm{sc}\ln\left(\frac{c_{\tau\mathrm{min,B}}}{\tau}\right)\right)\mathcal{H}\left(\frac{\tau_\mathrm{sc}}{|\tau_\mathrm{sc}|}\left(t_\mathrm{m}-\tau_\mathrm{sc}\ln\left(\frac{c_{\tau\mathrm{min,B}}}{\tau}\right)\right)\right)\right]\\
&+\frac{\lambda_\Omega\,\mu_\Omega\,c_{\mathrm{B1}}\,\tau_\mathrm{sc}}{t_\mathrm{c}}\tau\left[\left(\exp\left(\frac{t_\mathrm{m}+t_\mathrm{c}}{\tau_\mathrm{sc}}\right)-\frac{c_{\tau\mathrm{min,B}}}{\tau}\right)\mathcal{H}\left(\frac{\tau_\mathrm{sc}}{|\tau_\mathrm{sc}|}\left(t_\mathrm{m}+t_\mathrm{c}-\tau_\mathrm{sc}\ln\left(\frac{c_{\tau\mathrm{min,B}}}{\tau}\right)\right)\right)\right.\\
&\qquad\left.-\left(\exp\left(\frac{t_\mathrm{m}}{\tau_\mathrm{sc}}\right)-\frac{c_{\tau\mathrm{min,B}}}{\tau}\right)\mathcal{H}\left(\frac{\tau_\mathrm{sc}}{|\tau_\mathrm{sc}|}\left(t_\mathrm{m}-\tau_\mathrm{sc}\ln\left(\frac{c_{\tau\mathrm{min,B}}}{\tau}\right)\right)\right)\right]\\
&-\frac{\lambda_\Omega\,\mu_\Omega\,c_{\mathrm{BL}}}{t_\mathrm{c}}\left[\left(t_\mathrm{m}+t_\mathrm{c}-\tau_\mathrm{sc}\ln\left(\frac{c_{\tau*,\mathrm{B}}}{\tau}\right)\right)\mathcal{H}\left(\frac{\tau_\mathrm{sc}}{|\tau_\mathrm{sc}|}\left(t_\mathrm{m}+t_\mathrm{c}-\tau_\mathrm{sc}\ln\left(\frac{c_{\tau*,\mathrm{B}}}{\tau}\right)\right)\right)\right.\\
&\qquad\left.-\left(t_\mathrm{m}-\tau_\mathrm{sc}\ln\left(\frac{c_{\tau*,\mathrm{B}}}{\tau}\right)\right)\mathcal{H}\left(\frac{\tau_\mathrm{sc}}{|\tau_\mathrm{sc}|}\left(t_\mathrm{m}-\tau_\mathrm{sc}\ln\left(\frac{c_{\tau*,\mathrm{B}}}{\tau}\right)\right)\right)\right]\\
&-\frac{\lambda_\Omega\,\mu_\Omega\,c_{\mathrm{B1}}\,\tau_\mathrm{sc}}{t_\mathrm{c}}\tau\left[\left(\exp\left(\frac{t_\mathrm{m}+t_\mathrm{c}}{\tau_\mathrm{sc}}\right)-\frac{c_{\tau*,\mathrm{B}}}{\tau}\right)\mathcal{H}\left(\frac{\tau_\mathrm{sc}}{|\tau_\mathrm{sc}|}\left(t_\mathrm{m}+t_\mathrm{c}-\tau_\mathrm{sc}\ln\left(\frac{c_{\tau*,\mathrm{B}}}{\tau}\right)\right)\right)\right.\\
&\qquad\left.-\left(\exp\left(\frac{t_\mathrm{m}}{\tau_\mathrm{sc}}\right)-\frac{c_{\tau*,\mathrm{B}}}{\tau}\right)\mathcal{H}\left(\frac{\tau_\mathrm{sc}}{|\tau_\mathrm{sc}|}\left(t_\mathrm{m}-\tau_\mathrm{sc}\ln\left(\frac{c_{\tau*,\mathrm{B}}}{\tau}\right)\right)\right)\right]\\
&+\frac{\lambda_\Omega\,\mu_\Omega\,c_{\mathrm{BU}}}{t_\mathrm{c}}\left[\left(t_\mathrm{m}+t_\mathrm{c}-\tau_\mathrm{sc}\ln\left(\frac{c_{\tau*,\mathrm{B}}}{\tau}\right)\right)\mathcal{H}\left(\frac{\tau_\mathrm{sc}}{|\tau_\mathrm{sc}|}\left(t_\mathrm{m}+t_\mathrm{c}-\tau_\mathrm{sc}\ln\left(\frac{c_{\tau*,\mathrm{B}}}{\tau}\right)\right)\right)\right.\\
&\qquad\left.-\left(t_\mathrm{m}-\tau_\mathrm{sc}\ln\left(\frac{c_{\tau*,\mathrm{B}}}{\tau}\right)\right)\mathcal{H}\left(\frac{\tau_\mathrm{sc}}{|\tau_\mathrm{sc}|}\left(t_\mathrm{m}-\tau_\mathrm{sc}\ln\left(\frac{c_{\tau*,\mathrm{B}}}{\tau}\right)\right)\right)\right]\\
&-\frac{\lambda_\Omega\,\mu_\Omega\,c_{\mathrm{B1}}\,\tau_\mathrm{sc}}{t_\mathrm{c}}\tau\left[\left(\exp\left(\frac{t_\mathrm{m}+t_\mathrm{c}}{\tau_\mathrm{sc}}\right)-\frac{c_{\tau*,\mathrm{B}}}{\tau}\right)\mathcal{H}\left(\frac{\tau_\mathrm{sc}}{|\tau_\mathrm{sc}|}\left(t_\mathrm{m}+t_\mathrm{c}-\tau_\mathrm{sc}\ln\left(\frac{c_{\tau*,\mathrm{B}}}{\tau}\right)\right)\right)\right.\\
&\qquad\left.-\left(\exp\left(\frac{t_\mathrm{m}}{\tau_\mathrm{sc}}\right)-\frac{c_{\tau*,\mathrm{B}}}{\tau}\right)\mathcal{H}\left(\frac{\tau_\mathrm{sc}}{|\tau_\mathrm{sc}|}\left(t_\mathrm{m}-\tau_\mathrm{sc}\ln\left(\frac{c_{\tau*,\mathrm{B}}}{\tau}\right)\right)\right)\right]\\
&-\frac{\lambda_\Omega\,\mu_\Omega\,c_{\mathrm{BU}}}{t_\mathrm{c}}\left[\left(t_\mathrm{m}+t_\mathrm{c}-\tau_\mathrm{sc}\ln\left(\frac{c_{\tau\mathrm{max,B}}}{\tau}\right)\right)\mathcal{H}\left(\frac{\tau_\mathrm{sc}}{|\tau_\mathrm{sc}|}\left(t_\mathrm{m}+t_\mathrm{c}-\tau_\mathrm{sc}\ln\left(\frac{c_{\tau\mathrm{max,B}}}{\tau}\right)\right)\right)\right.\\
&\qquad\left.-\left(t_\mathrm{m}-\tau_\mathrm{sc}\ln\left(\frac{c_{\tau\mathrm{max,B}}}{\tau}\right)\right)\mathcal{H}\left(\frac{\tau_\mathrm{sc}}{|\tau_\mathrm{sc}|}\left(t_\mathrm{m}-\tau_\mathrm{sc}\ln\left(\frac{c_{\tau\mathrm{max,B}}}{\tau}\right)\right)\right)\right]\\
&+\frac{\lambda_\Omega\,\mu_\Omega\,c_{\mathrm{B1}}\,\tau_\mathrm{sc}}{t_\mathrm{c}}\tau\left[\left(\exp\left(\frac{t_\mathrm{m}+t_\mathrm{c}}{\tau_\mathrm{sc}}\right)-\frac{c_{\tau\mathrm{max,B}}}{\tau}\right)\mathcal{H}\left(\frac{\tau_\mathrm{sc}}{|\tau_\mathrm{sc}|}\left(t_\mathrm{m}+t_\mathrm{c}-\tau_\mathrm{sc}\ln\left(\frac{c_{\tau\mathrm{max,B}}}{\tau}\right)\right)\right)\right.\\
&\qquad\left.-\left(\exp\left(\frac{t_\mathrm{m}}{\tau_\mathrm{sc}}\right)-\frac{c_{\tau\mathrm{max,B}}}{\tau}\right)\mathcal{H}\left(\frac{\tau_\mathrm{sc}}{|\tau_\mathrm{sc}|}\left(t_\mathrm{m}-\tau_\mathrm{sc}\ln\left(\frac{c_{\tau\mathrm{max,B}}}{\tau}\right)\right)\right)\right].
\end{aligned}
\tag{B.130}
$$

Substituting back in the definition of c_{B1} (Equation B.127) into Equation B.130, then grouping the terms by common time intervals and simplifying:

$$
\begin{aligned}
&\bar{\Omega}_{\mathrm{AAC,B}}(t_\mathrm{m}) = \\
&\left[-\frac{\lambda_\Omega\,\mu_\Omega\,c_\mathrm{BL}}{t_\mathrm{c}}\left(t_\mathrm{m}-\tau_\mathrm{sc}\ln\left(\frac{c_{\tau\mathrm{min,B}}}{\tau}\right)\right)+\frac{c_\mathrm{B2}\,c_{\tau\mathrm{min,B}}}{c_{\tau*,\mathrm{B}}}\right] \\
&\quad\cdot\left[\mathcal{H}\left(\frac{\tau_\mathrm{sc}}{|\tau_\mathrm{sc}|}\left(t_\mathrm{m}-\tau_\mathrm{sc}\ln\left(\frac{c_{\tau\mathrm{min,B}}}{\tau}\right)\right)\right)-\mathcal{H}\left(\frac{\tau_\mathrm{sc}}{|\tau_\mathrm{sc}|}\left(t_\mathrm{m}+t_\mathrm{c}-\tau_\mathrm{sc}\ln\left(\frac{c_{\tau\mathrm{min,B}}}{\tau}\right)\right)\right)\right] \\
&+\left[-\frac{c_\mathrm{B2}}{c_{\tau*,\mathrm{B}}}\tau\exp\left(\frac{t_\mathrm{m}}{\tau_\mathrm{sc}}\right)\right] \\
&\quad\cdot\left[\mathcal{H}\left(\frac{\tau_\mathrm{sc}}{|\tau_\mathrm{sc}|}\left(t_\mathrm{m}-\tau_\mathrm{sc}\ln\left(\frac{c_{\tau\mathrm{min,B}}}{\tau}\right)\right)\right)-\mathcal{H}\left(\frac{\tau_\mathrm{sc}}{|\tau_\mathrm{sc}|}\left(t_\mathrm{m}-\tau_\mathrm{sc}\ln\left(\frac{c_{\tau*,\mathrm{B}}}{\tau}\right)\right)\right)\right] \\
&+\left[\lambda_\Omega\,\mu_\Omega\,c_\mathrm{BL}+\frac{c_\mathrm{B2}}{c_{\tau*,\mathrm{B}}}\tau\exp\left(\frac{t_\mathrm{m}+t_\mathrm{c}}{\tau_\mathrm{sc}}\right)\right] \\
&\quad\cdot\left[\mathcal{H}\left(\frac{\tau_\mathrm{sc}}{|\tau_\mathrm{sc}|}\left(t_\mathrm{m}+t_\mathrm{c}-\tau_\mathrm{sc}\ln\left(\frac{c_{\tau\mathrm{min,B}}}{\tau}\right)\right)\right)-\mathcal{H}\left(\frac{\tau_\mathrm{sc}}{|\tau_\mathrm{sc}|}\left(t_\mathrm{m}+t_\mathrm{c}-\tau_\mathrm{sc}\ln\left(\frac{c_{\tau*,\mathrm{B}}}{\tau}\right)\right)\right)\right] \\
&+\left[\frac{\lambda_\Omega\,\mu_\Omega}{t_\mathrm{c}}\left(c_\mathrm{BL}-c_\mathrm{BU}\right)\left(t_\mathrm{m}-\tau_\mathrm{sc}\ln\left(\frac{c_{\tau*,\mathrm{B}}}{\tau}\right)\right)-2c_\mathrm{B2}\right] \\
&\quad\cdot\left[\mathcal{H}\left(\frac{\tau_\mathrm{sc}}{|\tau_\mathrm{sc}|}\left(t_\mathrm{m}-\tau_\mathrm{sc}\ln\left(\frac{c_{\tau*,\mathrm{B}}}{\tau}\right)\right)\right)-\mathcal{H}\left(\frac{\tau_\mathrm{sc}}{|\tau_\mathrm{sc}|}\left(t_\mathrm{m}+t_\mathrm{c}-\tau_\mathrm{sc}\ln\left(\frac{c_{\tau*,\mathrm{B}}}{\tau}\right)\right)\right)\right] \\
&+\left[\lambda_\Omega\,\mu_\Omega\,c_\mathrm{BU}-\frac{c_\mathrm{B2}}{c_{\tau*,\mathrm{B}}}\tau\exp\left(\frac{t_\mathrm{m}+t_\mathrm{c}}{\tau_\mathrm{sc}}\right)\right] \\
&\quad\cdot\left[\mathcal{H}\left(\frac{\tau_\mathrm{sc}}{|\tau_\mathrm{sc}|}\left(t_\mathrm{m}+t_\mathrm{c}-\tau_\mathrm{sc}\ln\left(\frac{c_{\tau*,\mathrm{B}}}{\tau}\right)\right)\right)-\mathcal{H}\left(\frac{\tau_\mathrm{sc}}{|\tau_\mathrm{sc}|}\left(t_\mathrm{m}+t_\mathrm{c}-\tau_\mathrm{sc}\ln\left(\frac{c_{\tau\mathrm{max,B}}}{\tau}\right)\right)\right)\right] \\
&+\left[\frac{c_\mathrm{B2}}{c_{\tau*,\mathrm{B}}}\tau\exp\left(\frac{t_\mathrm{m}}{\tau_\mathrm{sc}}\right)\right] \\
&\quad\cdot\left[\mathcal{H}\left(\frac{\tau_\mathrm{sc}}{|\tau_\mathrm{sc}|}\left(t_\mathrm{m}-\tau_\mathrm{sc}\ln\left(\frac{c_{\tau*,\mathrm{B}}}{\tau}\right)\right)\right)-\mathcal{H}\left(\frac{\tau_\mathrm{sc}}{|\tau_\mathrm{sc}|}\left(t_\mathrm{m}-\tau_\mathrm{sc}\ln\left(\frac{c_{\tau\mathrm{max,B}}}{\tau}\right)\right)\right)\right] \\
&+\left[\frac{\lambda_\Omega\,\mu_\Omega\,c_\mathrm{BU}}{t_\mathrm{c}}\left(t_\mathrm{m}-\tau_\mathrm{sc}\ln\left(\frac{c_{\tau\mathrm{max,B}}}{\tau}\right)\right)+\frac{c_\mathrm{B2}\,c_{\tau\mathrm{max,B}}}{c_{\tau*,\mathrm{B}}}\right] \\
&\quad\cdot\left[\mathcal{H}\left(\frac{\tau_\mathrm{sc}}{|\tau_\mathrm{sc}|}\left(t_\mathrm{m}-\tau_\mathrm{sc}\ln\left(\frac{c_{\tau\mathrm{max,B}}}{\tau}\right)\right)\right)-\mathcal{H}\left(\frac{\tau_\mathrm{sc}}{|\tau_\mathrm{sc}|}\left(t_\mathrm{m}+t_\mathrm{c}-\tau_\mathrm{sc}\ln\left(\frac{c_{\tau\mathrm{max,B}}}{\tau}\right)\right)\right)\right],
\end{aligned}
\tag{B.131}
$$

where

$$
c_\mathrm{B2}=\frac{\lambda_\Omega\,\mu_\Omega^2\,\tau_\mathrm{sc}}{\beta\,t_\mathrm{c}}. \tag{B.132}
$$

Finally, Equation B.131 can converted from the measurement time (t_m) back to the particle relaxation time (τ) domain using $\mathcal{H}(\tau-\tau_x)=\mathcal{H}\left((\tau_\mathrm{sc}/|\tau_\mathrm{sc}|)\left(t_\mathrm{m}-\tau_\mathrm{sc}\ln\left(c_{\tau x}/\tau\right)\right)\right)$ (Equation 4.39 of the main text) as follows:

$$
\begin{aligned}
\bar{\Omega}_{\mathrm{AAC}}(\tau) = &\left[-\frac{\lambda_\Omega\,\mu_\Omega\,c_{\mathrm{BL}}}{t_\mathrm{c}}\left(t_\mathrm{m}-\tau_\mathrm{sc}\ln\left(\frac{c_{\tau\,\mathrm{min,B}}}{\tau}\right)\right)+\frac{c_{\mathrm{B2}}\,c_{\tau\,\mathrm{min,B}}}{c_{\tau*,\mathrm{B}}}\right]\\
&\quad\cdot\left[\mathcal{H}\left(\tau-\tau_{\mathrm{min,B}}\right)-\mathcal{H}\left(\tau-\tau_{\mathrm{min,B,tc}}\right)\right]\\
&+\left[-\frac{c_{\mathrm{B2}}}{c_{\tau*,\mathrm{B}}}\tau\exp\left(\frac{t_\mathrm{m}}{\tau_\mathrm{sc}}\right)\right]\\
&\quad\cdot\left[\mathcal{H}\left(\tau-\tau_{\mathrm{min,B}}\right)-\mathcal{H}\left(\tau-\tau^*_{\mathrm{sc,B}}\right)\right]\\
&+\left[\lambda_\Omega\,\mu_\Omega\,c_{\mathrm{BL}}+\frac{c_{\mathrm{B2}}}{c_{\tau*,\mathrm{B}}}\tau\exp\left(\frac{t_\mathrm{m}+t_\mathrm{c}}{\tau_\mathrm{sc}}\right)\right]\\
&\quad\cdot\left[\mathcal{H}\left(\tau-\tau_{\mathrm{min,B,tc}}\right)-\mathcal{H}\left(\tau-\tau^*_{\mathrm{sc,B,tc}}\right)\right]\\
&+\left[\frac{\lambda_\Omega\,\mu_\Omega}{t_\mathrm{c}}\left(c_{\mathrm{BL}}-c_{\mathrm{BU}}\right)\left(t_\mathrm{m}-\tau_\mathrm{sc}\ln\left(\frac{c_{\tau*,\mathrm{B}}}{\tau}\right)\right)-2c_{\mathrm{B2}}\right]\\
&\quad\cdot\left[\mathcal{H}\left(\tau-\tau^*_{\mathrm{sc,B}}\right)-\mathcal{H}\left(\tau-\tau^*_{\mathrm{sc,B,tc}}\right)\right]\\
&+\left[\lambda_\Omega\,\mu_\Omega\,c_{\mathrm{BU}}-\frac{c_{\mathrm{B2}}}{c_{\tau*,\mathrm{B}}}\tau\exp\left(\frac{t_\mathrm{m}+t_\mathrm{c}}{\tau_\mathrm{sc}}\right)\right]\\
&\quad\cdot\left[\mathcal{H}\left(\tau-\tau^*_{\mathrm{sc,B,tc}}\right)-\mathcal{H}\left(\tau-\tau_{\mathrm{max,B,tc}}\right)\right]\\
&+\left[\frac{c_{\mathrm{B2}}}{c_{\tau*,\mathrm{B}}}\tau\exp\left(\frac{t_\mathrm{m}}{\tau_\mathrm{sc}}\right)\right]\\
&\quad\cdot\left[\mathcal{H}\left(\tau-\tau^*_{\mathrm{sc,B}}\right)-\mathcal{H}\left(\tau-\tau_{\mathrm{max,B}}\right)\right]\\
&+\left[\frac{\lambda_\Omega\,\mu_\Omega\,c_{\mathrm{BU}}}{t_\mathrm{c}}\left(t_\mathrm{m}-\tau_\mathrm{sc}\ln\left(\frac{c_{\tau\,\mathrm{max,B}}}{\tau}\right)\right)+\frac{c_{\mathrm{B2}}\,c_{\tau\,\mathrm{max,B}}}{c_{\tau*,\mathrm{B}}}\right]\\
&\quad\cdot\left[\mathcal{H}\left(\tau-\tau_{\mathrm{max,B}}\right)-\mathcal{H}\left(\tau-\tau_{\mathrm{max,B,tc}}\right)\right]
\end{aligned}
\tag{B.133}
$$

where τ_x and $\tau_{x,\mathrm{tc}}$ are the same as those derived based on limited trajectory theory (defined by Equations B.43 and B.93, respectively) and are restatements of Equations 4.35 and 4.40 of the main text, respectively. Examples of this average transfer function (i.e. based on Equation B.133) are shown in Figure 4.3 of the main text.

Analytical solution for $\bar{\Omega}_{\mathrm{AAC,B,F1}}$ of Equation B.129

Based on integral form 1 (i.e. $\Omega_{\mathrm{AAC,B,F1}}$) shown in Equation B.128:

$$\begin{aligned}\bar{\Omega}_{\mathrm{AAC,B,F1}} &= \frac{1}{t_c}\int_{t_m}^{t_m+t_c} \Omega_{\mathrm{AAC,B,F1}}\,\mathrm{d}t'_m \\ \bar{\Omega}_{\mathrm{AAC,B,F1}} &= \frac{1}{t_c}\int_{t_m}^{t_m+t_c} \lambda_\Omega\,\mu_\Omega\,c_{\mathrm{B}y}\,\mathcal{H}\left(\frac{\tau_{sc}}{|\tau_{sc}|}\left(t'_m-\tau_{sc}\ln\left(\frac{c_{\tau x,\mathrm{B}}}{\tau}\right)\right)\right)\mathrm{d}t'_m.\end{aligned} \tag{B.134}$$

Assuming τ_{sc} is greater than zero (denoted by $\bar{\Omega}_{\mathrm{AAC,B,F1+}}$), Equation B.134 becomes:

$$\begin{aligned}\bar{\Omega}_{\mathrm{AAC,B,F1+}} &= \frac{1}{t_c}\int_{t_m}^{t_m+t_c} \lambda_\Omega\,\mu_\Omega\,c_{\mathrm{B}y}\,\mathcal{H}\left(t'_m-\tau_{sc}\ln\left(\frac{c_{\tau x,\mathrm{B}}}{\tau}\right)\right)\mathrm{d}t'_m \\ &= \frac{\lambda_\Omega\,\mu_\Omega\,c_{\mathrm{B}y}}{t_c}\left(t'_m-\tau_{sc}\ln\left(\frac{c_{\tau x,\mathrm{B}}}{\tau}\right)\right)\mathcal{H}\left(t'_m-\tau_{sc}\ln\left(\frac{c_{\tau x,\mathrm{B}}}{\tau}\right)\right)\Bigg|_{t_m}^{t_m+t_c} \\ \bar{\Omega}_{\mathrm{AAC,B,F1+}} &= \frac{\lambda_\Omega\,\mu_\Omega\,c_{\mathrm{B}y}}{t_c}\Bigg[\left(t_m+t_c-\tau_{sc}\ln\left(\frac{c_{\tau x,\mathrm{B}}}{\tau}\right)\right)\mathcal{H}\left(t_m+t_c-\tau_{sc}\ln\left(\frac{c_{\tau x,\mathrm{B}}}{\tau}\right)\right) \\ &\qquad -\left(t_m-\tau_{sc}\ln\left(\frac{c_{\tau x,\mathrm{B}}}{\tau}\right)\right)\mathcal{H}\left(t_m-\tau_{sc}\ln\left(\frac{c_{\tau x,\mathrm{B}}}{\tau}\right)\right)\Bigg].\end{aligned} \tag{B.135}$$

As shown in Section B.5.1, this solution (Equation B.135) can be expanded to consider both $\tau_{sc}>0$ and $\tau_{sc}<0$ based on Equation B.121 (i.e. only differ by the inequality sign represented within their Heaviside functions), and thus both cases can be represented using one equation as follows:

$$\begin{aligned}\bar{\Omega}_{\mathrm{AAC,B,F1}} = \frac{\lambda_\Omega\,\mu_\Omega\,c_{\mathrm{B}y}}{t_c}\Bigg[&\left(t_m+t_c-\tau_{sc}\ln\left(\frac{c_{\tau x,\mathrm{B}}}{\tau}\right)\right)\mathcal{H}\left(\frac{\tau_{sc}}{|\tau_{sc}|}\left(t_m+t_c-\tau_{sc}\ln\left(\frac{c_{\tau x,\mathrm{B}}}{\tau}\right)\right)\right) \\ &-\left(t_m-\tau_{sc}\ln\left(\frac{c_{\tau x,\mathrm{B}}}{\tau}\right)\right)\mathcal{H}\left(\frac{\tau_{sc}}{|\tau_{sc}|}\left(t_m-\tau_{sc}\ln\left(\frac{c_{\tau x,\mathrm{B}}}{\tau}\right)\right)\right)\Bigg].\end{aligned} \tag{B.136}$$

Analytical solution for $\bar{\Omega}_{\mathrm{AAC,B,F2}}$ of Equation B.129

Based on integral form 2 (i.e. $\Omega_{\mathrm{AAC,B,F2}}$) shown in Equation B.128:

$$\begin{aligned}\bar{\Omega}_{\mathrm{AAC,B,F2}} &= \frac{1}{t_\mathrm{c}}\int_{t_\mathrm{m}}^{t_\mathrm{m}+t_\mathrm{c}} \Omega_{\mathrm{AAC,B,F2}}\,\mathrm{d}t'_\mathrm{m} \\ \bar{\Omega}_{\mathrm{AAC,B,F2}} &= \frac{1}{t_\mathrm{c}}\int_{t_\mathrm{m}}^{t_\mathrm{m}+t_\mathrm{c}} \lambda_\Omega\,\mu_\Omega\,c_{\mathrm{B}w}\,\tau \exp\left(\frac{t_\mathrm{m}}{\tau_\mathrm{sc}}\right)\mathcal{H}\left(\frac{\tau_\mathrm{sc}}{|\tau_\mathrm{sc}|}\left(t'_\mathrm{m}-\tau_\mathrm{sc}\ln\left(\frac{c_{\tau x,\mathrm{B}}}{\tau}\right)\right)\right)\mathrm{d}t'_\mathrm{m}.\end{aligned} \tag{B.137}$$

Assuming τ_sc is greater than zero (denoted by $\bar{\Omega}_{\mathrm{AAC,B,F2+}}$), Equation B.137 becomes:

$$\bar{\Omega}_{\mathrm{AAC,B,F2+}} = \frac{\lambda_\Omega\,\mu_\Omega\,c_{\mathrm{B}w}\,\tau}{t_\mathrm{c}}\int_{t_\mathrm{m}}^{t_\mathrm{m}+t_\mathrm{c}} \exp\left(\frac{t'_\mathrm{m}}{\tau_\mathrm{sc}}\right)\mathcal{H}\left(t'_\mathrm{m}-\tau_\mathrm{sc}\ln\left(\frac{c_{\tau x,\mathrm{B}}}{\tau}\right)\right)\mathrm{d}t'_\mathrm{m}. \tag{B.138}$$

Apply integration by parts to Equation B.138 as follows:

$$\begin{aligned} u = \mathcal{H}\left(t'_\mathrm{m}-\tau_\mathrm{sc}\ln\left(\frac{c_{\tau x,\mathrm{B}}}{\tau}\right)\right) &\rightarrow \mathrm{d}u = \delta\left(t'_\mathrm{m}-\tau_\mathrm{sc}\ln\left(\frac{c_{\tau x,\mathrm{B}}}{\tau}\right)\right)\mathrm{d}t'_\mathrm{m} \\ \mathrm{d}v = \exp\left(\frac{t'_\mathrm{m}}{\tau_\mathrm{sc}}\right)\mathrm{d}t'_\mathrm{m} &\rightarrow v = \tau_\mathrm{sc}\exp\left(\frac{t'_\mathrm{m}}{\tau_\mathrm{sc}}\right),\end{aligned} \tag{B.139}$$

where δ Dirac delta function defined in Equation B.102. Therefore, using integration by parts based on Equation B.139, Equation B.138 becomes:

$$\begin{aligned}\bar{\Omega}_{\mathrm{AAC,B,F2+}} = \frac{\lambda_\Omega\,\mu_\Omega\,c_{\mathrm{B}w}\,\tau}{t_\mathrm{c}}\Bigg[&\tau_\mathrm{sc}\exp\left(\frac{t'_\mathrm{m}}{\tau_\mathrm{sc}}\right)\mathcal{H}\left(t'_\mathrm{m}-\tau_\mathrm{sc}\ln\left(\frac{c_{\tau x,\mathrm{B}}}{\tau}\right)\right)\Bigg|_{t_\mathrm{m}}^{t_\mathrm{m}+t_\mathrm{c}} \\ &-\int_{t_\mathrm{m}}^{t_\mathrm{m}+t_\mathrm{c}}\tau_\mathrm{sc}\exp\left(\frac{t'_\mathrm{m}}{\tau_\mathrm{sc}}\right)\delta\left(t'_\mathrm{m}-\tau_\mathrm{sc}\ln\left(\frac{c_{\tau x,\mathrm{B}}}{\tau}\right)\right)\mathrm{d}t'_\mathrm{m}\Bigg].\end{aligned} \tag{B.140}$$

Furthermore, noting that $\delta\left(t'_\mathrm{m}-\tau_\mathrm{sc}\ln\left(\frac{c_{\tau x,\mathrm{B}}}{\tau}\right)\right)$ vanishes everywhere except $t'_\mathrm{m}=\tau_\mathrm{sc}\ln\left(\frac{c_{\tau x,\mathrm{B}}}{\tau}\right)$, Equation B.140 becomes:

$$\begin{aligned}\bar{\Omega}_{\mathrm{AAC,B,F2+}} &= \frac{\lambda_\Omega\,\mu_\Omega\,c_{\mathrm{B}w}\,\tau}{t_\mathrm{c}}\left[\tau_\mathrm{sc}\exp\left(\frac{t'_\mathrm{m}}{\tau_\mathrm{sc}}\right)\mathcal{H}\left(t'_\mathrm{m}-\tau_\mathrm{sc}\ln\left(\frac{c_{\tau x,\mathrm{B}}}{\tau}\right)\right)\Bigg|_{t_\mathrm{m}}^{t_\mathrm{m}+t_\mathrm{c}}\right.\\ &\qquad\left.-\tau_\mathrm{sc}\exp\left(\frac{\tau_\mathrm{sc}\ln\left(\frac{c_{\tau x,\mathrm{B}}}{\tau}\right)}{\tau_\mathrm{sc}}\right)\int_{t_\mathrm{m}}^{t_\mathrm{m}+t_\mathrm{c}}\delta\left(t'_\mathrm{m}-\tau_\mathrm{sc}\ln\left(\frac{c_{\tau x,\mathrm{B}}}{\tau}\right)\right)\mathrm{d}t'_\mathrm{m}\right]\\ &= \frac{\lambda_\Omega\,\mu_\Omega\,c_{\mathrm{B}w}\,\tau}{t_\mathrm{c}}\left(\tau_\mathrm{sc}\exp\left(\frac{t'_\mathrm{m}}{\tau_\mathrm{sc}}\right)-\frac{\tau_\mathrm{sc}\,c_{\tau x,\mathrm{B}}}{\tau}\right)\mathcal{H}\left(t'_\mathrm{m}-\tau_\mathrm{sc}\ln\left(\frac{c_{\tau x,\mathrm{B}}}{\tau}\right)\right)\Bigg|_{t_\mathrm{m}}^{t_\mathrm{m}+t_\mathrm{c}}\\ \bar{\Omega}_{\mathrm{AAC,B,F2+}} &= \frac{\lambda_\Omega\,\mu_\Omega\,c_{\mathrm{B}w}\,\tau_\mathrm{sc}}{t_\mathrm{c}}\tau\left[\left(\exp\left(\frac{t_\mathrm{m}+t_\mathrm{c}}{\tau_\mathrm{sc}}\right)-\frac{c_{\tau x,\mathrm{B}}}{\tau}\right)\mathcal{H}\left(t_\mathrm{m}+t_\mathrm{c}-\tau_\mathrm{sc}\ln\left(\frac{c_{\tau x,\mathrm{B}}}{\tau}\right)\right)\right.\\ &\qquad\left.-\left(\exp\left(\frac{t_\mathrm{m}}{\tau_\mathrm{sc}}\right)-\frac{c_{\tau x,\mathrm{B}}}{\tau}\right)\mathcal{H}\left(t_\mathrm{m}-\tau_\mathrm{sc}\ln\left(\frac{c_{\tau x,\mathrm{B}}}{\tau}\right)\right)\right].\end{aligned} \tag{B.141}$$

As shown in Section B.5.1, this solution (Equation B.141) can be expanded to consider both $\tau_\mathrm{sc}>0$ and $\tau_\mathrm{sc}<0$ based on Equation B.121 (i.e. only differ by the inequality sign represented within their Heaviside functions), and thus both cases can be represented using one equation as follows:

$$\begin{aligned}&\bar{\Omega}_{\mathrm{AAC,B,F2}} =\\ &\frac{\lambda_\Omega\,\mu_\Omega\,c_{\mathrm{B}w}\,\tau_\mathrm{sc}}{t_\mathrm{c}}\tau\left[\left(\exp\left(\frac{t_\mathrm{m}+t_\mathrm{c}}{\tau_\mathrm{sc}}\right)-\frac{c_{\tau x,\mathrm{B}}}{\tau}\right)\mathcal{H}\left(\frac{\tau_\mathrm{sc}}{|\tau_\mathrm{sc}|}\left(t_\mathrm{m}+t_\mathrm{c}-\tau_\mathrm{sc}\ln\left(\frac{c_{\tau x,\mathrm{B}}}{\tau}\right)\right)\right)\right.\\ &\qquad\left.-\left(\exp\left(\frac{t_\mathrm{m}}{\tau_\mathrm{sc}}\right)-\frac{c_{\tau x,\mathrm{B}}}{\tau}\right)\mathcal{H}\left(\frac{\tau_\mathrm{sc}}{|\tau_\mathrm{sc}|}\left(t_\mathrm{m}-\tau_\mathrm{sc}\ln\left(\frac{c_{\tau x,\mathrm{B}}}{\tau}\right)\right)\right)\right].\end{aligned} \tag{B.142}$$

B.7 Parameters of scanning AAC: uniform axial flow

Note: Similar to the other sections in this appendix, this section and its subsections use simplified notation of the parameter subscripts, as outlined in Section B.1, based on the common AAC operation and theory instances included within the title and header of this section.

B.7.1 Average setpoint of scanning AAC over t_c

Similar to the definition of the average transfer function of the scanning AAC (i.e. Equation 4.33 of the main text), the average particle relaxation setpoint of the AAC ($\bar{\tau}^*_{sc}$) over the counting time (t_c) of the downstream particle detector can be found by[1] (restatement of Equation 4.43 in main text):

$$\bar{\tau}^*_{sc} = \frac{1}{t_c}\int_{t_m}^{t_m+t_c} \tau^*_{sc}(t'_m)\,dt'_m. \tag{B.143}$$

Furthermore, the form of τ^*_{sc} based on limited trajectory or particle streamline theory is the same ($c_{\tau*}\exp(-t_m/\tau_{sc})$) as shown by Equations B.50 and B.78, respectively, and summarized in Table 4.2 of the main text. Therefore, substituting this consistent form into Equation B.143:

$$\bar{\tau}^*_{sc} = \frac{1}{t_c}\int_{t_m}^{t_m+t_c} c_{\tau*}\exp\left(\frac{-t'_m}{\tau_{sc}}\right)dt'_m, \tag{B.144}$$

and letting:

$$u = \frac{-t'_m}{\tau_{sc}} \rightarrow du = \frac{-1}{\tau_{sc}}dt'_m \rightarrow dt'_m = -\tau_{sc}\,du, \tag{B.145}$$

becomes:

$$\begin{aligned}\bar{\tau}^*_{sc} &= \frac{-\tau_{sc}\,c_{\tau*}}{t_c}\int \exp(u)\,du = \frac{-\tau_{sc}\,c_{\tau*}}{t_c}\exp\left(\frac{-t'_m}{\tau_{sc}}\right)\Bigg|_{t_m}^{t_m+t_c}\\ \bar{\tau}^*_{sc} &= \frac{-c_{\tau*}\,\tau_{sc}}{t_c}\left[\exp\left(\frac{-(t_m+t_c)}{\tau_{sc}}\right)-\exp\left(\frac{-t_m}{\tau_{sc}}\right)\right].\end{aligned} \tag{B.146}$$

As previously stated, this solution (i.e. Equation B.146) applies to both limited trajectory and particle streamline theory as the form of τ^*_{sc} based on either theory is the same ($c_{\tau*}\exp(-t_m/\tau_{sc})$).

B.7.2 Classes per decade of AAC scan

The definition of $\mathrm{CPD_{sc}}$ (i.e. Equation 4.44 of main text) can be simplified by considering the particle relaxation setpoints ($\bar{\tau}^*_{\mathrm{sc},1}$ and $\bar{\tau}^*_{\mathrm{sc},2}$) between two consecutive measurements (i.e. $t_{\mathrm{m2}} = t_{\mathrm{m1}} + t_{\mathrm{c}}$) as follows:

$$\mathrm{CPD_{sc}} = \frac{2-1}{\left|\log\left(\bar{\tau}^*_{\mathrm{sc},2}\right) - \log\left(\bar{\tau}^*_{\mathrm{sc},1}\right)\right|} = \frac{1}{\left|\log\left(\frac{\bar{\tau}^*_{\mathrm{sc},2}}{\bar{\tau}^*_{\mathrm{sc},1}}\right)\right|}. \tag{B.147}$$

Therefore, the CPD of the measurements collected by the scanning AAC can be determined by the ratio of particle relaxation setpoints between two consecutive measurements. Furthermore, the form of $\bar{\tau}^*_{\mathrm{sc}}$ based on limited trajectory or particle streamline theory is the same as shown in Section B.7.1 and summarized in Table 4.4 of the main text. Therefore, the ratio of $\bar{\tau}^*_{\mathrm{sc}}$ at consecutive measurement times can be found based on the definition of $\bar{\tau}^*_{\mathrm{sc}}$ (i.e. Equation B.146) as follows:

$$\begin{aligned}
\frac{\bar{\tau}^*_{\mathrm{sc},2}}{\bar{\tau}^*_{\mathrm{sc},1}} &= \frac{\frac{-c_{\tau*}\,\tau_{\mathrm{sc}}}{t_{\mathrm{c}}}\left[\exp\left(\frac{-(t_{\mathrm{m2}}+t_{\mathrm{c}})}{\tau_{\mathrm{sc}}}\right) - \exp\left(\frac{-t_{\mathrm{m2}}}{\tau_{\mathrm{sc}}}\right)\right]}{\frac{-c_{\tau*}\,\tau_{\mathrm{sc}}}{t_{\mathrm{c}}}\left[\exp\left(\frac{-(t_{\mathrm{m1}}+t_{\mathrm{c}})}{\tau_{\mathrm{sc}}}\right) - \exp\left(\frac{-t_{\mathrm{m1}}}{\tau_{\mathrm{sc}}}\right)\right]} \\
&= \frac{\left[\exp\left(\frac{-(t_{\mathrm{m1}}+t_{\mathrm{c}}+t_{\mathrm{c}})}{\tau_{\mathrm{sc}}}\right) - \exp\left(\frac{-(t_{\mathrm{m1}}+t_{\mathrm{c}})}{\tau_{\mathrm{sc}}}\right)\right]}{\left[\exp\left(\frac{-(t_{\mathrm{m1}}+t_{\mathrm{c}})}{\tau_{\mathrm{sc}}}\right) - \exp\left(\frac{-t_{\mathrm{m1}}}{\tau_{\mathrm{sc}}}\right)\right]} \\
\frac{\bar{\tau}^*_{\mathrm{sc},2}}{\bar{\tau}^*_{\mathrm{sc},1}} &= \exp\left(\frac{-t_{\mathrm{c}}}{\tau_{\mathrm{sc}}}\right).
\end{aligned} \tag{B.148}$$

Substituting Equation B.148 into Equation B.147, the classes per decade of the measurements collected by the scanning AAC is:

$$\mathrm{CPD_{sc}} = \frac{1}{\left|\log\left(\exp\left(\frac{-t_{\mathrm{c}}}{\tau_{\mathrm{sc}}}\right)\right)\right|}. \tag{B.149}$$

As previously stated, this solution (i.e. Equation B.149) applies to both limited trajectory and particle streamline theory as the the form of $\bar{\tau}^*_{\mathrm{sc}}$ based on either theory is the same as shown in Section B.7.1 and summarized in Table 4.4 of the main text.

B.7.3 Range of AAC scan

The range of particle relaxation times measured by the scanning AAC is smaller than the steady-state AAC due to the residence time of particles in the classifier (t_f). Measurements cannot be collected until the particles at the classifier inlet at the start of the scan pass through the classifier (i.e. $t_m = t_f$). Furthermore, measurements can only be collected for particles that experience the changing centrifugal force field during their entire residence time within the classifier. Therefore, measurements cannot be collected for particles at the classifier outlet after the scan duration (i.e $t_m = t_{sc}$).

As shown in the following subsections (Sections B.7.3 and B.7.3), the ratio of $\bar{\tau}^*_{sc}$ to τ^*_{ss} based on limited trajectory or particle streamline theory is the same (Equations B.154 or B.158, respectively) as follows:

$$\frac{\bar{\tau}^*_{sc}}{\tau^*_{ss}} = \frac{-\omega^2 t_f}{\omega_S^2 t_c \left[1 - \exp\left(\frac{-t_f}{\tau_{sc}}\right)\right]} \left[\exp\left(\frac{-(t_m + t_c)}{\tau_{sc}}\right) - \exp\left(\frac{-t_m}{\tau_{sc}}\right)\right]. \tag{B.150}$$

At the start of the scan, $\omega = \omega_S$ and $t_m = t_f$, substituting these values into Equation B.150 to determine the offset between the setpoints of the scanning and steady-state AAC:

$$\begin{aligned} \frac{\bar{\tau}^*_{sc}}{\tau^*_{ss}}\bigg|_S &= \frac{-\omega_S^2 t_f}{\omega_S^2 t_c \left[1 - \exp\left(\frac{-t_f}{\tau_{sc}}\right)\right]} \left[\exp\left(\frac{-(t_f + t_c)}{\tau_{sc}}\right) - \exp\left(\frac{-t_f}{\tau_{sc}}\right)\right] \\ \frac{\bar{\tau}^*_{sc}}{\tau^*_{ss}}\bigg|_S &= \frac{-t_f}{t_c \left[\exp\left(\frac{t_f}{\tau_{sc}}\right) - 1\right]} \left[\exp\left(\frac{-t_c}{\tau_{sc}}\right) - 1\right]. \end{aligned} \tag{B.151}$$

At the end of the scan, $\omega = \omega_E$ and $t_m = t_{sc}$, substituting these values into Equation B.150 to determine the offset between the setpoints of the scanning and steady-state AAC:

$$\begin{aligned} \frac{\bar{\tau}^*_{sc}}{\tau^*_{ss}}\bigg|_E &= \frac{-\omega_E^2 t_f}{\omega_S^2 t_c \left[1 - \exp\left(\frac{-t_f}{\tau_{sc}}\right)\right]} \left[\exp\left(\frac{-(t_{sc} + t_c)}{\tau_{sc}}\right) - \exp\left(\frac{-t_{sc}}{\tau_{sc}}\right)\right] \\ \frac{\bar{\tau}^*_{sc}}{\tau^*_{ss}}\bigg|_E &= \frac{-\omega_E^2 t_f}{\omega_S^2 t_c \exp\left(\frac{t_{sc} - t_f}{\tau_{sc}}\right) \left[\exp\left(\frac{t_f}{\tau_{sc}}\right) - 1\right]} \left[\exp\left(\frac{-t_c}{\tau_{sc}}\right) - 1\right]. \end{aligned} \tag{B.152}$$

Limited trajectory

Taking the ratio of $\bar{\tau}^*_{sc}$ (Equation B.146) to τ^*_{ss} (Equation B.34) for the scanning and steady-state AAC setpoints based on limited trajectory theory, respectively, then substituting in the definition for $c_{\tau*}$ (i.e. Equation B.52) becomes:

$$\frac{\bar{\tau}^*_{sc}}{\tau^*_{ss}} = \frac{\frac{-\tau_{sc}}{t_c}\left[\exp\left(\frac{-(t_m+t_c)}{\tau_{sc}}\right)-\exp\left(\frac{-t_m}{\tau_{sc}}\right)\right]\frac{1}{2c_{sc}}\left[\ln\left(\frac{r_2}{r_1}\right)+\frac{1}{2}\ln\left(\frac{Q_a+Q_{sh}-Q_s\left(1-r_1^2/r_2^2\right)}{Q_a+Q_{sh}-Q_{sh}\left(1-r_1^2/r_2^2\right)}\right)\right]}{\frac{1}{2K_{ss}}\left[\ln\left(\frac{r_2}{r_1}\right)+\frac{1}{2}\ln\left(\frac{Q_a+Q_{sh}-Q_s\left(1-r_1^2/r_2^2\right)}{Q_a+Q_{sh}-Q_{sh}\left(1-r_1^2/r_2^2\right)}\right)\right]}. \tag{B.153}$$

Finally, substituting the definitions of K_{ss} and c_{sc} (i.e. Equations B.18 and B.45, respectively) into Equation B.153, and simplifying:

$$\begin{aligned}
\frac{\bar{\tau}^*_{sc}}{\tau^*_{ss}} &= \frac{\omega^2 t_f}{\omega_S^2\,\tau_{sc}\left[1-\exp\left(\frac{-t_f}{\tau_{sc}}\right)\right]}\frac{-\tau_{sc}}{t_c}\left[\exp\left(\frac{-(t_m+t_c)}{\tau_{sc}}\right)-\exp\left(\frac{-t_m}{\tau_{sc}}\right)\right] \\
\frac{\bar{\tau}^*_{sc}}{\tau^*_{ss}} &= \frac{-\omega^2 t_f}{\omega_S^2\,t_c\left[1-\exp\left(\frac{-t_f}{\tau_{sc}}\right)\right]}\left[\exp\left(\frac{-(t_m+t_c)}{\tau_{sc}}\right)-\exp\left(\frac{-t_m}{\tau_{sc}}\right)\right].
\end{aligned} \tag{B.154}$$

Particle streamline

Similar to the derivation based on limited trajectory theory in the previous Section (B.7.3), taking the ratio of $\bar{\tau}^*_{sc,B}$ (Equation B.146) to $\tau^*_{ss,B}$ (Equation B.72) for the scanning and steady-state AAC setpoints based on particle streamline theory, respectively:

$$\frac{\bar{\tau}^*_{sc,B}}{\tau^*_{ss,B}} = \frac{\frac{-c_{\tau*,B}\,\tau_{sc}}{t_c}\left[\exp\left(\frac{-(t_m+t_c)}{\tau_{sc}}\right) - \exp\left(\frac{-t_m}{\tau_{sc}}\right)\right]}{\frac{2Q_{sh}}{\pi\omega^2(r_1+r_2)^2L}}. \tag{B.155}$$

Substituting the definition of $c_{\tau*,B}$ (Equation B.79) into Equation B.155:

$$\begin{aligned}
\frac{\bar{\tau}^*_{sc,B}}{\tau^*_{ss,B}} &= \frac{\frac{-\tau_{sc}}{t_c}\left[\exp\left(\frac{-(t_m+t_c)}{\tau_{sc}}\right) - \exp\left(\frac{-t_m}{\tau_{sc}}\right)\right]\frac{1}{c_{sc}}\frac{2\left(r_2^2-r_1^2\right)}{(\beta+1)(r_1+r_2)^2}}{\frac{2Q_{sh}}{\pi\omega^2(r_1+r_2)^2L}} \\
\frac{\bar{\tau}^*_{sc,B}}{\tau^*_{ss,B}} &= \frac{-\tau_{sc}}{t_c}\left[\exp\left(\frac{-(t_m+t_c)}{\tau_{sc}}\right) - \exp\left(\frac{-t_m}{\tau_{sc}}\right)\right]\frac{\pi\omega^2(r_2^2-r_1^2)L}{c_{sc}\,Q_{sh}(\beta+1)}.
\end{aligned} \tag{B.156}$$

Substituting the definitions of β and c_{sc} (i.e. Equations B.70 and B.80, respectively) into Equation B.156, and simplifying:

$$\begin{aligned}
\frac{\bar{\tau}^*_{sc,B}}{\tau^*_{ss,B}} &= \frac{-\tau_{sc}}{t_c}\left[\exp\left(\frac{-(t_m+t_c)}{\tau_{sc}}\right) - \exp\left(\frac{-t_m}{\tau_{sc}}\right)\right]\frac{1}{\omega_S^2\,\tau_{sc}\left[1-\exp\left(\frac{-t_f}{\tau_{sc}}\right)\right]}\frac{\pi\omega^2(r_2^2-r_1^2)L}{Q_{sh}(\frac{Q_a}{Q_{sh}}+1)} \\
\frac{\bar{\tau}^*_{sc,B}}{\tau^*_{ss,B}} &= \frac{-\omega^2}{\omega_S^2\,t_c\left[1-\exp\left(\frac{-t_f}{\tau_{sc}}\right)\right]}\left[\exp\left(\frac{-(t_m+t_c)}{\tau_{sc}}\right) - \exp\left(\frac{-t_m}{\tau_{sc}}\right)\right]\frac{\pi(r_2^2-r_1^2)L}{Q_a+Q_{sh}}.
\end{aligned} \tag{B.157}$$

Finally, substituting in the definition of t_f (Equation 4.12 of main text) into Equation B.157:

$$\frac{\bar{\tau}^*_{sc,B}}{\tau^*_{ss,B}} = \frac{-\omega^2\,t_f}{\omega_S^2\,t_c\left[1-\exp\left(\frac{-t_f}{\tau_{sc}}\right)\right]}\left[\exp\left(\frac{-(t_m+t_c)}{\tau_{sc}}\right) - \exp\left(\frac{-t_m}{\tau_{sc}}\right)\right]. \tag{B.158}$$

B.8 Inversion of transfer function of scanning AAC

Note: Similar to the other sections in this appendix, this section and its subsections use simplified notation of the parameter subscripts, as outlined in Section B.1, based on the common AAC operation and theory instances included within the title and header of this section.

Similar to the process developed by Stolzenburg and McMurry [229] for the steady-state DMA, by Wang and Flagan [261] for the scanning DMA or in Section A.2 for the steady-state AAC, the particle number concentration (N_{det}) that passes through the scanning AAC at time t_i can be determined from:

$$N_{\text{det}}(t_i) = \int \eta(\tau)\, \bar{\Omega}_{\text{AAC}}(\tau, t_i)\, \mathrm{d}N(\tau), \tag{B.159}$$

where $\eta(\tau)$ is the counting efficiency of the downstream particle detector and $N(\tau)$ is the particle number concentration of the aerosol source at particle relaxation time τ, while $\bar{\Omega}(\tau, t_i)$ is the average transfer function of the scanning AAC over the counting time of the particle detector at time t_i. Using the same conversion for $\mathrm{d}N(\tau)$ to $\mathrm{d}N(\tau)/\mathrm{d}\log\tau$ derived in Section A.2 of Chapter A and substituting it (Equation A.32) into Equation B.159, and assuming η and $\mathrm{d}N(\tau)/\mathrm{d}\log\tau$ are constant[3] over the width of $\bar{\Omega}_{\text{AAC}}$ simplifies to:

$$\begin{aligned} N_{\text{det}}(t_i) &= \int \eta(\tau)\, \bar{\Omega}_{\text{AAC}}(\tau, t_i) \frac{\mathrm{d}N(\tau)}{\mathrm{d}\log\tau} \frac{1}{\ln(10)} \frac{1}{\tau} \mathrm{d}\tau \\ N_{\text{det}}(t_i) &= \eta(\bar{\tau}^*_{\text{sc},i}) \left.\frac{\mathrm{d}N(\tau)}{\mathrm{d}\log\tau}\right|_{\bar{\tau}^*_{\text{sc},i}} \frac{1}{\ln(10)} \int \frac{\bar{\Omega}_{\text{AAC}}(\tau, t_i)}{\tau} \mathrm{d}\tau. \end{aligned} \tag{B.160}$$

Since the AAC transfer function is centered around $\bar{\tau}^*_{\text{sc},i}$ at time t_i in the scan, this value is used to estimate the constants (i.e. η and $\mathrm{d}N(\tau)/\mathrm{d}\log\tau$). Isolating the spectral density in terms of particle relaxation time (i.e. $\mathrm{d}N/\mathrm{d}\log\tau$) classified at time t_i by the scanning AAC from Equation B.160:

$$\left.\frac{\mathrm{d}N(\tau)}{\mathrm{d}\log\tau}\right|_{\bar{\tau}^*_{\text{sc},i}} = \frac{N_{\text{det}}(t_i) \ln(10)}{\eta(\bar{\tau}^*_{\text{sc},i})\, \beta^*_{\text{sc},i}}, \tag{B.161}$$

where $\beta^*_{\text{sc},i}$ is the non-dimensional deconvolution parameter of the transfer function of the scanning AAC at time t_i as follows:

[3] This assumption that the aerosol concentration (N) is constant over the width of the AAC transfer function is valid if the AAC classification is operated with a sufficiently high resolution and the particle detector is operated with a sufficiently low counting time.

$$\beta^*_{\mathrm{sc},i} = \int \frac{\bar{\Omega}_{\mathrm{AAC}}(\tau, t_i)}{\tau} \mathrm{d}\tau. \tag{B.162}$$

The spectral density of the aerosol can also be found in terms of aerodynamic diameter (i.e. $\mathrm{d}N/\mathrm{d}\log d_{\mathrm{a}}$) by applying the chain rule to Equation B.161 as follows:

$$\frac{\mathrm{d}N}{\mathrm{d}\log d_{\mathrm{a}}} = \frac{\mathrm{d}N}{\mathrm{d}\log \tau} \frac{\mathrm{d}\log \tau}{\mathrm{d}\log d_{\mathrm{a}}}, \tag{B.163}$$

where $\mathrm{d}\log \tau/\mathrm{d}\log d_{\mathrm{a}}$ was previously determined in Section A.4 of Appendix A, specifically Equation A.49.

B.9 Deconvolution parameter ($\beta^*_{sc,LT}$) of scanning AAC: limited trajectory, idealized & uniform axial flow

Note: Similar to the other sections in this appendix, this section and its subsections use simplified notation of the parameter subscripts, as outlined in Section B.1, based on the common AAC operation and theory instances included within the title and header of this section.

Substituting the definition of $\bar{\Omega}_{AAC}$ based on limited trajectory theory (Equation B.92) into the definition of the β^*_{sc} (Equation B.162) and organizing into separate integrals by the ranges of particle relaxation times becomes:

$$
\begin{aligned}
\beta^*_{\mathrm{sc,LT}} &= \int \frac{\bar{\Omega}_{\mathrm{AAC,LT}}(\tau, t)}{\tau}\mathrm{d}\tau \\
\beta^*_{\mathrm{sc,LT}} &= \underbrace{\int_{\tau_{\min}}^{\tau_{\min,\mathrm{tc}}} \frac{1}{\tau}\left[\frac{c_{f11}\,\tau_{\mathrm{sc}}}{t_{\mathrm{c}}}\mathcal{EI}\left(c_{\tau\min}\,c_{f12}\right) - \frac{c_{f13}}{t_{\mathrm{c}}}\left(t_{\mathrm{m}} - \tau_{\mathrm{sc}}\ln\left(\frac{c_{\tau\min}}{\tau}\right)\right)\right]\mathrm{d}\tau}_{\beta^*_{\mathrm{sc,LT,1}}} \\
&\quad + \underbrace{\int_{\tau_{\min}}^{\tau_{13}} \frac{1}{\tau}\left[-\frac{c_{f11}\,\tau_{\mathrm{sc}}}{t_{\mathrm{c}}}\mathcal{EI}\left(c_{f12}\,\tau\exp\left(\frac{t_{\mathrm{m}}}{\tau_{\mathrm{sc}}}\right)\right)\right]\mathrm{d}\tau}_{\beta^*_{\mathrm{sc,LT,2}}} \\
&\quad + \underbrace{\int_{\tau_{\min,\mathrm{tc}}}^{\tau_{13,\mathrm{tc}}} \frac{1}{\tau}\left[\frac{c_{f11}\,\tau_{\mathrm{sc}}}{t_{\mathrm{c}}}\mathcal{EI}\left(c_{f12}\,\tau\exp\left(\frac{t_{\mathrm{m}}+t_{\mathrm{c}}}{\tau_{\mathrm{sc}}}\right)\right) + c_{f13}\right]\mathrm{d}\tau}_{\beta^*_{\mathrm{sc,LT,3}}} \\
&\quad + \underbrace{\int_{\tau_{13}}^{\tau_{13,\mathrm{tc}}} \frac{1}{\tau}\left[-\frac{c_{f11}\,\tau_{\mathrm{sc}}}{t_{\mathrm{c}}}\mathcal{EI}\left(c_{\tau13}\,c_{f12}\right) + \left(\frac{c_{f13}}{t_{\mathrm{c}}} - \frac{c_{f31}}{t_{\mathrm{c}}}\right)\left(t_{\mathrm{m}} - \tau_{\mathrm{sc}}\ln\left(\frac{c_{\tau13}}{\tau}\right)\right)\right]\mathrm{d}\tau}_{\beta^*_{\mathrm{sc,LT,4}}} \\
&\quad + \underbrace{\int_{\tau_{13,\mathrm{tc}}}^{\tau_{23,\mathrm{tc}}} \frac{c_{f31}}{\tau}\mathrm{d}\tau}_{\beta^*_{\mathrm{sc,LT,5}}} \\
&\quad + \underbrace{\int_{\tau_{23}}^{\tau_{23,\mathrm{tc}}} \frac{1}{\tau}\left[\frac{c_{f21}\,\tau_{\mathrm{sc}}}{t_{\mathrm{c}}}\mathcal{EI}\left(c_{\tau23}\,c_{f22}\right) + \left(\frac{c_{f31}}{t_{\mathrm{c}}} - \frac{c_{f23}}{t_{\mathrm{c}}}\right)\left(t_{\mathrm{m}} - \tau_{\mathrm{sc}}\ln\left(\frac{c_{\tau23}}{\tau}\right)\right)\right]\mathrm{d}\tau}_{\beta^*_{\mathrm{sc,LT,6}}} \\
&\quad + \underbrace{\int_{\tau_{23,\mathrm{tc}}}^{\tau_{\max,\mathrm{tc}}} \frac{1}{\tau}\left[\frac{c_{f21}\,\tau_{\mathrm{sc}}}{t_{\mathrm{c}}}\mathcal{EI}\left(c_{f22}\,\tau\exp\left(\frac{t_{\mathrm{m}}+t_{\mathrm{c}}}{\tau_{\mathrm{sc}}}\right)\right) + c_{f23}\right]\mathrm{d}\tau}_{\beta^*_{\mathrm{sc,LT,7}}} \\
&\quad + \underbrace{\int_{\tau_{23}}^{\tau_{\max}} \frac{1}{\tau}\left[-\frac{c_{f21}\,\tau_{\mathrm{sc}}}{t_{\mathrm{c}}}\mathcal{EI}\left(c_{f22}\,\tau\exp\left(\frac{t_{\mathrm{m}}}{\tau_{\mathrm{sc}}}\right)\right)\right]\mathrm{d}\tau}_{\beta^*_{\mathrm{sc,LT,8}}} \\
&\quad + \underbrace{\int_{\tau_{\max}}^{\tau_{\max,\mathrm{tc}}} \frac{1}{\tau}\left[-\frac{c_{f21}\,\tau_{\mathrm{sc}}}{t_{\mathrm{c}}}\mathcal{EI}\left(c_{\tau\max}\,c_{f22}\right) + \frac{c_{f23}}{t_{\mathrm{c}}}\left(t_{\mathrm{m}} - \tau_{\mathrm{sc}}\ln\left(\frac{c_{\tau\max}}{\tau}\right)\right)\right]\mathrm{d}\tau}_{\beta^*_{\mathrm{sc,LT,9}}}.
\end{aligned}
\tag{B.164}
$$

All of the terms in Equation B.164 consist of different combinations of the following three integral forms:

$$
\beta^*_{\mathrm{sc,LT,F1}} = \int_{\tau_{\mathrm{L}}}^{\tau_{\mathrm{U}}} \frac{a}{\tau}\mathrm{d}\tau, \tag{B.165}
$$

$$\beta^*_{sc,LT,F2} = \int_{\tau_L}^{\tau_U} \frac{a \ln\left(\frac{b}{\tau}\right)}{\tau} d\tau, \tag{B.166}$$

$$\beta^*_{sc,LT,F3} = \int_{\tau_L}^{\tau_U} \frac{a \mathcal{EI}(b\tau)}{\tau} d\tau, \tag{B.167}$$

where a and b are constants. These integral forms $\beta^*_{sc,LT,F1}$, $\beta^*_{sc,LT,F2}$ and $\beta^*_{sc,LT,F3}$, are solved in Section B.9.1 (specifically Sections B.9.1, B.9.1 and B.9.1, respectively). Based on the solutions for these integral forms, the terms of Equation B.164 (i.e. $\beta^*_{sc,LT,1}$ to $\beta^*_{sc,LT,9}$) are solved in Section B.9.2 (specifically Sections B.9.2 to B.9.2). Therefore substituting the solutions for terms $\beta^*_{sc,LT,1}$ to $\beta^*_{sc,LT,9}$ (Equations B.189, B.193, B.197, B.201, B.205, B.202, B.198, B.194 and B.190, respectively) into Equation B.164 and simplifying:

$$
\begin{aligned}
\beta^*_{\mathrm{sc,LT}} &= \int \frac{\bar{\Omega}_{\mathrm{AAC,LT}}(\tau, t)}{\tau} \mathrm{d}\tau \\
\beta^*_{\mathrm{sc,LT}} &= - c_{f11}\, \mathcal{EI}\left(c_{\tau\min} c_{f12}\right) - \frac{t_\mathrm{c}\, c_{f13}}{2\tau_\mathrm{sc}} \\
&\quad - \frac{c_{f11}\, \tau_\mathrm{sc}}{t_\mathrm{c}} \ln\left(\frac{c_{\tau 13}}{c_{\tau\min}}\right)\left[\gamma + \frac{1}{2}\ln\left(\left|c_{f12}^2\, c_{\tau 13}\, c_{\tau\min}\right|\right)\right] \\
&\quad - \frac{c_{f11}\, c_{f12}\, \tau_\mathrm{sc}}{t_\mathrm{c}}\Big[c_{\tau 13}\, {}_3\mathcal{F}_3\left(\{1,1,1\},\{2,2,2\}, c_{f12}\, c_{\tau 13}\right) \\
&\qquad - c_{\tau\min}\, {}_3\mathcal{F}_3\left(\{1,1,1\},\{2,2,2\}, c_{f12}\, c_{\tau\min}\right)\Big] \\
&\quad + \frac{c_{f11}\, \tau_\mathrm{sc}}{t_\mathrm{c}} \ln\left(\frac{c_{\tau 13}}{c_{\tau\min}}\right)\left[\gamma + \frac{1}{2}\ln\left(\left|c_{f12}^2\, c_{\tau 13}\, c_{\tau\min}\right|\right)\right] \\
&\quad + \frac{c_{f11}\, c_{f12}\, \tau_\mathrm{sc}}{t_\mathrm{c}}\Big[c_{\tau 13}\, {}_3\mathcal{F}_3\left(\{1,1,1\},\{2,2,2\}, c_{f12}\, c_{\tau 13}\right) \\
&\qquad - c_{\tau\min}\, {}_3\mathcal{F}_3\left(\{1,1,1\},\{2,2,2\}, c_{f12}\, c_{\tau\min}\right)\Big] + c_{f13} \ln\left(\frac{c_{\tau 13}}{c_{\tau\min}}\right) \\
&\quad + c_{f11}\, \mathcal{EI}\left(c_{\tau 13} c_{f12}\right) + \frac{t_\mathrm{c}\left(c_{f13} - c_{f31}\right)}{2\tau_\mathrm{sc}} + c_{f31} \ln\left(\frac{c_{\tau 23}}{c_{\tau 13}}\right) \\
&\quad - c_{f21}\, \mathcal{EI}\left(c_{\tau 23} c_{f22}\right) + \frac{t_\mathrm{c}\left(c_{f31} - c_{f23}\right)}{2\tau_\mathrm{sc}} \\
&\quad + \frac{c_{f21}\, \tau_\mathrm{sc}}{t_\mathrm{c}} \ln\left(\frac{c_{\tau\max}}{c_{\tau 23}}\right)\left[\gamma + \frac{1}{2}\ln\left(\left|c_{f22}^2\, c_{\tau\max}\, c_{\tau 23}\right|\right)\right] \\
&\quad + \frac{c_{f21}\, c_{f22}\, \tau_\mathrm{sc}}{t_\mathrm{c}}\Big[c_{\tau\max}\, {}_3\mathcal{F}_3\left(\{1,1,1\},\{2,2,2\}, c_{f22}\, c_{\tau\max}\right) \\
&\qquad - c_{\tau 23}\, {}_3\mathcal{F}_3\left(\{1,1,1\},\{2,2,2\}, c_{f22}\, c_{\tau 23}\right)\Big] + c_{f23} \ln\left(\frac{c_{\tau\max}}{c_{\tau 23}}\right) \\
&\quad - \frac{c_{f21}\, \tau_\mathrm{sc}}{t_\mathrm{c}} \ln\left(\frac{c_{\tau\max}}{c_{\tau 23}}\right)\left[\gamma + \frac{1}{2}\ln\left(\left|c_{f22}^2\, c_{\tau\max}\, c_{\tau 23}\right|\right)\right] \\
&\quad - \frac{c_{f21}\, c_{f22}\, \tau_\mathrm{sc}}{t_\mathrm{c}}\Big[c_{\tau\max}\, {}_3\mathcal{F}_3\left(\{1,1,1\},\{2,2,2\}, c_{f22}\, c_{\tau\max}\right) \\
&\qquad - c_{\tau 23}\, {}_3\mathcal{F}_3\left(\{1,1,1\},\{2,2,2\}, c_{f22}\, c_{\tau 23}\right)\Big] \\
&\quad + c_{f21}\, \mathcal{EI}\left(c_{\tau\max} c_{f22}\right) + \frac{t_\mathrm{c}\, c_{f23}}{2\tau_\mathrm{sc}} \\
\beta^*_{\mathrm{sc,LT}} &= c_{f11}\left[\mathcal{EI}\left(c_{\tau 13}\, c_{f12}\right) - \mathcal{EI}\left(c_{\tau\min}\, c_{f12}\right)\right] \\
&\quad + c_{f13} \ln\left(\frac{c_{\tau 13}}{c_{\tau\min}}\right) + c_{f31} \ln\left(\frac{c_{\tau 23}}{c_{\tau 13}}\right) + c_{f23} \ln\left(\frac{c_{\tau\max}}{c_{\tau 23}}\right) \\
&\quad + c_{f21}\left[\mathcal{EI}\left(c_{\tau\max}\, c_{f22}\right) - \mathcal{EI}\left(c_{\tau 23}\, c_{f22}\right)\right].
\end{aligned}
\tag{B.168}
$$

B.9.1 Solving integral forms ($\beta^*_{\mathrm{sc,LT,F}x}$) of deconvolution parameter integral

Analytical solution for $\beta^*_{\mathrm{sc,LT,F1}}$ (Equation B.165)

Based on Equation B.165:

$$\begin{aligned}\beta^*_{\mathrm{sc,LT,F1}} &= \int_{\tau_\mathrm{L}}^{\tau_\mathrm{U}} \frac{a}{\tau}\mathrm{d}\tau = a\big[\ln(\tau_\mathrm{U}) - \ln(\tau_\mathrm{L})\big] \\ \beta^*_{\mathrm{sc,LT,F1}} &= a\ln\left(\frac{\tau_\mathrm{U}}{\tau_\mathrm{L}}\right).\end{aligned} \tag{B.169}$$

Analytical solution for $\beta^*_{\mathrm{sc,LT,F2}}$ (Equation B.166)

Letting:

$$u = \ln\left(\frac{b}{\tau}\right) \rightarrow \mathrm{d}u = -\frac{1}{\tau}\mathrm{d}\tau \rightarrow \mathrm{d}\tau = -\tau\,\mathrm{d}u, \tag{B.170}$$

and substituting it into Equation B.166 as follows:

$$\begin{aligned}\beta^*_{\mathrm{sc,LT,F2}} &= \int_{\tau_\mathrm{L}}^{\tau_\mathrm{U}} \frac{a\ln\left(\frac{b}{\tau}\right)}{\tau}\mathrm{d}\tau = a\int -u\,\mathrm{d}u \\ \beta^*_{\mathrm{sc,LT,F2}} &= -\frac{a}{2}\left[\ln^2\left(\frac{b}{\tau_\mathrm{U}}\right) - \ln^2\left(\frac{b}{\tau_\mathrm{L}}\right)\right].\end{aligned} \tag{B.171}$$

Furthermore noting that $(x^2-y^2) = (x+y)(x-y)$, Equation B.171 simplifies to the following:

$$\begin{aligned}\beta^*_{\mathrm{sc,LT,F2}} &= -\frac{a}{2}\left[\ln\left(\frac{b}{\tau_\mathrm{U}}\right) + \ln\left(\frac{b}{\tau_\mathrm{L}}\right)\right]\left[\ln\left(\frac{b}{\tau_\mathrm{U}}\right) - \ln\left(\frac{b}{\tau_\mathrm{L}}\right)\right] \\ \beta^*_{\mathrm{sc,LT,F2}} &= -\frac{a}{2}\ln\left(\frac{b^2}{\tau_\mathrm{U}\,\tau_\mathrm{L}}\right)\ln\left(\frac{\tau_\mathrm{L}}{\tau_\mathrm{U}}\right).\end{aligned} \tag{B.172}$$

Analytical solution for $\beta^*_{\mathrm{sc,LT,F3}}$ (Equation B.167)

Based on Equation B.167:

$$\beta^*_{\mathrm{sc,LT,F3}} = \int_{\tau_\mathrm{L}}^{\tau_\mathrm{U}} \frac{a\,\mathcal{EI}(b\,\tau)}{\tau}\mathrm{d}\tau. \tag{B.173}$$

Based Equation 6.6.1 of NIST [194], the Exponential Integral ($\mathcal{EI}(x)$) can be represented as:

$$\mathcal{EI}(x) = \gamma + \ln(x) + \sum_{n=1}^{\infty} \frac{x^n}{n\,n!}, \tag{B.174}$$

for $x > 0$ and where γ is Euler's Constant (0.5772156649). To consider negative input values $\mathcal{EI}(x)$ can be approximated as:

$$\mathcal{EI}(x) = \gamma + \ln(|x|) + \sum_{n=1}^{\infty} \frac{x^n}{n\,n!}, \tag{B.175}$$

for $x \geq -16.452$. This approximation has been verified to agree within 1% of both the values calculated by the Exponential Integral function within Matlab and numerical integration of $\exp(x)/x$ over this range with 0.001 resolution. To check if the scanning AAC theory falls within this range, consider all of the $\mathcal{EI}(x)$ inputs within Equation B.164 over their respective integral limits. Only the extreme limits need to be considered. Therefore, any input terms to $\mathcal{EI}(x)$ containing τ_{13} or τ_{23} can be ignored as $\tau_{\min} < \tau_{13} < \tau_{23} < \tau_{\max}$.

Therefore based on the definitions of $\tau_{\min}$, $c_{\tau\min}$, c_{f12} and $\tau_{x,\mathrm{tc}}$ (Equations B.48, B.49, B.55 and B.93, respectively), the lower integral limits of the $\mathcal{EI}(x)$ inputs within Equation B.164 all simplify to the same constant as follows:

$$\begin{aligned} c_{\tau\min}\,c_{f12} &= c_{f12}\,\tau_{\min}\exp\left(\frac{t_\mathrm{m}}{\tau_\mathrm{sc}}\right) = c_{f12}\,\tau_{\mathrm{min,tc}}\exp\left(\frac{t_\mathrm{m}+t_\mathrm{c}}{\tau_\mathrm{sc}}\right) \\ c_{\tau\min}\,c_{f12} &= -\ln\left(\frac{Q_\mathrm{a}+Q_\mathrm{sh}-Q_\mathrm{s}\left(1-r_1^2/r_2^2\right)}{Q_\mathrm{a}+Q_\mathrm{sh}-Q_\mathrm{sh}\left(1-r_1^2/r_2^2\right)}\right). \end{aligned} \tag{B.176}$$

Similarly, based on the definitions of $\tau_{\max}$, $c_{\tau\max}$, c_{f22} and $\tau_{x,\mathrm{tc}}$ (Equations B.46, B.47, B.59 and B.93, respectively), the upper integral limits of the $\mathcal{EI}(x)$ inputs within Equation B.164 all simplify to the same constant as follows:

$$\begin{aligned} c_{\tau\max}\,c_{f22} &= c_{f22}\,\tau_{\max}\exp\left(\frac{t_\mathrm{m}}{\tau_\mathrm{sc}}\right) = c_{f22}\,\tau_{\mathrm{max,tc}}\exp\left(\frac{t_\mathrm{m}+t_\mathrm{c}}{\tau_\mathrm{sc}}\right) \\ c_{\tau\max}\,c_{f22} &= -2\ln\left(\frac{r_2}{r_1}\right). \end{aligned} \tag{B.177}$$

Therefore, if $c_{\tau min}\, c_{f12} \geq -16.452$ and $c_{\tau max}\, c_{f22} \geq -16.452$ are satisfied, the approximation for the Exponential Integral Function (Equation B.175) is valid for the theory inputs of the scanning AAC. This criteria is satisfied over the entire operating range of the commercial AAC from Cambustion ($r_1 = 56$ mm, $r_2 = 60$ mm, $Q_a = 0.3$ to 1.5 L/min, $Q_s = 0.3$ to 1.5 L/min and $Q_{sh} = 1.5$ to 15 L/min) with $c_{\tau min}\, c_{f12} = -0.13$ to -0.02 and $c_{\tau max}\, c_{f22} = -0.14$. Therefore, substituting this approximation for $\mathcal{EI}(x)$ (Equation B.175) into Equation B.173:

$$\begin{aligned}\beta^*_{sc,LT,F3} &= a\int_{\tau_L}^{\tau_U}\frac{1}{\tau}\left[\gamma+\ln\left(|b\,\tau|\right)+\sum_{n=1}^{\infty}\frac{(b\,\tau)^n}{n\,n!}\right]\mathrm{d}\tau \\ \beta^*_{sc,LT,F3} &= a\Bigg[\underbrace{\int_{\tau_L}^{\tau_U}\frac{\gamma}{\tau}\mathrm{d}\tau}_{\beta^*_{sc,LT,F31}}+\underbrace{\int_{\tau_L}^{\tau_U}\frac{\ln\left(|b\,\tau|\right)}{\tau}\mathrm{d}\tau}_{\beta^*_{sc,LT,F32}}+\underbrace{\int_{\tau_L}^{\tau_U}\sum_{n=1}^{\infty}\frac{b^n\,\tau^{n-1}}{n\,n!}\mathrm{d}\tau}_{\beta^*_{sc,LT,F33}}\Bigg].\end{aligned} \tag{B.178}$$

Solving the first term (i.e. $\beta^*_{sc,LT,F31}$) of Equation B.178 as follows:

$$\beta^*_{sc,LT,F31} = \int_{\tau_L}^{\tau_U}\frac{\gamma}{\tau}\mathrm{d}\tau = \boldsymbol{\gamma\ln\left(\frac{\tau_U}{\tau_L}\right)}. \tag{B.179}$$

Solving the second term (i.e. $\beta^*_{sc,LT,F32}$) of Equation B.178 by letting:

$$u = \ln\left(|b\,\tau|\right) \rightarrow \mathrm{d}u = \frac{1}{\tau}\mathrm{d}\tau, \tag{B.180}$$

and substituting it into the equation as follows:

$$\begin{aligned}\beta^*_{sc,LT,F32} &= \int_{\tau_L}^{\tau_U}\frac{\ln\left(|b\,\tau|\right)}{\tau}\mathrm{d}\tau = \int u\,\mathrm{d}u = \frac{u^2}{2} = \left.\frac{\ln^2\left(|b\,\tau|\right)}{2}\right|_{\tau_L}^{\tau_U} \\ \beta^*_{sc,LT,F32} &= \frac{1}{2}\Big[\ln^2\left(|b\,\tau_U|\right)-\ln^2\left(|b\,\tau_L|\right)\Big].\end{aligned} \tag{B.181}$$

Furthermore noting that $(x^2-y^2) = (x+y)(x-y)$, Equation B.181 simplifies to the following:

$$\beta^*_{sc,LT,F32} = \frac{1}{2}\ln\left(|b^2\,\tau_U\,\tau_L|\right)\ln\left(\left|\frac{\tau_U}{\tau_L}\right|\right). \tag{B.182}$$

Solving the third term (i.e. $\beta^*_{sc,LT,F33}$) of Equation B.178 as follows:

$$\beta^*_{sc,LT,F33} = \int_{\tau_L}^{\tau_U}\sum_{n=1}^{\infty}\frac{b^n\,\tau^{n-1}}{n\,n!}\mathrm{d}\tau = \left.\sum_{n=1}^{\infty}\frac{b^n\,\tau^n}{n^2\,n!}\right|_{\tau_L}^{\tau_U}. \tag{B.183}$$

However, based on Equation 15.2.1 of NIST [194]:

$$\sum_{n=1}^{\infty} \frac{b^n \tau^n}{n^2\, n!} = b\,\tau\, {}_3\mathcal{F}_3\left(\{1,1,1\},\{2,2,2\}, b\,\tau\right), \tag{B.184}$$

where $\mathcal{F}$ is the generalized hypergeometric function. Therefore, Equation B.183 becomes:

$$\beta^*_{\mathrm{sc,LT,F33}} = b\Big[\tau_{\mathrm{U}}\, {}_3\mathcal{F}_3\left(\{1,1,1\},\{2,2,2\}, b\,\tau_{\mathrm{U}}\right) - \tau_{\mathrm{L}}\, {}_3\mathcal{F}_3\left(\{1,1,1\},\{2,2,2\}, b\,\tau_{\mathrm{L}}\right)\Big]. \tag{B.185}$$

Therefore, substituting the solutions for $\beta^*_{\mathrm{sc,LT,F31}}$, $\beta^*_{\mathrm{sc,LT,F32}}$ and $\beta^*_{\mathrm{sc,LT,F33}}$ (Equations B.179, B.182 and B.185, respectively) into the definition of $\beta^*_{\mathrm{sc,LT,F3}}$ (Equation B.178):

$$\begin{aligned}\beta^*_{\mathrm{sc,LT,F3}} =& a\,\gamma \ln\left(\frac{\tau_{\mathrm{U}}}{\tau_{\mathrm{L}}}\right) + \frac{a}{2}\ln\left(\left|b^2\,\tau_{\mathrm{U}}\,\tau_{\mathrm{L}}\right|\right)\ln\left(\left|\frac{\tau_{\mathrm{U}}}{\tau_{\mathrm{L}}}\right|\right) \\ &+ a\,b\left[\tau_{\mathrm{U}}\, {}_3\mathcal{F}_3\left(\{1,1,1\},\{2,2,2\}, b\,\tau_{\mathrm{U}}\right) - \tau_{\mathrm{L}}\, {}_3\mathcal{F}_3\left(\{1,1,1\},\{2,2,2\}, b\,\tau_{\mathrm{L}}\right)\right].\end{aligned} \tag{B.186}$$

B.9.2 Solving terms ($\beta^*_{\mathrm{sc,LT},x}$) of deconvolution parameter

Analytical solutions for $\beta^*_{\mathrm{sc,LT},1}$ and $\beta^*_{\mathrm{sc,LT},9}$ of Equation B.164

Based on term 1 (i.e. $\beta^*_{\mathrm{sc,LT},1}$) shown in Equation B.164:

$$\begin{aligned}
\beta^*_{\mathrm{sc,LT},1} &= \int_{\tau_{\min}}^{\tau_{\min,\mathrm{tc}}} \frac{1}{\tau}\left[\frac{c_{f11}\,\tau_{\mathrm{sc}}}{t_{\mathrm{c}}}\mathcal{EI}\left(c_{\tau\min}\,c_{f12}\right) - \frac{c_{f13}}{t_{\mathrm{c}}}\left(t_{\mathrm{m}} - \tau_{\mathrm{sc}}\ln\left(\frac{c_{\tau\min}}{\tau}\right)\right)\right]\mathrm{d}\tau \\
\beta^*_{\mathrm{sc,LT},1} &= \int_{\tau_{\min}}^{\tau_{\min,\mathrm{tc}}} \left[\frac{c_{f11}\,\tau_{\mathrm{sc}}}{t_{\mathrm{c}}}\mathcal{EI}\left(c_{\tau\min}\,c_{f12}\right) - \frac{c_{f13}\,t_{\mathrm{m}}}{t_{\mathrm{c}}}\right]\frac{1}{\tau}\mathrm{d}\tau \\
&\quad + \int_{\tau_{\min}}^{\tau_{\min,\mathrm{tc}}} \frac{c_{f13}}{t_{\mathrm{c}}}\tau_{\mathrm{sc}}\ln\left(\frac{c_{\tau\min}}{\tau}\right)\frac{1}{\tau}\mathrm{d}\tau.
\end{aligned} \tag{B.187}$$

Substituting the integral solutions of $\beta^*_{\mathrm{sc,LT,F1}}$ and $\beta^*_{\mathrm{sc,LT,F2}}$ (i.e. Equations B.169 and B.172) into Equation B.187 as follows:

$$\begin{aligned}
\beta^*_{\mathrm{sc,LT},1} = &\left[\frac{c_{f11}\,\tau_{\mathrm{sc}}}{t_{\mathrm{c}}}\mathcal{EI}\left(c_{\tau\min}\,c_{f12}\right)\right. \\
&\left. - \frac{c_{f13}\,t_{\mathrm{m}}}{t_{\mathrm{c}}}\right]\ln\left(\frac{\tau_{\min,\mathrm{tc}}}{\tau_{\min}}\right) - \frac{\frac{c_{f13}\,\tau_{\mathrm{sc}}}{t_{\mathrm{c}}}}{2}\ln\left(\frac{c^2_{\tau\min}}{\tau_{\min,\mathrm{tc}}\,\tau_{\min}}\right)\ln\left(\frac{\tau_{\min}}{\tau_{\min,\mathrm{tc}}}\right).
\end{aligned} \tag{B.188}$$

Substituting the definitions of τ_x and $\tau_{x,\mathrm{tc}}$ (Equations B.43 and B.93, respectively) into Equation B.188 to convert from the particle relaxation time (τ) to the measurement time (t_{m}) domain:

$$\begin{aligned}
\beta^*_{\mathrm{sc,LT},1} = &\left[\frac{c_{f11}\,\tau_{\mathrm{sc}}}{t_{\mathrm{c}}}\mathcal{EI}\left(c_{\tau\min}\,c_{f12}\right) - \frac{c_{f13}\,t_{\mathrm{m}}}{t_{\mathrm{c}}}\right]\ln\left(\frac{c_{\tau\min}\exp\left(\frac{-(t_{\mathrm{m}}+t_{\mathrm{c}})}{\tau_{\mathrm{sc}}}\right)}{c_{\tau\min}\exp\left(\frac{-t_{\mathrm{m}}}{\tau_{\mathrm{sc}}}\right)}\right) \\
&- \frac{c_{f13}\,\tau_{\mathrm{sc}}}{2t_{\mathrm{c}}}\ln\left(\frac{c^2_{\tau\min}}{c_{\tau\min}\exp\left(\frac{-(t_{\mathrm{m}}+t_{\mathrm{c}})}{\tau_{\mathrm{sc}}}\right)c_{\tau\min}\exp\left(\frac{-t_{\mathrm{m}}}{\tau_{\mathrm{sc}}}\right)}\right)\ln\left(\frac{c_{\tau\min}\exp\left(\frac{-t_{\mathrm{m}}}{\tau_{\mathrm{sc}}}\right)}{c_{\tau\min}\exp\left(\frac{-(t_{\mathrm{m}}+t_{\mathrm{c}})}{\tau_{\mathrm{sc}}}\right)}\right) \\
\beta^*_{\mathrm{sc,LT},1} = &-c_{f11}\,\mathcal{EI}\left(c_{\tau\min}\,c_{f12}\right) - \frac{t_{\mathrm{c}}\,c_{f13}}{2\tau_{\mathrm{sc}}}.
\end{aligned} \tag{B.189}$$

Following the same approach, term 9 (i.e. $\beta^*_{\mathrm{sc,LT},9}$) shown in Equation B.164 is equivalent to:

$$\begin{aligned}\beta^{*}_{\mathrm{sc,LT,9}} &= \int_{\tau_{\max}}^{\tau_{\max,\mathrm{tc}}} \frac{1}{\tau}\left[-\frac{c_{f21}\,\tau_{\mathrm{sc}}}{t_{\mathrm{c}}}\mathcal{EI}\left(c_{\tau\max}\,c_{f22}\right)+\frac{c_{f23}}{t_{\mathrm{c}}}\left(t_{\mathrm{m}}-\tau_{\mathrm{sc}}\ln\left(\frac{c_{\tau\max}}{\tau}\right)\right)\right]\mathrm{d}\tau \\ \beta^{*}_{\mathrm{sc,LT,9}} &= c_{f21}\,\mathcal{EI}\left(c_{\tau\max}\,c_{f22}\right)+\frac{t_{\mathrm{c}}\,c_{f23}}{2\tau_{\mathrm{sc}}}.\end{aligned} \tag{B.190}$$

Analytical solutions for $\beta^*_{\mathrm{sc,LT,2}}$ and $\beta^*_{\mathrm{sc,LT,8}}$ of Equation B.164

Based on term 2 (i.e. $\beta^*_{\mathrm{sc,LT,2}}$) shown in Equation B.164:

$$\beta^*_{\mathrm{sc,LT,2}} = \int_{\tau_{\min}}^{\tau_{13}} \frac{1}{\tau}\left[-\frac{c_{f11}\,\tau_{\mathrm{sc}}}{t_{\mathrm{c}}} \mathcal{EI}\left(c_{f12}\,\tau \exp\left(\frac{t_{\mathrm{m}}}{\tau_{\mathrm{sc}}}\right)\right)\right] \mathrm{d}\tau. \tag{B.191}$$

Substituting the integral solution of $\beta^*_{\mathrm{sc,LT,F3}}$ (i.e. Equation B.186) into Equation B.191 as follows:

$$\begin{aligned}
\beta^*_{\mathrm{sc,LT,2}} =& \frac{-c_{f11}\,\tau_{\mathrm{sc}}}{t_{\mathrm{c}}}\,\gamma \ln\left(\frac{\tau_{13}}{\tau_{\min}}\right) \\
&+ \frac{\frac{-c_{f11}\,\tau_{\mathrm{sc}}}{t_{\mathrm{c}}}}{2} \ln\left(\left|\left(c_{f12}\exp\left(\frac{t_{\mathrm{m}}}{\tau_{\mathrm{sc}}}\right)\right)^2 \tau_{13}\,\tau_{\min}\right|\right) \ln\left(\left|\frac{\tau_{13}}{\tau_{\min}}\right|\right) \\
&+ \frac{-c_{f11}\,\tau_{\mathrm{sc}}}{t_{\mathrm{c}}} \left(c_{f12}\exp\left(\frac{t_{\mathrm{m}}}{\tau_{\mathrm{sc}}}\right)\right) \\
&\quad \cdot \left[\tau_{13}\,{}_3\mathcal{F}_3\left(\{1,1,1\},\{2,2,2\},\left(c_{f12}\exp\left(\frac{t_{\mathrm{m}}}{\tau_{\mathrm{sc}}}\right)\right)\tau_{13}\right)\right. \\
&\qquad \left. - \tau_{\min}\,{}_3\mathcal{F}_3\left(\{1,1,1\},\{2,2,2\},\left(c_{f12}\exp\left(\frac{t_{\mathrm{m}}}{\tau_{\mathrm{sc}}}\right)\right)\tau_{\min}\right)\right].
\end{aligned} \tag{B.192}$$

Substituting the definitions of τ_x (Equation B.43) into Equation B.192 to convert from the particle relaxation time (τ) to the measurement time (t_{m}) domain:

$$
\begin{aligned}
\beta^*_{\mathrm{sc,LT,2}} = &- \frac{c_{f11}\,\tau_{\mathrm{sc}}}{t_{\mathrm{c}}}\gamma \ln\left(\frac{c_{\tau 13}\exp\left(\frac{-t_{\mathrm{m}}}{\tau_{\mathrm{sc}}}\right)}{c_{\tau\min}\exp\left(\frac{-t_{\mathrm{m}}}{\tau_{\mathrm{sc}}}\right)}\right) \\
&- \frac{c_{f11}\,\tau_{\mathrm{sc}}}{2t_{\mathrm{c}}}\ln\left(\left|\frac{c_{\tau 13}\exp\left(\frac{-t_{\mathrm{m}}}{\tau_{\mathrm{sc}}}\right)}{c_{\tau\min}\exp\left(\frac{-t_{\mathrm{m}}}{\tau_{\mathrm{sc}}}\right)}\right|\right) \\
&\quad \cdot \ln\left(\left|\left(c_{f12}\exp\left(\frac{t_{\mathrm{m}}}{\tau_{\mathrm{sc}}}\right)\right)^2 c_{\tau 13}\exp\left(\frac{-t_{\mathrm{m}}}{\tau_{\mathrm{sc}}}\right) c_{\tau\min}\exp\left(\frac{-t_{\mathrm{m}}}{\tau_{\mathrm{sc}}}\right)\right|\right) \\
&- \frac{c_{f11}\,\tau_{\mathrm{sc}}}{t_{\mathrm{c}}} c_{f12}\exp\left(\frac{t_{\mathrm{m}}}{\tau_{\mathrm{sc}}}\right)\left[c_{\tau 13}\exp\left(\frac{-t_{\mathrm{m}}}{\tau_{\mathrm{sc}}}\right)\right. \\
&\quad \cdot {}_3\mathcal{F}_3\left(\{1,1,1\},\{2,2,2\}, c_{f12}\exp\left(\frac{t_{\mathrm{m}}}{\tau_{\mathrm{sc}}}\right) c_{\tau 13}\exp\left(\frac{-t_{\mathrm{m}}}{\tau_{\mathrm{sc}}}\right)\right) \\
&\quad - c_{\tau\min}\exp\left(\frac{-t_{\mathrm{m}}}{\tau_{\mathrm{sc}}}\right) \\
&\quad \left. \cdot {}_3\mathcal{F}_3\left(\{1,1,1\},\{2,2,2\}, c_{f12}\exp\left(\frac{t_{\mathrm{m}}}{\tau_{\mathrm{sc}}}\right) c_{\tau\min}\exp\left(\frac{-t_{\mathrm{m}}}{\tau_{\mathrm{sc}}}\right)\right)\right] \\
\beta^*_{\mathrm{sc,LT,2}} = &- \frac{c_{f11}\,\tau_{\mathrm{sc}}}{t_{\mathrm{c}}}\ln\left(\frac{c_{\tau 13}}{c_{\tau\min}}\right)\left[\gamma + \frac{1}{2}\ln\left(\left|c_{f12}^2\, c_{\tau 13}\, c_{\tau\min}\right|\right)\right] \\
&- \frac{c_{f11}\, c_{f12}\,\tau_{\mathrm{sc}}}{t_{\mathrm{c}}}\left[c_{\tau 13}\,{}_3\mathcal{F}_3\left(\{1,1,1\},\{2,2,2\}, c_{f12}\, c_{\tau 13}\right)\right. \\
&\quad \left. - c_{\tau\min}\,{}_3\mathcal{F}_3\left(\{1,1,1\},\{2,2,2\}, c_{f12}\, c_{\tau\min}\right)\right].
\end{aligned}
\tag{B.193}
$$

Following the same approach, term 8 (i.e. $\beta^*_{\mathrm{sc,LT,8}}$) shown in Equation B.164 is equivalent to:

$$
\begin{aligned}
\beta^*_{\mathrm{sc,LT,8}} = &\int_{\tau_{23}}^{\tau_{\max}} \frac{1}{\tau}\left[-\frac{c_{f21}\,\tau_{\mathrm{sc}}}{t_{\mathrm{c}}}\mathcal{EI}\left(c_{f22}\,\tau\exp\left(\frac{t_{\mathrm{m}}}{\tau_{\mathrm{sc}}}\right)\right)\right]\mathrm{d}\tau \\
\beta^*_{\mathrm{sc,LT,8}} = &- \frac{c_{f21}\,\tau_{\mathrm{sc}}}{t_{\mathrm{c}}}\ln\left(\frac{c_{\tau\max}}{c_{\tau 23}}\right)\left[\gamma + \frac{1}{2}\ln\left(\left|c_{f22}^2\, c_{\tau\max}\, c_{\tau 23}\right|\right)\right] \\
&- \frac{c_{f21}\, c_{f22}\,\tau_{\mathrm{sc}}}{t_{\mathrm{c}}}\left[c_{\tau\max}\,{}_3\mathcal{F}_3\left(\{1,1,1\},\{2,2,2\}, c_{f22}\, c_{\tau\max}\right)\right. \\
&\quad \left. - c_{\tau 23}\,{}_3\mathcal{F}_3\left(\{1,1,1\},\{2,2,2\}, c_{f22}\, c_{\tau 23}\right)\right].
\end{aligned}
\tag{B.194}
$$

Analytical solutions for $\beta^*_{\mathrm{sc,LT},3}$ and $\beta^*_{\mathrm{sc,LT},7}$ of Equation B.164

Based on term 3 (i.e. $\beta^*_{\mathrm{sc,LT},3}$) shown in Equation B.164:

$$\begin{aligned}\beta^*_{\mathrm{sc,LT},3} &= \int_{\tau_{\mathrm{min,tc}}}^{\tau_{13,\mathrm{tc}}} \frac{1}{\tau}\left[\frac{c_{f11}\,\tau_{\mathrm{sc}}}{t_{\mathrm{c}}}\mathcal{EI}\left(c_{f12}\,\tau\exp\left(\frac{t_{\mathrm{m}}+t_{\mathrm{c}}}{\tau_{\mathrm{sc}}}\right)\right)+c_{f13}\right]\mathrm{d}\tau \\ \beta^*_{\mathrm{sc,LT},3} &= \int_{\tau_{\mathrm{min,tc}}}^{\tau_{13,\mathrm{tc}}} \frac{c_{f11}\,\tau_{\mathrm{sc}}}{t_{\mathrm{c}}}\frac{\mathcal{EI}\left(c_{f12}\,\tau\exp\left(\frac{t_{\mathrm{m}}+t_{\mathrm{c}}}{\tau_{\mathrm{sc}}}\right)\right)}{\tau}\mathrm{d}\tau+\int_{\tau_{\mathrm{min,tc}}}^{\tau_{13,\mathrm{tc}}}\frac{c_{f13}}{\tau}\mathrm{d}\tau.\end{aligned} \tag{B.195}$$

Substituting the integral solutions of $\beta^*_{\mathrm{sc,LT,F1}}$ and $\beta^*_{\mathrm{sc,LT,F3}}$ (i.e. Equations B.169 and B.186) into Equation B.195 as follows:

$$\begin{aligned}\beta^*_{\mathrm{sc,LT},3} =& c_{f13}\ln\left(\frac{\tau_{13,\mathrm{tc}}}{\tau_{\mathrm{min,tc}}}\right)+\frac{c_{f11}\,\tau_{\mathrm{sc}}}{t_{\mathrm{c}}}\,\gamma\ln\left(\frac{\tau_{13,\mathrm{tc}}}{\tau_{\mathrm{min,tc}}}\right) \\ &+\frac{\frac{c_{f11}\,\tau_{\mathrm{sc}}}{t_{\mathrm{c}}}}{2}\ln\left(\left|\left(c_{f12}\exp\left(\frac{t_{\mathrm{m}}+t_{\mathrm{c}}}{\tau_{\mathrm{sc}}}\right)\right)^2\tau_{13,\mathrm{tc}}\,\tau_{\mathrm{min,tc}}\right|\right)\ln\left(\left|\frac{\tau_{13,\mathrm{tc}}}{\tau_{\mathrm{min,tc}}}\right|\right) \\ &+\frac{c_{f11}\,\tau_{\mathrm{sc}}}{t_{\mathrm{c}}}\left(c_{f12}\exp\left(\frac{t_{\mathrm{m}}+t_{\mathrm{c}}}{\tau_{\mathrm{sc}}}\right)\right) \\ &\cdot\left[\tau_{13,\mathrm{tc}}\,{}_3\mathcal{F}_3\left(\{1,1,1\},\{2,2,2\},\left(c_{f12}\exp\left(\frac{t_{\mathrm{m}}+t_{\mathrm{c}}}{\tau_{\mathrm{sc}}}\right)\right)\tau_{13,\mathrm{tc}}\right)\right. \\ &\left.-\tau_{\mathrm{min,tc}}\,{}_3\mathcal{F}_3\left(\{1,1,1\},\{2,2,2\},\left(c_{f12}\exp\left(\frac{t_{\mathrm{m}}+t_{\mathrm{c}}}{\tau_{\mathrm{sc}}}\right)\right)\tau_{\mathrm{min,tc}}\right)\right].\end{aligned} \tag{B.196}$$

Substituting the definition of $\tau_{x,\mathrm{tc}}$ (Equation B.93) into Equation B.196 to convert from the particle relaxation time (τ) to the measurement time (t_{m}) domain:

$$
\begin{aligned}
\beta^*_{\mathrm{sc,LT,3}} =& \frac{c_{f11}\,\tau_{\mathrm{sc}}}{t_{\mathrm{c}}}\gamma \ln\left(\frac{c_{\tau 13}\exp\left(\frac{-(t_{\mathrm{m}}+t_{\mathrm{c}})}{\tau_{\mathrm{sc}}}\right)}{c_{\tau\min}\exp\left(\frac{-(t_{\mathrm{m}}+t_{\mathrm{c}})}{\tau_{\mathrm{sc}}}\right)}\right) \\
&+ \frac{c_{f11}\,\tau_{\mathrm{sc}}}{2t_{\mathrm{c}}}\ln\left(\left|\frac{c_{\tau 13}\exp\left(\frac{-(t_{\mathrm{m}}+t_{\mathrm{c}})}{\tau_{\mathrm{sc}}}\right)}{c_{\tau\min}\exp\left(\frac{-(t_{\mathrm{m}}+t_{\mathrm{c}})}{\tau_{\mathrm{sc}}}\right)}\right|\right) \\
&\cdot \ln\left(\left|\left(c_{f12}\exp\left(\frac{t_{\mathrm{m}}+t_{\mathrm{c}}}{\tau_{\mathrm{sc}}}\right)\right)^2 c_{\tau 13}\exp\left(\frac{-(t_{\mathrm{m}}+t_{\mathrm{c}})}{\tau_{\mathrm{sc}}}\right)c_{\tau\min}\exp\left(\frac{-(t_{\mathrm{m}}+t_{\mathrm{c}})}{\tau_{\mathrm{sc}}}\right)\right|\right) \\
&+ \frac{c_{f11}\,\tau_{\mathrm{sc}}}{t_{\mathrm{c}}}c_{f12}\exp\left(\frac{t_{\mathrm{m}}+t_{\mathrm{c}}}{\tau_{\mathrm{sc}}}\right)\Bigg[c_{\tau 13}\exp\left(\frac{-(t_{\mathrm{m}}+t_{\mathrm{c}})}{\tau_{\mathrm{sc}}}\right) \\
&\quad \cdot {}_3\mathcal{F}_3\left(\{1,1,1\},\{2,2,2\},c_{f12}\exp\left(\frac{t_{\mathrm{m}}+t_{\mathrm{c}}}{\tau_{\mathrm{sc}}}\right)c_{\tau 13}\exp\left(\frac{-(t_{\mathrm{m}}+t_{\mathrm{c}})}{\tau_{\mathrm{sc}}}\right)\right) \\
&\quad - c_{\tau\min}\exp\left(\frac{-(t_{\mathrm{m}}+t_{\mathrm{c}})}{\tau_{\mathrm{sc}}}\right) \\
&\quad \cdot {}_3\mathcal{F}_3\left(\{1,1,1\},\{2,2,2\},c_{f12}\exp\left(\frac{t_{\mathrm{m}}+t_{\mathrm{c}}}{\tau_{\mathrm{sc}}}\right)c_{\tau\min}\exp\left(\frac{-(t_{\mathrm{m}}+t_{\mathrm{c}})}{\tau_{\mathrm{sc}}}\right)\right)\Bigg] \\
&+ c_{f13}\ln\left(\frac{c_{\tau 13}\exp\left(\frac{-(t_{\mathrm{m}}+t_{\mathrm{c}})}{\tau_{\mathrm{sc}}}\right)}{c_{\tau\min}\exp\left(\frac{-(t_{\mathrm{m}}+t_{\mathrm{c}})}{\tau_{\mathrm{sc}}}\right)}\right) \\
\beta^*_{\mathrm{sc,LT,3}} =& \frac{c_{f11}\,\tau_{\mathrm{sc}}}{t_{\mathrm{c}}}\ln\left(\frac{c_{\tau 13}}{c_{\tau\min}}\right)\left[\gamma + \frac{1}{2}\ln\left(|c_{f12}^2\,c_{\tau 13}\,c_{\tau\min}|\right)\right] \\
&+ \frac{c_{f11}\,c_{f12}\,\tau_{\mathrm{sc}}}{t_{\mathrm{c}}}\Big[c_{\tau 13}\,{}_3\mathcal{F}_3\left(\{1,1,1\},\{2,2,2\},c_{f12}\,c_{\tau 13}\right) \\
&\quad - c_{\tau\min}\,{}_3\mathcal{F}_3\left(\{1,1,1\},\{2,2,2\},c_{f12}\,c_{\tau\min}\right)\Big] + c_{f13}\ln\left(\frac{c_{\tau 13}}{c_{\tau\min}}\right).
\end{aligned}
\tag{B.197}
$$

Following the same approach, term 7 (i.e. $\beta^*_{\mathrm{sc,LT,7}}$) shown in Equation B.164 is equivalent to:

$$
\begin{aligned}
\beta^*_{\mathrm{sc,LT,7}} =& \int_{\tau_{23,\mathrm{tc}}}^{\tau_{\max,\mathrm{tc}}}\frac{1}{\tau}\left[\frac{c_{f21}\,\tau_{\mathrm{sc}}}{t_{\mathrm{c}}}\mathcal{EI}\left(c_{f22}\,\tau\exp\left(\frac{t_{\mathrm{m}}+t_{\mathrm{c}}}{\tau_{\mathrm{sc}}}\right)\right)+c_{f23}\right]\mathrm{d}\tau \\
\beta^*_{\mathrm{sc,LT,7}} =& \frac{c_{f21}\,\tau_{\mathrm{sc}}}{t_{\mathrm{c}}}\ln\left(\frac{c_{\tau\max}}{c_{\tau 23}}\right)\left[\gamma+\frac{1}{2}\ln\left(|c_{f22}^2\,c_{\tau\max}\,c_{\tau 23}|\right)\right] \\
&+ \frac{c_{f21}\,c_{f22}\,\tau_{\mathrm{sc}}}{t_{\mathrm{c}}}\Big[c_{\tau\max}\,{}_3\mathcal{F}_3\left(\{1,1,1\},\{2,2,2\},c_{f22}\,c_{\tau\max}\right) \\
&\quad - c_{\tau 23}\,{}_3\mathcal{F}_3\left(\{1,1,1\},\{2,2,2\},c_{f22}\,c_{\tau 23}\right)\Big] + c_{f23}\ln\left(\frac{c_{\tau\max}}{c_{\tau 23}}\right).
\end{aligned}
\tag{B.198}
$$

Analytical solutions for $\beta^*_{\mathrm{sc,LT},4}$ and $\beta^*_{\mathrm{sc,LT},6}$ of Equation B.164

Based on term 4 (i.e. $\beta^*_{\mathrm{sc,LT},4}$) shown in Equation B.164:

$$\begin{aligned}\beta^*_{\mathrm{sc,LT},4} &= \int_{\tau_{13}}^{\tau_{13,\mathrm{tc}}} \frac{1}{\tau}\left[-\frac{c_{f11}\,\tau_{\mathrm{sc}}}{t_{\mathrm{c}}}\mathcal{EI}\left(c_{\tau 13}\,c_{f12}\right) + \left(\frac{c_{f13}}{t_{\mathrm{c}}} - \frac{c_{f31}}{t_{\mathrm{c}}}\right)\left(t_{\mathrm{m}} - \tau_{\mathrm{sc}}\ln\left(\frac{c_{\tau 13}}{\tau}\right)\right)\right]\mathrm{d}\tau \\ &= \int_{\tau_{13}}^{\tau_{13,\mathrm{tc}}} \left[-\frac{c_{f11}\,\tau_{\mathrm{sc}}}{t_{\mathrm{c}}}\mathcal{EI}\left(c_{\tau 13}\,c_{f12}\right) + \frac{t_{\mathrm{m}}\left(c_{f13}-c_{f31}\right)}{t_{\mathrm{c}}}\right]\frac{1}{\tau}\mathrm{d}\tau \\ &\quad + \int_{\tau_{13}}^{\tau_{13,\mathrm{tc}}} \frac{-\tau_{\mathrm{sc}}\left(c_{f13}-c_{f31}\right)}{t_{\mathrm{c}}}\frac{\ln\left(\frac{c_{\tau 13}}{\tau}\right)}{\tau}\mathrm{d}\tau.\end{aligned} \tag{B.199}$$

Substituting the integral solutions of $\beta^*_{\mathrm{sc,LT,F1}}$ and $\beta^*_{\mathrm{sc,LT,F2}}$ (i.e. Equations B.169 and B.172) into Equation B.199 as follows:

$$\begin{aligned}\beta^*_{\mathrm{sc,LT},4} = &\left[-\frac{c_{f11}\,\tau_{\mathrm{sc}}}{t_{\mathrm{c}}}\mathcal{EI}\left(c_{\tau 13}\,c_{f12}\right) + \frac{t_{\mathrm{m}}\left(c_{f13}-c_{f31}\right)}{t_{\mathrm{c}}}\right]\ln\left(\frac{\tau_{13,\mathrm{tc}}}{\tau_{13}}\right) \\ &+ \frac{\frac{\tau_{\mathrm{sc}}\left(c_{f13}-c_{f31}\right)}{t_{\mathrm{c}}}}{2}\ln\left(\frac{c^2_{\tau 13}}{\tau_{13,\mathrm{tc}}\,\tau_{13}}\right)\ln\left(\frac{\tau_{13}}{\tau_{13,\mathrm{tc}}}\right).\end{aligned} \tag{B.200}$$

Substituting the definitions of τ_x and $\tau_{x,\mathrm{tc}}$ (Equations B.43 and B.93, respectively) into Equation B.200 to convert from the particle relaxation time (τ) to the measurement time (t_{m}) domain:

$$\begin{aligned}\beta^*_{\mathrm{sc,LT},4} = &\left[-\frac{c_{f11}\,\tau_{\mathrm{sc}}}{t_{\mathrm{c}}}\mathcal{EI}\left(c_{\tau 13}\,c_{f12}\right) + \frac{t_{\mathrm{m}}\left(c_{f13}-c_{f31}\right)}{t_{\mathrm{c}}}\right]\ln\left(\frac{c_{\tau 13}\exp\left(\frac{-(t_{\mathrm{m}}+t_{\mathrm{c}})}{\tau_{\mathrm{sc}}}\right)}{c_{\tau 13}\exp\left(\frac{-t_{\mathrm{m}}}{\tau_{\mathrm{sc}}}\right)}\right) \\ &+ \frac{\tau_{\mathrm{sc}}\left(c_{f13}-c_{f31}\right)}{2t_{\mathrm{c}}}\ln\left(\frac{c^2_{\tau 13}}{c_{\tau 13}\exp\left(\frac{-(t_{\mathrm{m}}+t_{\mathrm{c}})}{\tau_{\mathrm{sc}}}\right)c_{\tau 13}\exp\left(\frac{-t_{\mathrm{m}}}{\tau_{\mathrm{sc}}}\right)}\right) \\ &\cdot\ln\left(\frac{c_{\tau 13}\exp\left(\frac{-t_{\mathrm{m}}}{\tau_{\mathrm{sc}}}\right)}{c_{\tau 13}\exp\left(\frac{-(t_{\mathrm{m}}+t_{\mathrm{c}})}{\tau_{\mathrm{sc}}}\right)}\right) \\ \beta^*_{\mathrm{sc,LT},4} = &c_{f11}\,\mathcal{EI}\left(c_{\tau 13}\,c_{f12}\right) + \frac{t_{\mathrm{c}}\left(c_{f13}-c_{f31}\right)}{2\tau_{\mathrm{sc}}}.\end{aligned} \tag{B.201}$$

Following the same approach, term 6 (i.e. $\beta^*_{\mathrm{sc,LT},6}$) shown in Equation B.164 is equivalent to:

$$\beta^*_{\mathrm{sc,LT},6} = \int_{\tau_{23}}^{\tau_{23,\mathrm{tc}}} \frac{1}{\tau}\left[\frac{c_{f21}\,\tau_{\mathrm{sc}}}{t_{\mathrm{c}}}\mathcal{EI}\left(c_{\tau 23}\,c_{f22}\right) + \left(\frac{c_{f31}}{t_{\mathrm{c}}} - \frac{c_{f23}}{t_{\mathrm{c}}}\right)\left(t_{\mathrm{m}} - \tau_{\mathrm{sc}}\ln\left(\frac{c_{\tau 23}}{\tau}\right)\right)\right]\mathrm{d}\tau$$

$$\beta^*_{\mathrm{sc,LT},6} = -\,c_{f21}\,\mathcal{EI}\left(c_{\tau 23}\,c_{f22}\right) + \frac{t_{\mathrm{c}}\left(c_{f31} - c_{f23}\right)}{2\tau_{\mathrm{sc}}}. \tag{B.202}$$

Analytical solution for $\beta^*_{\mathrm{sc,LT,5}}$ of Equation B.164

Based on term 5 (i.e. $\beta^*_{\mathrm{sc,LT,5}}$) shown in Equation B.164:

$$\beta^*_{\mathrm{sc,LT,5}} = \int_{\tau_{13,\mathrm{tc}}}^{\tau_{23,\mathrm{tc}}} \frac{c_{f31}}{\tau} \mathrm{d}\tau. \tag{B.203}$$

Substituting the integral solution of $\beta^*_{\mathrm{sc,LT,F1}}$ (i.e. Equation B.169) into Equation B.203 as follows:

$$\beta^*_{\mathrm{sc,LT,5}} = c_{f31} \ln\left(\frac{\tau_{23,\mathrm{tc}}}{\tau_{13,\mathrm{tc}}}\right). \tag{B.204}$$

Substituting the definition of $\tau_{x,\mathrm{tc}}$ (Equation B.93) into Equation B.204 to convert from the particle relaxation time (τ) to the measurement time (t_m) domain:

$$\begin{aligned}
\beta^*_{\mathrm{sc,LT,5}} &= c_{f31} \ln\left(\frac{c_{\tau 23} \exp\left(\frac{-(t_\mathrm{m}+t_\mathrm{c})}{\tau_\mathrm{sc}}\right)}{c_{\tau 13} \exp\left(\frac{-(t_\mathrm{m}+t_\mathrm{c})}{\tau_\mathrm{sc}}\right)}\right) \\
\beta^*_{\mathrm{sc,LT,5}} &= c_{f31} \ln\left(\frac{c_{\tau 23}}{c_{\tau 13}}\right).
\end{aligned} \tag{B.205}$$

B.10 Deconvolution parameter ($\beta^*_{sc,PS,B}$) of scanning AAC: particle streamline, non-idealized, balanced flows & uniform axial flow

Substituting the definition of $\bar{\Omega}_{AAC}$ based on particle streamline theory (Equation B.133) into the definition of the β^*_{sc} (Equation B.162) and organizing into separate integrals by the ranges of particle relaxation times becomes:

$$
\begin{aligned}
\beta^*_{sc,PS,B} &= \int \frac{\bar{\Omega}_{AAC,B}(\tau,t)}{\tau} d\tau \\
\beta^*_{sc,PS,B} &= \underbrace{\int_{\tau_{min,B}}^{\tau_{min,B,tc}} \frac{1}{\tau}\left[-\frac{\lambda_\Omega\,\mu_\Omega\,c_{BL}}{t_c}\left(t_m-\tau_{sc}\ln\left(\frac{c_{\tau min,B}}{\tau}\right)\right)+\frac{c_{B2}\,c_{\tau min,B}}{c_{\tau*,B}}\right]d\tau}_{\beta^*_{sc,PS,B1}} \\
&+ \underbrace{\int_{\tau_{min,B}}^{\tau^*_{sc,B}} \frac{1}{\tau}\left[-\frac{c_{B2}}{c_{\tau*,B}}\tau\exp\left(\frac{t_m}{\tau_{sc}}\right)\right]d\tau}_{\beta^*_{sc,PS,B2}} \\
&+ \underbrace{\int_{\tau_{min,B,tc}}^{\tau^*_{sc,B,tc}} \frac{1}{\tau}\left[\lambda_\Omega\,\mu_\Omega\,c_{BL}+\frac{c_{B2}}{c_{\tau*,B}}\tau\exp\left(\frac{t_m+t_c}{\tau_{sc}}\right)\right]d\tau}_{\beta^*_{sc,PS,B3}} \\
&+ \underbrace{\int_{\tau^*_{sc,B}}^{\tau^*_{sc,B,tc}} \frac{1}{\tau}\left[\frac{\lambda_\Omega\,\mu_\Omega}{t_c}\left(c_{BL}-c_{BU}\right)\left(t_m-\tau_{sc}\ln\left(\frac{c_{\tau*,B}}{\tau}\right)\right)-2c_{B2}\right]d\tau}_{\beta^*_{sc,PS,B4}} \\
&+ \underbrace{\int_{\tau^*_{sc,B,tc}}^{\tau_{max,B,tc}} \frac{1}{\tau}\left[\lambda_\Omega\,\mu_\Omega\,c_{BU}-\frac{c_{B2}}{c_{\tau*,B}}\tau\exp\left(\frac{t_m+t_c}{\tau_{sc}}\right)\right]d\tau}_{\beta^*_{sc,PS,B5}} \\
&+ \underbrace{\int_{\tau^*_{sc,B}}^{\tau_{max,B}} \frac{1}{\tau}\left[\frac{c_{B2}}{c_{\tau*,B}}\tau\exp\left(\frac{t_m}{\tau_{sc}}\right)\right]d\tau}_{\beta^*_{sc,PS,B6}} \\
&+ \underbrace{\int_{\tau_{max,B}}^{\tau_{max,B,tc}} \frac{1}{\tau}\left[\frac{\lambda_\Omega\,\mu_\Omega\,c_{BU}}{t_c}\left(t_m-\tau_{sc}\ln\left(\frac{c_{\tau max,B}}{\tau}\right)\right)+\frac{c_{B2}\,c_{\tau max,B}}{c_{\tau*,B}}\right]d\tau}_{\beta^*_{sc,PS,B7}}.
\end{aligned}
\tag{B.206}
$$

All of the terms in Equation B.206 consist of different combinations of the following three integral forms:

$$\beta^*_{\mathrm{sc,PS,F1}} = \int_{\tau_\mathrm{L}}^{\tau_\mathrm{U}} \frac{a}{\tau} \mathrm{d}\tau, \tag{B.207}$$

$$\beta^*_{\mathrm{sc,PS,F2}} = \int_{\tau_\mathrm{L}}^{\tau_\mathrm{U}} \frac{a \ln\left(\frac{b}{\tau}\right)}{\tau} \mathrm{d}\tau, \tag{B.208}$$

$$\beta^*_{\mathrm{sc,PS,F3}} = \int_{\tau_\mathrm{L}}^{\tau_\mathrm{U}} a \mathrm{d}\tau, \tag{B.209}$$

where a and b are constants. These integral forms $\beta^*_{\mathrm{sc,PS,F1}}$, $\beta^*_{\mathrm{sc,PS,F2}}$ and $\beta^*_{\mathrm{sc,PS,F3}}$, are solved in Section B.10.1 (specifically Sections B.10.1, B.10.1 and B.10.1, respectively). Based on the solutions for these integral forms, the terms of Equation B.206 (i.e. $\beta^*_{\mathrm{sc,PS,B1}}$ to $\beta^*_{\mathrm{sc,PS,B7}}$) are solved in Section B.10.2 (specifically Sections B.10.2 to B.10.2). Therefore substituting the solution for terms $\beta^*_{\mathrm{sc,PS,B1}}$ to $\beta^*_{\mathrm{sc,PS,B7}}$ (Equations B.218, B.222, B.226, B.230, B.227, B.223, and B.219, respectively) into Equation B.206 as follows:

$$\begin{aligned}
\beta^*_{\mathrm{sc,PS,B}} &= \int \frac{\bar{\Omega}_{\mathrm{AAC,B}}(\tau, t)}{\tau} \mathrm{d}\tau \\
\beta^*_{\mathrm{sc,PS,B}} &= -\frac{c_{\mathrm{B2}}\, c_{\tau\mathrm{min,B}}\, t_\mathrm{c}}{c_{\tau*,\mathrm{B}}\, \tau_\mathrm{sc}} - \frac{\lambda_\Omega\, \mu_\Omega\, c_\mathrm{BL}\, t_\mathrm{c}}{2\tau_\mathrm{sc}} \\
&\quad - c_{\mathrm{B2}} \left(1 - \frac{c_{\tau\mathrm{min,B}}}{c_{\tau*,\mathrm{B}}}\right) \\
&\quad + \lambda_\Omega\, \mu_\Omega\, c_\mathrm{BL} \ln\left(\frac{c_{\tau*,\mathrm{B}}}{c_{\tau\mathrm{min,B}}}\right) + c_{\mathrm{B2}} \left(1 - \frac{c_{\tau\mathrm{min,B}}}{c_{\tau*,\mathrm{B}}}\right) \\
&\quad + \frac{2c_{\mathrm{B2}}\, t_\mathrm{c}}{\tau_\mathrm{sc}} + \frac{\lambda_\Omega\, \mu_\Omega\, t_\mathrm{c}}{2\tau_\mathrm{sc}} \left(c_\mathrm{BL} - c_\mathrm{BU}\right) \\
&\quad + \lambda_\Omega\, \mu_\Omega\, c_\mathrm{BU} \ln\left(\frac{c_{\tau\mathrm{max,B}}}{c_{\tau*,\mathrm{B}}}\right) + c_{\mathrm{B2}} \left(1 - \frac{c_{\tau\mathrm{max,B}}}{c_{\tau*,\mathrm{B}}}\right) \\
&\quad + c_{\mathrm{B2}} \left(\frac{c_{\tau\mathrm{max,B}}}{c_{\tau*,\mathrm{B}}} - 1\right) \\
&\quad - \frac{c_{\mathrm{B2}}\, c_{\tau\mathrm{max,B}}\, t_\mathrm{c}}{c_{\tau*,\mathrm{B}}\, \tau_\mathrm{sc}} + \frac{\lambda_\Omega\, \mu_\Omega\, c_\mathrm{BU}\, t_\mathrm{c}}{2\tau_\mathrm{sc}}.
\end{aligned} \tag{B.210}$$

Substituting the definitions of $c_{\tau\mathrm{min,B}}$ (Equation B.82) and $c_{\tau\mathrm{max,B}}$ (Equation B.84) into Equation B.210 and simplifying:

$$
\begin{aligned}
\beta^*_{\mathrm{sc,PS,B}} =& -\frac{c_{\mathrm{B2}}\left(1-\frac{\beta}{\mu_\Omega}\right)c_{\tau*,\mathrm{B}}\,t_\mathrm{c}}{c_{\tau*,\mathrm{B}}\,\tau_\mathrm{sc}} - \frac{\lambda_\Omega\,\mu_\Omega\,c_{\mathrm{BL}}\,t_\mathrm{c}}{2\tau_\mathrm{sc}} \\
&- c_{\mathrm{B2}}\left(1-\frac{\left(1-\frac{\beta}{\mu_\Omega}\right)c_{\tau*,\mathrm{B}}}{c_{\tau*,\mathrm{B}}}\right) \\
&+ \lambda_\Omega\,\mu_\Omega\,c_{\mathrm{BL}}\ln\left(\frac{c_{\tau*,\mathrm{B}}}{\left(1-\frac{\beta}{\mu_\Omega}\right)c_{\tau*,\mathrm{B}}}\right) + c_{\mathrm{B2}}\left(1-\frac{\left(1-\frac{\beta}{\mu_\Omega}\right)c_{\tau*,\mathrm{B}}}{c_{\tau*,\mathrm{B}}}\right) \\
&+ \frac{2c_{\mathrm{B2}}\,t_\mathrm{c}}{\tau_\mathrm{sc}} + \frac{\lambda_\Omega\,\mu_\Omega\,t_\mathrm{c}}{2\tau_\mathrm{sc}}\left(c_{\mathrm{BL}}-c_{\mathrm{BU}}\right) \\
&+ \lambda_\Omega\,\mu_\Omega\,c_{\mathrm{BU}}\ln\left(\frac{\left(1+\frac{\beta}{\mu_\Omega}\right)c_{\tau*,\mathrm{B}}}{c_{\tau*,\mathrm{B}}}\right) + c_{\mathrm{B2}}\left(1-\frac{\left(1+\frac{\beta}{\mu_\Omega}\right)c_{\tau*,\mathrm{B}}}{c_{\tau*,\mathrm{B}}}\right) \\
&+ c_{\mathrm{B2}}\left(\frac{\left(1+\frac{\beta}{\mu_\Omega}\right)c_{\tau*,\mathrm{B}}}{c_{\tau*,\mathrm{B}}}-1\right) \\
&- \frac{c_{\mathrm{B2}}\left(1+\frac{\beta}{\mu_\Omega}\right)c_{\tau*,\mathrm{B}}\,t_\mathrm{c}}{c_{\tau*,\mathrm{B}}\,\tau_\mathrm{sc}} + \frac{\lambda_\Omega\,\mu_\Omega\,c_{\mathrm{BU}}\,t_\mathrm{c}}{2\tau_\mathrm{sc}} \\
\beta^*_{\mathrm{sc,PS,B}} =& \lambda_\Omega\,\mu_\Omega\,c_{\mathrm{BU}}\ln\left(1+\frac{\beta}{\mu_\Omega}\right) - \lambda_\Omega\,\mu_\Omega\,c_{\mathrm{BL}}\ln\left(1-\frac{\beta}{\mu_\Omega}\right).
\end{aligned}
\tag{B.211}
$$

Furthermore, substituting the definitions of c_{BL} (Equation B.125) and c_{BU} (Equation B.126) into Equation B.211 and simplifying:

$$
\begin{aligned}
\beta^*_{\mathrm{sc,PS,B}} =& \lambda_\Omega\,\mu_\Omega\left(1+\frac{\mu_\Omega}{\beta}\right)\ln\left(1+\frac{\beta}{\mu_\Omega}\right) - \lambda_\Omega\,\mu_\Omega\left(1-\frac{\mu_\Omega}{\beta}\right)\ln\left(1-\frac{\beta}{\mu_\Omega}\right) \\
\beta^*_{\mathrm{sc,PS,B}} =& \lambda_\Omega\,\mu_\Omega\left[\ln\left(\frac{1+\frac{\beta}{\mu_\Omega}}{1-\frac{\beta}{\mu_\Omega}}\right) + \frac{\mu_\Omega}{\beta}\ln\left(1-\left(\frac{\beta}{\mu_\Omega}\right)^2\right)\right].
\end{aligned}
\tag{B.212}
$$

This solution (i.e. Equation B.212) assumes λ_Ω and μ_Ω are constant over the width of the scanning AAC transfer function (i.e. the AAC is operated with sufficiently high resolution, and the particle detector is operated with sufficiently low counting time).

B.10.1 Solving integral forms ($\beta^*_{sc,PS,Fx}$) of deconvolution parameter integral

Analytical solution for $\beta^*_{sc,PS,F1}$ (Equation B.207)

$\beta^*_{sc,PS,F1}$ (Equation B.207) is the same integral form as $\beta^*_{sc,LT,F1}$ (Equation B.165), therefore the solution (Equation B.169) derived in Section B.9.1 applies as follows:

$$\beta^*_{sc,PS,F1} = \int_{\tau_L}^{\tau_U} \frac{a}{\tau} d\tau = \boldsymbol{a \ln\left(\frac{\tau_U}{\tau_L}\right)}. \tag{B.213}$$

Analytical solution for $\beta^*_{sc,PS,F2}$ (Equation B.208)

$\beta^*_{sc,PS,F2}$ (Equation B.208) is the same integral form as $\beta^*_{sc,LT,F2}$ (Equation B.166), therefore the solution (Equation B.172) derived in Section B.9.1 applies as follows:

$$\beta^*_{sc,PS,F1} = \int_{\tau_L}^{\tau_U} \frac{a \ln\left(\frac{b}{\tau}\right)}{\tau} d\tau = \boldsymbol{-\frac{a}{2} \ln\left(\frac{b^2}{\tau_U \tau_L}\right) \ln\left(\frac{\tau_L}{\tau_U}\right)}. \tag{B.214}$$

Analytical solution for $\beta^*_{sc,PS,F3}$ (Equation B.209)

Based on Equation B.209:

$$\beta^*_{sc,PS,F3} = \int_{\tau_L}^{\tau_U} a \, d\tau = \boldsymbol{a(\tau_U - \tau_L)}. \tag{B.215}$$

B.10.2 Solving terms ($\beta^*_{\mathrm{sc,PS,B}x}$) of deconvolution parameter

Analytical solutions for $\beta^*_{\mathrm{sc,PS,B1}}$ and $\beta^*_{\mathrm{sc,PS,B7}}$ of Equation B.206

Based on term 1 (i.e. $\beta^*_{\mathrm{sc,PS,B1}}$) shown in Equation B.206:

$$\begin{aligned}
\beta^*_{\mathrm{sc,PS,B1}} &= \int_{\tau_{\mathrm{min,B}}}^{\tau_{\mathrm{min,B,tc}}} \frac{1}{\tau}\left[-\frac{\lambda_\Omega\,\mu_\Omega\,c_{\mathrm{BL}}}{t_{\mathrm{c}}}\left(t_{\mathrm{m}}-\tau_{\mathrm{sc}}\ln\left(\frac{c_{\tau\mathrm{min,B}}}{\tau}\right)\right)+\frac{c_{\mathrm{B2}}\,c_{\tau\mathrm{min,B}}}{c_{\tau*,\mathrm{B}}}\right]\mathrm{d}\tau \\
\beta^*_{\mathrm{sc,PS,B1}} &= \int_{\tau_{\mathrm{min,B}}}^{\tau_{\mathrm{min,B,tc}}}\left[-\frac{\lambda_\Omega\,\mu_\Omega\,c_{\mathrm{BL}}\,t_{\mathrm{m}}}{t_{\mathrm{c}}}+\frac{c_{\mathrm{B2}}\,c_{\tau\mathrm{min,B}}}{c_{\tau*,\mathrm{B}}}\right]\frac{1}{\tau}\mathrm{d}\tau \\
&\quad+\int_{\tau_{\mathrm{min,B}}}^{\tau_{\mathrm{min,B,tc}}}\frac{\lambda_\Omega\,\mu_\Omega\,c_{\mathrm{BL}}\,\tau_{\mathrm{sc}}}{t_{\mathrm{c}}}\frac{\ln\left(\frac{c_{\tau\mathrm{min,B}}}{\tau}\right)}{\tau}\mathrm{d}\tau.
\end{aligned} \tag{B.216}$$

Substituting the integral solutions of $\beta^*_{\mathrm{sc,PS,F1}}$ and $\beta^*_{\mathrm{sc,PS,F2}}$ (i.e. Equations B.213 and B.214) into Equation B.216 as follows:

$$\begin{aligned}
\beta^*_{\mathrm{sc,PS,B1}} &= \left[-\frac{\lambda_\Omega\,\mu_\Omega\,c_{\mathrm{BL}}\,t_{\mathrm{m}}}{t_{\mathrm{c}}}+\frac{c_{\mathrm{B2}}\,c_{\tau\mathrm{min,B}}}{c_{\tau*,\mathrm{B}}}\right]\ln\left(\frac{\tau_{\mathrm{min,B,tc}}}{\tau_{\mathrm{min,B}}}\right) \\
&\quad-\frac{\frac{\lambda_\Omega\,\mu_\Omega\,c_{\mathrm{BL}}\,\tau_{\mathrm{sc}}}{t_{\mathrm{c}}}}{2}\ln\left(\frac{c^2_{\tau\mathrm{min,B}}}{\tau_{\mathrm{min,B,tc}}\,\tau_{\mathrm{min,B}}}\right)\ln\left(\frac{\tau_{\mathrm{min,B}}}{\tau_{\mathrm{min,B,tc}}}\right).
\end{aligned} \tag{B.217}$$

Substituting the definitions of τ_x and $\tau_{x,\mathrm{tc}}$ (Equations B.43 and B.93, respectively) into Equation B.217 to convert from the particle relaxation time (τ) to the measurement time (t_{m}) domain:

$$\begin{aligned}
\beta^*_{\mathrm{sc,PS,B1}} &= \left[-\frac{\lambda_\Omega\,\mu_\Omega\,c_{\mathrm{BL}}\,t_{\mathrm{m}}}{t_{\mathrm{c}}}+\frac{c_{\mathrm{B2}}\,c_{\tau\mathrm{min,B}}}{c_{\tau*,\mathrm{B}}}\right]\ln\left(\frac{c_{\tau\mathrm{min,B}}\exp\left(\frac{-(t_{\mathrm{m}}+t_{\mathrm{c}})}{\tau_{\mathrm{sc}}}\right)}{c_{\tau\mathrm{min,B}}\exp\left(\frac{-t_{\mathrm{m}}}{\tau_{\mathrm{sc}}}\right)}\right) \\
&\quad-\frac{\lambda_\Omega\,\mu_\Omega\,c_{\mathrm{BL}}\,\tau_{\mathrm{sc}}}{2t_{\mathrm{c}}}\ln\left(\frac{c^2_{\tau\mathrm{min,B}}}{c_{\tau\mathrm{min,B}}\exp\left(\frac{-(t_{\mathrm{m}}+t_{\mathrm{c}})}{\tau_{\mathrm{sc}}}\right)c_{\tau\mathrm{min,B}}\exp\left(\frac{-t_{\mathrm{m}}}{\tau_{\mathrm{sc}}}\right)}\right) \\
&\quad\cdot\ln\left(\frac{c_{\tau\mathrm{min,B}}\exp\left(\frac{-t_{\mathrm{m}}}{\tau_{\mathrm{sc}}}\right)}{c_{\tau\mathrm{min,B}}\exp\left(\frac{-(t_{\mathrm{m}}+t_{\mathrm{c}})}{\tau_{\mathrm{sc}}}\right)}\right) \\
\beta^*_{\mathrm{sc,PS,B1}} &= -\frac{c_{\mathrm{B2}}\,c_{\tau\mathrm{min,B}}\,t_{\mathrm{c}}}{c_{\tau*,\mathrm{B}}\,\tau_{\mathrm{sc}}}-\frac{\lambda_\Omega\,\mu_\Omega\,c_{\mathrm{BL}}\,t_{\mathrm{c}}}{2\tau_{\mathrm{sc}}}.
\end{aligned} \tag{B.218}$$

Following the same approach, term 7 (i.e. $\beta^*_{\mathrm{sc,LT,7}}$) shown in Equation B.206 is equivalent to:

$$\begin{aligned}\beta^*_{\mathrm{sc,PS,B7}} &= \int_{\tau_{\mathrm{max,B}}}^{\tau_{\mathrm{max,B,tc}}} \frac{1}{\tau}\left[\frac{\lambda_\Omega\,\mu_\Omega\,c_{\mathrm{BU}}}{t_{\mathrm{c}}}\left(t_{\mathrm{m}}-\tau_{\mathrm{sc}}\ln\left(\frac{c_{\tau\mathrm{max,B}}}{\tau}\right)\right)+\frac{c_{\mathrm{B2}}\,c_{\tau\mathrm{max,B}}}{c_{\tau*,\mathrm{B}}}\right]\mathrm{d}\tau \\ \beta^*_{\mathrm{sc,PS,B7}} &= -\frac{c_{\mathrm{B2}}\,c_{\tau\mathrm{max,B}}\,t_{\mathrm{c}}}{c_{\tau*,\mathrm{B}}\,\tau_{\mathrm{sc}}}+\frac{\lambda_\Omega\,\mu_\Omega\,c_{\mathrm{BU}}\,t_{\mathrm{c}}}{2\tau_{\mathrm{sc}}}.\end{aligned} \tag{B.219}$$

Analytical solutions for $\beta^*_{sc,PS,B2}$ and $\beta^*_{sc,PS,B6}$ of Equation B.206

Based on term 2 (i.e. $\beta^*_{sc,PS,B2}$) shown in Equation B.206:

$$\begin{aligned}\beta^*_{sc,PS,B2} &= \int_{\tau_{min,B}}^{\tau^*_{sc,B}} \frac{1}{\tau}\left[-\frac{c_{B2}}{c_{\tau*,B}}\tau\exp\left(\frac{t_m}{\tau_{sc}}\right)\right]d\tau \\ \beta^*_{sc,PS,B2} &= \int_{\tau_{min,B}}^{\tau^*_{sc,B}} -\frac{c_{B2}}{c_{\tau*,B}}\exp\left(\frac{t_m}{\tau_{sc}}\right)d\tau.\end{aligned} \tag{B.220}$$

Substituting the integral solution of $\beta^*_{sc,PS,F3}$ (i.e. Equation B.215) into Equation B.220 as follows:

$$\beta^*_{sc,PS,B2} = -\frac{c_{B2}}{c_{\tau*,B}}\exp\left(\frac{t_m}{\tau_{sc}}\right)\left(\tau^*_{sc,B} - \tau_{min,B}\right). \tag{B.221}$$

Substituting the definition of τ_x (Equation B.43) into Equation B.221 to convert from the particle relaxation time (τ) to the measurement time (t_m) domain:

$$\begin{aligned}\beta^*_{sc,PS,B2} &= -\frac{c_{B2}}{c_{\tau*,B}}\exp\left(\frac{t_m}{\tau_{sc}}\right)\left(c_{\tau*,B}\exp\left(\frac{-t_m}{\tau_{sc}}\right) - c_{\tau min,B}\exp\left(\frac{-t_m}{\tau_{sc}}\right)\right) \\ \beta^*_{sc,PS,B2} &= -c_{B2}\left(1 - \frac{c_{\tau min,B}}{c_{\tau*,B}}\right).\end{aligned} \tag{B.222}$$

Following the same approach, term 6 (i.e. $\beta^*_{sc,LT,6}$) shown in Equation B.206 is equivalent to:

$$\begin{aligned}\beta^*_{sc,PS,B6} &= \int_{\tau^*_{sc,B}}^{\tau_{max,B}} \frac{1}{\tau}\left[\frac{c_{B2}}{c_{\tau*,B}}\tau\exp\left(\frac{t_m}{\tau_{sc}}\right)\right]d\tau \\ \beta^*_{sc,PS,B6} &= c_{B2}\left(\frac{c_{\tau max,B}}{c_{\tau*,B}} - 1\right).\end{aligned} \tag{B.223}$$

Analytical solutions for $\beta^*_{sc,PS,B3}$ and $\beta^*_{sc,PS,B5}$ of Equation B.206

Based on term 3 (i.e. $\beta^*_{sc,PS,B3}$) shown in Equation B.206:

$$\begin{aligned}\beta^*_{sc,PS,B3} &= \int_{\tau_{min,B,tc}}^{\tau^*_{sc,B,tc}} \frac{1}{\tau}\left[\lambda_\Omega\,\mu_\Omega\,c_{BL} + \frac{c_{B2}}{c_{\tau*,B}}\tau\exp\left(\frac{t_m+t_c}{\tau_{sc}}\right)\right]\mathrm{d}\tau \\ \beta^*_{sc,PS,B3} &= \int_{\tau_{min,B,tc}}^{\tau^*_{sc,B,tc}} \frac{\lambda_\Omega\,\mu_\Omega\,c_{BL}}{\tau}\mathrm{d}\tau + \int_{\tau_{min,B,tc}}^{\tau^*_{sc,B,tc}} \frac{c_{B2}}{c_{\tau*,B}}\exp\left(\frac{t_m+t_c}{\tau_{sc}}\right)\mathrm{d}\tau.\end{aligned} \tag{B.224}$$

Substituting the integral solutions of $\beta^*_{sc,PS,F1}$ and $\beta^*_{sc,PS,F3}$ (i.e. Equations B.213 and B.215) into Equation B.224 as follows:

$$\beta^*_{sc,PS,B3} = \lambda_\Omega\,\mu_\Omega\,c_{BL}\ln\left(\frac{\tau^*_{sc,B,tc}}{\tau_{min,B,tc}}\right) + \frac{c_{B2}}{c_{\tau*,B}}\exp\left(\frac{t_m+t_c}{\tau_{sc}}\right)\left(\tau^*_{sc,B,tc} - \tau_{min,B,tc}\right). \tag{B.225}$$

Substituting the definition of $\tau_{x,tc}$ (Equation B.93) into Equation B.225 to convert from the particle relaxation time (τ) to the measurement time (t_m) domain:

$$\begin{aligned}\beta^*_{sc,PS,B3} &= \lambda_\Omega\,\mu_\Omega\,c_{BL}\ln\left(\frac{c_{\tau*,B}\exp\left(\frac{-(t_m+t_c)}{\tau_{sc}}\right)}{c_{\tau min,B}\exp\left(\frac{-(t_m+t_c)}{\tau_{sc}}\right)}\right) \\ &\quad + \frac{c_{B2}}{c_{\tau*,B}}\exp\left(\frac{t_m+t_c}{\tau_{sc}}\right)\left(c_{\tau*,B}\exp\left(\frac{-(t_m+t_c)}{\tau_{sc}}\right) - c_{\tau min,B}\exp\left(\frac{-(t_m+t_c)}{\tau_{sc}}\right)\right) \\ \beta^*_{sc,PS,B3} &= \lambda_\Omega\,\mu_\Omega\,c_{BL}\ln\left(\frac{c_{\tau*,B}}{c_{\tau min,B}}\right) + c_{B2}\left(1 - \frac{c_{\tau min,B}}{c_{\tau*,B}}\right).\end{aligned} \tag{B.226}$$

Following the same approach, term 5 (i.e. $\beta^*_{sc,LT,5}$) shown in Equation B.206 is equivalent to:

$$\begin{aligned}\beta^*_{sc,PS,B5} &= \int_{\tau^*_{sc,B,tc}}^{\tau_{max,B,tc}} \frac{1}{\tau}\left[\lambda_\Omega\,\mu_\Omega\,c_{BU} - \frac{c_{B2}}{c_{\tau*,B}}\tau\exp\left(\frac{t_m+t_c}{\tau_{sc}}\right)\right]\mathrm{d}\tau \\ \beta^*_{sc,PS,B5} &= \lambda_\Omega\,\mu_\Omega\,c_{BU}\ln\left(\frac{c_{\tau max,B}}{c_{\tau*,B}}\right) + c_{B2}\left(1 - \frac{c_{\tau max,B}}{c_{\tau*,B}}\right).\end{aligned} \tag{B.227}$$

Analytical solution for $\beta^*_{\mathrm{sc,PS,B4}}$ of Equation B.206

Based on term 4 (i.e. $\beta^*_{\mathrm{sc,PS,B4}}$) shown in Equation B.206:

$$\begin{aligned}
\beta^*_{\mathrm{sc,PS,B4}} &= \int_{\tau^*_{\mathrm{sc,B}}}^{\tau^*_{\mathrm{sc,B,tc}}} \frac{1}{\tau}\left[\frac{\lambda_\Omega\,\mu_\Omega}{t_\mathrm{c}}\left(c_\mathrm{BL}-c_\mathrm{BU}\right)\left(t_\mathrm{m}-\tau_\mathrm{sc}\ln\left(\frac{c_{\tau*,\mathrm{B}}}{\tau}\right)\right)-2c_\mathrm{B2}\right]\mathrm{d}\tau \\
\beta^*_{\mathrm{sc,PS,B4}} &= \int_{\tau^*_{\mathrm{sc,B}}}^{\tau^*_{\mathrm{sc,B,tc}}} \left[\frac{\lambda_\Omega\,\mu_\Omega\,t_\mathrm{m}}{t_\mathrm{c}}\left(c_\mathrm{BL}-c_\mathrm{BU}\right)-2c_\mathrm{B2}\right]\frac{1}{\tau}\mathrm{d}\tau \\
&\quad+\int_{\tau^*_{\mathrm{sc,B}}}^{\tau^*_{\mathrm{sc,B,tc}}} -\frac{\lambda_\Omega\,\mu_\Omega\,\tau_\mathrm{sc}}{t_\mathrm{c}}\left(c_\mathrm{BL}-c_\mathrm{BU}\right)\frac{\ln\left(\frac{c_{\tau*,\mathrm{B}}}{\tau}\right)}{\tau}\mathrm{d}\tau.
\end{aligned} \tag{B.228}$$

Substituting the integral solutions of $\beta^*_{\mathrm{sc,PS,F1}}$ and $\beta^*_{\mathrm{sc,PS,F2}}$ (i.e. Equations B.213 and B.214) into Equation B.228 as follows:

$$\begin{aligned}
\beta^*_{\mathrm{sc,PS,B4}} &= \left[\frac{\lambda_\Omega\,\mu_\Omega\,t_\mathrm{m}}{t_\mathrm{c}}\left(c_\mathrm{BL}-c_\mathrm{BU}\right)-2c_\mathrm{B2}\right]\ln\left(\frac{\tau^*_{\mathrm{sc,B,tc}}}{\tau^*_{\mathrm{sc,B}}}\right) \\
&\quad+\frac{\frac{\lambda_\Omega\,\mu_\Omega\,\tau_\mathrm{sc}}{t_\mathrm{c}}\left(c_\mathrm{BL}-c_\mathrm{BU}\right)}{2}\ln\left(\frac{c^2_{\tau*,\mathrm{B}}}{\tau^*_{\mathrm{sc,B,tc}}\,\tau^*_{\mathrm{sc,B}}}\right)\ln\left(\frac{\tau^*_{\mathrm{sc,B}}}{\tau^*_{\mathrm{sc,B,tc}}}\right).
\end{aligned} \tag{B.229}$$

Substituting the definitions of τ_x and $\tau_{x,\mathrm{tc}}$ (Equations B.43 and B.93, respectively) into Equation B.229 to convert from the particle relaxation (τ) to the measurement time (t_m) domain:

$$\begin{aligned}
\beta^*_{\mathrm{sc,PS,B4}} &= \left[\frac{\lambda_\Omega\,\mu_\Omega\,t_\mathrm{m}}{t_\mathrm{c}}\left(c_\mathrm{BL}-c_\mathrm{BU}\right)-2c_\mathrm{B2}\right]\ln\left(\frac{c_{\tau*,\mathrm{B}}\exp\left(\frac{-(t_\mathrm{m}+t_\mathrm{c})}{\tau_\mathrm{sc}}\right)}{c_{\tau*,\mathrm{B}}\exp\left(\frac{-t_\mathrm{m}}{\tau_\mathrm{sc}}\right)}\right) \\
&\quad+\frac{\lambda_\Omega\,\mu_\Omega\,\tau_\mathrm{sc}}{2t_\mathrm{c}}\left(c_\mathrm{BL}-c_\mathrm{BU}\right)\ln\left(\frac{c^2_{\tau*,\mathrm{B}}}{c_{\tau*,\mathrm{B}}\exp\left(\frac{-(t_\mathrm{m}+t_\mathrm{c})}{\tau_\mathrm{sc}}\right)c_{\tau*,\mathrm{B}}\exp\left(\frac{-t_\mathrm{m}}{\tau_\mathrm{sc}}\right)}\right) \\
&\quad\cdot\ln\left(\frac{c_{\tau*,\mathrm{B}}\exp\left(\frac{-t_\mathrm{m}}{\tau_\mathrm{sc}}\right)}{c_{\tau*,\mathrm{B}}\exp\left(\frac{-(t_\mathrm{m}+t_\mathrm{c})}{\tau_\mathrm{sc}}\right)}\right) \\
\beta^*_{\mathrm{sc,PS,B4}} &= \frac{2c_\mathrm{B2}\,t_\mathrm{c}}{\tau_\mathrm{sc}}+\frac{\lambda_\Omega\,\mu_\Omega\,t_\mathrm{c}}{2\tau_\mathrm{sc}}\left(c_\mathrm{BL}-c_\mathrm{BU}\right).
\end{aligned} \tag{B.230}$$